Constant Pressure Langevin Dynamics: Theory and Application to the Study of Phase Behaviour in Core-Softened Systems.

David Quigley

A thesis submitted for the degree of

Doctor of Philosophy

University of York

Department of Physics

August 2005

Abstract

The principles of statistical mechanics relevant to atomistic computer simulation are reviewed. This is followed by a review of algorithms for generating statistical ensembles.

An alternative method for statistical sampling of the isothermal-isobaric ensemble is formulated, based on Langevin dynamics in non-Hamiltonian systems. This is successfully tested on the Lennard-Jones system, and with bond-order models. The potential advantages of this sampling method are discussed.

The sampling scheme is then combined with modern Monte-Carlo and other simulation methods such as free energy calculation and meta-dynamics. The resulting suite of simulation tools is validated and used to map phase diagrams for a suitably chosen sequence of core-softened 'shoulder' potentials in three-dimensions. These models have possible relevance to the anomalous behaviour of liquid water and the phenomenon of liquid-liquid phase transitions in single component systems.

As the sequence evolves from the simple Lennard-Jones potential, a decrease in melting temperature is measured, followed by the emergence of a simple-hexagonal solid phase. This undergoes a phase transition to close-packing at high pressure. The melting temperature of this simple-hexagonal phase can *decrease* with increasing pressure over an appreciable portion of the phase diagram. A metastable isostructural transition is also mapped, potentially consistent with theories of water-like anomalies.

By integrating along paths connecting different parameterisations of the model, values are found which allow this transition to extend into the supercooled liquid. No liquid-liquid phase transition is however present and no water-like anomalies are generated. The limitations of the model which prevent formation of a second liquid phase are discussed.

Contents

List of Figures

Acknowledgements

I would like to acknowledge the supervision of Dr Matt Probert who provided an introduction to an interesting area of research, the freedom to explore it in the directions which I found most interesting, coffee, and correction of stray mathematics on multiple occasions. The help of Professor Rex Godby is also gratefully acknowledged, particularly for pointing out that things were 'not obvious' when I was worried that they should be.

I would like to thank Drs Maff Glover, Kris Delaney and Lee Hill for teaching me everything I now know about research skills, and Drs Keith Refson and Phil Hasnip for patient help with research which sadly didn't make it into this thesis. Useful suggestions from Professor Carlos Vega are also acknowledged.

Author's Declaration

I hereby declare that the research presented in this thesis is my own work, except where acknowledged with appropriate citations. No part of this thesis has previously been submitted at this or any other university.

Chapter 1

Introduction

A major driving force in condensed matter physics is the desire to predict macroscopic properties of materials from the microscopic behaviour of atoms and molecules. A range of methods is available for modelling of atoms, ranging from semi-empirical to first-principles quantum mechanical calculations.

This thesis is concerned with modelling the behaviour of systems at finite temperature and pressure. Connection to the microscopic requires some consideration of dynamics, that is the manner in which atoms explore configurations other than the zero-temperature ground state. Macroscopic properties can be extracted from this information via the principles of statistical mechanics. In chapter 2 we briefly review the relevant results in statistical mechanics fundamental to implementing and interpreting atomistic simulations of this kind.

The extent of data required for such calculations invariably requires that such studies are conducted computationally. Increasing availability of high-speed computers has greatly increased the range of models which can be studied statistically. Ensuring that *correct* statistics are generated is critical. To this end, algorithms for sampling atomic data under finite temperature and pressure have been developed in parallel to the increase in computational power. A review of existing algorithms is presented in chapter 3. These fall broadly into two categories. The first involves explicit simulation of atomic motion and is termed 'molecular dynamics' or MD for obvious reasons. The second is based on generating a sequence of random configurations according to known probability laws. This is termed Monte-Carlo (MC) after the spiritual home of similar random processes. Both methods have merits, leading to interest in hybrid schemes.

One such method for generating finite temperature statistics is that of Langevin dynamics. An extension of this method to sampling at a specified pressure is presented in chapter 4. This involves theoretical complications when incorporating modern methods for pressure

control. These have not previously been addressed in the literature. Implementation issues are also addressed, and the scheme is tested on a selection of model atomic systems.

In addition to predicting mechanical properties from model atomic systems, the state in which a material will exist under given thermodynamic conditions is of clear importance. Mapping of phase diagrams is a significant challenge to computer modelling, requiring information which is not directly accessible in a simulation of feasible size. A variety of advanced simulation methods for addressing this problem is available. These are reviewed in chapter 5. Implementations of these methods (in some cases involving the new Langevin dynamics scheme) are validated against known results.

A topic of recent interest in the field of phase-transitions is the phenomenon of liquid polymorphism in single component systems. The existence of two distinct liquid phases for certain elements is a recent discovery, leading to many simulations and theoretical studies. Chapter 6 reviews developments in this field. Attempts to reproduce the phenomena in simulations of core-softened model systems are given particular attention. Perhaps surprisingly, the prediction of phase behaviour for even these very simple models is a non-trivial task.

One core-softened model in particular has been the source of some considerable interest. This so-called ‘shoulder potential‘ has been proposed as a model for reproducing the anomalous expansion of water under cooling. The mechanism by which this process occurs has been suggested to be a liquid-liquid phase transition. Chapter 7 presents the first detailed investigation of this model in three-dimensions. Phase behaviour is explored as a function of the model parameters, employing many of the methods discussed in chapter 5.

The data accumulated in chapter 7 will be employed in chapter 8 to extrapolate the phase diagram to alternate parameterisations of the shoulder model. The presence of anomalous liquid behaviour consistent with predictions in the literature is sought.

Conclusions which can be drawn from the work presented are given in chapter 9.

The nature of the work conducted has required considerable development of computer code. The atomic simulation code created by the author is named GOLDILOCS (originally for Generation Of Langevin Dynamics In Liquid One-Component Systems). This will be referred to where relevant during the thesis. The GOLDILOCS source code and brief documentation can be found on the accompanying floppy disk. Also included are scripts and untilties developed for this work.

Chapter 2

Atomistic Simulation

This chapter will cover the general theory of atomistic simulation methods with reference to molecular dynamics (MD) or Monte-Carlo (MC) methods. A review of specific algorithms and implementation details will be given in chapter 3.

For the purposes of this chapter, the term *particle* refers to a dynamical entity, the position of which is evolved according to our equations of motion. This will be a single atom in the case of all work reported here, but could be a superparticle representing collective behaviour such as that of a vortex line in a type II superconductor.

2.1 Basics

2.1.1 Notation

In statistical mechanics it is important to make the distinction between averaged values of thermodynamic variables and their associated estimators or "instantaneous values". In this thesis calligraphic fonts are used to represent estimators of pressure, temperature and volume, and standard math fonts to represent time averaged quantities. Hence $T = \langle \mathcal{T} \rangle$, $P = \langle \mathcal{P} \rangle$, and $V = \langle \mathcal{V} \rangle$. The symbol $\mathcal{H}$ will always be used to represent the instantaneous Hamiltonian of the simulated particles which has the time average E, the total energy. H represents the time averaged enthalpy $H = \langle \mathcal{H} + P\mathcal{V} \rangle$. The symbols K and U will represent the instantaneous kinetic and potential energy respectively. The entropy will be denoted by S.

We will use the notation $\mathbf{r}^N$ and $\mathbf{p}^N$ to refer to the position and momentum vectors of all N particles simulated. Reduced temperature $\beta = 1/k_B T$ will be used for brevity where possible.

2.1.2 Phase Space

The principles of classical statistical mechanics are formed around the concept of phase space. This is the space with one axis for each position and momentum coordinate of all particles. For a system of N particles in 3 dimensions, this is a $6N$ dimensional space. A single point in this $6N$ dimensional space describes the position and momentum of all particles, and can be described as a phase space *configuration*.

The fundamental premise of classical statistical mechanics states that phase space configurations with an equal energy are equally likely to be visited. We shall see later that this is only true for systems with equations of motion that can be derived from a Hamiltonian. The probability of finding the system at a given point in phase space is defined by the probability density distribution function,

$$\rho\left(\mathbf{r}^N, \mathbf{p}^N\right) = f_{ens}\left(\mathcal{H}\right)/\Omega_{ens}, \tag{2.1}$$

where f_{ens} is some ensemble specific function of the Hamiltonian normalised by the corresponding partition function, Ω_{ens}. The dynamics particles are therefore governed by the Hamiltonian, and the choice of ensemble.

2.1.3 Models

In order to extract meaningful data from the trajectory of our system in phase space, we must have a model for the Hamiltonian which represents the interactions between particles. In principle, any model which allows us to calculate the configurational potential energy of a system from its phase space coordinates will suffice. In practise, models used in atomistic simulations meet the following criteria:

- The potential energy is differentiable with respect to particle positions. This allows calculation of forces analytically[1] which is a strict requirement for MD simulations, and can be useful in MC.
- The potential energy is a function of the $3N$ position coordinates only. This avoids velocity dependent forces in MD and is essential for MC in which we generally sample only the configurational space.

Two common classes of models that will be used in this thesis are pair-potentials and Tersoff style bond-order potentials.

[1] Systems interacting via a discontinuous potential, such as hard spheres, are treated by event-based methods somewhat different to those employed here.

Pair Potentials

In a pair potential, the configurational energy is written as a sum over pairwise terms, for example the familiar potential of Lennard-Jones (1924) in which the Hamiltonian becomes

$$\mathcal{H} = \sum_{i=1}^{N} \dot{\mathbf{p}}_i^2/2m_i + U\left(\mathbf{r}^N\right) = \sum_{i=1}^{N} \dot{\mathbf{p}}_i^2/2m_i + \sum_{i=1}^{N}\sum_{j=i+1}^{N} \phi\left(r_{ij}\right), \tag{2.2}$$

with

$$\phi\left(r\right) = 4\epsilon\left[\left(\frac{\sigma}{r}\right)^{12} - \left(\frac{\sigma}{r}\right)^{6}\right]. \tag{2.3}$$

The calculation of forces (if required) in this model is trivial when also decomposed into pairwise terms.

$$\mathbf{f}_{ij} = -\frac{\mathrm{d}}{\mathrm{d}r_{ij}}\phi\left(r_{ij}\right)\hat{\mathbf{r}}_{ij} \tag{2.4}$$

This is a good model for argon ($\epsilon \approx 120k_BT, \sigma \approx 0.34nm$) and other noble gases. The r^{-6} term can be justified as a manifestation of instantaneous dipole-dipole interaction, however the repulsive term is chosen to be computationally convenient and more suitable forms have been discussed at length. For the purposes of this work we will consider the Lennard-Jones potential purely as a model system.

Bond Order Potentials

The work of Abell (1985) has demonstrated (using tight binding theory), that atomic interactions can be approximated as a sum of positive and repulsive pair components weighted according to the local bonding environment. This provides the basis of the Tersoff bond-order potential (Tersoff, 1986, 1988):

$$U\left(\mathbf{r}^N\right) = \sum_{i=1}^{N}\sum_{j=i+1}^{N} f_c\left(r_{ij}\right)\left[f_R\left(r_{ij}\right) + \bar{B}_{ij}f_A\left(r_{ij}\right)\right] \tag{2.5}$$

Here f_R and f_A are exponentials and $\bar{B}_{ij} = \left(B_{ij} + B_{ji}\right)/2$, where B_{ij} is written as a sum over all three body terms:

$$\begin{aligned} B_{ij} &= g\left(\zeta_{ij}\right) \\ \zeta_{ij} &= \sum_{k\neq i,j} f_c\left(r_{ik}\right) h_{ijk}\left(r_{ij}, r_{ik}, \theta_{ijk}\right) \end{aligned} \tag{2.6}$$

The three body function $h_{ijk}\left(r_{ij}, r_{ik}, \theta_{ijk}\right)$ is usually chosen to match structures and energies measured experimentally or calculated via *ab-initio* techniques. This has the desired

effect of the attractive part of the energy being lowered due to the presence of other bonds on the attracting atoms.

The cut-off function $f_c(r)$ is chosen such that the interactions are limited to nearest neighbours only, although some potentials apply energy corrections which depend on second nearest neighbours also. This function must be smooth for reasons outlined above.

Calculation of forces is more complicated than in the pure pair potential case due to the differentiation of the bond order term. This is described in the documentation of the GOLDILOCS code which accompanies this thesis.

2.2 Ensembles

A microscopic ensemble can be defined as a collection of configurations, upon each of which the same thermodynamic restrictions have been placed. The choice of constrained thermodynamic variable specifies the ensemble, which in turn will change the phase space probability distribution. Problems which we may wish to study are often amenable to simulation in a particular ensemble, or to combinations of simulations in different ensembles as we shall see. Several ensembles are described below.

2.2.1 Microcanonical (NVE)

Application of Hamilton's equations to a model Hamiltonian,

$$\dot{\mathbf{r}}_i = \partial\mathcal{H}/\partial\mathbf{p}_i \tag{2.7a}$$

$$\dot{\mathbf{p}}_i = -\partial\mathcal{H}/\partial\mathbf{r}_i \tag{2.7b}$$

yields appropriate equations of motion which can be integrated to obtain dynamical information about the system. Performing this simulation using N particles within a domain of fixed shape and volume leads to conservation of the Hamiltonian. This corresponds to the NVE ensemble in which the total energy, particle number and system volume are constrained. The system is isolated from the environment with the microcanonical partition function Ω;

$$\Omega = \frac{E_0}{N!h^{3N}} \int_{-\infty}^{\infty} \int_{D(V)} \mathrm{d}\mathbf{r}^N \mathrm{d}\mathbf{p}^N \delta\left[\mathcal{H}\left(\mathbf{r}^N, \mathbf{p}^N\right) - E_0\right] \tag{2.8}$$

where $\mathcal{H}$ is the Hamiltonian of the current configuration, E_0 is the (fixed) total energy and $D(V)$ is the domain defined by the simulation cell. The factor h is Planck's constant. This will always cancel when computing measureable quantities in simulations where the

atomic degrees of freedom are treated classically. The phase space probability density function is:

$$\rho_{NVE}\left(\mathbf{r}^N, \mathbf{p}^N\right) = \frac{\delta\left[\mathcal{H}\left(\mathbf{r}^N, \mathbf{p}^N\right) - \mathcal{H}_0\right]}{\Omega} \tag{2.9}$$

The energy E_0 defines a contour on the phase space energy surface to which the system is restricted. Hence the system explores all areas of phase space that are accessible to it, (those with the correct energy) with equal probability. This assumes ergodicity (see later) which is not always guaranteed.

This direct applicability of Hamilton's equations represents the most basic molecular dynamics simulation.

2.2.2 Canonical (NVT)

Most systems of interest are not isolated. Energy is exchanged with the environment leading to fluctuations in thermodynamic properties. We often consider an infinite system using periodic boundary conditions resulting in a super-lattice of image cells identical to the simulation cell. In this case the energy is constant on the scale of the simulation cell everywhere in our infinite system. In reality energy will pass between the cells in our lattice, making the energy in each individual cell fluctuate.

The canonical (NVT) ensemble captures the energy fluctuations by coupling the N particle system to a heat bath of constant temperature and infinite energy. This leads to the canonical partition function Q,

$$Q = \frac{1}{N!h^{3N}} \int_{-\infty}^{\infty} \int_{D(V)} \mathrm{d}\mathbf{r}^N \mathrm{d}\mathbf{p}^N \exp\left[-\beta\mathcal{H}\left(\mathbf{r}^N, \mathbf{p}^N\right)\right]. \tag{2.10}$$

The system now occupies a contour of constant Helmholtz potential $\mathcal{F} = U - TS$, while points on the $6N$ dimensional energy surface are visited with a probability dependent purely on their energy. Algorithms for correctly sampling this ensemble will be reviewed in the next chapter.

2.2.3 Isothermal-Isobaric (NPT)

Density fluctuations in our microscopic system may also be desirable. These can be reproduced by coupling the system to an external piston. This causes the volume of the system to change depending on the internal pressure, giving us the required density

fluctuation. This is the isobaric-isothermal (NPT) ensemble. with partition function Δ;

$$\Delta = \frac{1}{V_0 N! h^{3N}} \int_0^\infty \int_{-\infty}^\infty \int_{D(V)} \mathrm{d}\mathbf{r}^N \mathrm{d}\mathbf{p}^N \mathrm{d}V \exp\left[-\beta \mathcal{H}\left(\mathbf{r}^N, \mathbf{p}^N\right) - \beta P \mathcal{V}\right] \tag{2.11}$$

where P is the external pressure applied by the piston and V is the system volume. Note that in the case of periodic boundary conditions it is convenient to think of the external pressure as being due to particles in adjacent image cells rather than a macroscopic piston. The system is specified by the Gibbs free energy $F = U - TS + PV$, visiting configurations of equal enthalpy with equal probability. Again algorithms for producing this ensemble will be reviewed in the next chapter.

Isoenthalpic (NPH)

A microcanonical counterpart to this ensemble can be conceived in which the system is coupled only to the external piston, and not to a heat bath. Such a system would conserve enthalpy with partition function

$$\Omega_{NPH} = \frac{H_0}{N! h^{3N}} \int_{-\infty}^\infty \int_{D(V)} \mathrm{d}\mathbf{r}^N \mathrm{d}\mathbf{p}^N \delta\left[\mathcal{H}\left(\mathbf{r}^N, \mathbf{p}^N\right) + P\mathcal{V} - H_0\right]. \tag{2.12}$$

We shall refer to this as the isoenthalpic (NPH) ensemble.

2.2.4 Grand Canonical Ensemble (μVT)

An alternative route to reproducing density fluctuations is to couple the system to a particle reservoir at constant chemical potential μ. Exchange of particles between the N particle system and this reservoir produce density fluctuations. The grand canonical partition function,

$$\Xi = \frac{1}{N! h^{3N}} \int_{-\infty}^\infty \int_{D(V)} \mathrm{d}\mathbf{r}^N \mathrm{d}\mathbf{p}^N \exp\left[-\beta \mathcal{H}\left(\mathbf{r}^N\right) + \beta \mu N\right] \tag{2.13}$$

indicates that configurations with equal $\mathcal{H} - \mu N$ will be visited with equal probability.

2.2.5 The Thermodynamic Limit

It would seem from the above that only the NPT and μPT ensembles represent truly physical conditions for a simulation. In fact, results obtained from any ensemble are equally valid when extrapolated to the $N = \infty$ case. This is the thermodynamic limit,

corresponding the the bulk material in which we are interested. In this regime, averages computed from all of the above ensembles are equivalent.

2.3 Sampling

The numerical work in this thesis will make extensive use of the two most widely used computational methods for obtaining statistical properties of model Hamiltonians. The goal is the same for each, to generate large numbers of sample configurations distributed in accordance with an ensemble probability function.

2.3.1 Monte-Carlo

The use of Monte-Carlo sampling to integrate over ensemble configurations was pioneered by Metropolis *et al.* (1953). In the Metropolis method, a Markov chain of configurations is linked by random moves in one or more degrees of freedom. A move from state m to state n is accepted with probability

$$P_{acc} = \frac{\rho^n}{\rho^m} = \frac{f^n_{ens}}{f^m_{ens}}. \tag{2.14}$$

It is easy to show that the resulting chain of configurations is distributed according to the specified ensemble. Typically, only position coordinates are sampled, as the momentum space dependence of most properties can be determined analytically (see section 2.4.3). Details of the Metropolis method for sampling the above ensembles are reviewed in chapter 3.

2.3.2 Molecular Dynamics

The term Molecular Dynamics generally refers to the computational method in which the phase space of a system is explored by numerically integrating equations of motion. It should be stressed that the *only* MD method in which the resulting trajectories are in any way "real" are those which integrate Hamilton's equations of motion. This approach was pioneered initially in an event-based hard sphere system by Alder and Wainwright (1957), with uniform time-step work for soft spheres first performed by Gibson *et al.* (1960). Early work on modelling bulk properties of argon using the Lennard-Jones potential was conducted by Rahman (1964) and Verlet (1967) who introduced many important algorithmic developments.

These early simulations were restricted to the microcanonical ensemble. Attempts were made to include temperature by periodically adjusting particle velocities. Such methods are now known to generate incorrectly distributed phase space configurations. A survey of molecular dynamics schemes for correct ensemble sampling will be reviewed in chapter 3. In each of these methods the dynamics of the particles are purely fictitious, employing modified equations of motion. Only averaged quantities over configurations sampled from these fictitious trajectories correspond to "real" properties.

2.3.3 Detailed Balance

To reach equilibrium, the entropy of a system must maximise to a constant value. This has consequences for the microscopic behaviour of the system which can be expressed through the principle of detailed balance. This can be expressed as

$$P\left(i \rightarrow j\right) \exp\left(-E_j/k_B T\right) = P\left(j \rightarrow i\right) \exp\left(-E_i/k_B T\right) \tag{2.15}$$

where $P(i \rightarrow j)$ represents the probability of traversing the path between configurations i and j. It follows that for configurations of equal energy, the forward and reverse paths are equally probable. Two specific requirements of detailed balance are presented below, the first applicable to molecular dynamics simulations, and the second to Monte-Carlo methods.

Note that methods exist for non-equilibrium atomistic simulation, but these will not be covered here. However, simulations of metastable states (such as supercooled liquids) can be conducted using equilibrium methods provided that the timescale of the simulation is short, i.e. shorter than the lifetime of the metastable state. In this limit ρ_{ens} will be constant over the length of the simulation.

Liouville Theorem

The behavior of a system has so far been represented by the probability ρ of it visiting a point in phase space. Consider the case where ρ could be a function of time as well as phase space. This implies that either the ensemble changes at some point in time, or that the Boltzmann factor of a given configuration depends on the time at which it is evaluated. Neither of these two scenarios is physical (in thermal equilibrium) if all variables in the phase space are accounted for. For a system of particles in a fixed ensemble the total time

derivative of ρ is therefore zero, and hence

$$\frac{\mathrm{d}\rho}{\mathrm{d}t} = \frac{\partial\rho}{\partial t} + \sum_{j}^{N_f} \dot{q}_j \frac{\partial\rho}{\partial q_j} + \dot{p}_j \frac{\partial\rho}{\partial p_j} = 0 \tag{2.16}$$

where q_j are the generalised coordinates of all N_f degrees of freedom in the entire system and p_j are the corresponding momenta. This is the Liouville theorem and holds for all Hamiltonian systems such as the NVE ensemble described above. It will be seen later that to produce the NVT and NPT ensembles use is often made of an extended phase space in which the Liouville theorem may be incorrect and must be generalised. However ρ in the $6N$ dimensional particle subspace must obey the Liouville theorem as stated in equation 2.16 for the simulation to be physical. This is an important test of the validity of a molecular dynamics simulation.

The stationary nature of the probability function implies time *reversibility*, a weaker condition than adherence to the Liouville equation. A system which satisfies this stronger requirement is often termed to be *symplectic*.

Markov Chain Symmetry

In the simplest Monte-Carlo method, moves are accepted between state i and state j with probability purely dependent on the initial and final energies;

$$P_{acc}(i \to j) = \max\left[1, \frac{\exp(-E_j/k_BT)}{\exp(-E_i/k_BT)}\right] \tag{2.17}$$

which can be represented as a matrix element M_{ij}. It is clear that equation 2.15 imposes a certain symmetry upon this matrix, which will only be preserved if the probability of *attempting* move $i \to j$ is equal to that for $j \to i$. This requires that at each step along a Markov chain, trail moves are made in *randomly* selected degrees of freedom. Any other selection method, (e.g. sequential) will eliminate a subset of possible moves (in particular reversal of the previous move) and lead to incorrect sampling. This requirement will be imposed strictly on all MC simulation conducted in this thesis.

2.3.4 Ergodicity

The issue of ergodicity is fundamental to any simulation from which physical data is to be extracted. The exact definition of ergodicity varies considerably between sources. An attempt at a comprehensive definition is given below.

Consider the quantity A which is a function of all phase space coordinates. Obtaining a meaningful mean and variance for this quantity requires many samples of independent phase space configurations distributed according to the probability density function ρ_{ens}. This defines the concept of an *ensemble average*. In a simulation which computes many sequential configurations, the mean and variance of these samples are equivalent to those computed over an ensemble if the following conditions are met.

1. The sample interval is greater than any correlation interval.
2. Our algorithm for generating configurations preserves the phase space probability function, i.e. is *symplectic*.
3. The simulation is of sufficient length that the distribution of samples converges to that specified by ρ_{ens}.

Failure to meet these conditions will generate incorrect statistics. Adherence to point 1 is easily accomplished once an estimate of the correlation interval is known, e.g. from the method of block averages (see e.g. Allen and Tildesley (1987)). Point two is dealt with by ensuring detailed balance. Point three requires that given sufficient time, a system will explore all areas of phase space available to it. This is the ergodic hypothesis and is yet to be rigorously proved for a single system. However it can be demonstrated to be true for systems with known ρ_{ens}. For example the phase space distribution of the canonical harmonic oscillator has become an important benchmark. If a sampling algorithm correctly generates this distribution it is generally assumed to be ergodic for all systems.

An ergodic system therefore, is one which samples phase space configurations with the correct probability density. It follows that for an ergodic system, there must be a *single* stationary probability density function. Time averages calculated during thermodynamically irreversible processes (such as glass transitions) are *not* equivalent to ensemble averages. Such processes, often referred to as containing non-ergodic traps, must be treated by other methods.

2.3.5 Finite Size Effects

As well as ensuring samples can be considered uncorrelated in time, it must be ensured that the system is sufficiently large to represent the system of interest. Using periodic boundary conditions, the simulation cell plus its image cells make up a superlattice, with the motion in each cell being perfectly correlated with the the motion in all other cells. Clearly this is unphysical and does not represent the thermodynamic limit. In order to ensure that this effect does not corrupt sampling, the size of the simulation cell must be

greater than the natural correlation length of the system. Correlations between particles in adjacent image cells are thereby screened and so do not affect the dynamics of the system.

Such large simulations are not always tractable, requiring analysis and correction of the finite size error in ensemble averages. The extent of this error may depend on the specific quantity in question as well as the state point at which it is evaluated. In particular, diverging correlations in the region of critical phenomena lead to substantial finite size error.

A strictly imposed requirement in all simulations reported here is adherence to the minimum image criterion. The simulation cell is of sufficient size that each particle interacts with only a single instance of any other particle, *not* with multiple images. For most simulations reported in this work, the simulation cell is orthorhombic and enforceing this is trivial. In some cases however, the cell can distort significantly requiring careful checks of this criterion.

2.4 Useful results

2.4.1 Fluctuations

Given the phase space probability density function for an ensemble as defined above, and the ergodic hypothesis, the time average of a sampled quantity A can be written as:

$$\langle A \rangle_{ens} = \frac{1}{\Omega_{ens}} \int_0^\infty \int_{-\infty}^\infty \int_{D(V)} A\left(\mathbf{r}^N, \mathbf{p}^N, V\right) \rho_{ens}\left(\mathbf{r}^N, \mathbf{p}^N, V\right) \mathrm{d}\mathbf{r}^N \mathrm{d}\mathbf{p}^N \mathrm{d}V \quad (2.18)$$

where we have allowed for a dependence on volume in the phase space density function ρ (NPT case) or in A itself (e.g. enthalpy.) Similarly we can write down an expression for the variance in A.

$$\left\langle \delta A^2 \right\rangle = \frac{1}{\Omega_{ens}} \int_0^\infty \int_{-\infty}^\infty \int_{D(V)} \left[A\left(\mathbf{r}^N, \mathbf{p}^N, V\right) - \langle A \rangle_{ens}\right]^2 \times \rho_{ens}\left(\mathbf{r}^N, \mathbf{p}^N, V\right) \mathrm{d}\mathbf{r}^N \mathrm{d}\mathbf{p}^N \mathrm{d}V \quad (2.19)$$

The variance about the mean, and therefore the magnitude of fluctuations in thermodynamic quantities is hence ensemble dependent. In the NVT ensemble, the fluctuations in the energy estimator $\mathcal{H}$ can be shown to be:

$$\left\langle \delta \mathcal{H}^2 \right\rangle_{NVT} = k_B T^2 C_V \quad (2.20)$$

where $C_V = (\partial E/\partial T)_V$ is the heat capacity at constant volume. These fluctuations can be split into contributions from the kinetic and potential energies:

$$\left\langle \delta K^2 \right\rangle_{NVT} = \frac{3N\left(k_B T\right)^2}{2} \tag{2.21}$$

$$\left\langle \delta U^2 \right\rangle_{NVT} = k_B T^2 \left(C_V - \frac{3}{2} N k_B \right) \tag{2.22}$$

The distribution of $\mathcal{H}$,K and U samples is dictated by the ensemble, and is easily shown to be Gaussian for all cases of interest.

In the NPT ensemble the important fluctuations are those present in the volume and enthalpy.

$$\left\langle \delta \mathcal{V}^2 \right\rangle_{NPT} = V k_B T \beta_T \tag{2.23}$$

$$\left\langle \delta \left(\mathcal{H} + P\mathcal{V} \right)^2 \right\rangle_{NPT} = k_B T^2 C_P \tag{2.24}$$

where $\beta_T = -V^{-1} \left(\partial V/\partial P\right)_T$ is the bulk modulus and $C_P = \left(\partial H/\partial T\right)_P$ is the heat capacity at constant pressure. Hence a correctly barostatted system will undergo Gaussian volume fluctuations with standard deviation $\left(V k_B T \beta_T\right)^{\frac{1}{2}}$. These results will be used to test the fluctuation behaviour of sampling algorithms.

2.4.2 Virial Estimators

Temperature

The classical virial theorem states

$$\left\langle x_i \frac{\partial \mathcal{H}}{\partial x_i} \right\rangle = k_B T \delta_{ij} \tag{2.25}$$

where x_i represents a single position or momentum phase space coordinate. Summing over contributions from all $3N$ momentum coordinates, we obtain the well known result

$$\left\langle \sum_{i=1}^{N} \frac{p_i^2}{2m_i} \right\rangle = \frac{3}{2} k_B \left\langle \mathcal{T} \right\rangle = \frac{3}{2} k_B T \tag{2.26}$$

which defines the temperature estimator $\mathcal{T}$. This has been stated here only to emphasise that we have used the relationship

$$\nabla_{p_i} \mathcal{H} = \frac{p_i}{m_i} \tag{2.27}$$

which assumes the system has a Hamiltonian. We will later deal with extended non-Hamiltonian systems. These require the caveat that the temperature computed from this estimator is that of the particle subsystem only, *not* that of the total extended system.

Pressure Estimator

We seek a pressure estimator $\mathcal{P}$,

$$\mathcal{P} = -\frac{\mathrm{d}\mathcal{H}}{\mathrm{d}\mathcal{V}} = -\sum_{i=1}^{N} \nabla_{r_i}\mathcal{H} \cdot \frac{\mathrm{d}\mathbf{r}_i}{\mathrm{d}\mathcal{V}} - \sum_{i=1}^{N} \nabla_{p_i}\mathcal{H} \cdot \frac{\mathrm{d}\mathbf{p}_i}{\mathrm{d}\mathcal{V}} - \frac{\partial\mathcal{H}}{\partial\mathcal{V}}. \tag{2.28}$$

If we consider a cubic simulation cell, and introduce scaled position and momentum coordinates such that

$$\begin{aligned} \mathbf{r}_i &= \mathbf{s}_i\mathcal{V}^{1/3} \\ \mathbf{p}_i &= m_i\dot{\mathbf{s}}_i\mathcal{V}^{1/3} \end{aligned} \tag{2.29}$$

then equation 2.28 reduces to

$$\mathcal{P} = \frac{Nk_B\mathcal{T}}{\mathcal{V}} + \frac{1}{3\mathcal{V}}\sum_{i=1}^{N}\mathbf{r}_i \cdot \mathbf{f}_i - \frac{\partial\mathcal{H}}{\partial\mathcal{V}} \tag{2.30}$$

where we have used equation 2.26 above and employed

$$\nabla_{r_i}\mathcal{H} = -\mathbf{f}_i. \tag{2.31}$$

which may be untrue in extended non-Hamiltonian systems. It should be emphasised that in such cases the "instantaneous pressure" will include contributions from the extended (possibly non-Hamiltonian) components which must cancel over the ensemble average if the simulation is correct. The pressure estimator given by equation 2.30 is therefore still appropriate.

The more general expression for the pressure tensor in a simulation cell of arbitrary shape is

$$\begin{aligned} \mathcal{P}_{\alpha,\beta} &= \frac{1}{\mathcal{V}}\left[\sum_{i=1}^{N}\frac{\left(\mathbf{p}_i\right)_\alpha\left(\mathbf{p}_i\right)_\beta}{m_i} + \left(\mathbf{r}_i\right)_\alpha\left(\mathbf{f}_i\right)_\beta - \left(\phi'\mathbf{h}^T\right)_{\alpha,\beta}\right] \\ \left(\phi'\right)_{\alpha,\beta} &= \frac{\partial\phi\left(\mathbf{r}^N,\mathbf{h}\right)}{\partial\left(\mathbf{h}\right)_{\alpha,\beta}} \end{aligned} \tag{2.32}$$

where $\mathbf{h}$ is the matrix of cell vectors.

$$\mathbf{h} = \begin{pmatrix} A_x & B_x & C_x \\ A_y & B_y & C_y \\ A_z & B_z & C_z \end{pmatrix}. \tag{2.33}$$

In Monte-Carlo simulations, the momentum phase space coordinates are generally not sampled, in which case the first term in equation 2.30 is replaced by its time average, i.e. the ideal gas pressure.

2.4.3 Free Energies and the Ideal Gas

The thermodynamics of the ideal gas will be required many times when comparing free energies calculated using various MD and MD based methods, or when calculating ensemble averages via an appropriate estimator as we have just seen for pressure. This warrants a brief review here to avoid inconsistency later.

Consider the following decomposition of the canonical partition function for interacting identical particles,

$$Q = \frac{1}{N!h^{3N}} \int_{D(V)} \mathrm{d}\mathbf{r}^N \exp\left[-\beta U\left(\mathbf{r}^N\right)\right] \int_{-\infty}^{\infty} \mathrm{d}\mathbf{p}^N \exp\left[-\beta \sum_{i=1}^{N} \frac{\mathbf{p}_i^2}{2m}\right]. \tag{2.34}$$

The integral over momentum space is easily evaluated as

$$P = \left(\frac{2\pi m}{\beta}\right)^{3N/2} \tag{2.35}$$

which is the same for all such systems. For the ideal gas ($U = 0$) we now have

$$\begin{aligned} Q_{id} &= \frac{V^N}{N!h^{3N}} \left(\frac{2\pi m}{\beta}\right)^{3N/2} \\ Q_{id} &= \frac{V^N}{N!\Lambda^{3N}} \end{aligned} \tag{2.36}$$

where we have identified the thermal de Broglie wavelength Λ. Equation 2.34 can be written as

$$\begin{aligned} Q &= \frac{1}{N!\Lambda^{3N}} \int_{D(V)} \mathrm{d}\mathbf{r}^N \exp\left[-\beta U\left(\mathbf{r}^N\right)\right] \\ Q &= \frac{Z(N,V,T)}{N!\Lambda^{3N}}. \end{aligned} \tag{2.37}$$

Z is the configurational partition function, i.e. that sampled by the most basic Monte-Carlo methods. Equivalently in the isothermal-isobaric ensemble

$$Z(N,P,T) = \int_{-\infty}^{\infty}\int_{D(\mathcal{V})} \mathrm{d}\mathbf{r}^N \mathrm{d}\mathcal{V} \exp\left[-\beta U\left(\mathbf{r}^N\right) - \beta P\mathcal{V}\right]. \tag{2.38}$$

A quantity often computed is the *residual* free energy. This is the total free energy minus that of the ideal gas under the same thermodynamic constraints. In the canonical ensemble the fundamental free energy is the Helmholtz potential F,

$$\beta F = -\ln Q = 3N\ln\Lambda + \ln N! - \ln Z(N,V,T) \tag{2.39}$$

which for the ideal gas becomes

$$\begin{aligned} \beta F_{id} &= 3N\ln\Lambda + \ln N! - N\ln V \\ &= 3N\ln\Lambda + N\ln\rho - N \end{aligned} \tag{2.40}$$

after employing Stirling's approximation ($\ln N! = N\ln N - N$) for large N and $\rho = N/V$. This depends only on the temperature and density, and hence the excess Helmholtz potential is appropriate for comparing systems for which these quantities are identical. In the isobaric-isothermal ensemble, the fundamental free energy is the Gibbs potential G,

$$\begin{aligned} \beta G &= -\ln\Delta = 3N\ln\Lambda + \ln N! - \ln Z(N,P,T) \\ &= \beta F + \beta PV \end{aligned} \tag{2.41}$$

which for the ideal gas becomes

$$\begin{aligned} \beta G_{id} &= \beta F_{id} + N \\ &= 3N\ln\Lambda + \ln N! - N\ln\left[Nk_BT/P\right] + N. \end{aligned} \tag{2.42}$$

The excess free energy is now the total, minus that of an ideal gas at the same temperature and pressure. This is useful, for example, in comparing the free energy of two phases along an isobar.

We will also make use of the chemical potential μ, which for a single component system is defined as either

$$\mu = \frac{\partial F}{\partial N} = \lim_{N\to\infty}\left[F(N+1) - F(N)\right] \tag{2.43}$$

for a system at fixed volume, or

$$\mu = \frac{\partial G}{\partial N} = \lim_{N\to\infty}\left[G(N+1) - G(N)\right] \tag{2.44}$$

if at fixed pressure. If we introduce the *specific* free energies $f = F/N$ and $g = G/N$ then the chemical potential (for a single component system) is identically the free energy per particle. We will utilise this relationship when combining chemical potential and free energy methods to locate phase transitions.

Chapter 3

Methods

In this chapter, existing techniques as surveyed for obtaining correct ensemble sampling from either MD or MC simulations. As we will see in chapter 5, the ability to generate accurate ensemble averges on demand is key to the calculation of free energies, and hence the study of phase behavior in model systems. Some consideration is also given to efficient implementation of these methods. Those employed in the GOLDILOCS code are noted where relevant. A new sampling method based on Langevin dynamics in non-Hamiltonian systems is presented in chapter 4.

3.1 Temperature Control in Molecular Dynamics

In this section methods for performing molecular dynamics in the canonical ensemble are discussed. Attention is focused on extended system methods which generate correctly distributed phase space trajectories. In particular the development of the Nosé-Hoover thermostat is explored, this being the more widely used scheme, and the standard against which new methods are generally tested.

3.1.1 Early Methods

Early attempts to extend molecular dynamics beyond the microcanonical ensemble fall broadly into two categories. The first involves direct control of the kinetic energy. In a popular approach, the velocity of all particles is periodically rescaled such that the kinetic energy instantaneously matches the desired temperature. The resulting phase space trajectories are discontinuous. This is rectified in the thermostat of Berendsen *et al.* (1984) in which the rescaling takes place over a specified relaxation time. These methods are used in the GOLDILOCS code only to locate an appropriate constant energy countour in

NVE simulations. They are switched off when sampling data. Rescaling methods do not produce trajectories corresponding to the canonical ensemble.

Methods in which the kinetic energy is held constant via Gauss' principle of least constraint have also been widely employed. Clearly these do not correspond to the canonical ensemble in which the kinetic energy fluctuates. In general, the early thermostats based on this principle are not useful for ensemble sampling. However a recent isokinetic method which guarantees canonical sampling of the configurational subspace will be briefly discussed in section 3.1.3.

In the second category, the particles are subjected to some stochastic process which alters their momenta. For example, in the thermostat employed by Andersen (1980), each particle undergoes a fictitious collision at a random interval. After each collision, a new velocity is assigned from the Maxwell Boltzmann distribution. As with the periodic rescaling method, the trajectories are discontinuous and irreversible.

Stochastic thermostats based on a Langevin equation will be covered in chapter 4.

3.1.2 The Nosé-Hoover Thermostat

Andersen (1980) suggested that it may be possible to construct a Hamiltonian with an auxilliary degree of freedom behaving as a heat bath. This led to the formulation of several such schemes (Hoover *et al.*, 1980; Nosé, 1984a) which were unified by Nosé (1984b). This method controls temperature using continuous dynamics. The method is analogous to the Andersen barostat method (see below). Instead of spatial dimensions scaled according to the barostat variable $\mathcal{V}$ the temporal dimension is scaled according to a new variable s such that

$$\begin{aligned} \mathbf{r}_i &= \mathbf{r}'_i \\ \mathbf{p}_i &= \mathbf{p}'_i/s \\ t &= \int^t \frac{\mathrm{d}t}{s}. \end{aligned} \tag{3.1}$$

where primes represent 'virtual' (scaled) variables. Changes in s will therefore influence velocity. The potential energy term associated with s in the Hamiltonian is then tuned such that s fluctuates and the resulting equations of motion lead to the correct partition function for the particle phase space, i.e. a function which reduces to equation 2.10 on integrating out the extended variables. The Nosé Hamiltonian is

$$H = \sum_{i=1}^{N} \frac{\mathbf{p}_i'^2}{2m_i s^2} + U\left(\mathbf{r}^N\right) + \frac{p_s^2}{2Q} + (3N+1)\, k_B T \ln s. \tag{3.2}$$

Here p_s is the conjugate momentum to s and Q is the fictitious mass associated with its motion. This results in the following equations of motion in the virtual variables;

$$\dot{\mathbf{r}}_i' = \mathbf{p}_i'/m_i s^2 \tag{3.3a}$$
$$\dot{\mathbf{p}}_i' = -\nabla_{\mathbf{r}_i} U\left(\mathbf{r}^N\right) \tag{3.3b}$$
$$\dot{s} = p_s/Q \tag{3.3c}$$
$$\dot{p}_s = \left[\sum_{i=1}^{N} \frac{\mathbf{p}_i'^2}{2m_i s^2} - (3N+1)\, k_B T\right]/s \tag{3.3d}$$

where dots denote derivatives with respect to t'. Performing a simulation in these variables necessitates sampling at non-uniform intervals in real time, which causes difficulties. The equations of motion can be transformed into real variables by the use of equations 3.1 (along with $p_s = p_s'/s$) leading to the following equations of motion.

$$\dot{\mathbf{r}}_i = \mathbf{p}_i/m_i \tag{3.4a}$$
$$\dot{\mathbf{p}}_i = -\nabla_{\mathbf{r}_i} U\left(\mathbf{r}^N\right) - s p_s \mathbf{p}_i/Q \tag{3.4b}$$
$$\dot{s} = s^2 p_s/Q \tag{3.4c}$$
$$\dot{p}_s = \left[\sum_{i=1}^{N} \mathbf{p}_i^2/m_i - 3N k_B T\right]/s - s^2 p_s/Q. \tag{3.4d}$$

Dots now denote derivatives with respect to t. Although these conserve the equivalent transformation of equation 3.2 they cannot be derived from it. The transformation is therefore non-canonical, leading to a non-Hamiltonian system of equations. The consequences of this are explored in the next chapter.

An alternative form of these equations in real variables was introduced by Hoover (1985). By taking equations 3.3a and rescaling the time such that $\mathrm{d}t_{old} = s\mathrm{d}t_{new}$ the variable s can be eliminated. The only influence of the thermostat on the equations of motion is the thermostat velocity p_s/Q which Hoover termed the friction coefficient ζ. The resulting NVT equations of motion are

$$\dot{\mathbf{r}}_i = \mathbf{p}_i/m_i \tag{3.5a}$$
$$\dot{\mathbf{p}}_i = -\nabla_{\mathbf{r}_i} U\left(\mathbf{r}^N\right) - \zeta \mathbf{p_i} \tag{3.5b}$$
$$\dot{\zeta} = \left[\sum_{i=1}^{N} \mathbf{p}_i^2/m_i - 3N k_B T\right]/Q. \tag{3.5c}$$

Hoover tested these equations on the one-dimensional harmonic oscillator and showed that phase space was not explored according to the appropriate phase space density function, (which can of course be calculated exactly). He attributed his results to the system

not being sufficiently chaotic, and hence it is generally assumed that this lack of ergodicity is not a problem in large N simulations.

A simple idea to introduce increased chaotic behavior in the Hoover scheme was introduced by Martyna *et al.* (1992). In this scheme a chain of M thermostats is used. The first thermostat is coupled to the particle degrees of freedom. The second thermostat is coupled to the first and so on. The following modifications to the particle equations of motion are made.

$$\dot{\mathbf{p}}_i = -\nabla_{\mathbf{r}_i} U\left(\mathbf{r}^N\right) - \zeta_1 \mathbf{p_i}$$

For the 1st thermostat ($i = 1$):

$$\dot{\zeta}_1 = \left[\sum_{i=1}^{N} \mathbf{p}_i^2/m_i - 3Nk_BT\right]/Q_1 - \zeta_2\zeta_1. \tag{3.6}$$

For $i = 2$ to $i = M - 1$:

$$\dot{\zeta}_i = \left[Q_{i-1}\zeta_{i-1}^2 - k_BT\right]/Q_i - \zeta_{i+1}\zeta_i. \tag{3.7}$$

For $i = M$:

$$\dot{\zeta}_m = \left[Q_{M-1}\zeta_{M-1}^2 - k_BT\right]/Q_M. \tag{3.8}$$

This extension overcomes the lack of ergodicity in the Nosé-Hoover scheme and produces the correct phase space density function for a single harmonic oscillator. However, as was observed by Smargiassi and Madden (1995), the correct phase space distribution is *not* obtained when an ensemble of independent harmonic oscillators is connected to a single Nosé-Hoover chain. The problem can be surmounted by coupling each degree of freedom degree to a separate chain of thermostats in a so called "massive thermostatting" scheme. It has also been noted, in contrast to the single thermostat case, that chains of Nosé-Hoover thermostats do not correctly sample away from equilibrium. A simple modification of the chain scheme has been proposed by Branca (2000) to correct this defficiency.

Both the Nosé-Hoover chain (NHC) and its massively thermostatting counterpart (MNHC) have been implemented in the GOLDILOCS code both with and without coupling to an extended system barostat (see below). This provides a suitable benchmark against which to compare the constant pressure Langevin dynamics methods developed in chapter 4.

3.1.3 Newer Methods

In this section, recently developed alternatives to the Nosé-Hoover chain approach are reviewed. Importance is placed on schemes for generating equilibrium dynamics. For a

review of thermostats for non-equilibrium simulations see (Hoover *et al.*, 2004).

Generalised Gaussian Moment Thermostatting

The probability of a given configuration in momentum space follows from the canonical phase space probability function after integrating out the configurational coordinates.

$$\rho\left(\mathbf{p}^N\right) = \frac{C}{Q}\exp\left[-\beta\sum_{i=1}^{N}\frac{\mathbf{p}_i^2}{2m_i}\right] \tag{3.9}$$

This is a Gaussian function of the $3N$ momentum variables with zero mean (first moment) and variance $3Nk_BT\sum m_i$ (second moment). The Nosé-Hoover equations (3.5a) can hence be seen as a feedback mechanism which forces the second moment to fluctuate about the canonical value. In this picture, a generalised scheme can be conceived in which other non-vanishing (i.e. even) moments of this distribution are controlled.

Precisely such a scheme has been developed by Liu and Tuckerman (2000), building on earlier work by Hoover and Holian (1996). The equations of motion for controlling the first M non-vanishing moments are

$$\dot{\mathbf{r}}_i = \mathbf{p}_i/m_i \tag{3.10a}$$

$$\dot{\mathbf{r}}_i = -\nabla_{\mathbf{r}_i}U\left(\mathbf{r}^N\right) - \sum_{n=1}^{M}\sum_{k=1}^{n}\frac{p_{\eta_n}}{Q_n}\frac{\left(k_BT\right)^{n-k}}{C_{k-1}}\mathcal{K}^{k-1} \tag{3.10b}$$

$$\dot{\eta}_n = \left[\left(k_BT\right)^{n-1} + \sum_{k=2}^{n}\frac{\left(k_BT\right)^{n-k}}{3NC_{k-2}}\mathcal{K}^{k-1}\right]\frac{p_{\eta_n}}{Q_n} \tag{3.10c}$$

$$\dot{p}_{\eta_n} = \frac{\mathcal{K}}{C_{n-1}} - 3N\left(k_BT\right)^n \tag{3.10d}$$

where $C_0 = 1$ and $C_n = \prod_{k=1}^{n}(3N+2k)$. These reduce to the Nosé-Hoover equations for $M = 1$. These have been rigorously shown to generate the canonical distribution using the non-Hamiltonian statistical mechanics of Tuckerman *et al.* (2001). Ergodicity has been demonstrated in the harmonic oscillator and several other one-dimensional model systems.

Generalised Nosé-Hoover

An alternative generalisation of the Nosé-Hoover method has been presented by Bulgac and Kusnezov (1990) who show that an infinite number of Nosé-like schemes exist which simulate coupling to a heat bath with either one or two auxiliary variables. The special

case of Branka *et al.* (2003) is of particular interest. In this scheme the kinetic energy term associated with the variable s is altered to give the following Hamiltonian.

$$H = \sum_{i=1}^{N} \frac{\mathbf{p}_i^2}{2m_i s^2} + U\left(\mathbf{r}^N\right) + \frac{p_s^{2n}}{2nQ} + (3N+1)\, k_B T \ln s. \tag{3.11}$$

The resulting equations of motion have been shown to correctly sample the 1D harmonic oscillator phase space for values of n in the range 2-3. This choice of n results in increased chaotic behavior in a similar fashion to NHC dynamics. This work still suffers from either a non-uniform time sampling in the imaginary variables, or a non-canonical transform to real variables.

Nosé-Poincaré Thermostat

Bond *et al.* (1999) have presented a scheme based on the original Nosé Hamiltonian subjected to a Poincaré time transform. The resulting Hamiltonian is identical to that of Dettmann and Morriss (1997), although this is not acknowledged.

$$H = \left(\sum_{i=1}^{N} \frac{\mathbf{p}_i^2}{2m_i s^2} + U\left(\mathbf{r}^N\right) + \frac{\pi^2}{2Q} + 3Nk_B T \ln s - \mathcal{H}_0 \right) s. \tag{3.12}$$

In contrast to the Nosé-Hoover method, the resulting equations are Hamiltonian, removing many theoretical complications. However the method still suffers from ergodicity problems, requiring a chain of thermostats to ensure correct sampling (Leimkuhler and Sweet, 2004). Sturgeon and Laird (2000) have coupled the Nosé-Poincaré thermostat to an Andersen barostat (see section 3.2.2) for sampling the NPT ensemble.

An intriguing development in deterministic thermostats has been presented by Laird and Leimkuhler (2003), who show that the Nosé-Poincaré/Dettmann thermostat is in fact the simplest case of a much more general scheme in which any Hamiltonian system can be used as a thermostat for any other. As an example, the canonical distribution function for a single harmonic oscillator is obtained by using both a system of many non-interacting oscillators, and a soft sphere system as the thermostat.

Isokinetic Methods

Simulations in which the kinetic energy of the particles is held absolutely constant via a constraint have long been employed in non-equilibrium molecular dynamics simulations (Evans *et al.*, 1983; Hoover *et al.*, 1982). More recently it has been formally shown by Minary *et al.* (2003a) that a general scheme for simulations in the "isokinetic" ensemble

is generally useful. The equilibrium partition function for the isokinetic ensemble is

$$Q = \frac{\mathcal{K}_0}{N!h^{3N}} \int_{-\infty}^{\infty} \int_{D(V)} \mathrm{d}\mathbf{r}^N \mathrm{d}\mathbf{p}^N \delta \left[\sum_{i=1}^{N} \frac{\mathbf{p}_i^2}{2m_i} - \frac{3}{2} k_B T \right] \exp\left[-\beta U\left(\mathbf{r}^N\right) \right]. \tag{3.13}$$

Simulations in this ensemble will clearly not produce canonically distributed momenta, but will sample configuration space with the correct probability. As with Monte-Carlo simulations, only configurational samples are used when computing quantities of interest. The dependence on momentum space averages can generally be calculated analytically. Minary *et al.* produce equations of motion to generate the isokinetic ensemble which possesses superior sampling efficiency to a Nosé-Hoover chain based integrator.

This method is of particular use when adiabatic separation between subsystems is required, such as in Car-Parrinello molecular dynamics simulations Minary *et al.* (2003b). The electronic and nuclear degrees of freedom can be coupled to separate isokinetic thermostats preventing unwanted exchange of energy. Another example is the free energy mapping method of Rosso *et al.* (2001) which requires adiabatic separation between a reaction coordinate and the remainder of the system.

3.2 Pressure Control in Molecular Dynamics

A mechanism for simulating the coupling of the particle system to a pressure bath is desirable for many reasons. For example, sampling of the NPT ensemble is required for methods which will be met in chapter 5. In addition the ability to simulate at a specified pressure rather than density is useful, e.g. to compute the temperature dependence of a quantity along an isobar. In contrast to heat bath coupling, few methods are available to accomplish this.

3.2.1 Early Methods

Analogous to early methods in temperature control, early attempts to regulate pressure in MD simulations involved periodic or gradual rescaling of the system volume by an amount proportional to the difference between the current and desired pressure. During the rescaling the fractional coordinates of each particle are kept constant, preventing cavitation. These methods do not generate trajectories consistent with the isobaric-isothermal ensemble.

3.2.2 Andersen-Hoover Method

The use of extended systems for generating ensemble trajectories was pioneered by Andersen (1980). In the original Andersen method, the volume $\mathcal{V}$ is introduced as an extra dynamical coordinate with fictitious mass W and momentum $p_{\mathcal{V}} = W\dot{\mathcal{V}}$. Fractional positions and velocities, $\mathbf{s}_i$ and $\dot{\mathbf{s}}_i$ are used. Andersen postulated the following Lagrangian for regulating pressure in a cubic cell of side L,

$$\mathcal{L} = \sum_{i=1}^{N} \frac{1}{2} m_i \dot{\mathbf{s}}_i^2 L^2 + \frac{1}{2W} p_{\mathcal{V}}^2 - U\left(\{\mathbf{s}_i L\}, \mathcal{V}\right) - P_{ext}\mathcal{V}. \tag{3.14}$$

Here U represents the particle configurational energy, and P_{ext} is the external pressure. Note that the absolute velocity of a particle $\dot{\mathbf{r}}_i$ is written as $\dot{\mathbf{s}}_i L$ and *not* $\dot{\mathbf{s}}_i L + \mathbf{s}_i \dot{L}$ as would be expected. This omission decouples the motion of the particles from that of the volume.

Andersen's Lagrangian leads to the following equations of motion after transformation into unscaled coordinates.

$$\dot{\mathbf{r}}_i = \frac{\mathbf{p}_i}{m_i} + \mathbf{r}_i \frac{1}{3}\frac{\mathrm{d}}{\mathrm{d}t}\ln\mathcal{V} \tag{3.15a}$$

$$\dot{\mathbf{p}}_i = -\nabla_{\mathbf{r}_i} U\left(\mathbf{r}^N, \mathcal{V}\right) - \frac{1}{3}\frac{\mathbf{p}_i}{m_i}\frac{\mathrm{d}}{\mathrm{d}t}\ln\mathcal{V} \tag{3.15b}$$

$$\dot{\mathcal{V}} = p_{\mathcal{V}}/W \tag{3.15c}$$

$$\dot{p}_{\mathcal{V}} = \mathcal{P} - P_{ext} \tag{3.15d}$$

after using the relationships

$$\begin{aligned} \frac{\mathrm{d}}{\mathrm{d}t}\left(\mathbf{s}_i \mathcal{V}^{1/3}\right) &= \dot{\mathbf{s}}_i \mathcal{V}^{1/3} + \frac{1}{3}\frac{\dot{\mathcal{V}}}{\mathcal{V}^{2/3}}\mathbf{s}_i = \frac{\mathbf{p}_i}{m_i} + \mathbf{r}_i \frac{1}{3}\frac{\mathrm{d}}{\mathrm{d}t}\ln\mathcal{V} \\ \frac{2}{3}\frac{\dot{\mathcal{V}}}{\mathcal{V}}\dot{s}_i &= \frac{1}{3}\frac{\mathbf{p}_i}{m_i}\frac{\mathrm{d}}{\mathrm{d}t}\ln\mathcal{V}, \end{aligned} \tag{3.16}$$

and identifying $\mathcal{P}$ as the virial pressure estimator. A glance at equations 3.15a to 3.15d suggests using the strain rate

$$\dot{\epsilon} = \frac{1}{3}\frac{\dot{\mathcal{V}}}{\mathcal{V}} = \frac{1}{3}\frac{\mathrm{d}}{\mathrm{d}t}\ln\mathcal{V} \tag{3.17}$$

in place of the volume expansion rate. The momentum associated with the changing volume is now $p_\epsilon = W\dot{\epsilon}$. This substitution was first made by Hoover (1985) leading to

the following equations of motion.

$$\dot{\mathbf{r}}_i = \frac{\mathbf{p}_i}{m_i} + \frac{p_\epsilon}{W}\mathbf{r}_i \tag{3.18a}$$

$$\dot{\mathbf{p}}_i = -\nabla_{\mathbf{r}_i} U\left(\mathbf{r}^N, \mathcal{V}\right) - \frac{p_\epsilon}{W}\mathbf{p}_i \tag{3.18b}$$

$$\dot{\mathcal{V}} = 3\mathcal{V}p_\epsilon/W \tag{3.18c}$$

$$\dot{p}_\epsilon = 3\mathcal{V}\left(\mathcal{P} - P_{ext}\right). \tag{3.18d}$$

These equations conserve the quantity

$$H' = \mathcal{H}\left(\mathbf{r}^N, \mathbf{p}^N\right) + P\mathcal{V} + p_\epsilon^2/2W. \tag{3.19}$$

This is however *not* a Hamiltonian. The transformation from Andersen's equations of motion is non-canonical due to omitting the $\mathbf{s}_i\dot{L}$ term when representing $\dot{\mathbf{r}}_i$ in the original Lagrangian. Equations 3.18a to 3.18b cannot be obtained from any Hamiltonian. Non-Hamiltonian statistical mechanics will be covered in section 4.3.

In this particular case, non-Hamiltonian effects lead to an extra probability weighting of $1/\mathcal{V}$ for phase-space configurations with equal values of equation 3.19. When coupled to a thermostat the Hoover equations will therefore fail to correctly sample the NPT ensemble.

Two suggestions have been made to correct this deficiency. The first of these was proposed by Melchionna *et al.* (1993) and has not been widely adopted due to failure when a constrained center of mass is used. The second was proposed by Martyna *et al.* (1994) in the form of the following equations of motion.

$$\dot{\mathbf{r}}_i = \frac{\mathbf{p}_i}{m_i} + \frac{p_\epsilon}{W}\mathbf{r}_i \tag{3.20a}$$

$$\dot{\mathbf{p}}_i = -\nabla_{\mathbf{r}_i} U - \left(1 + \frac{3}{N_f}\right)\frac{p_\epsilon}{W}\mathbf{p}_i \tag{3.20b}$$

$$\dot{\mathcal{V}} = 3\mathcal{V}p_\epsilon/W \tag{3.20c}$$

$$\dot{p}_\epsilon = 3\mathcal{V}\left(\mathcal{P} - P_{ext}\right) + \frac{3}{N_f}\sum_{i=1}^{N}\frac{\mathbf{p}_i^2}{m_i}. \tag{3.20d}$$

Here N_f is the number of degrees of freedom, accounting for any constraints (e.g. on the centre of mass). We shall see in section 4.3 that these equations correctly sample phase-space. When coupled to an appropriate thermostat, they sample the NPT ensemble and obey both the pressure

$$\langle\mathcal{P}\rangle_{NPT} = P_{ext} \tag{3.21}$$

and work virial theorems

$$\langle \mathcal{PV} \rangle_{NPT} = P_{ext} \langle \mathcal{V} \rangle_{NPT} - k_B T. \tag{3.22}$$

The uncorrected Hoover system does not obey these theorems. The corrected Andersen-Hoover barostat has been implemented in the GOLDILOCS code, both with Nosé-Hoover chain thermostats and in the context of constant pressure Langevin dynamics (see chapter 4).

3.2.3 The Parrinello-Rahman Method

The barostatic method developed above implicitly includes the constraint that the response of the simulation cell to applied pressure is isotropic. Furthermore, fluctuations about equilibrium are also restricted to be isotropic. This restriction is clearly physical only for simple fluids. In solids;

- The response to hydrostatic pressure may be anisotropic.
- We may wish to apply non-hydrostatic stress, i.e. shear, for which the response of the cell is very likely to be anisotropic.

This requires a simulation cell of deformable shape as well as varying size. The Andersen method was adapted to this criteria by Parrinello and Rahman (1980), who proposed a matrix Lagrangian in which the three cell vectors $\mathbf{A}$,$\mathbf{B}$ and $\mathbf{C}$ are arranged into a matrix $\mathbf{h}$,

$$\mathbf{h} = \begin{pmatrix} A_x & B_x & C_x \\ A_y & B_y & C_y \\ A_z & B_z & C_z \end{pmatrix} \tag{3.23}$$

The metric tensor $\mathbf{g}$ is $\mathbf{h}^T\mathbf{h}$, and the volume $\mathcal{V} = \det[\mathbf{h}]$. The Langrangian reads

$$\mathcal{L} = \sum_{i=1}^{N} \frac{1}{2} m_i \dot{\mathbf{s}}_i^T \mathbf{G} \dot{\mathbf{s}}_i + \frac{1}{2W_g} \mathrm{Tr}\left[\mathbf{h}^T\mathbf{h}\right] - U\left(\{\mathbf{s}_i L\}, \mathcal{V}\right) - P_{ext} \det[\mathbf{h}] \tag{3.24}$$

for a system under hydrostatic pressure, where W_g is the fictitious mass associated with the matrix $\mathbf{h}$. In an analogous way to the Andersen method, these can be written in absolute coordinates with $\mathbf{p}_g = W_g \dot{\epsilon}$ (the strain-rate matrix multiplied by the fictitious mass) as the cell momentum variable. Again, when coupled to a thermostat, these equations do not correctly sample the NPT ensemble for a fully flexible cell. As with equations 3.18a

the transformation into unscaled variables has created a non-Hamiltonian system of equations with the incorrect probability weighting for points in phase space. Furthermore, the Parrinello-Rahman equations suffer from a lack of modular invariance, i.e. the dynamics of a given structure are dependent on the choice of unit cell.

The method can also suffer from spurious rotations of the supercell in cases where the internal pressure can result in a net torque.

As with the Hoover equations above, a corrected method has been developed and justified by Martyna *et al.* (1994). The resulting equations of motion are

$$\dot{\mathbf{r}}_i = \frac{\mathbf{p}_i}{m_i} + \frac{\mathbf{p}_g}{W_g}\mathbf{r}_i \tag{3.25a}$$

$$\dot{\mathbf{p}}_i = -\nabla_{\mathbf{r}_i} U\left(\mathbf{r}^N, \mathbf{h}\right) - \frac{\mathbf{p}_g}{W_g}\mathbf{p}_i - \left(\frac{1}{N_f}\right)\frac{\mathrm{Tr}\left[\mathbf{p}_g\right]}{W_g}\mathbf{p}_i \tag{3.25b}$$

$$\dot{\mathbf{h}} = \frac{\mathbf{p}_g \mathbf{h}}{W_g} \tag{3.25c}$$

$$\dot{\mathbf{p}}_g = \mathcal{V}\left(\mathcal{P} - \mathbf{P}_{ext}\right) + \left[\frac{1}{N_f}\sum_{i=1}^{N}\frac{\mathbf{p}_i^2}{m_i}\right]\mathbf{I} \tag{3.25d}$$

which conserve the quantity

$$H' = \mathcal{H}\left(\mathbf{r}^N, \mathbf{p}^N\right) + \frac{1}{2W_g}\mathrm{Tr}\left[\mathbf{p}_g\mathbf{p}_g^T\right] + P_{ext}\det\left[\mathbf{h}\right] \tag{3.26}$$

These are non-Hamiltonian, but generate phase-space configurations with the correct probability for the NPT ensemble when coupled to a thermostat. The dynamics are also modularly invariant, building on the earlier work of Wentzcovitch (1991). At each step the matrix $\mathbf{p}_g$ is symmetrised to eliminate rotations, hence the dynamics explore a $6N + 12$ dimensional phase space. In this form the Parrinello-Rahman method obeys the tensorial virial theorems equivalent to equations 3.21 and 3.22. As with the Andersen-Hoover barostat, this scheme has been implemented in the GOLDILOCS code coupled to both Nosé-Hoover chains and in the context of constant pressure Langevin Dynamics.

Note that two earlier reformulations of the Parrinello-Rahman scheme which obey modular invariance were presented by Wentzcovitch (1991), the second of which is equivalent to a scheme by Cleveland (1988). It is unclear if these methods stand up to rigorous analysis using the subsequently developed non-Hamiltonian statistics of (Tuckerman *et al.*, 2001).

3.2.4 Anisotropic Stress

The above scheme is only formally correct in the case of hydrostatic external pressure. Parrinello and Rahman (1981) attempted to extend the orignal Lagrangian of equation 3.24 to anisotropic external stress. This was subsequently shown to be correct only in the limit of small anisotropy by Ray and Rahman (1984) who proposed an alternative method in which the strain rather than the stress is held constant. The resulting "isostrain ensemble" is not useful for the work reported in this thesis.

A rigorous method for applying anisotropic pressure has been developed by Souza and Martins (1997). Here the dynamical variable is the metric tensor $\mathbf{g}$, rather than the cell matrix $\mathbf{h}$. This formulation both eliminates rotations and satisfies modular invariance. The method is somewhat more complex than that implemented in the GOLDILOCS code, but is the clear method of choice if anisotropic stress is required. The Nosé-Poincaré method has been successfully combined with this metric tensor barostat by Hernandez (2001).

3.2.5 Alternatives

Two new formulations for NPT dynamics in which the volume is written as a function of the particle co-ordinates have recently been developed by Landau (2002) and Sun and Gong (2002). Here the potential energy term for the external pressure in the Hamiltonian leads to modified particle equations of motion which control pressure. Both of these methods can only be applied to systems in which the cell walls represent an impenetrable barrier. They cannot be combined with periodic boundary conditions and are therefore of no use here.

3.3 Integration Algorithms

As already indicated, in addition to possessing numerical stability, an integration algorithm must be symplectic. A necessary (but not complete) condition for this is time-reversibility which eliminates predictor-corrector methods (which have been widely used historically) if strictly correct ensemble averages are required.

A general method for obtaining a 'correct' algorithm has been presented by Tuckerman *et al.* (1992) using the Liouvillian formulation of classical mechanics.

Consider some quantity f which depends on the positions and momenta of each degree of freedom in our system, with no explicit time dependence. The total time derivative of

f can then be written as

$$\dot{f} = \sum_{j=1}^{N_f} \dot{q}_j \frac{\partial f}{\partial q_j} + \dot{p}_j \frac{\partial f}{\partial p_j} = i\hat{L}f, \tag{3.27}$$

where the index j runs over all degrees of freedom represented by the generalised coordinates q_j, and p_j are the corresponding conjugate momenta. This defines the Liouville operator $\hat{L}$. The solution to equation 3.27 is obviously

$$f(t) = exp\left(i\hat{L}t\right) f(0). \tag{3.28}$$

Hence the application of the time evolution operator $exp\left(i\hat{L}t\right)$ to f at time $t = 0$ will return the value of f at time t. This is completely general and applies to extended systems also. For example in the NPT ensemble the coordinates would run over the 3N degrees of freedom associated with the particles plus the thermostat and barostat variables. For this discussion we will restrict ourselves to the NVE case where we have the particle degrees of freedom only. In this case equation 3.28 can be written as

$$f\left[\mathbf{r}^N(t), \mathbf{p}^N(t)\right] = \exp\left(i\hat{L}t\right) f\left[\mathbf{r}^N(0), \mathbf{p}^N(0)\right], \tag{3.29}$$

with

$$\begin{aligned} i\hat{L} &= \dot{\mathbf{r}}\frac{\partial}{\partial \mathbf{r}} + \dot{\mathbf{p}}\frac{\partial}{\partial \mathbf{p}} \\ &= i\hat{L}_r + i\hat{L}_p \end{aligned} \tag{3.30}$$

Consider the case where f depends only on a single coordinate $\mathbf{r}$ with no momentum dependence. Now $i\hat{L} = i\hat{L}_r$. If the time evolution operator $\exp\left(i\hat{L}_r t\right)$ is applied to f at time $t = 0$

$$\exp\left(i\hat{L}_r t\right) f\left[\mathbf{r}(0)\right] = \exp\left(\dot{\mathbf{r}}\frac{\partial}{\partial \mathbf{r}} t\right) f\left[r(0)\right]. \tag{3.31}$$

Expanding the exponential as a series

$$\exp\left(i\hat{L}_r\right) f\left[\mathbf{r}(0)\right] = \left[1 + \dot{\mathbf{r}}(0)\, t\frac{\partial}{\partial \mathbf{r}} + \frac{\left(\dot{\mathbf{r}}(0)\, t\right)^2}{2!}\frac{\partial^2}{\partial \mathbf{r}^2} + \ldots\right] f\left[\mathbf{r}(0)\right], \tag{3.32}$$

results in the Taylor expansion for $f\left[\mathbf{r}(0)\right] + h]$ where $h = \dot{\mathbf{r}}(0)\, t$.

The application of the the operator $\exp\left(i\hat{L}_r t\right)$ has evolved the coordinate r through a time t, which is true for any number of coordinate dependencies. Similarly the application of $\exp\left(i\hat{L}_p t\right)$ will evolve the momenta.

This leads to the conclusion that the application of the operators $\exp\left(i\hat{L}_r t\right)$ and $\exp\left(i\hat{L}_p t\right)$ to the phase space vector $\mathbf{\Gamma}$ defining the position and momentum of each degree of freedom, will evolve each component through time.

For non-commuting operators $\mathcal{A}$ and $\mathcal{B}$,

$$\exp\left(\mathcal{A}+\mathcal{B}\right) \neq \exp\left(\mathcal{A}\right)\exp\left(\mathcal{B}\right). \tag{3.33}$$

Therefore

$$\exp\left(i\hat{L}t\right) \neq \exp\left(i\hat{L}_r t\right)\exp\left(i\hat{L}_p t\right). \tag{3.34}$$

Instead the Trotter identity is used,

$$e^{(\mathcal{A}+\mathcal{B})} = \lim_{P\to\infty}\left(e^{\mathcal{B}/2P}e^{\mathcal{A}/P}e^{\mathcal{B}/2P}\right)^P. \tag{3.35}$$

Time evolution operator is discretised by making the connection $\Delta t = t/P$, the time-step used in integrating our equations of motion. For a small time-step this will give large P making the Trotter expansion a good approximation. This leads to the following form for the total time evolution operator.

$$\exp\left(i\hat{L}t\right) = \left[\exp\left(\frac{i\hat{L}_p\Delta t}{2}\right)\exp\left(i\hat{L}_r\Delta t\right)\exp\left(\frac{i\hat{L}_p\Delta t}{2}\right)\right]^{\frac{t}{\Delta t}} \tag{3.36}$$

where the order of operation is from right to left in the usual way. Application of the operator in the square brackets once per time-step evolves the system of particles. Following through the operations for a single time-step, using only the first-order term in the expansion, the following sequence is obtained.

- $\mathbf{p}\left(t+\frac{1}{2}\Delta t\right) = \mathbf{p}\left(t\right) + \frac{\Delta t}{2}\dot{\mathbf{p}}\left(t\right)$
- $\mathbf{r}\left(t+\Delta t\right) = \mathbf{r}\left(t\right) + \frac{\Delta t}{m}\mathbf{p}\left(t+\frac{1}{2}\Delta t\right) = \mathbf{r}\left(t\right) + \frac{\Delta t}{m}\mathbf{p}\left(t\right) + \frac{1}{2m}\Delta t^2\dot{\mathbf{p}}\left(t\right)$
- $\mathbf{p}\left(t+\Delta t\right) = \mathbf{p}\left(t+\frac{1}{2}\Delta t\right) + \frac{\Delta t}{2}\dot{\mathbf{p}}\left(t+\Delta t\right)$

assuming that the forces are calculated after the full step in particle positions. This is in fact the velocity form of the much employed Verlet algorithm (Verlet, 1967) which is used in the GOLDILOCS code to evolve NVE trajectories. Each application of a part of the evolution operator causes a simple shift in phase space coordinates. This corresponds to a transformation with a Jacobian of unity and hence the algorithm is symplectic.

The Trotter identity can easily be generalised to include further terms in the Liouville

operator due to extended thermostat and barostat degrees of freedom. For example:

$$e^{(\mathcal{A}+\mathcal{B}+\mathcal{C})} = \lim_{P\to\infty} \left(e^{\mathcal{C}/2P} e^{\mathcal{B}/2P} e^{\mathcal{A}/P} e^{\mathcal{B}/2P} e^{\mathcal{C}/2P}\right)^P \tag{3.37}$$

An important property of algorithms obtained in this way is that they can be shown to exactly conserve a pseudo-Hamiltonian which differs from the exact Hamiltonian by a constant which depends only on the calculation time-step. This property results in zero long term drift in any conserved quantity, despite integration errors on small timescales.

These ideas have been applied to generate explicit reversible integrators for Nosé-Hoover based NVT and NPT ensembles (Martyna *et al.*, 1996), in which the full evolution operators (rather than the first order term only) are applied to phase space coordinates. These integrators have been implemented in the GOLDILOCS code for the canonical ensemble, as well as both isotropic and fully flexible isothermal-isobaric ensembles. Similar more Verlet-like algorithms have been obtained by Sergi *et al.* (1999).

3.4 Ensemble Monte-Carlo

As seen in section 2.4.3, the partition function (and hence any quantity of interest) can be separated into a known momentum space contribution and the configurational partition function. As momentum space need not be sampled, dynamics are not required provided samples are generated to the appropriate configuration space probability distribution. This can be accomplished using the Metropolis Monte-Carlo method briefly discussed in section 2.3.1. Provided with an initial configuration, subsequent configurations are generated by random displacements in one of more degrees of freedom. These displacements are accepted with probability given by equation 2.14. Specific details for the canonical, isothermal-isobaric and grand-canonical ensemble as implemented in the GOLDILOCS code are given below. Note that single particle moves only are implemented.

Discussion of advanced MC methods for studying phase transitions is deferred until chapter 5.

3.4.1 Canonical Ensemble (NVT)

In the canonical ensemble, configurations of N particles are generated in a cell of fixed volume with probability

$$\rho\left(\mathbf{r}^N\right) = \exp\left[-U\left(\mathbf{r}^N\right)/k_BT\right]/Z_{NVT} \tag{3.38}$$

MC simulations in this ensemble proceed by making trial moves of a single particle in which each component of the position vector is displaced by a uniformly random amount δr in the interval $-\Delta r/2 \rightarrow +\Delta r/2$.

The relative statistical weights of the configurations before and after the move determine the acceptance criteria.

$$P_{acc} = \min\left\{1, \exp\left[-\beta \Delta U\right]\right\} \tag{3.39}$$

with $\Delta U = U_{new} - U_{old}$. A uniform random number ξ on [0,1] is compared to P_{acc}. If $\xi < P_{acc}$ the move is accepted. Otherwise the particle is returned to its original position. Displacements which lower the configurational energy are hence more likely to be accepted. The effect of temperature is to increase acceptance of higher energy configurations. Note that in order to preserve the symmetry of the Markov chain, the particle for which a trial move is performed must be selected randomly and not sequentially. It is common to refer to N such trial displacements as a single MC cycle. The computational cost of one such cycle is broadly equivalent to a molecular dynamics step.

The choice of parameter Δr is a compromise. Larger trial moves will have a faster decorrelating effect, but will be accepted less often. Shorter moves will in general have a higher acceptance rate, but lead to larger correlation between steps. Simple tuning of Δr such that the acceptance rate is approximately 50% is common, but not necessarily optimal.

Force Biasing

Increased acceptance of larger moves can be achieved by employing the force biasing method of Pangali and Rao (1978). Trial moves for particle i are generated to the distribution

$$P_\lambda\left(\delta \mathbf{r}_i\right) = \exp\left[\lambda \beta \mathbf{f}_i \cdot \delta \mathbf{r}_i\right] / C_\lambda \tag{3.40}$$

where λ is the biasing parameter which varies from 0 to 1, and C_λ is a normalisation constant. Random moves to this distribution are easily generated with a simple rejection method. Moves in a direction close to that in which the force acts are favored. The modified acceptance criteria for moving particle i from m to n is

$$P_{acc} = \min\left\{1, \exp\left[-\beta \Delta U + \beta \lambda\left(\mathbf{f}_i^n - \mathbf{f}_i^m\right) \cdot \delta \mathbf{r}_i + \ln\left(C_\lambda^m / C_\lambda^n\right)\right]\right\}. \tag{3.41}$$

Use of the force biasing method allows a larger maximum displacement to be employed for a similar acceptance rate. This leads to faster exploration of configuration space and hence higher statistical efficiency.

3.4.2 Isobaric-Isothermal Ensemble (NPT)

The probability density distribution for the NPT ensemble in configuration space is

$$\rho\left(\mathbf{r}^N, \mathcal{V}\right) = \exp\left[-\beta U\left(\mathbf{r}^N, \mathcal{V}\right) - \beta P_{ext}\mathcal{V}\right]/Z_{NPT} \tag{3.42}$$

In NPT simulations, particle displacement moves are complemented by uniformly random displacements of the volume coordinate $\delta\mathcal{V}$ in the range $-\Delta\mathcal{V} \rightarrow +\Delta\mathcal{V}$. The fractional coordinates of the particles are kept constant during this move. A trial volume move results in a change of configurational *enthalpy* $\Delta H = \Delta U + P_{ext}\Delta\mathcal{V}$, which is accepted with probability

$$P_{acc} = \min\left\{1, \exp\left[-\beta\Delta H + N\ln\left(\mathcal{V}_{new}/\mathcal{V}_{old}\right)\right]\right\} \tag{3.43}$$

where the second term in the exponent accounts for the change in normalisation constant for the statistical weighting of configurations before and after the volume change. As with temperature, pressure is now a parameter in the acceptance probability.

Symmetry of the Markov chain is preserved by performing a volume move in preference to a particle displacement move with a fixed probability. The usual choice of $1/N$ is used in GOLDILOCS. The acceptance probability for particle moves is unchanged from the canonical case. Optimal choice of the parameter $\Delta\mathcal{V}$ is determined by similar arguments to the single particle case.

An anisotropic equivalent of this scheme is also available. Random displacements in the elements of the cell matrix $\mathbf{h}$ (equation 3.23), are accepted/rejected with probability appropriate to a fully flexible NPT ensemble.

Viral Biasing

An analogous method to force biasing is available for volume moves. This is the virial biasing method of Mezei (1980). Volume moves are chosen from the distribution

$$P\left(\delta\mathcal{V}\right) = \exp\left[\beta\lambda f_{\mathcal{V}}\delta\mathcal{V}\right]/D_\lambda \tag{3.44}$$

which can be generated using the transformation method. The "force" on the volume $f_{\mathcal{V}}$ is computed as the difference between the desired pressure and the current virial estimator (equation 2.30) . D_λ is the appropriate normalisation constant. The modified acceptance

criteria for virial-biased volume moves from state m to n is

$$P_{acc} = \min\{1, \exp\left[-\beta\Delta H + N\ln\left(\mathcal{V}_{new}/\mathcal{V}_{old}\right)\right] \times \exp\left[-\beta\lambda(f_v^m + f_v^n)\delta\mathcal{V}\right) + \ln D_\lambda^m/D_\lambda^n]\} \quad (3.45)$$

Use of this biasing volume allows larger trial volume steps without sarificing acceptance rate. This method is used in conjunction with force biasing in the GOLDILOCS code. An anisotropic virial biasing scheme is also available (Jedlovszky and Mezei, 1999).

3.4.3 Grand Canonical Ensemble (μVT)

Unlike the NVT and NPT ensembles, the grand canonical ensemble (GCE) is not traditionally accessible by molecular dynamics methods[1]. It corresponds to a variable number of particles in a fixed volume held in contact with a heat bath at temperature T, and a particle reservoir at chemical potential μ.

$$\rho\left(\mathbf{r}^N\right) = \exp\left[-\beta U\left(\mathbf{r}^N\right) + \beta\mu N\right]/\mathcal{Z} \quad (3.46)$$

where $\mathcal{Z}$ is the configurational grand-canonical partition function. Two types of trial moves are used in exchanging particles with the reservoir. Particle insertion moves involve the addition of particles at a random position in the simulation cell. The probability of accepting an insertion is

$$P_{acc}\left(N \to N+1\right) = \frac{V}{(N+1)}\exp\left[-\beta\Delta U + \beta\mu\right]. \quad (3.47)$$

Removal of a randomly selected particle is accepted with probability

$$P_{acc}\left(N \to N-1\right) = \frac{N}{V}\exp\left[-\beta\Delta U - \beta\mu\right]. \quad (3.48)$$

Note that the chemical potential in the above equations is that related to the configurational free energy only. The total chemical potential is recovered by a temperature dependent shift in this value, or employing the full partition function (2.13) when deriving the acceptance probabilities. In the later case this yields

$$P_{acc}\left(N \to N+1\right) = \frac{V}{\Lambda^3(N+1)}\exp\left[-\beta\Delta U + \beta\mu\right] \quad (3.49)$$

[1] A number of extended system and hybrid MD-MC schemes do however exist, see Boinepalli and Attard (2003) for a discussion.

and

$$P_{acc}\left(N \rightarrow N-1\right) = \frac{N\Lambda^3}{V} \exp\left[-\beta\Delta U - \beta\mu\right]. \tag{3.50}$$

Equations 3.47 and 3.48 will be used when performing multi-canonical sampling as described in section 5.6.1. Equations 3.49 and 3.50 will be used when employing grand canonical MC simulations as a reference point for computing absolute free energies.

It is common in GCE simulations to omit particle displacement moves. Sampling of points in configuration space is hence obtained purely by insertion of particles at random positions. In this case, simulations in the GCE ensemble are parameterless. Markov chain symmetry is ensured by attempting insertion and removal moves with equal probability.

3.5 Computational Considerations

3.5.1 Initial Conditions

Both the molecular dynamics and Monte-Carlo methods require an initial condition from which to generate samples. A brief description of how this is handled within GOLDILOCS is given below.

Positions

It is often useful to generate initial positions according to a known crystal structure, particularly when studying solids. The GOLDILOCS code can automatically generate simple-cubic (sc), face-centered cubic (fcc) and diamond structures as the initial condition in a cubic cell. For other structures, initial positions can be read from an external file. This allows a structure located in an earlier simulation to be re-used.

For simulating fluids, it is possible to heat a crystal configuration beyond the point of mechanical instability to create a disordered sample. This is however time consuming. Alternatively, the GOLDILOCS code can generate initial positions for a fluid by randomly positioning atoms within the simulation cell (subject to a user specified overlap constraint) in a similar vein to a grand canonical Monte-Carlo simulation.

Momenta

For molecular dynamics simulations, initial momenta are assigned randomly in the interval $[-1, 1]$. These are then rescaled such that the virial estimator matches the desired

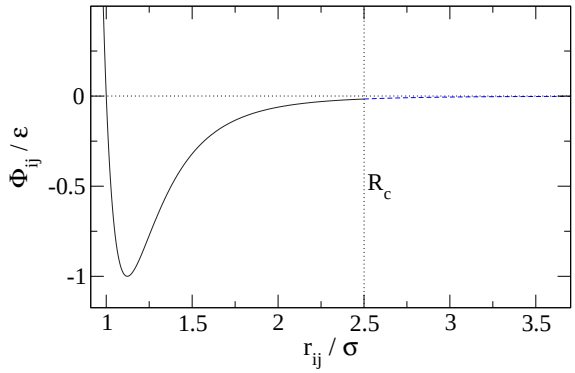

Figure 3.1: *Illustration of a truncated Lennard-Jones potential.*

temperature. The momenta are only adjusted to remove center of mass motion if this is to be formally constrained throughout the simulation.

Equilibration

Regardless of how the initial conditions are generated, it is vital that any resulting bias is removed before sampling of the equilibrium conditions can take place. This is generally performed by simulating an equilibration period many times longer than the correlation time of the system. In the case of NVT and NPT simulations, the system will also take a finite time (or number of MC cycles) to reach the specified temperature and/or pressure. Details of equilibration times used will be given for all simulations reported in this thesis.

3.5.2 Efficient Calculations of Forces

The performance bottleneck in any atomistic simulation is the calculation of energy and forces from the model Hamiltonian. This scales as $O\left(N^2\right)$ for pair-potentials and $O\left(N^3\right)$ for Tersoff-style bond-order potentials. Optimising this procedure is clearly highly desirable.The large quantity of data required to obtain detailed information of a model system can be extremely expensive to generate computationally. For even very simple models, computational efficiency becomes a major issue when many thousands of simulations are required.

Truncation of Pair Potentials

A simple speed efficiency gain for pair-potentials is gained by truncating the range of the interaction. Beyond some distance $r_{ij} > R_c$ the potential is never computed and is set to zero.

Clearly the truncated potential is only a good approximation to the real potential for large R_c. The truncation has two consequences. First the potential and its derivative (the force) are both discontinuous at $r_{ij} = R_c$. Second, long range contributions to the total energy and pressure are neglected, which although small for each pair interaction, will accumulate to a significant total over the entire system. Three schemes for dealing with these issues are as follows:

1. Truncate the potential at large R_c such that the energy and force discontinuities are small, and apply long range corrections to the total energy and pressure based on the average radial density at large r_{ij}. The large R_c leads to little reduction in cost, but corresponds closely to the "full" pair-potential.

2. Apply a positive shift in the pair potential of $\phi(R_c)$. This ensures that the energy tends exactly to zero at R_c but leaves a discontinuity in the force. However for large R_c this can be neglected. This is the "cut and shifted" pair potential method.

3. Shift the force by $-\frac{d\phi}{dr_{ij}}|_{R_c}$. The force now varies continuously to zero at the cut-off. The resulting difference in force between the original and force- shifted potential is then integrated to correct the energy. This "cut and force-shifted" method requires no long range corrections and produces self-consistent energies and forces.

The size of the simulation cell must be larger than twice R_c in any dimension to eliminate interaction of a particle with its own periodic images. In method 1, the long range corrections to the energy and pressure are given by

$$U_{LRC} = N\pi\rho^{*}\epsilon\left(\frac{16}{9}\right)\left[\left(\frac{\sigma}{R_c}\right)^{9} - \frac{3}{2}\left(\frac{\sigma}{R_c}\right)^{3}\right] \tag{3.51}$$

$$P_{LRC} = \sigma^{3}\pi\rho^{*2}\epsilon\left(\frac{16}{9}\right)\left[\frac{2}{3}\left(\frac{\sigma}{R_c}\right)^{9} - \left(\frac{\sigma}{R_c}\right)^{3}\right] \tag{3.52}$$

for the Lennard-Jones potential.

Methods 2 and 3 modify the interaction and hence resulting simulations obey different equations of state to the full pair-potential. Work reported in this thesis makes extensive use of molecular dynamics simulation, requiring the third method for continuous forces. This is used in all work unless otherwise stated, such as when making comparisons with results in the Literature for the "full" Lennard-Jones potential.

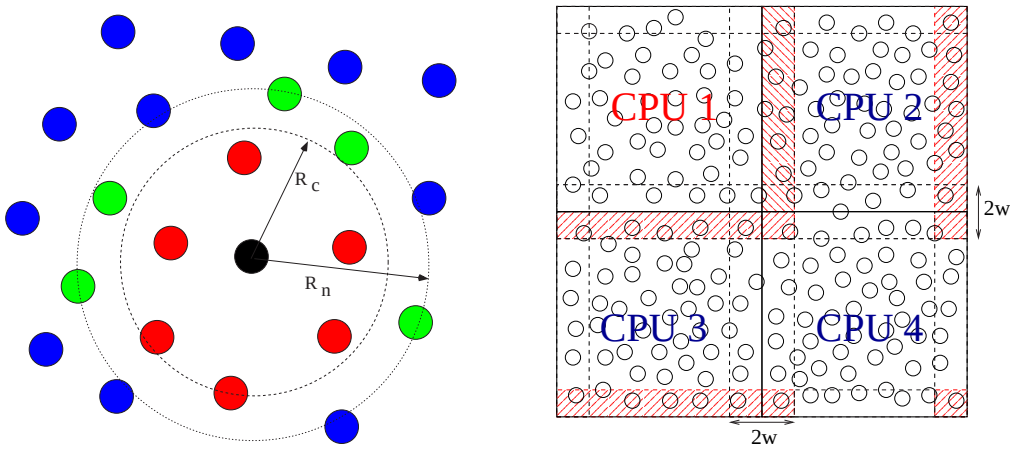

(a) (b)

Figure 3.2: *(a) The Verlet neighbour list. Neighbours within R_n are added to the list for the central particle. Other particles are not considered in subsequent energy computations. (b) The domain decomposition method. Each CPU evolves only its own particles, but considers particles in a halo of width w when computing interactions. The halo for CPU 1 is shown, employing periodic boundary conditions. The halo width w must be $> R_c$.*

The Verlet Neighbour List

For simple potentials, a significant part of the cost involved in computing a pair interaction can be determination of the interparticle distance. This is particularly true when employing non-orthogonal simulation cells. A simple solution is to maintain a periodically updated list of neighbours for each particle. When computing energies/forces, only the listed neighbours of each particle are considered. The distance R_n, within which particles are added to the neighbour list, must therefore be greater than the interaction distance R_c. An illustration is given in figure 3.2(a).

For small R_n the list must be updated frequently to prevent interactions with new neighbours being neglected. This increases the overhead cost of using these lists. For large R_n less updates are required, but the list may contain more information than is useful, reducing the benefit of their use. The minimum cell dimension must be increased to twice R_n or larger when using these lists. Typically, the use of neighbour lists becomes beneficial for system sizes of 300-400 atoms or greater, leading to substantial speed benefits. The method is particularly useful in solids, where the neighbours of a given atom rarely change.

3.5.3 Parallel Computation

Much of the work reported in this thesis has made use of parallel computer hardware, warranting a brief discussion here.

Recall that our reason for performing atomistic simulation is to obtain a series of independent samples from which we can compute an ensemble average. Many simulations of the same system, employing different randomly generated initial conditions will clearly generate samples faster than a single simulation. This rather obvious form of parallelisation requires no communication between processors and hence scales perfectly to an arbitrary number of compute nodes. Furthermore, we will often require an ensemble average to be computed for a variety of thermodynamic conditions and model parameters, introducing a second natural level of parallelisation. This *task parallelism* paradigm has been employed extensively for the calculations reported in this thesis. In its most simple form the method consists of running multiple copies of the GOLDILOCS code over several nodes of a computational cluster. Task parallelism has also been implemented *within* the GOLDILOCS code for performing free energy calculations (see section 5.4) using MPI message passing.

For some applications such as the method described in section 5.3.1, a single simulation of a large system is required. In these cases task parallism is less useful and methods of parallelisation of a single simulation become important. Two such methods are briefly described below.

Domain Decomposition

In the domain decomposition method, the simulation is divided into real space segments, each of which is assigned to a CPU. Each CPU evolves the trajectory of its own atoms only, but must compute forces involving atoms in other cells using a 'halo' of information regarding atoms assigned to other processors. Halo-swaps in which segments exchange information occur on a regular timescale. An illustration is given in figure 3.2(b).

In order for this method to be efficient, the size of each segment must be substantially larger than the effective range at which atoms interact. If not, then far more time is spent communicating information between segments than on computation. This method is therefore useful only for simulations with many tens of thousands of atoms. This regime lies well beyond any simulation that will be conducted in this work.

Functional Decomposition

An alternative approach to parallelisation of atomistic simulation has been implemented in the GOLDILOCS code. Consider the $N \times N$ matrix $\mathbf{F}$. The element F_{ij} is the force

on atom i due to atom j according to a simple pair-potential,

$$\begin{pmatrix} 0 & \mathbf{f}_{12} & \mathbf{f}_{13} & \mathbf{f}_{14} & \dots \\ \mathbf{f}_{21} & 0 & \mathbf{f}_{23} & \mathbf{f}_{24} & \dots \\ \mathbf{f}_{31} & \mathbf{f}_{32} & 0 & \mathbf{f}_{34} & \dots \\ \mathbf{f}_{41} & \mathbf{f}_{42} & \mathbf{f}_{43} & 0 & \dots \\ \vdots & \vdots & \vdots & \vdots & \end{pmatrix}.$$

Only the upper triangular portion need be considered, exploiting the symmetry $\mathbf{f}_{ij} = -\mathbf{f}_{ji}$, and the obvious $\mathbf{f}_{ii} = 0$. The columns of this matrix can be computed independently, and hence divided over the available processors. The total force on a particle is recovered by summing over each row at the end of the force computation.

This is simple to implement, and can easily be extended to bond-order potentials containing three-body terms. The method does not scale well beyond six or eight CPUs for the size of simulation typically employed in the this thesis, but provides a useful speedup nonetheless.

Chapter 4

Constant Pressure Langevin Dynamics

This chapter will discuss the benefits of, and justification for, performing Langevin dynamics in extended non-Hamiltonian systems as a method for sampling the isothermal-isobaric ensemble. Specifically the Andersen-Hoover and Parrinello-Rahman systems introduced in the previous chapter. Much of the following is reproduced from Quigley and Probert (2004).

4.1 Motivation

The Nosé-Hoover thermostat was introduced in section 3.1.2. This has become the widely adopted standard for molecular dynamics simulations in the canonical ensemble, despite difficulties in coping with the harmonic oscillator. These problems are illustrated in figure 4.1. Three simulations of a harmonic crystal containing eight atoms are presented. The duration of each simulation is approximately two thousand oscillation periods. The fictitious mass of the heat bath variable was chosen for optimal coupling at the oscillator frequency. As can be seen, the single Nosé-Hoover thermostat fails completely to generate the correct distribution. This occurs regardless of simulation length and therefore violates the ergodicity assumption. A single chain of ten thermostats also fails to converge the distribution within a reasonable simulation length as was stated in section 3.1.2. Only when a separate chain of thermostats is coupled to each degree of freedom is the canonical distribution of position samples recovered.

The extra computational expense of massive thermostatting over a single chain is negligible for most simulations. Despite this, many codes still employ single chain or even single thermostat Nosé-Hoover schemes. Simulations of solids at low temperature where the interaction is near-harmonic, or other situations in which harmonic interactions are

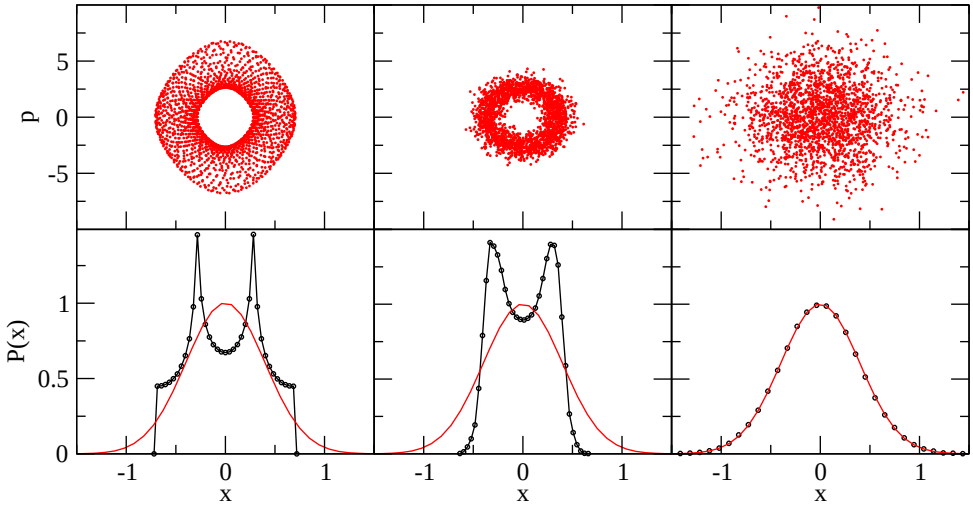

Figure 4.1: *The behaviour of Nosé-Hoover thermostats coupled to a harmonic crystal. The upper plots show Poincaré sections through the phase space of the crystal. The lower plots show the measured distribution of position samples for the corresponding oscillator compared to the known canonical function. In the left hand case a single Nosé-Hoover thermostat is used. In the centre, a single chain of Nosé-Hoover thermostats, and in the right hand case a separate Nosé-Hoover chain is coupled to each degree of freedom.*

employed, such as in path-integral molecular dynamics or free energy calculations are likely to be disastrously inefficient or simply wrong if massive thermostatting is not used.

Several other methods have been proposed, employing various generalisations of the Nosé-Hoover scheme. These thermostats all share the common property that their equations of motion are purely deterministic, although often chaotic. The mathematics employed in their justification (covered in this chapter) always *assume* no conservation laws are obeyed by the dynamics, other than those due to energy and momentum considerations, or explicitly imposed by constraints. It has been suggested by Tuckerman *et al.* (2001) that the pathology of the single thermostat or single chain Nosé-Hoover methods in harmonic potentials is due to creation of unexpected conservation laws through the coupling of the thermostat to the particle subsystem. These restrict the the system to paths in phase-space which satisfy these constraints, preventing ergodicity.

Here lies a potentially worrying issue. It is possible that other systems may exist in which unexpected conservation laws are generated when coupled to a deterministic thermostat. These may not occur globally, but could be a consequence of the local phase-space topology. As it is not possible to check the ergodicity of a general system, it can only be assumed that such problems do not occur. The purely stochastic Monte-Carlo method clearly does not suffer from these problems and is the method of choice for sampling configuration space. If however representative dynamics [1] are required then a thermostat

[1] It should be re-iterated at this point that in all thermostat methods the dynamics are purely fictitious and can therefore be only considered representative at best.

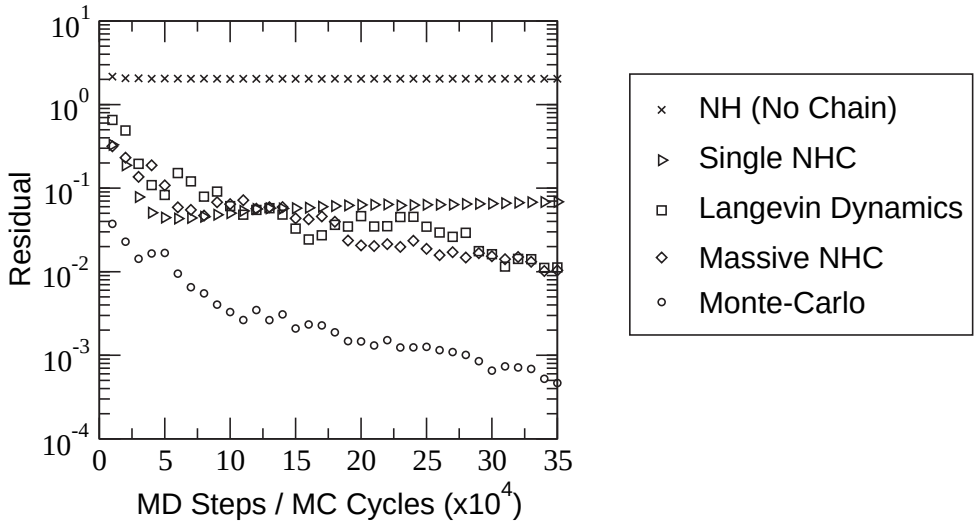

Figure 4.2: *Convergence of the canonical distribution of position samples for an oscillator in a harmonic crystal. The total squared residual from the exact function is plotted as a function of the run length for several methods. The Monte-Carlo sampling is clearly many times more efficient.*

employing a stochastic component in desirable.

Methods such as those based on the Langevin equation are often overlooked. As can be seen in figure 4.2 Langevin dynamics has a similar rate of convergence to the optimised multiple chain thermostat for the above harmonic crystal problem. The method includes stochastic forces to model the interaction of the particle subsystem with a heat bath, and hence can be guaranteed to generate no unexpected conservation laws.

4.2 Langevin Dynamics

A simple but effective method of performing Langevin dynamics simulations in the canonical ensemble uses the following equations of motion in the usual notation

$$\dot{\mathbf{r}}_i = \mathbf{p}_i/m_i \tag{4.1a}$$

$$\dot{\mathbf{p}}_i = \mathbf{f}_i - \gamma\mathbf{p}_i + \mathbf{R}_i, \tag{4.1b}$$

with $f_i = -\nabla_{\mathbf{r}_i} U\left(\mathbf{r}^N\right)$. Equation 4.1b is a special case of the Langevin equation. Our Hamiltonian system is now embedded in a Brownian medium. The friction coefficient γ represents viscous damping due to fictitious 'heat bath' particles. The stochastic force $\mathbf{R}_i$ represents the effect of collisions with these particles, leading to diffusion.

An appropriate distribution for $\mathbf{R}_i$ which will lead to thermal equilibrium is needed. Following Chandrasekhar (1943) it is assumed that the timescale of the collisional heat bath

process is very much smaller than the atomic motions of interest, and hence

$$\left\langle R_i^{\alpha}(t) R_i^{\beta}(t') \right\rangle = G\delta(t-t')\,\delta_{\alpha,\beta}, \tag{4.2}$$

where G is a constant to be determined, and the indices α and β run over the three components of $\mathbf{R}_i$. The stochastic force must represent the combined effect on particle i over a great many random collisions and can be expected to obey the central limit theorem. The distribution from which it is drawn should therefore be Gaussian. Conservation of momentum implies that this distribution should be centred on zero.

To quantify the diffusion introduced by the $\mathbf{R}_i$ term, consider an *ensemble* of identical single particle systems, each obeying equations 4.1a and 4.1b. The density of particles in phase space is hence given by an ensemble probability distribution function ρ. The fictitious heat bath particles belong to other members of the ensemble, and interact with the current system only via the friction and stochastic terms.

Fick's law of diffusion states that the probability current due to diffusion in configuration space is

$$\mathbf{j}(\mathbf{r}) = -D\nabla_r \rho, \tag{4.3}$$

where D is the diffusion coefficient. The diffusion coefficient is closely related to the mean square displacement.

$$D = \lim_{t\to\infty} \frac{1}{6t} < [\mathbf{r}(t) - \mathbf{r}(0)]^2 >, \tag{4.4}$$

which can be transformed in terms of the particle momentum (Kubo, 1966) to read

$$D = \frac{1}{3m^2} \int_0^{\infty} < \mathbf{p}(t_0) \cdot \mathbf{p}(t_0 + t) > \mathrm{d}t, \tag{4.5}$$

relating the friction coefficient to fluctuations in p at equilibrium. Equation 4.5 is a manifestation of the fluctuation-dissipation theorem. Similarly, diffusion in momentum space leads to a probability current

$$\mathbf{j}_p^{(1)}(\mathbf{p}) = -D_p \nabla_p \rho, \tag{4.6}$$

where D_p is the diffusion coefficient in momentum space. By analogy with equation 4.5, this can be related to the components of the stochastic force.

$$D_p = \int_0^{\infty} < R^{\alpha}(t_0) R^{\alpha}(t_0 + t) > \mathrm{d}t., \tag{4.7}$$

which identifies $G = D_p$. The friction term introduces a drift of probability in momentum

space with current

$$\mathbf{j}_p^{(2)}(\mathbf{p}) = -\gamma \mathbf{p}\rho. \tag{4.8}$$

A suitable value for D_p will maintain thermal equilibrium. To identify this, the total rate of change of the probability density ρ due to equations 4.1a and 4.1b is constructed, including only the linear response to the stochastic force via equations 4.6 and 4.8.

$$\begin{aligned}\frac{d\rho}{dt} &= \frac{\partial \rho}{\partial t} + \frac{\mathbf{p}}{m}\cdot\nabla_{\mathbf{r}}\rho + \mathbf{f}\cdot\nabla_{\mathbf{p}}\rho - \nabla_p\cdot\left[\mathbf{j}_p^{(1)}(\mathbf{p}) + \mathbf{j}_p^{(2)}(\mathbf{p})\right] \\ &= \frac{\partial \rho}{\partial t} + \frac{\mathbf{p}}{m}\cdot\nabla_{\mathbf{r}}\rho + \mathbf{f}\cdot\nabla_{\mathbf{p}}\rho + \nabla_p\cdot\left[\gamma\mathbf{p}\rho + D_p\nabla_p\rho\right].\end{aligned} \tag{4.9}$$

This is a Fokker-Planck equation, a deterministic equation for the behaviour of the probability density, equivalent to the stochastic equations 4.1a and 4.1b. It is simple to show that the canonical probability distribution is a solution of 4.9 only if

$$D_p = \gamma m k_B T. \tag{4.10}$$

This is the Einstein relation for diffusion in momentum space. Assuming ergodicity, the canonical distribution must be the *only* solution and hence equations 4.1a and 4.1b can be used to sample the canonical ensemble (Allen and Tildesley, 1987). Generalising to an ensemble of N particle systems,

$$\begin{aligned}&\frac{\partial}{\partial t}\rho + \sum_{i=1}^{N}\left[\frac{\mathbf{p}_i}{m}\cdot\nabla_{\mathbf{r}_i}\rho + \mathbf{f}_i\cdot\nabla_{\mathbf{p}_i}\rho\right] \\ &= \gamma\sum_{i=1}^{N}\nabla_{\mathbf{p}_i}\cdot\left[\mathbf{p}_i\rho - mk_BT\nabla_{\mathbf{p}_i}\rho\right].\end{aligned} \tag{4.11}$$

Note the similarity of this equation to equation 2.16, i.e. the above Fokker-Planck equation is analogous to Liouville's equation for the case where the particles obey equations 4.1a and 4.1b rather than Hamilton's equations. It is a conservation law for phase space probability with the Liouvillian contribution balanced by the divergence of the diffusion and drift terms. If the diffusion coefficient is given by 4.10 the total time derivative is zero as required for detailed balance.

Equation 4.7 implies that the r.m.s. effect of R_i is an impulse of magnitude $\sqrt{m\gamma k_B T}$ and duration dt. It is assumed that these collisions continually occur and hence $\mathbf{R}_i$ also changes continually (but not smoothly). For the purposes of an MD simulation, this impulse is approximated as constant over a time step. The *peak* value of the force to select

from a Gaussian distribution is therefore

$$R_{max} = \sqrt{\frac{2k_B T \gamma m}{\Delta t}}. \tag{4.12}$$

The canonical ensemble will hence be obtained by selecting a random deviate from a Gaussian distribution of zero mean and unit variance, scaled by $(\mathbf{R})_{max}$, for each component of $\mathbf{R}_i$ at each time-step.

The choice of the friction parameter γ is a compromise between statistical sampling efficiency and preservation of accuracy in short-term dynamics. In the case where the process approximated by the stochastic components can be simulated by another method, it is possible to determine an optimal value of γ numerically. Guidelines for the choice of γ will be discussed in detail later.

An integration algorithm for equations 4.1a and 4.1b can be obtained by applying the time-evolution operator formulation of Tuckerman *et al.* (1992) in the limit $\gamma \to 0$. The lack of a Liouville operator for the stochastic components of the dynamics requires that these are then included into the particle forces via the following substitutions:

$$\begin{aligned} \mathbf{f}_i(t) &\to \mathbf{f}_i(t) - \gamma \mathbf{p}_i(t) + \mathbf{R}_i(t) \\ \mathbf{f}_i(t+\Delta t) &\to \mathbf{f}_i(t+\Delta t) - \gamma \mathbf{p}_i(t+\Delta t) + \mathbf{R}_i(t+\Delta t) \end{aligned}$$

In the NVT case described here, this leads to standard Velocity-Verlet, modified with the above substitutions.

4.2.1 Langevin Equations for NPT Dynamics

The above Langevin dynamics method is a useful tool for sampling the canonical ensemble. Sampling the isothermal-isobaric ensemble is also useful. A Langevin Dynamics method to accomplish this is therefore desirable.

A general scheme for Langevin Dynamics in any Hamiltonian system has been presented by Kolb and Dunweg (1999). This was applied to the original extended system of Andersen, which is Hamiltonian when operated in fractional coordinates. The equations of motion for the volume, and the scaled momenta are converted to Langevin Equations. The resulting dynamics are shown to sample the isothermal-isobaric ensemble with superior efficiency to the "Langevin Piston" method of Feller *et al.* (1995), in which only the equation of motion for the volume is converted to a Langevin equation.

The most commonly employed extended systems are non-Hamiltonian. The Andersen-Hoover barostat (equations 3.20a to 3.20d) employs the strain rate as the auxiliary mo-

mentum. The response of the volume to pressure fluctuations is now logarithmic, making the method considerably more robust than the original Andersen scheme. The Parrinello-Rahman style scheme of equations 3.25a to 3.25d, which is desirable for solids, is also non-Hamiltonian. The remainder of this chapter is concerned with the theory, implementation and testing of Langevin dynamics in these two systems as a method for sampling the isothermal-isobaric ensemble.

4.3 The Statistical Mechanics of Extended Systems

The theory of non-Hamiltonian statistical mechanics must first be covered. The formalism introduced by Tuckerman *et al.* (1999, 2001) is employed here. The essential results are presented below. An alternative formalism employing algebraic brackets has been introduced by Sergi (2003).

For brevity, the entire phase-space vector is denoted by the the quantity x. The volume $\mathrm{d}x$ is an element of the *total* phase-space of our system which includes position and momentum coordinates for all particles, plus auxiliary degrees of freedom. If the system is subject to n_c conservation laws of the form

$$\Lambda\left(x\right) = \lambda \tag{4.13}$$

then partition function for the system can be immediately written as

$$\Omega = \int dx \prod_{k=1}^{n_c} \delta\left(\Lambda_k\left(x\right) = \lambda_k\right) \tag{4.14}$$

only if $\mathrm{d}x$ is constant everywhere in the phase space. This is easily shown to be true for all Hamiltonian systems in which the time evolution of the phase space vector corresponds to a transformation with a Jacobian of unity. In contrast, it is simple to construct non-Hamiltonian equations of motion for which dx is not constant. To generalise equation 4.14 to non-Hamiltonian systems, consider evolution by the equations of motion from some initial time $t = 0$ to time t. The Jacobian of this transformation $J\left(x_t : x_0\right)$ is the missing factor in equation 4.14 which will account for the changing volume of the phase space element. This Jacobian can be obtained from the following relationship

$$\begin{aligned} J\left(x_t : x_0\right) &= \exp\left[\int_0^t \kappa\left(x_{t'}, t'\right) dt'\right] \\ &= e^{w(x_t,t)-w(x_0,0)}, \end{aligned} \tag{4.15}$$

where κ is the phase space compressibility $\nabla_x \cdot \dot{x}$. The statement that the phase space compressibility is zero everywhere at all times for Hamiltonian systems is exactly equivalent to the Liouville theorem. This will clearly give a unitary Jacobian.

For non-zero compressibility

$$e^{w(x_t,t)} x_t = e^{w(x_0,0)} x_0, \tag{4.16}$$

and $e^{w(x_t,t)} x_t$ is therefore the invariant phase space measure for non-Hamiltonian systems. The factor $e^{w(x_t,t)}$ can be considered a metric determinant factor $\sqrt{g\left(x_t, t\right)}$ where g is the determinant of the phase space metric tensor G. This factor is unity for Hamiltonian systems and hence phase space is flat. For non-Hamiltonian systems the extended phase space is in general curved. Phase-space configurations of equal energy may not be equally probable in non-Hamiltonian systems. This violates the fundamental assumption underlying statistical mechanics. The probability density ρ for a given ensemble is weighted by the factor $\sqrt{g}$, and the Liouville theorem (2.3.3) no longer holds. A generalised Liouville theorem for non-Hamiltonian systems is required. This must state that the total time derivative of the ensemble probability density, weighted by this metric determinant factor, must be zero. In the present notation this is stated as

$$\frac{\partial}{\partial t} \sqrt{g} \rho + \dot{x} \cdot \nabla_x \sqrt{g} \rho = 0. \tag{4.17}$$

Tuckerman *et al.* (2001) have used this formalism to prove that Nosé-Hoover chains correctly sample the canonical ensemble. The probability density in the extended phase space is microcanonical due to conservation of the extended system energy. When weighted by the appropriate metric determinant factor, the microcanonical ensemble for the particle sub-space is recovered after integration over the auxiliary variables. This assumes ergodicity in the extended phase space, and that all conservation laws present have been accounted for. As has already been discussed, this cannot be guaranteed and may explain the pathology of the Nosé-Hoover method when applied to the harmonic oscillator. Similarly the isothermal-isobaric ensemble is shown to be reproduced when using the equations of Martyna *et al.* (1994). This is subject to equivalent assumptions for the pressure regulating auxiliary variables.

4.4 Langevin Dynamics in Non-Hamiltonian Systems

Complications with performing Langevin dynamics in non-Hamiltonian systems have not previously been addressed in the literature. The Einstein relation 4.10 was earlier used to

balance diffusion and drift away from a constant energy contour, resulting in the canonical ensemble. It did *not* account for any additional drift due to gradients in a non-Euclidean phase-space.[2] As these gradients vary across the phase-space manifold, the accessible portion of which will depend on the imposed thermodynamic constraints, constructing a generalised Einstein relation is clearly non-trivial.

4.4.1 The Andersen-Hoover System

Equations of Motion

The equations of motion proposed are shown below. These incorporate the corrected Andersen-Hoover equations 3.20a to 3.20d. The deterministic equations for the evolution of both the particle and barostat momenta have been converted to Langevin equations with different friction constants.

$$\dot{\mathbf{r}}_i = \frac{\mathbf{p}_i}{m_i} + \frac{p_\epsilon}{W}\mathbf{r}_i \tag{4.18a}$$

$$\dot{\mathbf{p}}_i = -\nabla_{\mathbf{r}_i} U - \left(1 + \frac{3}{N_f}\right)\frac{p_\epsilon}{W}\mathbf{p}_i - \gamma\mathbf{p}_i + \mathbf{R}_i \tag{4.18b}$$

$$\dot{\mathcal{V}} = 3\mathcal{V}p_\epsilon/W \tag{4.18c}$$

$$\dot{p}_\epsilon = 3\mathcal{V}\left(\mathcal{P} - P\right) + \frac{3}{N_f}\sum_{i=1}^{N}\frac{\mathbf{p}_i^2}{m_i} - \gamma_p p_\epsilon + R_p. \tag{4.18d}$$

R_p is a stochastic 'force' which acts on the barostat. The use of a Langevin equation for the barostat as well as the particles may have possible equilibration benefits, but is shown by the analysis that follows to be non-critical in generating the desired ensemble.

$\mathcal{P}$ is the pressure estimator given in equation 2.30. It is worth re-emphasising that in the non-Hamiltonian case this is *not* equivalent to an "instantaneous pressure." The response of the volume depends only on the difference between the Hamiltonian part of the pressure, and the external pressure.

The values of $\mathbf{R}_i$ are drawn from the same distribution as the NVT case above. Values of R_p are drawn from a Gaussian distribution of zero mean and unit variance scaled by

$$\sqrt{\frac{2k_B T W \gamma_p}{\Delta t}}. \tag{4.19}$$

In the uncoupled limit ($\gamma \to 0, \gamma_p \to 0$) equations 4.18a to 4.18b obey the Liouville

[2] In fact, equations 4.1a and 4.1b are themselves non-Hamiltonian. The Einstein relation can be considered a construction for time-averaged compensation of the drift gradient by a stochastic force.

theorem

$$\frac{\partial \rho}{\partial t} + \sum_{i=1}^{N} \dot{\mathbf{r}}_i \nabla_{\mathbf{r}_i} \rho + \sum_{i=1}^{N} \dot{\mathbf{p}}_i \nabla_{\mathbf{p}_i} \rho + \dot{p}_\epsilon \frac{\partial \rho}{\partial p_\epsilon} + \dot{\mathcal{V}} \frac{\partial \rho}{\partial \mathcal{V}} = 0 \tag{4.20}$$

and conserve the quantity

$$H' = \mathcal{H} + P\mathcal{V} + p_\epsilon^2 / 2W, \tag{4.21}$$

where $\mathcal{H}$ is the Hamiltonian of the particle sub-system.

Justification

To show that equations 4.18a to 4.18d correctly sample the isobaric-isothermal ensemble, the microcanonical ($\gamma = 0$) phase-space probability density for the extended system is identified as,

$$\rho^{ext}\left(\mathbf{r}^N, \mathbf{p}^N, p_\epsilon, \mathcal{V}\right) = \frac{1}{\Omega^{ext}} \delta\left[H'(t) - H'(0)\right]. \tag{4.22}$$

The corresponding canonical probability density (in the extended phase space) should therefore be

$$\rho^{ext}\left(\mathbf{r}^N, \mathbf{p}^N, p_\epsilon, \mathcal{V}\right) = \frac{1}{Q^{ext}} \exp\left[-\beta\left(\mathcal{H} + P\mathcal{V} + p_\epsilon^2/2W\right)\right] \tag{4.23}$$

when employing finite friction coefficients. Following the earlier procedure, the Fokker-Planck equation for the extended phase space density ρ resulting from equations 4.18a to 4.18d is constructed. As with the generalised Liouville equation, this Fokker-Planck equation must include the probability weighting due to non-zero phase space compressibility. The compressibility of equations 3.20a to 3.20d is

$$\begin{aligned} \kappa &= \sum_{i=1}^{N} \nabla_{\mathbf{r}_i} \cdot \dot{\mathbf{r}}_i + \sum_{i=1}^{N} \nabla_{\mathbf{p}_i} \cdot \dot{\mathbf{p}}_i + \frac{\partial \dot{\mathcal{V}}}{\partial V} + \frac{\partial \dot{p}_\epsilon}{\partial p_\epsilon} \\ &= \frac{N_f p_\epsilon}{W} - \left(1 + \frac{3}{N_f}\right) \frac{N_f p_\epsilon}{W} + \frac{3p_\epsilon}{W} + 0 \\ &= 0 \end{aligned} \tag{4.24}$$

The metric determinant factor is therefore unity and need not be included in the analysis. Thus theoretical complications associated with the diffusion drift balance are not

manifested in the Andersen-Hoover system. The Fokker-Planck equation is hence

$$\begin{aligned}\frac{\partial \rho}{\partial t} &+ \sum_{i=1}^{N}\left\{\left(\frac{\mathbf{p}_i}{m_i}+\frac{p_\epsilon}{W}\mathbf{r}_i\right)\cdot\nabla_{\mathbf{r}_i}\rho+\left[\mathbf{f}_i-\left(1+\frac{3}{N_f}\right)\frac{p_\epsilon}{W}\mathbf{p}_i\right]\cdot\nabla_{\mathbf{p}_i}\rho\right\}\\ &+ \left[3\mathcal{V}\left(\mathcal{P}-P\right)+\frac{3}{N_f}\sum_{i=1}^{N}\frac{\mathbf{p}_i^2}{m_i}\right]\frac{\partial\rho}{\partial p_\epsilon}+\dot{\mathcal{V}}\frac{\partial\rho}{\partial\mathcal{V}}\\ &= \gamma_p\frac{\partial}{\partial p_\epsilon}\left[p_\epsilon\rho+Wk_BT\frac{\partial}{\partial p_\epsilon}\rho\right]+\gamma\sum_{i=1}^{N}\nabla_{\mathbf{p}_i}\cdot\left[\mathbf{p}_i\rho+mk_BT\nabla_{\mathbf{p}_i}\rho\right],\end{aligned} \tag{4.25}$$

where $\rho = \rho^{ext}\left(\mathbf{r}^N, \mathbf{p}^N, p_\epsilon, \mathcal{V}\right)$. Equation 4.23 will be a solution if equations 4.18a to 4.18d correctly simulate coupling of the extended phase-space to a heat bath. This is easily confirmed. Upon substituting 4.23 into 4.25 the LHS represents the total time derivative of ρ and is zero. The RHS is also zero, a result guaranteed by using the Einstein relation in constructing the Langevin Equations, and employing an incompressible phase space. Again assuming ergodicity this must be the single stationary solution for a given particle Hamiltonian. Integration of this ρ over all barostat momentum p_ϵ yields a constant which is absorbed into the normalisation, and hence

$$\rho\left(\mathbf{r}^N, \mathbf{p}^N, \mathcal{V}\right) = \frac{1}{\Delta}\exp\left[-\beta\left(\mathcal{H}+P\mathcal{V}\right)\right]. \tag{4.26}$$

This is the correct probability density function for the isobaric-isothermal particle sub-system. Performing Langevin Dynamics in the Andersen-Hoover extended system will therefore correctly sample the isothermal-isobaric ensemble in the particle sub-space. In justifying this, only ergodicity has been assumed. In addition the effect of the stochastic force has been included only at the level of linear response. In contrast, *deterministic NPT schemes require the additional assumption that no unexpected conservation laws are generated.* However no approximations are required within this assumption. Both approaches clearly have merits.

The condition that a suitable canonical probability density for the extended phase space be a solution of the Fokker-Planck equations is not in itself a complete condition for correct sampling. In fact, we could simply set both γ and γ_p to zero and 4.23 would still satisfy 4.25. The equations of motion must also guarantee that the thermal equilibrium represented by the Fokker-Planck equation can be reached from the initial conditions. This is clearly not the case in the limit of zero friction where no heat can be "exchanged" in or out of the system. It will only be the case if the one or more Langevin equations employ finite friction leading to the required linear response term.

4.4.2 The Parrinello-Rahman System

Equations of Motion

An implementation of Langevin Dynamics in a fully flexible simulation cell follows from the Nosé-Hoover thermostatted Parrinello-Rahman scheme of Martyna *et al.* (1994) after removing the Nosé-Hoover chains and converting to Langevin equations in the momenta:

$$\dot{\mathbf{r}}_i = \frac{\mathbf{p}_i}{m_i} + \frac{\mathbf{p}_g}{W_g}\mathbf{r}_i \tag{4.27a}$$

$$\dot{\mathbf{p}}_i = -\nabla_{\mathbf{r}_i}\Phi\left(\mathbf{r}^N, \mathbf{h}\right) - \frac{\mathbf{p}_g}{W_g}\mathbf{p}_i - \left(\frac{1}{N_f}\right)\frac{\mathrm{Tr}\left[\mathbf{p}_g\right]}{W_g}\mathbf{p}_i - \gamma\mathbf{p}_i + \mathbf{R}_i \tag{4.27b}$$

$$\dot{\mathbf{h}} = \frac{\mathbf{p}_g\mathbf{h}}{W_g} \tag{4.27c}$$

$$\dot{\mathbf{p}}_g = \mathcal{V}\left(\mathcal{P} - P_{ext}\mathbf{I}\right) + \left[\frac{1}{N_f}\sum_{i=1}^{N}\frac{\mathbf{p}_i^2}{m_i}\right]\mathbf{I} - \gamma_p\mathbf{p}_g + \mathbf{R}_p \tag{4.27d}$$

The tensor $\mathcal{P}$ is that specified in equation 2.32. As before, the random forces $\mathbf{R}_i$ are drawn from the same distribution as in the NVT case. Each component of the barostat buffeting tensor $\mathbf{R}_p$ is drawn from a Gaussian distribution of unit mean and zero variance scaled by

$$\sqrt{\frac{2k_BTW_g\gamma_p}{\Delta t}}. \tag{4.28}$$

In the case where $\gamma = \gamma_p = 0$, equations 4.27a to 4.27d conserve the quantity

$$H' = \mathcal{H}\left(\mathbf{r}^N, \mathbf{p}^N\right) + \frac{1}{2W_g}\mathrm{Tr}\left[\mathbf{p}_g\mathbf{p}_g^T\right] + P\det\left[\mathbf{h}\right]. \tag{4.29}$$

Justification

The justification that equations 4.27a to 4.27d correctly sample the fully flexible NPT ensemble is somewhat more complex than the isotropic case above. The partition function for the NPT ensemble can be written as

$$\Delta = \int_0^\infty Q(\mathcal{V})e^{-\beta P\mathcal{V}}\,d\mathcal{V} \tag{4.30}$$

where Q is the canonical partition function

$$Q(\mathcal{V}) = \int_{-\infty}^{\infty}\int_{D(\mathcal{V}} e^{-\beta\mathcal{H}}\,d\mathbf{r}^N\,d\mathbf{p}^N. \tag{4.31}$$

We must express the isothermal-isobaric partition function in terms of the matrix $\mathbf{h}$, not the volume, to analyse equations 4.27a to 4.27d. The expression

$$\Delta = \int_{-\infty}^{\infty} Q(\mathbf{h}) e^{-\beta P \det[\mathbf{h}]} \, d\mathbf{h} \tag{4.32}$$

is *not* the correct NPT partition function. Each volume $\mathcal{V} = \det[\mathbf{h}]$ will be counted multiple times in the integral as the matrix $\mathbf{h}$ for a given volume is not uniquely defined. A set of cells with the same volume exists, which if the dynamics are modularly invariant, share a common canonical partition function $Q(\mathcal{V})$. Martyna *et al.* (1994) have shown that the correct NPT partition function is reproduced if the contribution from each $\mathbf{h}$ is weighted by the inverse of its volume squared. The isothermal-isobaric partition function expressed in terms of $\mathbf{h}$ is therefore

$$\Delta = \int_{-\infty}^{\infty} Q(\mathbf{h}) e^{-\beta P \det[\mathbf{h}]} \det[\mathbf{h}]^{-2} \, d\mathbf{h} \tag{4.33}$$

and the probability density is

$$\rho = \frac{1}{\Delta} \exp\left\{-\beta \left(\mathcal{H} + P \det[\mathbf{h}]\right)\right\} \det[\mathbf{h}]^{-2}. \tag{4.34}$$

This must be produced by equations 4.27a to 4.27d in the sub-space of the particle plus cell degrees of freedom. To determine if this is the case, the extended phase space in the $\gamma = \gamma_p = 0$ case is examined. Here the quantity H' (4.29) is conserved and the probability density is microcanonical.

$$\rho^{ext}\left(\mathbf{r}^N, \mathbf{p}^N, \mathbf{p}_g, \mathbf{h}\right) = \frac{1}{\Omega^{ext}} \delta\left[H'(t) - H'(0)\right]. \tag{4.35}$$

The corresponding canonical probability density (in the extended phase space) should therefore be

$$\rho^{ext}\left(\mathbf{r}^N, \mathbf{p}^N, \mathbf{p}_g, \mathbf{h}\right) = \frac{1}{Q^{ext}} \exp\left\{-\beta \left(\mathcal{H} + P \det[\mathbf{h}] + \mathrm{Tr}\left[\mathbf{p}_g \mathbf{p}_g^T\right] / 2W_g\right)\right\} \tag{4.36}$$

when the damping and stochastic components are used. This should be a solution of the Fokker-Planck equation equivalent to equations 4.27a to 4.27d if these are to correctly sample phase-space. In constructing this equation, any non-zero compressibility of the

extended phase space must again be accounted for. This is calculated as

$$\begin{aligned}\kappa &= \sum_{i=1}^{N} \nabla_{\mathbf{r}_i} \cdot \dot{\mathbf{r}}_i + \sum_{i=1}^{N} \nabla_{\mathbf{p}_i} \cdot \dot{\mathbf{p}}_i \\ &+ \sum_{\alpha=1}^{3}\sum_{\beta=1}^{3} \frac{\partial \left(\dot{\mathbf{h}}\right)_{\alpha,\beta}}{\partial \left(\mathbf{h}\right)_{\alpha,\beta}} + \sum_{\alpha=1}^{3}\sum_{\beta=1}^{3} \frac{\partial \left(\dot{\mathbf{p}}_g\right)_{\alpha,\beta}}{\partial \left(\mathbf{p}_g\right)_{\alpha,\beta}},\end{aligned} \tag{4.37}$$

which can be simplified to

$$\begin{aligned}\kappa &= 2\mathrm{Tr}\left[\mathbf{p}_g\right]/W_g - 3\mathrm{Tr}\left[\mathbf{p}_g\right]/W_g + 3\mathrm{Tr}\left[\mathbf{p}_g\right]/W_g + 0 \\ &= 2\mathrm{Tr}\left[\mathbf{p}_g\right]/W_g.\end{aligned} \tag{4.38}$$

The scalar strain rate $\dot{\epsilon}$ is identified as $\mathrm{Tr}\left[\mathbf{p}_g\right]/2W_g$. The Jacobian of the coordinate transform which takes the system from $t =' 0$ to $t' = t$ is therefore

$$J\left(t;0\right) = \exp\left(\int_0^t 6\dot{\epsilon}\, dt'\right), \tag{4.39}$$

and hence the phase space metric determinant factor is

$$\sqrt{g\left(t;0\right)} = \frac{V_{ref}^2}{\mathcal{V}^2} \propto \frac{1}{\det\left[\mathbf{h}\right]^2}, \tag{4.40}$$

where V_{ref} is the volume of the cell to which the strain is referenced. This is non-zero and hence the Einstein relation is invalid in the extended phase space. The Fokker-Planck equation is,

$$\begin{aligned}\frac{\partial \rho_w}{\partial t} &+ \sum_{i=1}^{N}\left(\frac{\mathbf{p}_i}{m_i} + \frac{\mathbf{p}_g}{W_g}\mathbf{r}_i\right)\cdot\nabla_{\mathbf{r}_i}\rho_w \\ &+ \sum_{i=1}^{N}\left[\mathbf{f}_i - \frac{\mathbf{p}_g}{W_g}\mathbf{p}_i - \left(\frac{1}{N_f}\right)\frac{\mathrm{Tr}\left[\mathbf{p}_g\right]}{W_g}\mathbf{p}_i\right]\cdot\nabla_{\mathbf{p}_i}\rho_w \\ &+ \sum_{\alpha,\beta}\left[\left(\mathcal{P}_{\alpha\beta} - P\delta_{\alpha\beta}\right)\det\left[\mathbf{h}\right] + \frac{1}{N_f}\sum_{i=1}^{N}\frac{\mathbf{p}_i^2}{m_i}\right]\frac{\partial\rho_w}{\partial(p_g)_{\alpha\beta}} \\ &+ \sum_{\alpha,\beta}\left(\frac{\mathbf{p}_g\mathbf{h}}{W_g}\right)_{\alpha\beta}\frac{\partial\rho_w}{\partial(h)_{\alpha\beta}} = \gamma\sum_{i=1}^{N}\nabla_{\mathbf{p}_i}\cdot\left[\mathbf{p}_i\rho_w + mk_BT\nabla_{\mathbf{p}_i}\rho_w\right] \\ &+ \gamma_p\sum_{\alpha,\beta}\frac{\partial}{\partial(p_g)_{\alpha\beta}}\left[(p_g)_{\alpha\beta}\rho_w + W_gk_BT\frac{\partial\rho_w}{\partial(p_g)_{\alpha\beta}}\right],\end{aligned} \tag{4.41}$$

where ρ_w is the weighted probability $\rho\left(\mathbf{r}^N, \mathbf{p}^N, \mathbf{p}_g, \mathbf{h}\right) / \det\left[\mathbf{h}\right]^2$. If ρ from equation 4.36 is substituted, the left hand side of this equation becomes zero. This is the total time derivative of ρ_w which is zero in accordance with the generalised Liouville theorem. The background system in which the Langevin dynamics simulation is conducted therefore has a constant, but non-uniform weighted microcanonical probability density which conserves equation 4.29. The right hand side is however not zero. The non-Hamiltonian probability gradients have invalidated the balance of diffusion and friction for the Langevin equation in the cell momentum as anticipated. In the case where symmetric pressure and cell buffetting tensors have been used to eliminate cell rotations, the imbalance is proportional to γ_p.

If γ_p is set to zero while retaining a finite particle friction coefficient γ, thermal equilibrium is still guaranteed for the cell degrees of freedom via thermalisation with the particles. This may require longer equilibration times than the isotropic case where we can couple the cell directly to the Langevin heat bath, but avoids the need to construct a generalised Einstein relation for the non-Euclidean phase-space. The diffusion drift balance is only maintained in directions perpendicular to probability gradients, where the Einstein relation holds.

In this case 4.36 is indeed a solution of the Fokker-Planck equation, and the corresponding weighted density is

$$\sqrt{g}\rho\left(\mathbf{r}^N, \mathbf{p}^N, \mathbf{p}_g, \mathbf{h}\right) = \frac{\exp\left\{-\beta\left(\mathcal{H} + P\det\left[\mathbf{h}\right] + \mathrm{Tr}\left[\mathbf{p}_g\mathbf{p}_g^T\right]\right)\right\}}{Q^{ext}\det\left[\mathbf{h}\right]^2}. \tag{4.42}$$

Assuming ergodicity in $\mathbf{p}_g$, the distribution in the particle plus cell phase space is

$$\begin{aligned}\sqrt{g}\rho\left(\mathbf{r}^N, \mathbf{p}^N, \mathbf{h}\right) &= \int_{-\infty}^{\infty}\sqrt{g}\rho\left(\mathbf{r}^N, \mathbf{p}^N, \mathbf{p}_g, \mathbf{h}\right)d\mathbf{p}_g \\ &= \frac{1}{\Delta}\exp\left\{-\beta\left(\mathcal{H} + P\det\left[\mathbf{h}\right]\right)\right\}\det\left[\mathbf{h}\right]^{-2}. \end{aligned}\tag{4.43}$$

where the constant resulting from the integration is absorbed into the new normalisation. This is exactly the correct function for the fully flexible NPT ensemble as identified in equation 4.34. Again assuming ergodicity, this must be the only solution of 4.41 and hence the equations 4.27a to 4.27d correctly sample the NPT ensemble *provided γ_p is set to zero.*

4.5 Numerical Integration

In this section, numerical algorithms for the two methods introduced in the previous section are obtained following the same strategy employed by Kolb and Dunweg (1999) for Hamiltonian system. This involves applying the formalism introduced in section 3.3 to the equations in the zero friction limit. Integrators for the finite friction case are then recovered by adding the dissipative friction and diffusive stochastic forces to the interaction force wherever it appears. The integrator for the Andersen-Hoover based scheme only is derived here. The analysis for the Parrinello-Rahman style scheme proceeds in an almost identical fashion.

The Liouville operator for equations 4.18a to 4.18d in the limit of zero friction is

$$\begin{aligned} iL &= \dot{\mathbf{r}}\frac{\partial}{\partial \mathbf{r}} + \dot{\mathbf{p}}\frac{\partial}{\partial \mathbf{p}} + \dot{\epsilon}\frac{\partial}{\partial \epsilon} + \dot{p}_\epsilon \frac{\partial}{\partial p_\epsilon} \\ &= iL_r + iL_p + iL_\epsilon + iL_{p_\epsilon}. \end{aligned} \tag{4.44}$$

The following Trotter factorisation of the resulting time-step evolution operators was found to be the most convenient:

$$e^{iL\Delta t} = e^{iL_\epsilon \Delta t/2} e^{iL_{p_\epsilon}\Delta t/2} e^{iL_p \Delta t/2} e^{iL_r \Delta t} e^{iL_p \Delta t/2} e^{iL_{p_\epsilon}\Delta t/2} e^{iL_\epsilon \Delta t/2}, \tag{4.45}$$

which leads to the following integration algorithm if the application of each time-evolution operator is interpreted as a Verlet-like step.

1. $\mathcal{V}^{t+\frac{1}{2}\Delta t} = \mathcal{V}^t + \frac{\Delta t}{2}\dot{\mathcal{V}}\left[\mathcal{V}^t, p_\epsilon^t\right]$
2. $p_\epsilon^{t+\frac{1}{2}\Delta t} = p_\epsilon^t + \frac{\Delta t}{2}\dot{p}_\epsilon\left[\mathbf{r}_i^t, \mathbf{p}_i^t, \mathcal{V}^{t+\frac{1}{2}\Delta t}, p_\epsilon^t\right]$
3. $\mathbf{p}_i^{t+\frac{1}{2}\Delta t} = \mathbf{p}_i^t + \frac{\Delta t}{2}\dot{\mathbf{p}}_i\left[\mathbf{r}_i^t, \mathbf{p}_i^t, p_\epsilon^{t+\frac{1}{2}\Delta t}\right]$
4. $\mathbf{r}_i^{t+\Delta t} = \mathbf{r}_i^t + \Delta t\dot{\mathbf{r}}_i\left[\mathbf{r}_i^t, \mathbf{p}_i^{t+\frac{1}{2}\Delta t}, p_\epsilon^{t+\frac{1}{2}\Delta t}\right]$
5. $\mathbf{p}_i^{t+\Delta t} = \mathbf{p}_i^{t+\frac{1}{2}\Delta t} + \frac{\Delta t}{2}\dot{\mathbf{p}}_i\left[\mathbf{r}_i^{t+\Delta t}, \mathbf{p}_i^{t+\frac{1}{2}\Delta t}, p_\epsilon^{t+\frac{1}{2}\Delta t}\right]$
6. $p_\epsilon^{t+\Delta t} = p_\epsilon^{t+\frac{1}{2}\Delta t} + \frac{\Delta t}{2}\dot{p}_\epsilon\left[\mathbf{r}_i^{t+\Delta t}, \mathbf{p}_i^{t+\Delta t}, \mathcal{V}^{t+\frac{1}{2}\Delta t}, p_\epsilon^{t+\frac{1}{2}\Delta t}\right]$
7. $\mathcal{V}^{t+\Delta t} = \mathcal{V}^t + \frac{\Delta t}{2}\dot{\mathcal{V}}\left[\mathcal{V}^{t+\frac{1}{2}\Delta t}, p_\epsilon^{t+\Delta t}\right].$

Making the appropriate substitution for the particle forces at each time-step, the Langevin buffeting and damping terms are included and denoted as extra dependences of the time derivatives.

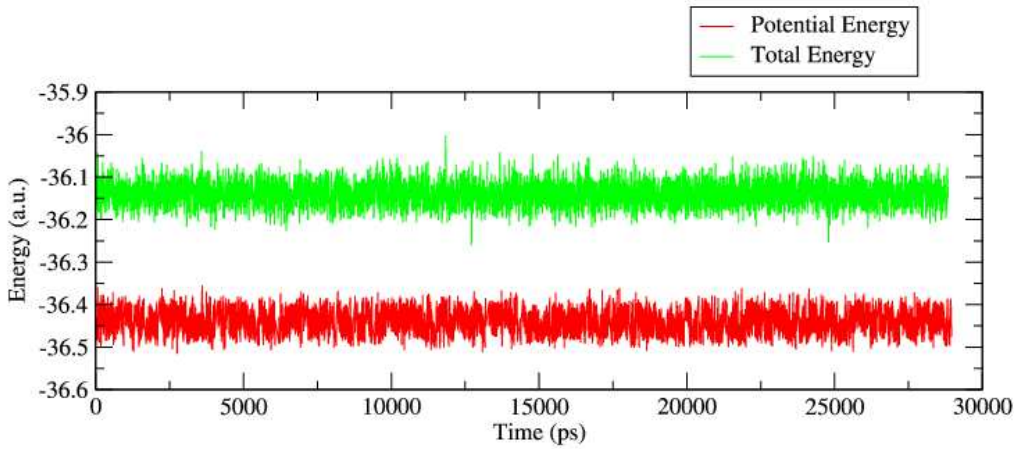

Figure 4.3: *Long term stability of the fully flexible Langevin NPT algorithm. The figure shows the total and potential energy in a simulation of 216 silicon atoms in the diamond structure at 298 K, 1 atm. The total run length at equilibrium corresponds to 12 million MD steps, with no discernable drift in the energies. The potential of Tersoff (1989) is used in the GOLDILOCS code to model silicon.*

1. $\mathcal{V}^{t+\frac{1}{2}\Delta t} = \mathcal{V}^{t} + \frac{\Delta t}{2}\dot{\mathcal{V}}\left[\mathcal{V}^{t}, p_{\epsilon}^{t}\right]$
2. $p_{\epsilon}^{t+\frac{1}{2}\Delta t} = p_{\epsilon}^{t} + \frac{\Delta t}{2}\dot{p}_{\epsilon}\left[\mathbf{r}_{i}^{t}, \mathbf{p}_{i}^{t}, \mathcal{V}^{t+\frac{1}{2}\Delta t}, p_{\epsilon}^{t}, \gamma_{p} p_{\epsilon}^{t}, R_{p}^{t}\right]$
3. $\mathbf{p}_{i}^{t+\frac{1}{2}\Delta t} = \mathbf{p}_{i}^{t} + \frac{\Delta t}{2}\dot{\mathbf{p}}_{i}\left[\mathbf{r}_{i}^{t}, \mathbf{p}_{i}^{t}, p_{\epsilon}^{t+\frac{1}{2}\Delta t}, \gamma \mathbf{p}_{i}^{t}, \mathbf{R}_{i}^{t}\right]$
4. $\mathbf{r}_{i}^{t+\Delta t} = \mathbf{r}_{i}^{t} + \Delta t \dot{\mathbf{r}}_{i}\left[\mathbf{r}_{i}^{t}, \mathbf{p}_{i}^{t+\frac{1}{2}\Delta t}, p_{\epsilon}^{t+\frac{1}{2}\Delta t}\right]$
5. $\mathbf{p}_{i}^{t+\Delta t} = \mathbf{p}_{i}^{t+\frac{1}{2}\Delta t} + \frac{\Delta t}{2}\dot{\mathbf{p}}_{i}\left[\mathbf{r}_{i}^{t+\Delta t}, \mathbf{p}_{i}^{t+\frac{1}{2}\Delta t}, p_{\epsilon}^{t+\frac{1}{2}\Delta t} \gamma \mathbf{p}_{i}^{t+\Delta t}, \mathbf{R}_{i}^{t+\Delta t}\right]$
6. $p_{\epsilon}^{t+\Delta t} = p_{\epsilon}^{t+\frac{1}{2}\Delta t} + \frac{\Delta t}{2}\dot{p}_{\epsilon}\left[\mathbf{r}_{i}^{t+\Delta t}, \mathbf{p}_{i}^{t+\Delta t}, \mathcal{V}^{t+\frac{1}{2}\Delta t}, p_{\epsilon}^{t+\Delta t}, \gamma_{p} p_{\epsilon}^{t+\Delta t}, R_{p}^{t+\Delta t}\right]$
7. $\mathcal{V}^{t+\Delta t} = \mathcal{V}^{t+\frac{1}{2}\Delta t} + \frac{\Delta t}{2}\dot{\mathcal{V}}\left[\mathcal{V}^{t+\frac{1}{2}\Delta t}, p_{\epsilon}^{t+\Delta t}\right].$

This and the equivalent fully-flexible algorithm are implemented within the GOLDILOCS code. The integrators have been found to be suitably stable. The formal energy conservation properties of algorithms derived in the Liouvillian formalism has however been lost due to the introduction of velocity dependent and stochastic forces. In thermal equilibrium, and provided that a correctly distributed set of pseudo-random numbers is employed, the net effect of these forces is zero for times longer than the timescale $(1/\gamma)$ of the stochastic process. It is therefore expected that the total energy will fluctuate, but with zero long term drift. This is demonstrated for the fully-flexible algorithm in figure 4.3. The inclusion of velocity dependent and stochastic forces has also sacrificed time reversibility. Despite this, it is shown in the above Fokker-Planck equations that the total

time derivative of the weighted probability density is zero for both systems. The method is therefore still symplectic to within the assumptions implicit in the Fokker-Planck formalism.

4.6 Parameters

Performing Langevin dynamics in the above non-Hamiltonian systems has been shown to sample the NPT ensemble. The dynamics must also remain representative of the system in question by careful choice of the friction coefficient γ, ensuring that the stochastic component does not dominate over that generated from the model Hamiltonian. In addition, careful choice of barostat 'mass' parameter W or W_g is also required to ensure the effect of density fluctuations is realistic.

4.6.1 Particle Friction Coefficient using Memory Functions

This section explores the utility of the memory function for calculating an estimate for the parameter γ, as discussed by Kneller and Hinsen (2001).

Definition

The memory function ξ for a correlation function ψ is defined as

$$\frac{d\psi}{dt} = -\int_0^t \xi\left(t-\tau\right)\psi\left(\tau\right)d\tau. \tag{4.46}$$

The rate at which a system decorrelates is the cumulative sum of the correlation function at all previous times, weighted by the memory function. For atomistic simulation, a suitable correlation function to work with is the velocity autocorrelation function. This is defined as

$$\psi\left(t\right) = \frac{\left\langle \mathbf{v}_i\left(t\right)\cdot\mathbf{v}_i\left(0\right)\right\rangle}{\left\langle \mathbf{v}_i\left(0\right)\cdot\mathbf{v}_i\left(0\right)\right\rangle} \tag{4.47}$$

where the average runs over all particles $i = 1\ldots N$ at time t. This is easily calculated from a molecular dynamics trajectory. It describes the average decorrelating effect on the trajectory of an *individual* particle, due to all other particles in the system.

Calculation

In principle, a memory function can be calculated directly from the Laplace transform of the corresponding correlation function. In practice, such calculations are prone to severe numerical problems. An alternative method has been proposed by Kneller and Hinsen (2001) and adopted here. This is based on an autoregressive model of the process responsible for the temporal decorrelation of our single particle motion. Although in principle deterministic, the process is the result of the combined influence of a great many degrees of freedom (the other particles in the system) and can be treated as stochastic. The memory function is hence recovered by employing signal processing techniques used to quantity the effect of this 'noise.'

The autoregressive model is implemented in the freely available code NMOLDYN (Rog *et al.*, 2003). An interface to the code has been created by the author, allowing memory functions to be calculated from GOLDILOCS trajectories.

Application to Langevin Dynamics

The generalised Langevin equation employs a time-dependent friction kernel and is written as

$$\dot{\mathbf{p}}_i = \mathbf{f}_i - \int_0^t \xi\left(t-\tau\right)\mathbf{p}_i\left(\tau\right)d\tau + \mathbf{R}_i, \tag{4.48}$$

which in the extended phase space of the Andersen-Hoover system becomes

$$\dot{\mathbf{p}}_i = -\nabla_{\mathbf{r}_i}\Phi - \left(1+\frac{3}{N_f}\right)\frac{p_\epsilon}{W}\mathbf{p}_i - \int_0^t \xi\left(t-\tau\right)\mathbf{p}_i\left(\tau\right)d\tau + \mathbf{R}_i \tag{4.49}$$

for the particle degrees of freedom. In the Parrinello-Rahman phase space, the equivalent is

$$\dot{\mathbf{p}}_i = -\nabla_{\mathbf{r}_i}\Phi - \frac{\mathbf{p}_g}{W_g} - \left(\frac{3}{N_f}\right)\frac{\mathrm{Tr}\left[\mathbf{p}_g\right]}{W_g}\mathbf{p}_i - \int_0^t \xi\left(t-\tau\right)\mathbf{p}_i\left(\tau\right)d\tau + \mathbf{R}_i. \tag{4.50}$$

Comparing to equations 4.18b and 4.27b, it can be seen that the stochastic component of the dynamics is generated within the approximation

$$\xi(t') = \gamma\delta(t-t'). \tag{4.51}$$

To retain consistency with this approximation, the value of gamma should be equal to

$$\gamma = \xi_0 = \int_0^\infty \xi_{act}(\tau)d\tau, \tag{4.52}$$

Given the memory function for the 'real' system, it is hence possible to determine the effective friction coefficient experienced by a particle. This value, denoted here as γ_{nat} marks the watershed between two ways in which the Langevin equation can be employed in a simulation. If $\gamma < \gamma_{nat}$, the particle dynamics will dominate effectively generating a 'Langevin thermostat'. Alternatively, with $\gamma > \gamma_{nat}$, true Langevin dynamics simulations are obtained, in which some short term accuracy in short-term dynamics is sacrificed in favour of increased statistical efficiency.

Of course if a true bulk simulation from which to compute a memory function was available, there would be little utility in performing a smaller Langevin dynamics simulation from which to obtain thermodynamic averages. However computing a memory function from a large simulation with a cheap classical potential may provide a useful starting point in identifying optimal parameters for a much smaller *ab-initio* simulation. In addition, a friction coefficient calculated from a memory function will give a starting point from which values at other state points can be estimated.

4.6.2 Choice of Cell Mass

Martyna *et al.* (1996) state that the fictitious mass associated with the Andersen-Hoover barostat should be chosen according to

$$W = 3Nk_bT/\omega_b^2, \tag{4.53}$$

where ω_b is a frequency associated with the volume oscillation. This relationship can be recovered in the ideal gas limit of equations 4.18a to 4.18d. In this case the volume oscillates harmonically at ω_b. Similarly the Parrinello-Rahman cell mass should be chosen according to

$$W_g = (N_f + 3)k_BT/3\omega_b^2. \tag{4.54}$$

The choice of fictitious mass therefore reduces to the determination of an appropriate frequency. If this is very small, the motion of the cell becomes effectively decoupled from that of the particles. If this is too large, the barostat may dominate over the interaction forces. For simple liquids, choosing the barostat frequency to be approximately ten times smaller than $2\pi\gamma$ (the frequency associated with the diffusion-drift process) is generally suitable. For solids however, care must be taken that ω_b does not interfere with the vibrational frequencies of the crystal. A method for identifying a suitable ω_b for solids is given in example 4.7.1. This is based on ensuring that the effect of the Langevin dynamics in frequency space is not disrupted by ω_b.

It should be noted that the choice of ω_b for these Langevin dynamics schemes can be

considerably more difficult than in the Nosé-Hoover case. The latter method operates at a well defined *single* frequency ω_{NH} which can be related to the fictitious mass Q of the heat bath variable. It is therefore trivial to choose ω_b to be well separated from this, avoiding disruption of the thermostatic process. Langevin dynamics methods for temperature control operate over a wide frequency *range* (Allen and Tildesley, 1987). Avoiding this may therefore sometimes require ω_b to be smaller than in the Nosé-Hoover case. Experience has shown that failure to do so can lead to poor temperature control. This requirement of a smaller ω_b could negatively impact statistical efficiency. No problems of this nature have been encountered in the examples below. However, the simulations reported in chapter 7 have manifested these issues when simulating extreme pressures at low temperature. In this regime the stochastic forces are weak in comparison to the applied compressive stress, and are hence easily disrupted by a poor choice of ω_b.

4.6.3 Choice of Cell Friction Coefficient

For Langevin dynamics in the Andersen-Hoover system, a value of the cell friction coefficient γ_p should also be specified. It is possible to perform a simulation employing zero friction for the cell, and hence to compute a memory function for its motion. This is not useful in practise. An optimised choice of γ_p has little effect on the particle dynamics and hence offers little improvement in overall sampling efficiency. In the GOLDILOCS code γ_p is set to $0.1\omega_b/2\pi$, i.e. the timescale associated with the diffusion drift process along the volume axis is ten times slower than the expected volume oscillation period.

4.7 Examples

Example simulations of three systems are presented below. These are intended to be illustrative of the methodology rather than a complete listing of all cases tested.

4.7.1 Lennard-Jonesium

The Lennard-Jones pair potential has become the standard benchmark for the testing of algorithms. Much development work was conducted with this model. Two examples are given here. The potential is truncated at $r_{ij} = 2.5\sigma$. The force-shifting method is employed as described in section 3.5.2. Measured quantities are presented here in the usual dimensionless reduced units. Energies are quoted as multiples of the well depth ϵ, lengths as multiples of σ. Reduced temperature T^* is calculated as k_BT/ϵ, with pressure $P^* = P\sigma^3/\epsilon$. Time is measured in units $t^* = (m/\epsilon)^{1/2}\sigma$ where m is the atomic mass.

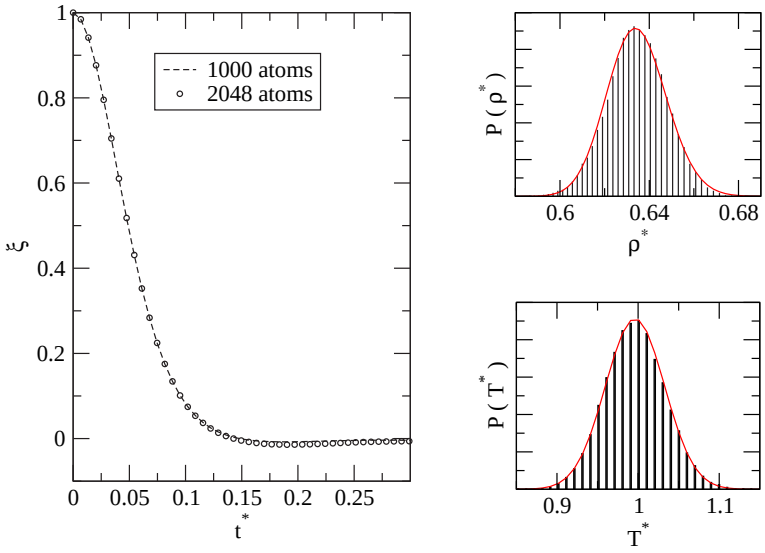

Figure 4.4: *Memory function for the Lennard-Jones liquid at $T^* = 1$, $P^* = 0.5$ (left). Increasing the system size provides no useful increase in accuracy. The distribution of temperature and density samples during the subsequent Langevin dynamics simulation are shown on the left compared to the expected function for the NPT ensemble (solid lines).*

Bulk Liquid

At a temperature $T^* = 1$ and pressure $P^* = 0.5$ the truncated and force-shifted Lennard-Jones potential lies firmly in the liquid region with a density of approximately $\rho^* = 0.63$. The memory function computed from a large NVE simulation at this density and temperature is shown in figure 4.4. A natural friction coefficient of $\gamma_{nat} = 0.50$ is obtained by numerical integration. Simulations were conducted using a value 10 times larger than this for increased sampling efficiency. As this is a simple liquid with no well defined natural frequencies, ω_b for the Andersen-Hoover barostat can be chosen with some freedom. This was set to one tenth $2\pi\gamma$, avoiding possible resonance of the volume with the particle thermostat.

A time-step of 0.0045 is employed in a cubic cell of 500 atoms. The system was equilibrated for $10,000$ steps and then sampled every 10 steps for a further $500,000$. The resulting distributions of temperature and density samples are shown in figure 4.4. The mean and variance of the density distribution yield an average density of $\rho^* = 0.6337 \pm 0.0003$ and bulk modulus $\beta_T^* = 2.90 \pm 0.02$. These compare to $\rho^* = 0.6335 \pm 0.0003$ and $\beta_T^* = 2.90 \pm 0.02$ from a simulation of the same length using multiple Nosé-Hoover chains. Errors are corrected for correlation between samples by using both the block averaging method (see Allen and Tildesley (1987)) and by explicit calculation of the volume autocorrelation function. The volume correlation times for both simulations is approximately 85 samples.

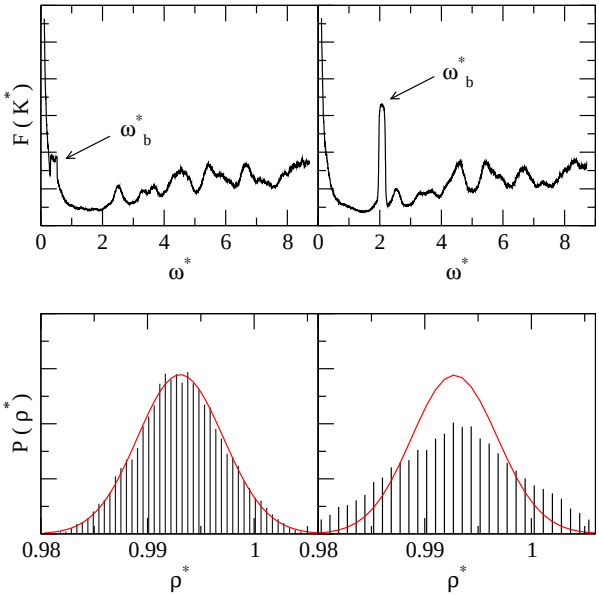

Figure 4.5: *Fourier Transformed temperature (top) and corresponding distribution of density samples compared to the correct function (bottom). In the left hand case the cell frequency has been chosen to be smaller than the lowest characteristic frequency of the solid. The natural motions of the crystal are not disturbed and correct sampling of density is achieved. In the right hand case the choice of ω_b has disrupted the crystal vibrations, leading to incorrect sampling.*

Bulk Solid

At a temperature $T^* = 0.167$ and pressure $P^* = 1.18$, the density of the solid is approximately $\rho^* = 1.05$. A memory function computed from a 4,000 atom NVE simulation suggests a friction coefficient of $\gamma = 0.23$ as suitable. An appropriate choice for the frequency ω_b must now be located. The strategy adopted is to examine the Fourier transform of some dynamical quantity in our simulation. This will exhibit a feature at ω_b, which is required to be well separated from the characteristic frequencies of the crystal.

The cell motion interacts with the particles in two ways. The first is through the additional force which acts on each particle proportional to the cell momentum (equations 4.18b and 4.27b). This is a single particle effect. The second is through the rescaling of all particle coordinates as the cell moves. This effects all N particles simultaneously. Choosing to Fourier transform a single particle property, such as the velocity autocorrelation function is not useful. To gain reasonable statistics this is generally computed by averaging over all particles, during which the single particle influence of the cell motion will vanish. We should therefore compute the Fourier transform of a property dependent on all N particles, such as the total kinetic energy or temperature estimator.

A suitable ω_b can hence be found by performing an NVT Langevin dynamics simulation and computing the Fourier transform of the temperature. A series of short NPT simulations with varying ω_b can then be conducted, and the effect on the temperature

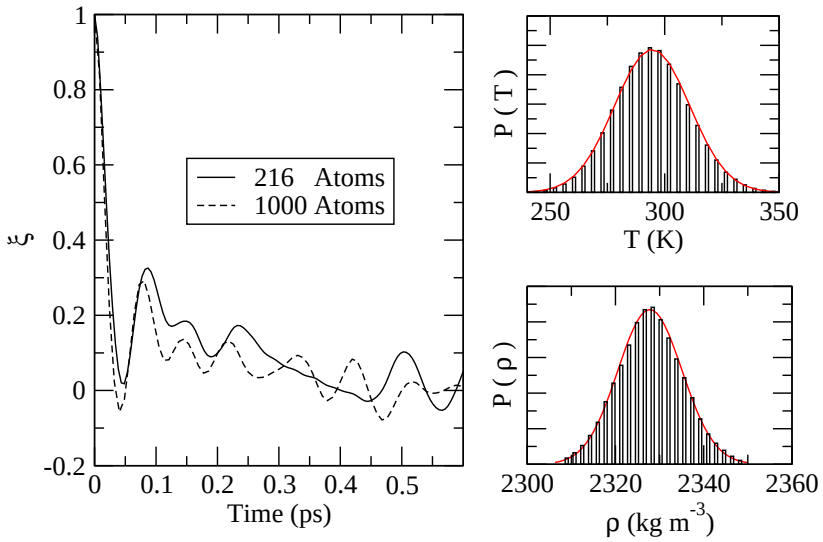

Figure 4.6: *NVE memory function (left) and NPT temperature and volume sample distributions (right) for silicon at 295 K, 1 atm. The NPT runs were conducted at atmospheric pressure. The solid lines shown are the theoretical distributions, calculated assuming* $\beta_T = 95.6\,GPa$ *in the volume case. Experimentally* $\rho = 2330\,kg\,m^{-3}$, $\beta_T = 100\,GPa$.

spectrum determined. The spectrum for two values of ω_b and the resulting distribution of density samples is shown in figure 4.5. Simulations were conducted with the fully flexible Langevin NPT algorithm.

Clearly this procedure is time consuming. However once a suitable value for ω_b has been identified, it can be expected to be suitable for simulations at a range of temperatures and pressures. The information can therefore be re-used, provided the distribution of temperature and density samples is checked for each simulation, computing a new ω_b if necessary.

Data from the simulation on the left of figure 4.5 have been compared to the Nosé-Hoover case with similar accuracy to that for the liquid simulations above.

4.7.2 Silicon

The silicon model implemented in the GOLDILOCS code is the bond-order potential of Tersoff (1989). This is known to reproduce the solid phases of silicon with reasonable accuracy. In this section a simulation of the bulk diamond structure is performed at room temperature and pressure. Results are compared to experiment.

A silicon memory function was computed from NVE simulations at the experimental density using both 216 and 1000 atoms. Temperatures were rescaled during equilibration to a temperature of 295 K. A time-step of 1.8 fs was determined to maintain suitable conservation of the energy. The resulting memory functions are shown in figure 4.6. It would

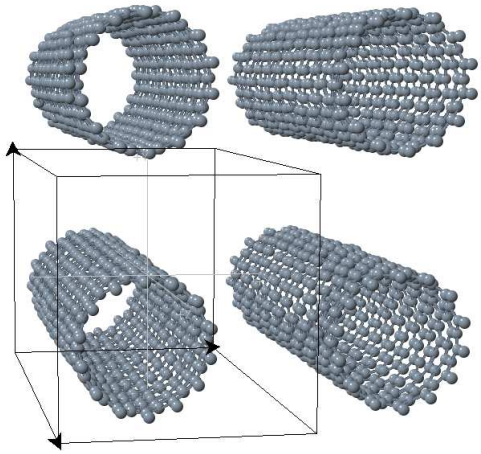

Figure 4.7: *Illustration of the nanotube supercell. The isotropic cell dynamics constrain the shape of the cell such that interaction (and hence pressure) is removed in directions perpendicular to the tube.*

seem that the memory function has not yet converged to that of the bulk, however we can expect the calculated friction coefficient to be representative.

The resulting transport coefficients indicate optimal thermostat relaxation times of 14.3 and 20.0 ps from the 216 and 1000 atom cell respectively. An NPT Langevin dynamics run is then conducted based on this information. A relaxation time of 5 ps was chosen for the thermostat, sacrificing some accuracy in short-term dynamics. A suitable value of $\omega_b = 2.1 \times 10^{-5}$ rad fs^{-1} was identified from a Fourier transformed NVT temperature profile as for the Lennard-Jones case above.

Using these parameters, a Langevin Dynamics simulation of 216 atoms in a fully flexible cell was conducted for 4,000,000 time-steps using a larger time-step of 2.4 fs. Temperature and volume were sampled every 10 steps. The resulting distributions of temperature and volume are plotted in figure 4.6. The bulk modulus calculated from the fluctuations in volume is $\beta_T = 95.6 \pm 0.2$ GPa. Both this and the average density are in good agreement with experiment.

4.7.3 Carbon Nanotubes

In this section we shall use the constant pressure Langevin Dynamics methodology to study the effect of axial stress on the length on a (8,8) single-walled carbon nanotube. Interactions between carbon atoms are modelled using the potential of Brenner (1990); Brenner *et al.* (1991). This is a simple modification of the Tersoff potential employed in the previous section.

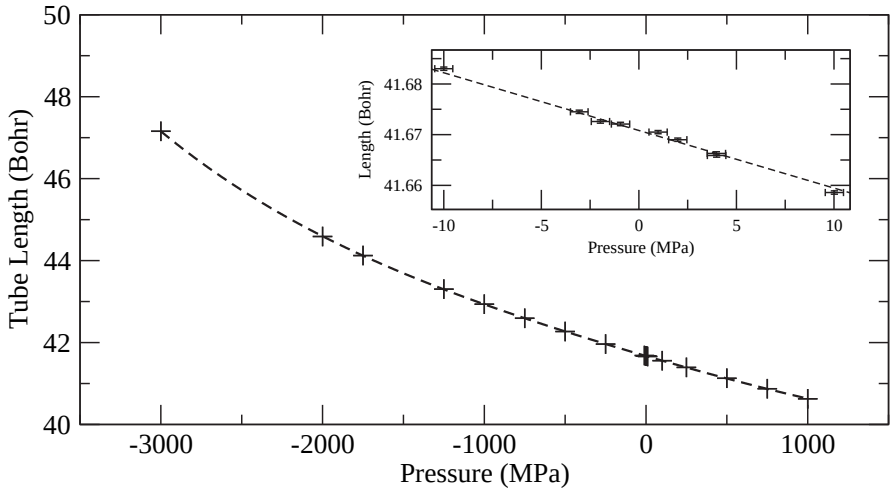

Figure 4.8: *Nanotube length against applied pressure. Error bars become visible only at magnification (inset).*

Boundary Conditions

In order to apply pressure in one direction only (i.e. along the tube,) interactions between nanotubes in adjacent image cells must be eliminated. This is achieved by ensuring that the distance between the tube and its images is much larger than the cut-off range of the Brenner potential. The use of isotropic cell dynamics ensures that this condition remains satisfied as illustrated in figure 4.7. The cell vectors perpendicular to the tube direction do change, but not sufficiently that forces appear between tubes. The effective pressure is therefore applied along the tube only, the other diagonal components of the applied pressure tensor having no effect.

Simulations and Results

For a range of applied pressures, ranging from 3 GPa of tension to 1 GPa of compression, a series of Langevin dynamics simulations were conducted at a temperature of 100 K. A time-step of Δt =2.4 fs is used. An equilibration period of $5,000\Delta t$ is employed before evolving for a further $100,000$ time-steps. The tube length is sampled every $10\Delta t$. Thermostat and barostat relaxation times are set at 100 fs and 15 ps respectively. These are taken from earlier simulations of graphite (Quigley and Probert, 2005). The resulting plot of tube length against applied pressure is shown in figure 4.8.

The Young's modulus computed from the linear portion of this plot is 36.2 GPa. This does not compare well with the calculations of Ogata and Shibutani (2003), who measure the modulus for (8,8) tubes as 979 GPa with tight-binding calculations, and 1008 GPa when employing density functional theory within the LDA. Ogata and Shibutani employed a stress range of 0 to 100 GPa at zero temperature to compute these values, which agree

well with experimental measurements in the range $900 - 1000$ GPa, and the in-plane bulk modulus of graphite (≈ 1000 GPa).

No finite temperature simulation studies have been reported in the literature.

Using the Brenner potential at zero temperature within the GOLDILOCS code, a Young's modulus of 37.8 GPa is measured for tensions between range 0-3 GPa. This indicates that the discrepency is a fault of the Brenner potential and not of the sampling scheme. It should be noted that an improved version of the Brenner potential is available (Brenner *et al.*, 2002) which gives significant improvements in energies and forces. Simulations with this potential may give improved elastic properties. It is clear that the original Brenner potential is not suitable for simulations of nanotubes under stress.

Chapter 5

Phase Transitions

In this chapter the physics of phase transitions is discussed with particular focus on temperature/pressure driven transitions in single component atomic systems. The issues associated with locating phase transitions by simulation of a model system will be discussed. The work presented in this thesis is concerned with equilibrium phase transitions only. The systems of interest obey classical statistics. Intrinsically quantum phase transitions such those involved in superconductivity and Bose-Einstein condensation are not relevent to this discussion.

5.1 Phase Transitions

It is useful to consider each phase of a substance as corresponding to a minimum on the free energy landscape defined by the Hamiltonian and thermodynamic conditions. Elementary statistical mechanics states that a system will preferentially occupy the minimum with the lowest free energy, providing a means for determining which phase will be manifested under given conditions.

For all phase transitions there is a change in some order parameter. In the case of melting this is easily identified as a crystalline long-range order parameter which varies from one (perfect order) to zero (disordered) across the transition. For the liquid-gas transition the order parameter is related to the density difference between the two phases. It is common to divide phase transitions into those in which the order parameter varies discontinuously across the transition (first order) and those in which the change is continuous. This classification of either first-order or continuous behaviour has widely replaced the classification of Ehrenfest[1].

[1] In the Ehrenfest classification, the order of a phase transition is that of the lowest derivative of the Gibbs free energy which exhibits a discontinuity at the transition.

5.1.1 Stability

It is important to distinguish between thermodynamic and mechanical stability. Any phase which corresponds to a minimum on the free energy landscape will be mechanically stable. The lowest free energy state is *thermodynamically* stable and will be obtained preferentially in equilibrium. Other mechanically stable states are termed *metastable* states. If the system is ergodic, a system initially in a metastable state will eventually locate the thermodynamically stable minimum. Hence a metastable state has a finite lifetime. A relevant example is a supercooled liquid, i.e. a liquid which has been cooled below its thermodynamic melting temperature without freezing to a solid. A system initially in a thermodynamically stable state will remain so indefinitely. The lifetime in a metastable minimum is related to its height above that of the thermodynamically stable state, and to any free energy barrier which separates them. This can be very short on thermodynamic timescales, e.g. a superheated solid. The lifetime can also be very long, for example in the diamond phase of carbon which is metastable with respect to graphite under ambient conditions. The lifetime in this case is extremely long due to the small energy difference between the two forms and a large energy barrier between them.

If more than one metastable phase exists, it is possible for a transition to exist between them without proceding via the thermodynamically stable state. This is referred to as a metastable phase transition. For example Crain *et al.* (1994) have presented evidence of a transition between two metastable high density phases of silicon which does not involve the thermodynamically stable diamond structure.

5.1.2 Phase Coexistence

Well away from a phase boundary, a single phase has much lower free energy than any other. In this limit the Boltzmann probability of this single phase will dominate. Close to a phase boundary the free energy minima of two phases are of similar depth. The associated Boltzmann factors are no longer separated by orders of magnitude. It becomes possible for the second phase to be explored with appreciable probability. In this situation a sample of a substance will begin to nucleate a second phase, existing in a mixed state subject to the increase in energy associated with forming an interface. At exactly the transition temperature and pressure the two minima are of equal free energy and coexist with equal chemical potential μ. An illustration of free energy progression during a first-order transition is shown in figure 5.1.

For transitions in which the order parameter varies discontinuously, a mixed phase state can sometimes be enforced by applying a constraint. Suppose that in figure 5.1, the value

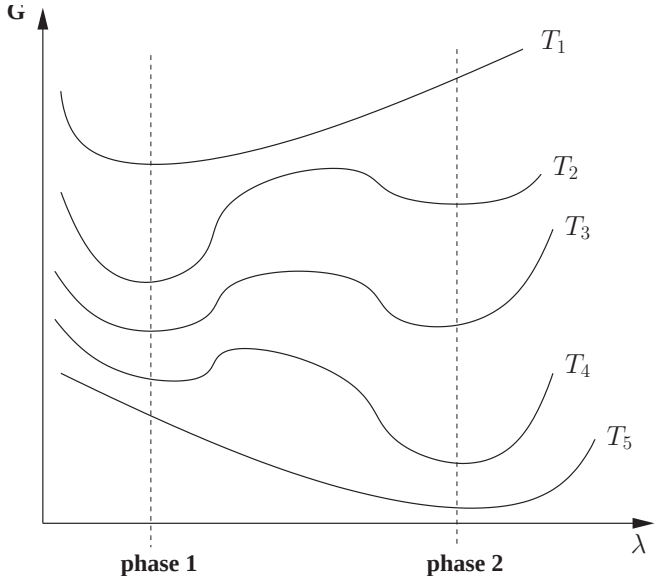

Figure 5.1: *Evolution of the free energy G with temperature during a phase transition between two states with different values of the parameter λ (sketch). At T_1 only phase 1 is stable. At T_2 the second phase has become metastable. T_3 is the transition temperature at which the free energies of both phases phases are equal. At T_4 phase 2 is thermodynamically stable, with phase 1 existing as a metastable state. At T_5 only phase 2 is accessible.*

of λ at T_3 was constrained to lie between the values at the two minima. This configuration lies on an energy barrier, i.e. is not favourable. The system can lower its free energy by separating into fractions of phase 1 and phase 2 such that constraint on λ is satisfied, again subject to the cost of creating an interface. For values of λ in the tail of the energy barrier, the cost of creating an interface is too great and the system remains in a single phase metastable state. Phase separation will occur only in situations were the mixed phase region is highly unfavourable. It is hence an indication of first order behaviour.

5.1.3 Critical Phenomena

It is logical to ask where a line of phase transitions (a phase boundary) comes to an end. In some cases two lines intersect at a triple point where three phases can coexist in stable equilibrium. Metastable transitions can end in a spinodal line, i.e. that which marks the boundary between metastable and mechanically unstable behaviour. A third possibility exists. The line of phase transitions can end in a critical point at which the distinction between the two phases disappears. The best known examples are the liquid-gas transition and the magnetisation transition in ferromagnets and spin lattices such as the Ising model. The former is of relevance here. Multiple critical points may exist for some systems. This is a point of much interest as will be seen in the next chapter.

In the region of a critical point the behaviour of a system is singular. The details of the

singularity are specific to a universality class rather than being related to the microscopic details of the system. The behaviour of the Lennard-Jones liquid-gas critical point is for example analogous to that of the Ising model. The application of scaling theory (which is not covered here - see Stanley (1971) for an introduction) leads to power law descriptions of critical behaviour. When applied to critical points in fluids the following results are obtained.

$$\Delta\rho \sim (-t)^{\beta} \tag{5.1a}$$

$$\kappa_T \sim |t|^{-\gamma} \tag{5.1b}$$

$$C_P \sim |t|^{-\alpha}, \tag{5.1c}$$

where the reduced temperature $t = (T - T_c)/T_c$ and T_c is the temperature at the critical point. κ_T is the isothermal compressibility, which is the inverse of the bulk modulus. Estimates of the critical temperature can be made by fitting measured data to these forms. The critical exponents α, β and γ are related by the Griffiths inequality

$$\alpha + \gamma + 2\beta = 2. \tag{5.2}$$

With the critical temperature known, the density ρ_c^* at the critical point can be obtained from the law of rectilinear diamters

$$\frac{\rho_{liq}^* + \rho_{gas}^*}{2} = \rho_c^* + A\left(T^* - T_c^*\right). \tag{5.3}$$

From equation 2.24 and 2.23, if C_P and κ_T diverge, then fluctuations in enthalpy and density become unbounded. The correlation length ξ measures the spatial range over which the system exists in a single phase. At criticality this behaves as

$$\xi \sim |t|^{-\nu}, \tag{5.4}$$

diverging to distances much larger than any simulation cell. This makes precise location of the critical point difficult by simulation.

5.1.4 Computer Simulation

In fact, phase transitions in general present a real challenge for computer simulation. For a given model Hamiltonian, can the preferred phase at a given temperature, pressure and density be identified? Can boundaries between phases on a pressure-temperature, temperature-density or density-pressure phase diagram be located? Fundamental differences exist between the behaviour of a model system with a small number or particles

($10^2 \rightarrow 10^4$), and the thermodynamic limit in which the number of particles in extremely large ($\sim 10^{23}$). The timescale accessible to simulation (~ 100 ps) is also very small on the thermodynamic timescale. Despite these issues, the location of phase transitions via computer simulation has become feasible for increasingly complex model systems.

Discussion of methods available to computer simulation for the location of phase transitions follows. Attention is concentrated on methods which have been implemented for the work in this thesis. For a wider discussion see the recent review by Bruce and Wilding (2003).

5.2 Single-Phase Methods

Naively, location of phase transitions in a computer simulated model system is a trivial matter. As an example, consider melting from a crystalline solid at a specific pressure. In three dimensions this is a 1st order phase transition. A simple procedure would seem to be:

1. Beginning from a perfect solid, conduct a series of NPT simulations at increasing temperature. Measure a crystal order parameter for each simulation and locate the first temperature at which this decays to zero. This will be accompanied by a discontinuous volume change.

2. Refine the result by sampling at smaller temperature intervals. Measure the average length scales over which the system exists in each phase. Locate the temperature where the length scales are equal, and hence the phase boundary.

This strategy is doomed to failure due to finite size effects in both the spatial and temporal limitations of a real simulation. Consider the situation at T_3 in figure 5.1. Consider the case where the solid is phase 1 and the liquid is phase 2. If the system is heated from the solid to temperature T_3, nucleation of the liquid phase would be expected. On the ergodic timescale, all areas of phase space are explored with the correct weight, the barrier crossing required for nucleation should therefore occur. However, due to the height of the barrier, such events are extremely rare on the picosecond timescales accessible to simulation. In addition, with a small system size, the cost of creating an interface between two phases is large on the energy scale of the simulation. Configurations from which nucleation can occur are therefore also rare. Nucleation of the liquid phase is suppressed until significantly higher temperatures, at which the barrier crossing probability is much higher and the energy cost of the interface is comparable to the free energy recovered in

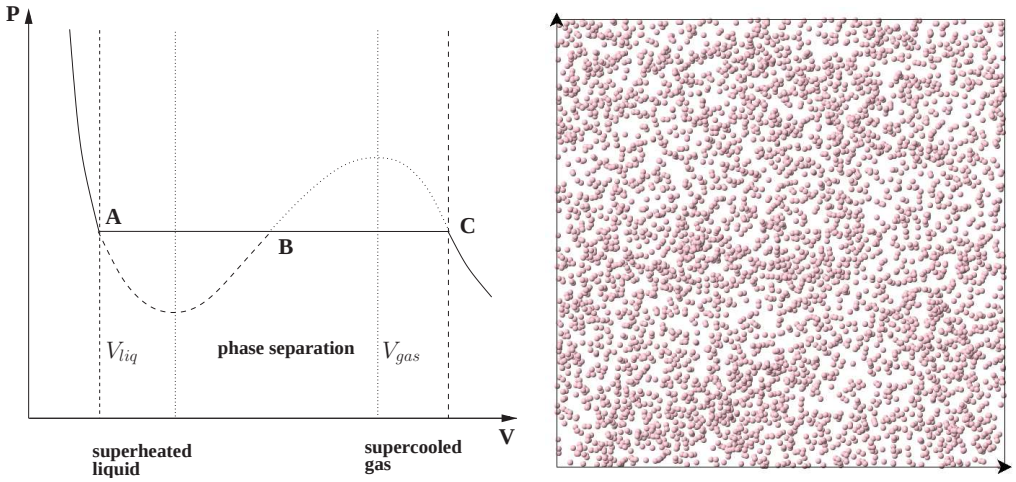

Figure 5.2: *Isotherm in the liquid-gas region (left). In true bulk the system will proceed directly along the line A-C on increasing volume. This line marks the coexistence pressure. In a finite size system, suppression of nucleation leads to the hysteresis shown. Liquid-vapour coexistence in a system of 5,000 Lennard-Jones particles created by simulating at constant density and temperature inside the co-existence region in shown on the right.*

the transition. In fact melting may not be observed until temperature T_5 when the solid phase has become mechanically unstable.

For these reasons, a single phase simulation will not give the correct transition temperatures with achievable system sizes. For example, McBride *et al.* (2005) have shown that a single phase simulation of ice will superheat to temperatures of 90^o C before melting is observed!

5.2.1 Hysteresis and the Maxwell Construction

It is however possible to locate a first-order phase transition to within useful accuracy with single phase simulations. Consider the liquid-gas transition. Beginning from a liquid state, an isotherm can be traced by sampling the pressure over a series of NVT simulations. As the volume is increased the sampled pressure decreases. This continues as the volume increases into the metastable region, and eventually reaches a minimum before the onset of phase separation. Decreasing the volume from a gas state will lead to a pressure maximum in the supercooled regime. An example of the resulting hysteresis is shown in figure 5.2. This is often referred to as a van der Waals loop as the effect can be reproduced from the well known van der Waals equation of state. Loops of this kind are often taken as a definitive indication of a first-order phase transition. The hysteresis is a manifestation of finite size effects and will not occur in the thermodynamic limit.

The transition pressure can be computed from an isotherm of this kind. At fixed volume,

the relevent free energy is the Helmholtz potential, the derivative of which with respect to volume is

$$\left.\frac{\partial F}{\partial V}\right|_T = -\left\langle P\right\rangle_{NVT}. \tag{5.5}$$

At the coexistence pressure P_{coex} the difference in free energy between the two phases is zero. This must be equal to the integral of the above equation between the two equilibrium volumes at the coexistence pressure.

$$F_{liq} - F_{gas} = \int_{V_{gas}}^{V_{liq}} PdV \tag{5.6}$$

P_{coex} is therefore the pressure at which the van der Waals loop is divided into two segments of equal area. This is the Maxwell construction illustrated in 5.2. At the critical temperature the volume difference vanishes and there is no metastable region. The critical isotherm exhibits an inflection at the critical volume. Isotherms above the critical temperature exhibit positive gradient only.

Single phase methods are employed in chapter 7 to locate an approximate liquid-gas critical temperature as a starting point for more accurate methods. The liquid portion of the van Der Waals loop is plotted for a range of temperatures. The critical temperature is estimated as the lowest temperature for which the isotherm has no region of positive gradient.

Other Transitions

The Maxwell construction is only useful for transitions in which phase separation can occur within a simulation. The cost of forming a solid-liquid or solid-solid interface is prohibitive. In these cases a simulation constrained at a forbidden density will prefer to cavitate, forming regions of a single phase and of vacuum.

5.3 Two-Phase Methods

While nucleation of a second phase is unlikely to occur spontaneously in a simulation of tractable size, the problem can be bypassed by specifying initial conditions in which two phases are already present. Such simulations can yield information about the thermodynamics of a phase transition. This approach is most useful for studies of melting where a realistic interface between solid and liquid is easily constructed.

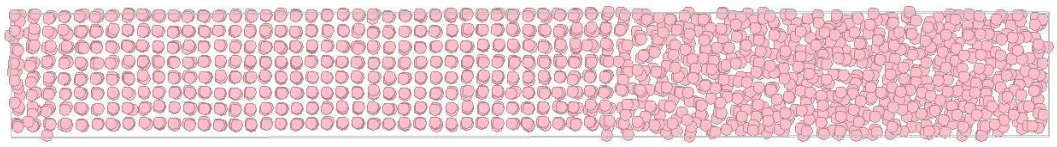

Figure 5.3: *Snapshot of equilibrium in a two-phase melting simulation of 2048 Lennard-Jones particles. The interface was initially constructed along the (100) direction in the centre of the cell.*

5.3.1 Melting transition

To construct such an interface, a supercell of the solid structure is first created. The atoms which are to remain in the solid phase are constrained at their initial positions by either excluding them from Monte-Carlo moves, or employing Lagrange multipliers in the molecular dynamics case. The remaining atoms are simulated at a temperature beyond the point of mechanical instability. This creates a solid-liquid interface along any crystal plane of interest. The direction along which the lowest free energy interface can be formed is typically the (100) for cubic crystals and the $(10\bar{1}0)$ in hexagonal systems.

If this construction is performed in a fixed cell, both phases will have the same density. As the melting transition is generally first order such a constraint is unphysical. Resulting simulations will exhibit anisotropic pressure as the liquid attempts to expand at the expense of the solid, perpendicular to the interface. Alternatively, the construction can be performed in a variable cell (NPT) simulation with the solid atoms held constrained with respect to the cell vectors. However this leads to to anisotropic expansion of the solid portion, again leading to non hydrostatic internal pressure. Morris and Song (2002) have attempted to overcome this problem by adjusting the dimensions of the cell on one side of the interface cell until the pressure is hydrostatic.

Two phase solid-liquid simulations with initial conditions such as these have been employed in two ways.

NVE Method

Simulations are conducted in the NVE ensemble. If the conserved energy results in a temperature above melting, part of the solid will melt. This process absorbs latent heat, and hence the temperature will lower. Similarly if the temperature is too low part of the system will solidify, releasing latent heat and causing the temperature to rise. Provided that the system does not entirely melt or entirely solidify, an equilibrium will be reached at which the average temperature is exactly the melting temperature. Combined with the average pressure at equilibrium, this gives a single point on the melting curve. Further points can be obtained by repeating at different densities. This method has been employed

to study the high pressure melting of Aluminium by Morris and Song (2002) using an embedded atom potential, and by Alfè (2003) using *ab-initio* methods.

The range of initial temperatures which will result in location of the melting temperature is clearly dependent on the size of the simulated system. As the interface will prefer to remain along the same crystal direction, the system should have larger extent in the direction normal to it. An snaphot of a simulation using this methodology is shown in figure 5.3.

NPT Method

The cell is simulated in the NPT ensemble. The particle Hamiltonian $\mathcal{H}$ is not conserved. If the specified temperature is above the melting temperature at this pressure then the entire system will melt. Similarly if the temperature is too low the entire system will freeze. A series of such simulations will bracket the actual melting temperature. The ultimate accuracy of this method is limited by the slow timescale of melting/freezing at temperatures very close to the phase boundary, these being beyond that accessible to simulation. This method has the advantage of locating the melting temperature at a specific pressure. Although requiring multiple simulations, the system size can be somewhat smaller. Simulations employing Langevin dynamics in the Parrinello-Rahman style system are ideally suited to this purpose. Specification of a hydrostatic pressure will lead to the correct solid and liquid densities without needed to manually adjust the cells to correct anisotropy.

NPH Method

A third possibility will be investigated in this work. Hypothetically, if a system could be simulated in the constant enthalpy NPH ensemble, the benefits of methods 1 and 2 would both be present. Provided the initial enthalpy resulted in a temperature close to the melting line, the system would locate the transition accurately as in method 1. The NPH ensemble in a fully flexible cell would also have the benefits of method 2, operating as a specified pressure, and eliminating concerns regarding non-hydrostatic pressure.

Currently no simulation scheme is available which correctly samples the NPH ensemble. The closest available method being equations 3.18a to 3.18d which reproduce the NPH ensemble to within fluctuations in the barostat momentum. If these fluctuations can be made sufficiently small, i.e. smaller than the specific latent heat of the melting transition, then a pseudo-NPH ensemble which seeks the melting transition in a coexisting simulation is feasible. This possibility will be investigated in chapter 7.

For solid-solid transitions the interfacial region may possess complex structure which cannot be reproduced *á-priori*, and may be substantial in spatial extent. The two phase approach is therefore not useful in these cases.

5.4 Free Energy Calculations

A phase coexistence curve is simply the locus of state points for which the chemical potentials of two phases are equal. For a pure system boundaries can be located by sampling the Gibbs free energy surface for both phases, and interpolating to locate the line of intersection.

Unfortunately, free energy is not a quantity which can be sampled directly in a computer simulation. Derivatives of free energy *can* be sampled, allowing the free energy difference between state points to be computed as an integral over a reversible path which connects them. Hence if the free energy is known at a given state point it can be calculated at all others for which such a path exists. Hysteresis effects ensure that paths which cross first-order phase transitions are irreversible and cannot be employed for these purposes.

5.4.1 Fluids

The relevant free energy derivatives are those with respect to volume

$$\left.\frac{\partial F}{\partial V}\right|_T = -\left\langle P\right\rangle_{NVT} \tag{5.7}$$

and inverse temperature

$$\left.\frac{\partial F}{\partial \beta}\right|_\rho = \left\langle E\right\rangle_{NVT}. \tag{5.8}$$

The integration is a two stage process. Beginning from a temperature and density at which the free energy is known, the density is varied along an isotherm to that at which the free energy is required. The temperature of the system is then varied along an isochore to give the final free energy. The two stages are independent and can be computed in parallel. In practice the integrals are evaluated by sampling the free energy derivative at a discrete number of points along each path. The simulations at each point are independent and can again be performed in parallel. The GOLDILOCS implementation of these free energy calculations is a simple shell-script running on an parallel computer. An initial NPT ensemble simulation is launched to determine the density at the required temperature and pressure. When this is complete, two further calculations are launched to sample the above integrals. Parallelism over sample points is handled within the GOLDILOCS

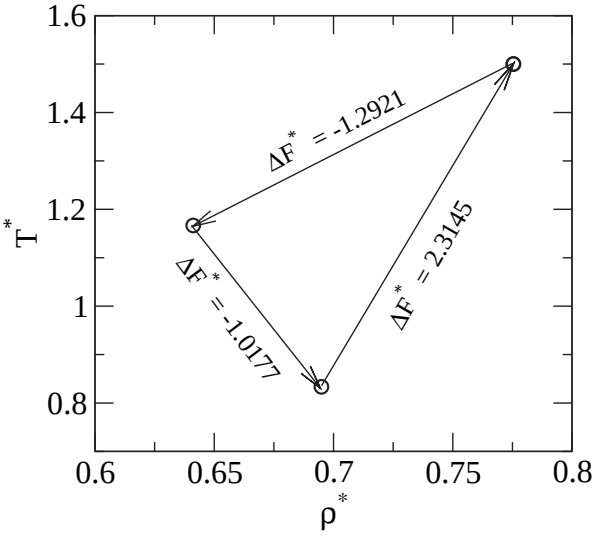

Figure 5.4: *Thermodynamic integration around a closed loop in the temperature-density plane. The change in free energy along each line is computed from separate integrations along one isotherm and one isochore. The change in free energy for each two stage process is shown.*

code using MPI message passing. Integration over sampled points is performed using the trapezoidal rule. To estimate the integration error in this process, a closed loop in the $T-\rho$ plane can be constructed. Integration around this loop should give zero total change in the Helmholtz potential. A three-step example using the Lennard-Jones potential is shown in figure 5.4. Each integration over density or temperature employed 10 sample points. The free energy derivative at each point was computed as an ensemble average over $50,000$ MD steps after equilibrating for $10,000$. A time-step of $\Delta t^* = 0.0015$ was used. The quantity

$$\frac{\sum |\Delta F_i^*|}{\sum \Delta F_i^*} \tag{5.9}$$

is less than 0.1%, indicating a suitably small integration error.

Any sufficiently dilute fluid will behave as an ideal gas. As the Helmholtz free energy of a (classical) ideal gas is known to be

$$F_{id} = -\frac{3}{2\beta}\frac{V^N}{N!}\ln\left(\frac{2\pi m}{\beta}\right), \tag{5.10}$$

this provides a point of known free energy if no other is available. In order for this path to be reversible, it must avoid the first order liquid-gas transition, requiring that liquid state points are reached by integration around the liquid-gas critical point. Obtaining liquid free energies therefore requires a prior estimate of this critical point. It is numerically convenient to integrate with respect to density rather than volume in this case, as the variation of pressure with volume is extremely slow close to the ideal gas limit. The free

energy F_1 after integrating along an isotherm can then be written

$$F_1(\rho) = F^{id}(\rho) + \int_0^\rho \frac{\langle P \rangle_{NVT} - k_B T \rho'}{\rho'^2} d\rho'. \tag{5.11}$$

5.4.2 The Einstein Crystal Method for Solids

A method for calculating the free energy of crystalline solids has been proposed by Frenkel and Ladd (1984). Rather than employing a thermodynamic path, a fictitious path is used which connects the solid of interest to an Einstein crystal at the same temperature and density. The Helmholtz free energy of an Einstein crystal is easily shown to be

$$F^{Ein} = U(\mathbf{r}^0) - \frac{d}{2\beta} \ln\left(\frac{2\pi}{\alpha\beta}\right) - \frac{d}{2\beta} \ln\left(\frac{2\pi m}{\beta}\right) \tag{5.12}$$

Here $\mathbf{r}^0$ represents the configuration at which all particles occupy their equilibrium lattice sites with potential energy $U(\mathbf{r}^0)$. The spring constant α is the same for each lattice site. A path between this system and the model solid of interest is constructed by employing a mixed Hamiltonian

$$\mathcal{H}_\lambda = \lambda \mathcal{H}^{Ein} + (1-\lambda)\mathcal{H}^{model} \tag{5.13}$$

such that the potential energy

$$U(\lambda) = U(\mathbf{r}^0) + \lambda \sum_{i=1}^{N} \frac{1}{2}\alpha \left|\mathbf{r}_i - \mathbf{r}_i^0\right|^2 + (1-\lambda)\left[U(\mathbf{r}^N) - U(\mathbf{r}^0)\right]. \tag{5.14}$$

By constructing the partition function Q for the mixed system, and hence the Helmholtz free energy $F = -k_B T \ln Q$, it is easy to show that the required derivative takes the following convenient form,

$$\begin{aligned} \left.\frac{\partial F}{\partial \lambda}\right|_\lambda &= \left\langle \frac{\partial U(\lambda)}{\partial \lambda} \right\rangle_{\lambda,NVT} \\ &= \left\langle \sum_{i=1}^{N} \frac{1}{2}\alpha \left|\mathbf{r}_i - \mathbf{r}_i^0\right|^2 + \left[U(\mathbf{r}^N) - U(\mathbf{r}^0)\right] \right\rangle_{\lambda,NVT} \end{aligned} \tag{5.15}$$

which is easily computed from a simulation.

Implementation

For optimal accuracy, the free energy difference between the model solid and the reference Einstein crystal should be as small as possible. This can be achieved by choosing the

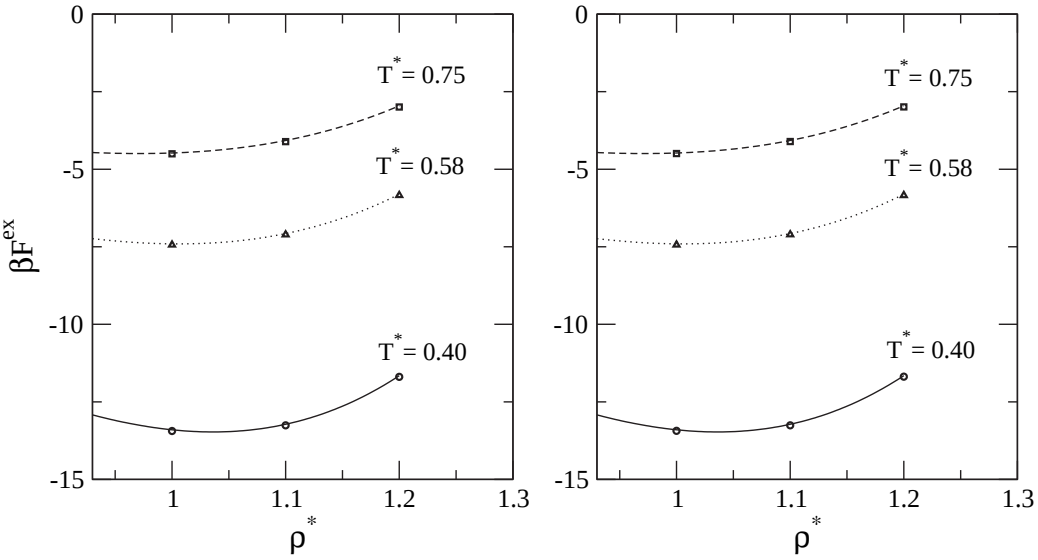

Figure 5.5: *Comparison of excess free energy calculated using the GOLDILOCS implementation of the Frenkel-Ladd Einstein crystal method (symbols) with the equation of state by van der Hoef (2000) (lines). In both figures the free energy derivative is sampled at 12 values of λ. The left hand figure employs NVT Langevin dynamics simulations of 3,000 sampled time-steps per λ-point, compared to 30,000 in the right hand figure. No useful increase in accuracy is obtained.*

spring constant α such that the mean squared displacement from lattice positions is similar for both systems. This quantity is known exactly as a function of α for the reference crystal, and can be obtained for the model solid using a brief simulation.

During a simulation at a given λ, the centre of mass of the simulated solid may drift. Atoms may therefore become separated from their original lattice site by a considerable distance, resulting in large values of the harmonic potential energy. This causes the integral of 5.15 to diverge, introducing numerical difficulties. For this reason it is preferable to implement a centre of mass constraint when computing solid free energies in this way. This is easily achievable in a Langevin dynamics simulation with the use of a Langrange multiplier. The free energy of a constrained crystal differs from that which the quantity of interest. This difference can be calculated, leading to the result (see e.g. Frenkel and Smit (1996)) that the free energy of the model solid is given by

$$F = -\frac{3N}{2\beta}\ln\left[\frac{4\pi^2 m}{\alpha\beta^2}\right] - \int_0^1 d\lambda \left\langle \frac{\partial U(\lambda)}{\partial\lambda}\right\rangle^{CM}_{\lambda,NVT} - \frac{3}{2\beta}\ln\left(\alpha\beta/2\pi\right) - \frac{3}{2\beta}\ln N + \frac{1}{\beta}\ln\rho \tag{5.16}$$

where the superscript CM denotes that the free energy derivative in equation 5.15 is evaluated with a fixed centre of mass. The Einstein crystal method in this form has been implemented in the GOLDILOCS code. A task parallel approach has been adopted. The optimal spring constant for a given calculation is automatically calculated as the average

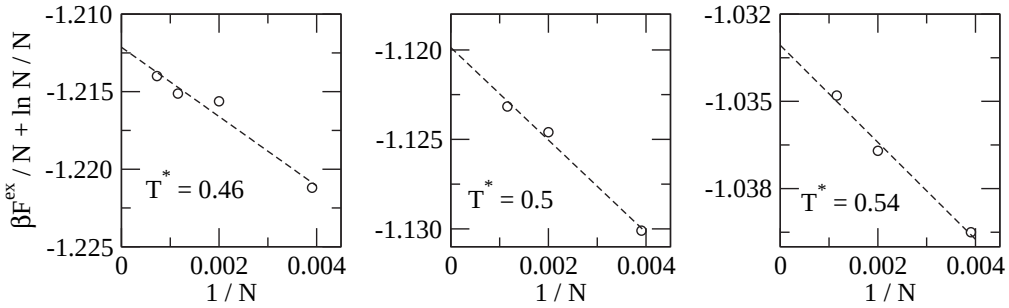

Figure 5.6: *Finite size corrections to the Frenkel-Ladd method. The quantity $\beta F^{ex}/N + \ln N/N$ is plotted vs $1/N$ for the fcc Lennard-Jones solid using a range of system sizes. Three temperatures are shown at $P^* = 0.047$. The potential is truncated at 2.5σ and force-shifted.*

of a number of short simulations in parallel with $\lambda = 0$. This is then used to launch a series of independent simulations for a range of λ values between 0 and 1. MPI message passing is employed in a similar fashion to the liquid case described above.

This implementation has been validated against the equation of state for the Lennard-Jones FCC solid given by van der Hoef (2000). This equation has been computed by thermodynamic integration from the Lennard-Jones triple point, at which the free energy is known from the Johnson *et al.* (1993) fluid equation of state. For consistency with this work, the GOLDILOCS tests have been computed using the full Lennard-Jones potential, truncated (but not shifted) at 6σ with long range corrections applied. This large cut-off requires a simulation cell of 2048 atoms to avoid self interactions at the densities studied. Nine free energies computed as above are shown in figure 5.5. In each case the optimal spring constant was identified over 12 parallel simulations of $5,000\,\Delta t$ duration before sampling the free energy derivative at 12 λ-points. The time-step used was $t^* = 0.0045$. Agreement with the equation of state is extremely good.

Finite Size Corrections

The effect of finite system size on the free energies computed by this method has been analysed by Polson *et al.* (2000). It is shown that the leading correction term to the excess free energy per atom is equal to $\ln N/N\beta$. A plot of $1/N$ against $F^{ex}/N + \ln N/\beta N$ for various system sizes N can be extrapolated to the $N = \infty$ limit to obtain an estimate of the corrected F^{ex}. An example is shown in figure 5.6.

These corrections have been computed from simulations of three system sizes for solid free energies reported in chapter 7. These have made little difference to phase behaviour, the correction being much less than 1% in all cases.

5.4.3 Chemical Potential Methods

For single component systems, the chemical potential is exactly the Gibbs free energy per particle. Here two methods are discussed for computing the chemical potential. These will be used in combination in the next chapter to compute a starting point for thermodynamic integration of liquids.

Grand Canonical Monte-Carlo

This method has been covered in section 3.4.3. Here the chemical potential is specified for a fixed volume. The average particle number and pressure are sampled, allowing the Helmholtz potential to be computed from

$$F = \mu \left\langle N \right\rangle_{\mu VT} - \left\langle P \right\rangle_{\mu VT} V. \tag{5.17}$$

Finite size errors in the density and pressure for a given chemical potential can be estimated by repeating the simulation with a range of system volumes. Free-energies calculated in this way are sufficiently accurate to use as starting points for thermodynamic integration. A starting point at a temperature and density close to the region of interest is preferable in order to minimise integration error. A method for obtaining an approximate chemical potential at a specified temperature and pressure/density is therefore required.

The Widom Method

A commonly used method is the test particle insertion method of Widom (1963). From equation 2.43 it is clear that

$$\mu = -k_B T \ln(Q_{N+1}/Q_N), \tag{5.18}$$

which reduces to

$$\mu = -k_B T \ln\left(\frac{V/\Lambda^3}{N+1}\right) - k_B T \ln\left\{\frac{\int d\mathbf{r}^{N+1} \exp\left[-\beta U(\mathbf{r}^{N+1})\right]}{\int d\mathbf{r}^{N} \exp\left[-\beta U(\mathbf{r}^{N})\right]}\right\}. \tag{5.19}$$

The first term is simply the chemical potential of the ideal gas. The second term must therefore be the excess chemical potential, and can be re-written as

$$\begin{aligned} \mu_{ex} &= -k_B T \ln \int d\mathbf{r}_{N+1} \left\langle \exp\left(-\beta \Delta U\right) \right\rangle_{NVT} / V \\ &= -k_B T \ln A \end{aligned} \tag{5.20}$$

The quantity A is the canonical ensemble average (over the N particle system) of the Boltzmann factor associated with the insertion of a particle, further averaged over all possible insertion positions. Computation of the chemical potential using this result is algorithmically trivial. In a NVT simulation (using any correct sampling method) the energy ΔU of a test particle inserted into a random position is computed at regular intervals. This 'ghost' particle is not included in the dynamics, but provides a mechanism for computing ΔU without actual increase of the particle number, which remains constant. The average of $\exp(-\beta\Delta U)$ over the ensemble and all possible insertion positions is hence obtained by combined ensemble averaging and stochastic sampling of the integral over insertion positions. A similar expression can be obtained for computing the excess chemical potential in the isothermal-isobaric ensemble, requiring averages over an NPT simulation.

In obtaining equation 5.20, 2.43 has been employed which assumes the limit of large N. Excess chemical potentials computed from the Widom method are therefore heavily influenced by finite-size effects. A procedure for applying corrections has been proposed by Siepmann *et al.* (1992).

Validation

Validation of the grand-canonical MC and Widom implementations in the GOLDILOCS code has been performed against the equation of state parameterised by Johnson *et al.* (1993). This requires implementation of the full Lennard-Jones potential truncated but not shifted at 4σ to make a valid comparison. Long range corrections to the energy and pressure are applied during the simulation. Both NVT and NPT particle insertion methods have been implemented. In each case simulations using 864 particles were conducted at a temperature of $T^* = 2.0$ over $60,000\,\Delta t$ after equilibrating over $10,000\,\Delta t$. A time-step of $\Delta t^* = 0.0045$ is employed with test particle insertions performed every $10\Delta t$. NVT simulations were performed initially at densities in the range $\rho^* = 0.2 - 0.8$. Pressures identified from these were used in a subsequent set of NPT simulations. Langevin dynamics sampling methods were used in both cases. A thermostat relaxation time suitable for the full range of densities was found to be 0.44 reduced time units. For the NPT simulations a barostat relaxation time of 2.76 was used.

Grand-canonical Monte-Carlo simulations were conducted using chemical potentials for each density identified from the equation of state. The size of the simulation cell was chosen such that expected average number of atoms was close to 864 in each case. $60,000$ Monte-Carlo cycles were averaged over, after equilibrating for $10,000$. The results for both the Grand-canonical Monte-Carlo and Widom tests are shown in figure 5.7.

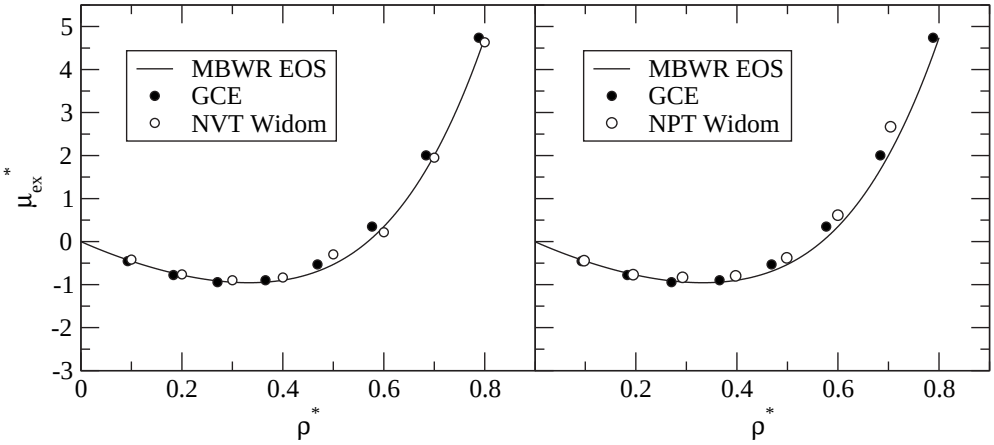

Figure 5.7: *Chemical potential as a function of density at $T^* = 2.0$ computed with the Widom method and using grand-canonical Monte-Carlo simulations, both within the GOLDILOCS code. The equation of state of Johnson et al. (1993) is shown for comparison.*

A procedure for obtaining a fluid state of known free energy energy is therefore as follows. At a pressure P_0 and temperature T_0 in the region of interest, conduct a NPT simulation (using the Langevin dynamics method or otherwise). Perform test particle insertions during this simulation and compute the resulting chemical potential μ. This will be approximate due to the large finite-size dependence of the Widom method. Using this approximate chemical potential, conduct a well-converged grand-canonical Monte-Carlo simulation at T_0, measuring the pressure P (similar but not equal to P_0) and density. The free energy is then computed from equation 5.17 providing a starting point T_0, P for thermodynamic integration.

Note that all grand-canonical Monte-Carlo simulations in figure 5.7 are of the same length. Hence a lower number of successful insertions are averaged over at higher density, leading to the visible decrease in accuracy above $\rho^* = 0.5$. Reference points for thermodynamic integration will be chosen at lower densities to ensure high accuracy with achievable simulation lengths.

5.4.4 Error Estimates

Using combinations of the methods presented in this section it is possible to compute as a function of either pressure or temperature the free energy of two phases. Solid-solid and solid-liquid phase boundaries can then be located as discussed. Some thought must be given to the accuracy of this approach. As has been noted by Bruce and Wilding (2003) there is no "reliable and comprehensive" method of computing an uncertainty on phase boundaries computed in this fashion. Each phase involved may have both finite-size and statistical errors in the reference free energy, as well as in each free energy derivative

sampled along a path. Errors in numerical integration may also be significant.

As will be described in chapter 7, attempts have been made to locate the dominant source of error for the work presented therein. Error bars on liquid free energies are in general dominated by statistical uncertainty in the reference free energy. This is a controllable and quantifiable source of error in the case where grand-canonical Monte-Carlo simulations are used to compute the reference point. Integration errors are estimated (using loops of the kind used in 5.4.1) to be an order of magnitude smaller than this. For solids, the error bar is dominated by finite-size effects. These are larger than in the liquid, and are largely corrected for by the methodology outlined in section 5.4.2. An error bar equal to the largest deviation from linear behaviour in $F^{ex}/N + \ln N/\beta N$ is taken as representative.

5.5 Gibbs-Duhem Integration

Performing extensive free energy calculations to locate a complete phase boundary is an extremely slow and laborious process, requiring a series of free energy calculations for each point on the coexistence curve. The Gibbs-Duhem integration method of Kofke (1993) provides an alternative. Provided with a single accurately located point on a phase boundary, this method will automatically trace the remaining points with little or no user input.

The Gibbs-Duhem equation relates a change in chemical potential to a step in the P-T plane.

$$nd\mu = SdT - VdP \tag{5.21}$$

Applying this equation to phases α and β separately and taking the difference of the resulting two equations,

$$\begin{aligned}(S_\alpha - S_\beta)dT - (V_\alpha - V_\beta)dP &= n_\alpha d\mu_\alpha - n_\beta d\mu_\beta \\ &= d\mathcal{G}_\alpha - d\mathcal{G}_\beta \end{aligned} \tag{5.22}$$

for a single component system. The condition that this step occurs along a phase boundary is now imposed. The LHS of equation 5.22 must vanish as $\mathcal{G}$ must be equal for both phases at every point along the coexistence curve. This leaves

$$\frac{dP}{dT} = \frac{S_\alpha - S_\beta}{V_\alpha - V_\beta} = \frac{\Delta S}{\Delta V}. \tag{5.23}$$

As $\Delta\mathcal{G} = 0$ the difference in enthalpy between the two phases ΔH (or the latent heat L)

must equal $T\Delta S$ giving

$$\frac{dP}{dT} = \frac{\Delta H}{T\Delta V} \tag{5.24}$$

or

$$\frac{dP}{d\beta} = -\frac{\Delta H}{\beta\Delta V} \tag{5.25}$$

This is the Clausius-Clapeyron equation. Tracing the coexistence curve $P = f(T)$ can be accomplished by numerically integrating the derivative $f'(\beta)$ given by equation 5.25, from an initial point identified by free energy calculations or otherwise. This is the Gibbs-Duhem method in its most basic form.

In addition to tracing a phase boundary in the $P - T$ plane, the method calculates the density of both phases and the latent heat of the transition at every point as a by-product. All latent heats referred to in subsequent chapters have been obtained in this fashion.

5.5.1 Calculation of f'

The derivative f' is evaluated by sampling both phases separately at the current temperature and pressure and computing their enthalpy and volume as an average over NPT ensemble trajectories (Vega, 2005) such as those produced by the constant pressure Langevin dynamics method developed in chapter 4.

Note that if the free energy barrier between the two phases is small, a simulation of phase α may spontaneously transform to phase β or vice-versa. Methods are available for preventing such transformations, however these have not been required in the current work. Other methods have been employed in situations where this could occur, i.e. close to the liquid-gas critical temperature.

5.5.2 Implementation and Validation

The Gibbs-Duhem methodology has been automated with the GOLDILOCS code by employing a simple wrapper script. This script employs the fourth order Runge-Kutta scheme (see e.g. Press *et al.* (1986)) to integrate the Clausius Clapeyron equation. The

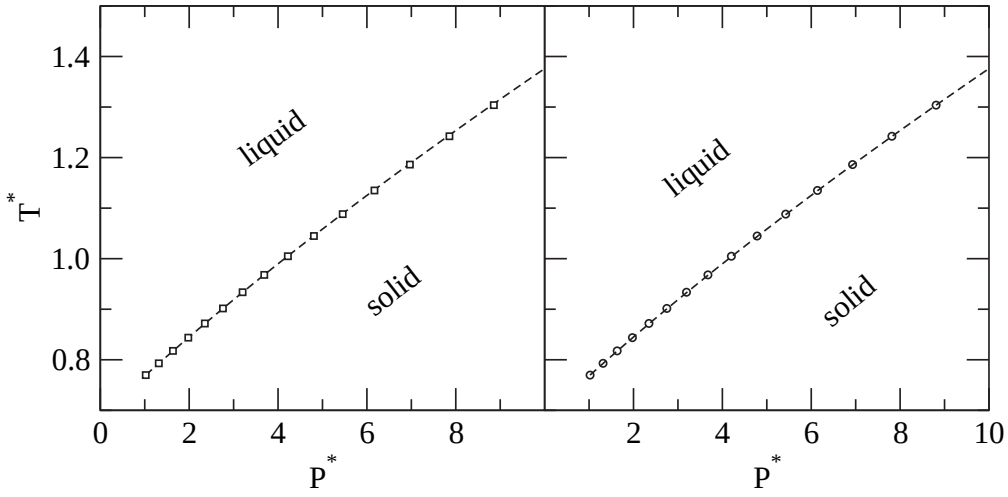

Figure 5.8: *The Lennard-Jones melting curve with $r_c = 3.5\sigma$ calculated using both constant pressure Langevin Dynamics (left) and NPT Monte-Carlo (right). Both calculations employed the Gibbs-Duhem integration script described in section 5.5.2 and the GOLDILOCS code. The dashed line is a plot of equation 5.27 as parameterised by Agrawal and Kofke.*

procedure takes the form

$$K_1 = f'(\beta_n, P_n) \tag{5.26a}$$
$$K_2 = f'(\beta_n + h/2, P_n + K_1/2) \tag{5.26b}$$
$$K_3 = f'(\beta_n + h/2, P_n + K_2/2) \tag{5.26c}$$
$$K_4 = f'(\beta_n + h, P_n + K_3) \tag{5.26d}$$
$$P_{n+1} = K_1/6 + K_2/3 + K_3/3 + K_4/6 \tag{5.26e}$$

requiring four pairs of simulations at each step in inverse temperature. For each pair, the script generates appropriate input files and launches two NPT calculations in parallel. The required averages are then extracted from the output and employed in the above equations.

This implementation has been validated against the Lennard-Jones melting curve data obtained by Agrawal and Kofke (1995). These authors used Gibbs-Duhem integration to parameterise the equation

$$P^* = \beta^{-5/4} \exp\left[-0.4759\sqrt{\beta}\right] \left(16.89 + A\beta + B\beta^2\right), \tag{5.27}$$

for the coexistence pressure, obtaining values of $A = -7.19$ and $B = -3.028$. As with this work, the GOLDILOCS tests employed a cut-off of $r_c = 3.5\sigma$ (with long-range corrections) and 500 atoms per simulation. Reproducing this curve constitutes a further test of the efficient ensemble sampling provided by the constant pressure Langevin Dynamics scheme. For each simulation, $10,000$ equilibration steps were employed with $50,000$ sampling steps. A time-step of $\Delta t^* = 0.0045$ was employed with conservative relaxation

times for the thermostatic and barostatic processes of 0.44 and 11.7 respectively.

For comparison, the same Gibbs-Duhem series was computed using NPT Monte-Carlo simulations. These employed maximum atomic and volume displacements of $\Delta r_{max} = 0.2\sigma$ and $\Delta V_{max} = 8.3\sigma^3$ for the liquid. For the fcc solid values of $\Delta r_{max} = 0.16\sigma$ and $\Delta V_{max} = 3.8\sigma^3$ were used. With equal equilibration and sampling lengths of 5000 cycles, this produces similar accuracy to the Langevin dynamics. Total execution time for both sampling methods was comparable. For both series a step in inverse temperature of -0.038 was employed.

Both simulations agree extremely well with the data of Agrawal and Kofke. This validates both the Gibbs-Duhem implementation and the NPT ensemble sampling of the constant pressure Langevin dynamics scheme.

5.5.3 Error Estimates

Errors in Gibbs-Duhem integration arise from statistical and finite-size errors in the sampled enthalpy and volume of both phases at each point. These can be reduced to an acceptable level by using large system sizes and long simulation times at each point. The acceptable level is taken to be that arising in the free energy calculations used to locate the starting point for the series. Integration error must also be accounted for. A simple error estimate of this is obtained by explicit free energy calculations of both phases at the last point in the series. An alternative method is to re-run the integration in reverse. An error estimate is obtained from the difference between the starting point of the forward series and the end point of the reverse series. These methods will be employed as appropriate in chapter 7.

5.6 Monte-Carlo Methods

Each of the methods discussed so far requires sampling from standard ensembles using a model Hamiltonian. The method used to perform the sampling can be Molecular/Langevin dynamics or Monte-Carlo. A second set of methods exist which require sampling of other ensembles which are not accessible to dynamical methods. Although it may be possible in principle to generate equations of motion which sample any ensemble of interest, their construction is non-trivial. Within the Monte-Carlo methodology it is simple to calculate Metropolis acceptance criteria for an arbitrary ensemble. This leads to the possibility of methods which sample from a specially modified distribution with properties beneficial to the study of phase transitions.

5.6.1 Histogram Reweighting/Multi-canonical Sampling

One such method is based on the reweighting of histograms combined with multi-canonical sampling. The latter has been introduced by Berg and Neuhaus (1991), owing its origins to the umbrella sampling method of Torrie and Valleau (1974). The combined scheme will be employed in chapter 7 to locate liquid-vapour coexistence curves. The implementation used with the GOLDILOCS code follows a tutorial by Wilding (2001). The methodology is described below.

A Starting Point

The particle number histogram $P(N)$ is easily constructed from a grand canonical Monte-Carlo simulation at a given temperature and chemical potential. This is simply the distribution function for samples of the particle number N, computed from the equilibrated portion of the simulation. To begin tracing the phase transition line, a particle number histogram at an initial point at or near the liquid-vapour coexistence line is required. For temperatures close to the critical temperature T_c, the energy barrier between the two phases is small. This allows a single unmodified GCE simulation to visit both phases, crossing the small barrier many times during a simulation.

Given an initial estimate at temperature T_0 slightly lower than T_c, the chemical potential μ can be fine tuned until the number density histogram is bimodal with approximately equal area under each peak. This provides an estimate of a point T_0, μ_0 near the coexistence curve.

Histogram Reweighting

Histogram reweighting (Ferrenberg and Swendsen, 1988) can be employed to improve this estimate without the need for further simulation. At the simulated inverse temperature $\beta_0 = 1/k_B T_0$, and chemical potential μ_0, the probability associated with the j^{th} sampled configuration of N_j particles with potential energy U_j is

$$P\left(N_j, \Phi_j | \beta_0, \mu_0\right) \propto \exp\left[-\beta_0 \left(U_j - \mu_0 N_j\right)\right], \tag{5.28}$$

Each sample has a weight of unity. At some other temperature β_1 and chemical potential μ_1, the probability of the same sample is now

$$P\left(N_j, \Phi_j | \beta_1, \mu_1\right) \propto \exp\left[-\beta_1 \left(U_j - \mu_1 N_j\right)\right], \tag{5.29}$$

The ratio of these two probabilities is

$$\frac{P\left(N_j, U_j|\beta_1, \mu_1\right)}{P\left(N_j, \Phi_j|\beta_0, \mu_0\right)} = e^{-(\beta_1-\beta_0)E_j+(\beta_1\mu_1-\beta_0\mu_0)N_j} \tag{5.30}$$

which gives us a statistical weight which can be assigned to each sample at β_0,μ_0 to obtain the particle number histogram at β_1,μ_1. This is exact in principle. However regions which are poorly sampled at β_0,μ_0 may become important at β_1,μ_1 limiting the range of the method to small changes in T and μ. As β_0,μ_0 represents a point near a coexistence curve, μ_1 can be fine tuned until the re-weighted bimodal histogram has exactly equal areas under each peak. This gives an improved estimate of an initial point on the coexistence curve.

Multi-canonical sampling

At some lower temperature on the phase boundary, the energy barrier is not sufficiently low that it will be traversed in a normal GCE simulation. Consider sampling of a modified probability distribution

$$\tilde{\rho} \propto \exp\left[-\beta\left(U - \mu N + \eta\left(N\right)\right)\right], \tag{5.31}$$

In which the preweighting function

$$\eta(N_j) = \mu N_j - U_j. \tag{5.32}$$

This corresponds to an extended sampling distribution which will give $\tilde{\rho}$ uniform[2] over the entire range of N, including the energy barrier. This is simply the logarithm of the unmodified particle number distribution (equation 5.29),

$$\ln\left[P\left(N\right)\right] = \beta\left(\mu N_j - \Phi_j\right). \tag{5.33}$$

Hence if the particle number histogram $P(N)$ at the current T and μ is known, or can be approximated, a preweighting function can be constructed which will flatten the probability distribution over the entire range of N. The modified acceptance criteria for insertion and removal moves within this modified ensemble are

$$P_{acc}\left(N \rightarrow N+1\right) = \min\left[1, \frac{V}{(N+1)}\frac{P(N)}{P(N+1)}\exp\left\{-\beta\left(\Delta U - \mu\right)\right\}\right] \tag{5.34}$$

[2]Note that a flat distribution is not necessarily the most efficient choice of histogram to sample. A procedure for multi-canonical simulations using an iteratively tuned optimal ensemble has recently been presented by Trebst *et al.* (2004).

and

$$P_{acc}\left(N \rightarrow N-1\right) = \min\left[1, \frac{P(N)}{P(N-1)}\frac{N}{V}\exp\left\{-\beta\left(\Delta U + \mu\right)\right\}\right], \tag{5.35}$$

which are used in place of equations 3.47 and 3.48. The effect of this flattening on the resulting samples of any thermodynamic observable, including the number density itself, can be removed by assigning each sample a weight given by $P(N)$. This recovers the original grand-canonical distribution, but with information on *both sides* of the energy barrier.

In practice, the required form of $\eta(N_j)$ is not known exactly, as this would require *á-priori* knowledge of $P(N)$, which is precisely that which simulation is attempting to measure. However, an estimate of $P(N)$ can be obtained using histogram reweighting from another temperature, which is then improved in the multi-canonical simulation.

Tracing phase boundaries

The combination of histogram reweighting and multi-canonical sampling provides a powerful tool for tracing the liquid-vapour coexistence curve. The method proceeds as follows:

1. Perform an unbiased GCE simulation at some temperature close to (but below) the critical temperature and at a chemical potential near the transition line.
2. Use histogram reweighting to improve this estimate of μ and perform a second GCE simulation.
3. Re-weight the resulting $P(N)$ to a lower temperature, and tune μ until this is bimodal with two peaks of equal area.
4. Using this tuned μ, and the re-weighted $P(N)$ as the preweighting function, perform a multi-canonical GCE simulation at this temperature.
5. Unfold from this biased simulation the actual statistics. Correct the estimate of μ by reweighting the new histogram.
6. Repeat steps 3 to 6.

The scheme steps along the phase boundary, self correcting any deviations. All but step 1 can be completely automated. This has been accomplished using GOLDILOCS and a series of auxiliary codes to perform the integration under $P(N)$ and the reweighting procedure. These are invoked by a Unix shell script which performs the steps in temperature.

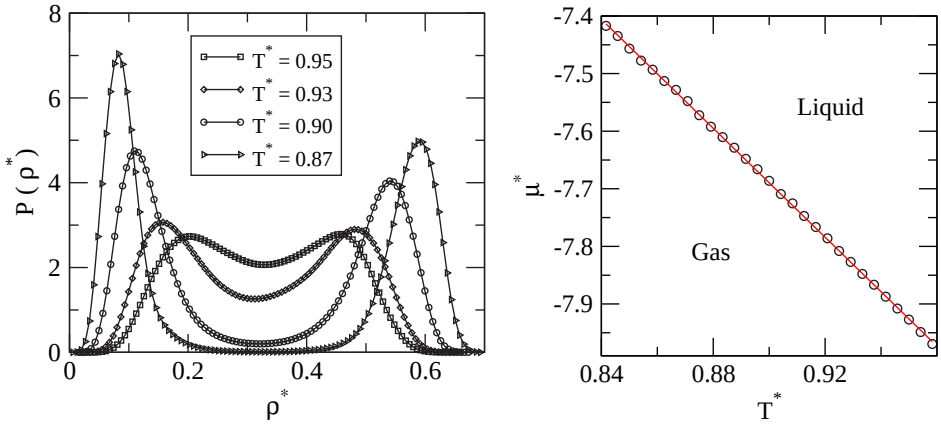

Figure 5.9: *Particle number histograms at decreasing temperatures produced using multi-canonical sampling with histogram reweighting applied to the Lennard-Jones liquid-vapour transition (left). The resulting chemical potential as a function of temperature along the phase boundary is shown on the right.*

The implementation has been tested by studying the Lennard-Jones liquid-vapour transition. The potential is truncated and force-shifted for comparison with results for core-softened potentials in chapter 7. With the cut-off at $R_c = 2.5\sigma$, the critical temperature is substantially reduced from that obtained with the full Lennard-Jones potential. The procedure was begun from an initial temperature of $T^* = 0.96$, at which $P(N)$ possesed equal area under two peaks at $\mu^* = 7.9671$.

In this and the subsequent multi-canonical simulations, a cubic simulation cell of side 7.13σ was employed. Each simulation consisted of $10,000$ equilibration cycles followed by a further $250,000$ from which samples were taken. A step of $\Delta T^* = 0.004$ was used in descending along the coexistence curve. Sample particle number histograms from the procedure are shown in figure 5.9 along with the resulting phase boundary in the $\mu - T$ plane. The phase boundary in the P-T plane can be obtained by unfolding the sampled pressure data from the GCE simulations.

The critical phenomena associated with the liquid-vapour transition have not been studied in detail in this thesis. An *estimate* of critical temperatures has been made by fitting the density data obtained from the above procedure to equation 5.1a, and extrapolating to zero density difference. This provides a suitably accurate value for observing trends in the critical temperature. Methods are however available for obtaining detailed information on critical properties. See e.g. Bruce and Wilding (1992); Wilding (1995) for studies of the Lennard-Jones fluid.

5.6.2 Other Methods

Other Monte-Carlo methods which have not been employed in this thesis are briefly described below.

Gibbs Ensemble

A popular method for studying liquid-vapour equilibria is the Gibbs-ensemble approach of Panagiotopoulos (1987). Problems associated with sampling of the interface are avoided by simulating in two coupled single phase cells of fixed total volume and particle number. The probability distribution for the combined system is

$$\rho_G \propto \frac{N!}{N_I N_{II}} \exp\left[N_I \ln V_I + N_{II} \ln V_{II} - \beta U_I(N_I) - \beta U_{II}(N_{II})\right] \tag{5.36}$$

where the subscripts I and II refer to the two coupled cells. Acceptance criteria for three kinds of trial move can be obtained.

1. Particle displacements within a cell.
2. Moves of particles between cells.
3. Exchange of volume between cells.

It can be shown that simulations in this scheme will come to equilibrium with equal chemical potential associated with each cell. At a specified temperature the method will therefore locate two phases of different densities. The coexistence pressure may be sampled during simulations at this equilibrium.

This approach has not been adopted in this work. As will become clear in chapter 6 this work is concerned with systems which may posses two fluid phase transitions. At a given temperature the Gibbs-Ensemble technique is capable of finding only two of these phases per simulation. In contrast the histogram reweighting/multi-canonical sampling scheme will exhibit a third peak if an extra fluid phase is present. In addition the multi-canonical scheme requires a single simulation cell, making it simples to accommodate within the GOLDILOCS code.

Phase Switching Monte-Carlo

Also worthy of note are the recently developed phase-switching Monte-Carlo methods. These operate in the spirit of multi-canonical sampling, sampling two phases within a

single simulation. In the context of solid-solid transitions the method is termed lattice-switch Monte-Carlo (Bruce *et al.*, 1997, 2000). Rather than traversing the complex interfacial region, the method snaps from one phase to another in a single MC move of the cell vectors. Fractional co-ordinates are held fixed during this move. Sampling takes place in a modified ensemble in which 'gateway' configurations from which the lattice switch can occur are preferentially biased. The method was introduced in the context of hard-sphere systems.

Generalisation to soft potentials is a very recent development and hence phase switching methods have not been employed in this thesis. A phase-switching method for the freezing transition has also been presented (Wilding and Bruce, 2000) and tested for the hard-sphere system. Recent application to the Lennard-Jones system has been reported by Errington (2003).

It is hoped that the results in chapter 7 may be refined in further work employing the phase-switching methodology.

5.7 Augmented Meta-dynamics

For each of the above methods, some prior information regarding the phases involved is required. For example, to study the melting transition the structure of the solid must be known. For simulations of real systems this is often known from experiment. In the case of model systems, the mechanically stable crystal structures are not known *á-priori*. A simple atomistic simulation is likely to explore only local minima in phase-space close to its initial conditions. Minima corresponding to other crystal structures will not be explored. The simulation may be initialised with a variety of crystal structures, but cannot guarantee that others exist which have not been considered.

5.7.1 Methodology

A method is therefore needed for accelerating the sampling of rare events, such as traversing an energy barrier between two crystal structures. Several such methods are available. This work concentrates on the meta-dynamics method of Laio and Parrinello (2002). This is briefly described below.

In an atomic simulation, N collective coordinates are identified encapsulating motions of interest. With these coordinates constrained, a traditional ensemble molecular dynamics or Monte-Carlo simulation is conducted, during which the generalised forces on the collective coordinates are averaged. These are used to evolve the collective coordinates

through a meta-step in the direction of steepest descent. The process repeats, allowing the collective coordinates to explore the energy landscape generated by the wider system. The scheme's utility lies in artificial augmentations to this landscape, preventing return to previously visited states. The basin in which the simulation begins becomes flattened by these augmentations, forcing the simulation to locate other, previously unknown, stable states. While other schemes for escaping minima explore only the zero temperature energy landscape, meta-dynamics simulations operate at finite temperature and pressure, exploring a free energy landscape.

By keeping track of the number and height of augmentations required to escape a minimum, the depth of the basin can be estimated directly from the simulations, providing information on relative stabilities of atomic configurations. The meta-dynamics methodology has been mainly applied to studies of chemical reactions, in which the collective degrees of freedom are chosen as a suitable reaction coordinate. See e.g. Iannuzzi *et al.* (2003); Gervasio *et al.* (2004); Ensing *et al.* (2004) for examples using Car-Parrinello molecular dynamics.

5.7.2 Application to Crystal Structures

The application of meta-dynamics for the location of crystal structures has been introduced by Martonak *et al.* (2003). Here the collective coordinates are the components of the cell vectors in a MD simulation. These constitute a six dimensional free energy landscape in the case where symmetry of the matrix $\mathbf{h}$ (3.23) is enforced. The derivative of the Gibbs free energy with respect to $\mathbf{h}$ leads to a force of

$$\begin{aligned} - \quad & \frac{\partial \mathcal{G}}{\partial h_{ij}} = -\frac{\partial}{\partial h_{ij}} \left(\mathcal{H} - TS + P\det(\mathbf{h}) \right) \\ = \quad & V \left\{ \left[(\mathcal{P} - P)\, \mathbf{h}^{-1} \right]_{ij} + \left[(\mathcal{P} - P)\, \mathbf{h}^{-1} \right]_{ji} \right\} \left(1 - \frac{1}{2}\delta_{ij} \right). \end{aligned} \tag{5.37}$$

where P is the external pressure and $V = \det(\mathbf{h})$. The pressure tensor $\mathcal{P}$ is computed as a canonical ensemble average over a run in which the cell vectors are constrained. As the above force is symmetric, the six independent components can be organised into a vector $\mathbf{F}_{therm}$. Similarly the independents components of $\mathbf{h}$ can be arranged into the vector $\mathbf{h}_v$.

A steepest descent step of length δh can now be performed along the Gibbs free energy surface in $\mathbf{h}_v$.

$$\mathbf{h}_v^{(t+1)} = \mathbf{h}_v^{(t)} + \delta h \frac{\mathbf{F}_{therm}}{|\mathbf{F}_{therm}|} \tag{5.38}$$

The fractional co-ordinates of the ions are kept constant during this step. This constitutes one meta-step. The process is repeated, equilibrating an MD run in the new cell, averaging

the new pressure tensor, taking a new step and repeating. The system will explore the minimum of the Gibbs free energy surface in which the system was initialised.

The meta-dynamics can be driven out of the initial minimum, into another, corresponding to a second crystal structure which is stable/metastable at the same temperature and pressure. This is accomplished by augmenting the free energy surface with the goal of 'filling-in' the minimum in which the system began, forcing the system into a new configuration..

At each step, a Gaussian of height W is constructed at every point on the six-dimensional surface which the meta-dynamics has already visited.

$$\mathcal{G}_{aug} = \sum_{t'<t} W exp\left(-\frac{|\mathbf{h}_v^{(t)} - \mathbf{h}_v^{(t')}|^2}{2\delta h^2}\right) \tag{5.39}$$

The 'force' on the cell vectors now becomes

$$\mathbf{F} = \mathbf{F}_{therm} + \mathbf{F}_{aug} = -\nabla_h \mathcal{G} - \nabla_h \mathcal{G}_{aug} \tag{5.40}$$

As long as the system remains inside the initial basin of attraction, the force $\mathbf{F}_{therm}$ will point roughly toward the minimum, whereas the augmentation force $\mathbf{F}_{aug}$ will tend to point away from it. Hence

$$I = \mathbf{F}_{therm} \cdot \mathbf{F}_{aug} / |\mathbf{F}_{therm}||\mathbf{F}_{aug}| \approx -1. \tag{5.41}$$

At the cusp between two minima, the two contributions to the force will become parallel and their dot product will sharply change from -1 to +1. If a transition is detected in this way, the augmentation force can be switched off allowing the system to fall into the second mimima. Evolution can then switch to ordinary MD to sample the second phase, or the system can be quenched to obtain the perfect crystal.

As with the original Parrinello-Rahman method, meta-dynamics in this form suffers from a lack of modular invariance. False transitions between different unit cells of the same structure can therefore occur. As the cell has no explicit momentum conjugate in this scheme, the method of Wentzcovitch (1991) cannot be used to correct this problem. Each transition detected must be carefully checked for a change in structure.

5.7.3 Implementation and Validation

Given a code which can simulate a cell of arbitrary shape in the canonical ensemble, implementation of the Martonak *et al.* method is trivial. The implementation in the

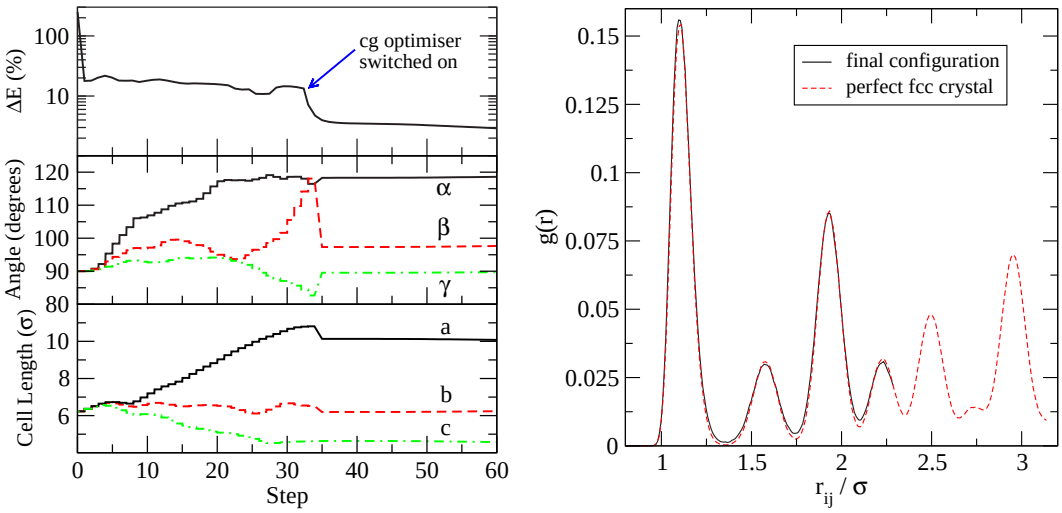

Figure 5.10: *Evolution of the potential energy difference (from a perfect fcc crystal) and cell vectors during a meta-dynamics + conjugate gradient optimisation 256 Lennard-Jones atoms at* $T^* = 0.17$ *and zero pressure (left). Initial positions were generated randomly in a cubic cell. The right hand plot shows the distribution of neighbour distances* $g(r)$ *for the final configuration and for a perfect fcc crystal at* $T^* = 0.375$ *and* $P^* = 1.18$.

GOLDILOCS code has been tested with a simple problem. An initial configuration of Lennard-Jones atoms in random positions will behave as a glass at a temperature of $T^* = 0.17$. This is easily confirmed by simulation. At temperatures below the glass temperature the system is easily trapped in a local minimum. The meta-dynamics method should be able to escape this initial free energy basin and locate a close-packed (lower energy) crystal structure.

Results shown in figure 5.10 are for a system of 256 atoms randomly placed (subject to an forbidden overlap distance of 0.87σ) in cube of side 6.23σ. This corresponds to the density at $T^* = 0$, $P^* = 0$. The meta-dynamics simulation employed a time-step of $t^* = 0.004$, for 100 equilibration and 500 sampled steps per meta-step. A temperature of $T^* = 0.17$ and zero pressure were imposed. A step size of $\delta h = 0.25\sigma$ was used, with augmentations to the energy landscape of height $W = 50\epsilon$.

As the dynamics are not initialised in a well defined based of attraction, the value of equation 5.41 is not a useful indicator. However after 34 meta-steps, the system had become visibly ordered. At this point the evolution of the system was passed to a conjugate gradient (CG) enthalpy minimisation algorithm. The GOLDILOCS CG minimiser is of the Polak-Ribiere type, using code adapted from Press *et al.* (1986). Enthalpy is minimised with respect to both the atomic coordinates and the cell vectors. The final configuration was then used in a constant pressure Langevin dynamics simulation of $35,000\,\Delta t$ at $T^* = 0.375$ and $P^* = 1.18$. A time-step of $\Delta t^* = 0.0028$ was used. The distribution of pair distances $g(r)$ averaged over the equilibrated portion is also shown in figure 5.10

along with the equivilent results for a perfect fcc crystal. This indicates that the dynamics have located the fcc minimum. The energy is within 2.4% of that obtained for a perfect fcc crystal. Total excecution time was less than 5 minutes on a single workstation.

Repeat simulations with 288, 384 and 500 atoms each located the fcc structure in less than 50 meta-dynamics steps. No simulation located the hcp-structure. The small energy difference between the fcc and hcp structures will likely require increased care in the choice of δh and W if the hcp minimum is to be identified.

The meta-dynamics method will be used in chapter 7 to locate crystal structures for core-softened pair potentials.

Chapter 6

Liquid-Liquid Phase Transitions

The occurrence of two or more liquid phases in a system is often observed when dealing with mixtures and other systems which are made up of multiple components. These phases are important in industrial chemistry contexts and are in many ways well understood.

The presence of two thermodynamically distinct liquid states in *single* component systems is somewhat more unusual. Experimental and theoretical evidence of liquid-liquid phase transitions (LLPT) in elemental melts has been accumulated only during the last decade. This will be reviewed in section 6.1. Note that this applies only to classical phase transitions in which both phases obey Boltzmann statistics. Intrinsically quantum low temperature transitions (e.g. in helium) are not of interest here.

The presence of thermodynamic anomalies in liquid metals and in water can possibly be explained by the LLPT phenomenon. This has lead to the study of simple core-softened model systems (which may manifest two liquid phases) as a mechanism for understanding these anomalies. These studies will be reviewed in section 6.2, motivating the study of three-dimensional core-softened potentials presented in chapter 7.

6.1 Elemental Systems

6.1.1 Phosphorus

Much of the recent interest in liquid-liquid phase transitions can be attributed to the experimental observations of liquid phosphorus by Katayama *et al.* (2000). This study located a maximum in the melting curve at high pressure as shown in figure 6.1. The negative slope of the melting curve can only be reconciled with the Clausius Clapeyron equation

if the liquid in this region is of higher density than the solid, which seems unlikely to be true if the liquid can only exist in the expected tetrahedral molecular form.

X-ray diffraction studies of the liquid structure either side of the melting curve maximum produced rapidly changing radial distribution functions over only a 0.1 GPa range. The two forms agree extremely well with data from an earlier *ab-initio* study of liquid phosphorus by Hohl and Jones (1994). In this study the low pressure tetrahedral liquid was observed to polymerise under pressure to a higher density form. Further experimental work supports this polymeric structure by analogy with the structure factors of polymeric solid phosphorus and arsenic (Katayama, 2002). Recently Katayama *et al.* (2004) have demonstated macroscopic phase separation of the molecular and polymeric liquid, confirming that the abrupt change in structure is the consequence of a first order liquid-liquid phase transformation.

More recent *ab-initio* studies have provided further information on the structure of liquid phosphorus. It has been shown that the phase transition can be temperature induced as well as pressure induced, with a cut-off temperature of 2000K above which the tetrahedral low density liquid cannot be formed (Morishita, 2001a). These studies have also produced detailed information on bond angle distributions in the polymeric liquid, and band structure calculations showing that the band gap present in the low density liquid vanishes in the polymeric form leading to metallic character (Morishita, 2001b, 2002). Sufficiently small systems sizes are employed that the resulting phase boundaries can be expected to require substantial finite-size corrections.

The work of Morishita has been confirmed by Senda *et al.* (2002a,b), and more recently by Ghiringhelli and Meijer (2005). The experimental work of Katayama has recently been reproduced by Monaco *et al.* (2003) who have accurately located the phase boundary in the P-T plane, also shown in figure 6.1. Ballone and Jones (2004) have constructed a reactive force field model for phosphorus fitted to *ab-initio* data. The two liquid phases have been reproduced via Monte-Carlo simulations of this model. The exact location of the phase boundary within this model has not yet been mapped.

6.1.2 Hydrogen

The phase diagram of hydrogen under extreme conditions is of clear importance for studies of stellar interiors. As the most simple elemental substance, it has attracted much attention from first-principles studies. These are complicated by the light mass of the hydrogram atom, often requiring that nuclear quantum effects are included to reproduce experimental data.

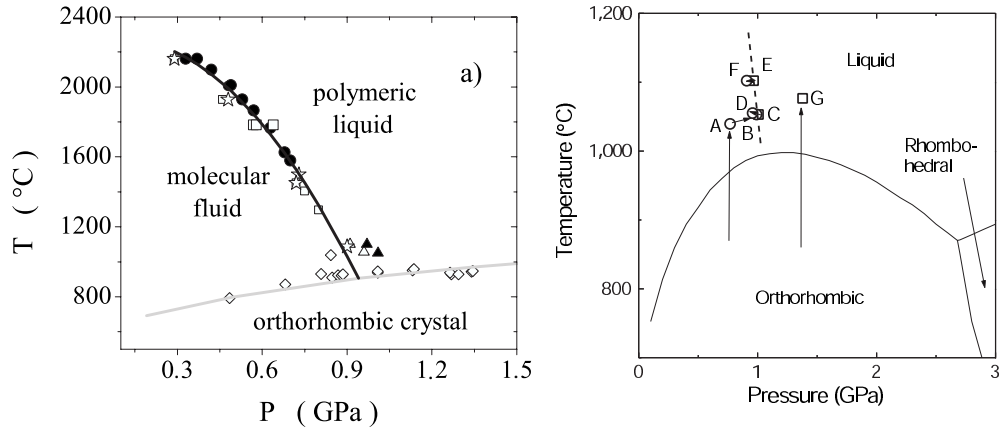

Figure 6.1: *The high pressure phase diagram of liquid phosphorus as mapped by Monaco et al. (left) and by Katayama et al. (right) in which the melting curve maximum can be seen.*

Under high pressure, hydrogen gas can be compressed to a liquid consisting of H_2 molecules. Upon further compression/cooling this freezes to a hexagonal close packed (hcp) solid structure with a freely rotating H_2 molecule at each lattice site. It has long been considered that at extreme pressures, this molecular hcp solid will compress to an atomic crystal with metallic character.

Recent experimental measurements of the hcp solid melting temperature have been conducted by Datchi *et al.* (2000). Two semi-empirical equations for melting curves are used to extrapolate the results to higher pressure. In one case, this predicts a maximum in the melting temperature with respect to pressure. Beyond this, the liquid state persists at lower temperatures. The predicted maximum coincides with the point at which H_2 molecules dissociate into a metallic liquid as simulated by Pfaffenzeller and Hohl (1997) using *ab-initio* molecular dynamics. Suggestions that the metallic state of hydrogen is in fact a low temperature atomic liquid have followed. Scandolo (2002) has also studied the dissociation/metallisation in the liquid using *ab-initio* molecular dynamics. In this case the change is accompanied by a small but rapid change in volume, suggesting a first-order phase transition. This must cause a discontinuity in slope where it intersects the melting curve. It is suggested that the direction of the melting curve changes during this discontinuity, and hence the LLPT is the mechanism responsible for the maximum. Experiments at higher temperatures (2200 to 4400 K) by Weir and Mitchell (1995) indicate a continuous change. Scandolo suggests that these studies can be reconciled if the line of first-order liquid-liquid transitions ends in a critical point at approximately $2,000$ K as shown in figure 6.2. However, quantum Monte-Carlo (QMC) calculations conducted by Militzer *et al.* (1999) indicate the first-order nature persists to temperatures of $10,000$ K. These may be heavily dominated by finite-size effects (system sizes accessible to QMC are extremely small). Improved QMC calculations near the proposed critical point are underway (De-

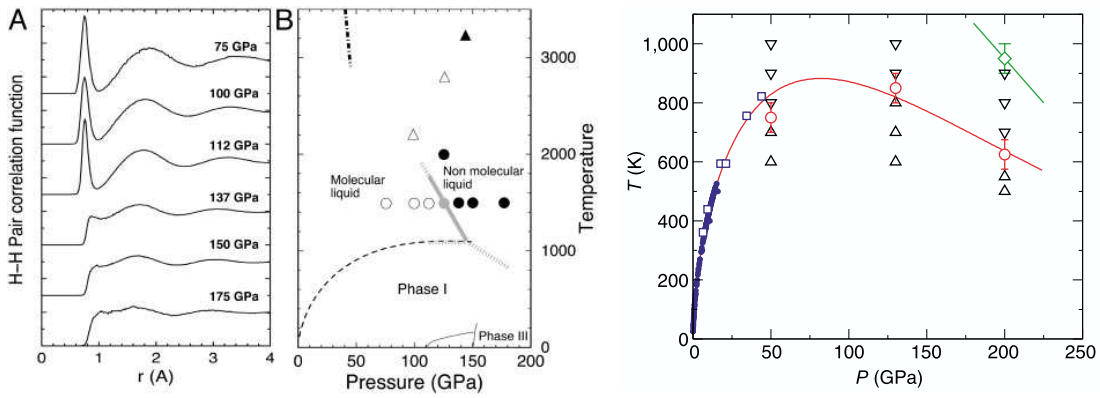

Figure 6.2: *Phase diagrams of hydrogen from two* ab-initio *molecular dynamics studies. On the left is the diagram proposed by Scandolo (2002). Radial distribution functions are shown for each of the circular points. These form a path which crosses the LLPT. The phase diagram of Bonev* et al. *(2004) is shown on the right. Dots and squares indicate previous experimental data of the melting curve. Triangles indicate two-phase simulations used to bracket the melting curve. The first-order LLPT is detected at the diamond symbol.*

laney, 2005).

In recent work, Bonev *et al.* (2004) have employed two-phase NPT simulations to confirm that the melting curve exhibits a maximum. These were conducted with first-principles Car-Parrinello molecular dynamics. In common with the above *ab-initio* studies, the nuclei are treated as classical particles. This approximation is justified by showing that the first order free energy correction due to nuclear quantum effects is nearly identical for both phases. Transitions between the molecular fluid and a metallic liquid are observed at pressures *higher* than the melting curve maximum. In this region a volume discontinuity is observed along with the hysteresis indicative of a first-order transition. These results suggest the melting curve maximum is not a direct consequence of a liquid-liquid phase transition. The phase diagram as studied by Bonev *et al.* is shown in figure 6.2.

6.1.3 Carbon

There is some indirect experimental evidence suggesting a LLPT in carbon. This comes from an investigation into the melting curve of graphite (Togaya, 1997). Very few state points were measured as shown in figure 6.3. These indicate a similar change in direction of the melting curve slope to that seen in phosphorus at the LLPT. This assumption is based on only two data points, and there are doubts about some of the measurement methods used. In particular temperature was not measured directly but was inferred from the melting enthalpy which was assumed to be pressure independent.

Despite these doubts, the results are in broad agreement with earlier experimental works

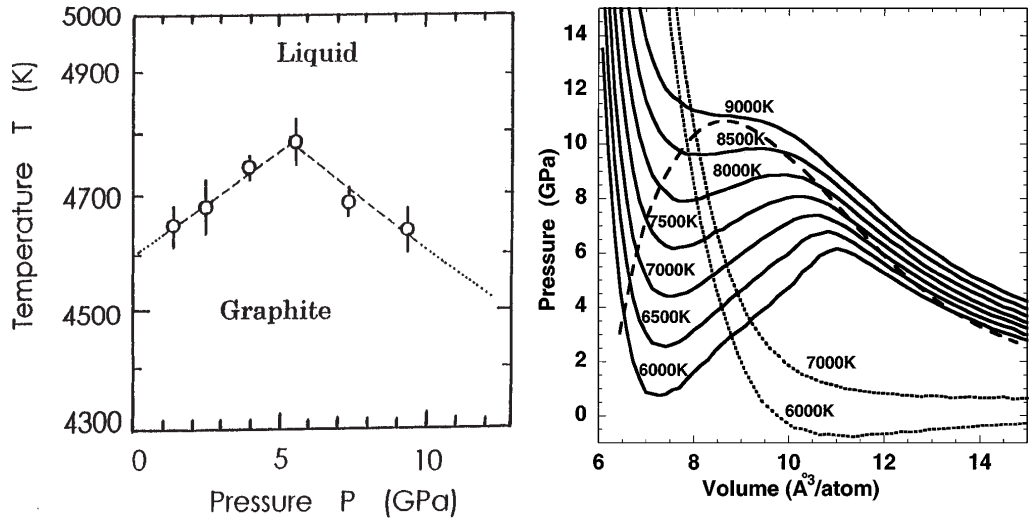

Figure 6.3: *Melting curve of graphite as measured by Togaya (left). A similar maximum to that observed in phosphorus and hydrogen is seen. The right hand figure shows Van der Waals loops liquid carbon isotherms as simulated by Glosli and Ree.*

on the phase diagram of carbon (Bundy, 1989; Bundy *et al.*, 1996), which have led to speculation of a LLPT based on theoretical models of graphitic and diamond-like liquids (Vanthiel and Ree, 1989).

The method of tight-binding molecular dynamics (TBMD) has historically led to good results in studying solid phases of carbon. Studies of the liquid using this method were conducted by Sugino (1999) and Morris *et al.* (1995). In both cases, an increase in co-ordination number with increasing pressure was observed *without* a phase transition.

A liquid-liquid transition was however predicted by Glosli and Ree (1999). Their NVT simulations used a well established bond order model for atomic interactions in carbon (Brenner, 1990; Brenner *et al.*, 1991). The transition manifested itself as a rapid decrease in volume for a small increase in pressure, accompanied by a change in the co-ordination number from 2 (sp bonding) to 4 (sp^3 bonding.) No sp^2 bonded liquid was observed. Plots of isotherms (figure 6.3) obtained from several simulation points showed classic signs of a first order phase transition which seemed to correspond with Togaya's melting curve maximum. Glosli and Ree also showed that removing the torsional energy term (introduced by Brenner to include effects of rotation about a carbon-carbon double bond) left a model which produced no liquid-liquid transition.

Recent simulations using density functional theory (DFT) do not agree with this result (Wu *et al.*, 2002). They show no volume discontinuity, merely an increase in co-ordination with increasing pressure, and no exclusion of the sp^2 bonded liquid. Other DFT calculation of high pressure carbon show the same trend (Grumbach and Martin, 1996; Galli *et al.*, 1989). Wu *et al.* have shown that the disagreement is due to the

torsional energy term in the Brenner potential causing an energy barrier to sp^2 bonding which is inappropriate for the modelling of bulk carbon. This barrier should in fact be much lower.

Interestingly, simulations using a second generation of the Brenner Potential (Brenner *et al.*, 2002) agree with the *ab-initio* results (Kum *et al.*, 2003). This newer model for carbon therefore does not contain the inappropriate energy barrier to sp^2 bonding and may be useful for the study of other phenomena in bulk carbon.

It would seem that the evidence points toward there being no liquid-liquid transition in carbon.

6.1.4 Others

The above materials have formed the focus of much discussion on elemental liquid-liquid phase transitions. Hydrogen is a material of fundamental physical importance, whereas high pressure studies of carbon have obvious implications for studies of planetary interiors. The interest in phosphorus is largely due to it being the first elemental melt for which definitive evidence of a first order transition exists. It should be stressed however that the phenomenon is by no means unique to these systems. Many elemental melts are known to undergo structural changes which may or may not be associated with a phase transition. In many cases these changes coincide with the metallisation of the liquid.

For example, Brazhkin *et al.* (1999) have conducted studies of three elemental melts under extreme pressure. For sulphur [1] evidence for two additional lines of phase transitions are located in the liquid between 1000 and 1500 K at pressure of 4 GPa upward. These may correspond to structural changes simulated by Tse and Klug (1999) using *ab-initio* molecular dynamics. Selenium is found to posses a transition at temperatures between 1000 and 1200 K from 2 GPa upwards. This has also been studied in the experiments of Katayama (2001); Katayama *et al.* (2001).

Liquid iodine is also shown to posses two structural changes between 2 and 4 GPa at temperature of 800 K upwards. Brazhkin *et al.* discuss discuss general theoretical models for first order phase transitions in elemental melts. A treatment specific to iodine has been presented by Likalter (2002). A tight-binding potential which reproduces two phases liquid has been developed by Koslowski and Stepanov (2003).

Umnov *et al.* (1992) have also presented experimental evidence for a transition in Bismuth, and in Tellurium (Brazhkin *et al.*, 1992). Funamori and Tsuji (2002) have measured

[1] Liquid sulphur also undergoes a well known λ transition at $159\,^{\circ}C$ between S_8 rings and polymeric chains.

an anomalous expansion under increasing pressure for liquid Tellurium which may be related to this transition. In many of these cases a melting curve maximum is also observed and the structural change is accompanied by a rapid decrease in volume.

A liquid-liquid transition has been reported by Sastry and Angell (2003) in a rather different regime. Using two-phase simulations of the Stillinger-Weber potential (Stillinger and Weber, 1985), a metastable first order transition is located in the supercooled region. There is no conclusive experimental evidence for such a transition. Simulations using more accurate or *ab-initio* models have not been reported. This transition may therefore be a peculiarity of the Stillinger-Weber model, as in the Brenner potential for carbon.

This is by no means a comprehensive survey, (see Angilella *et al.* (2003) for a recent review article) but serves to illustrate the extent of the phenomenon..

6.2 Core-Softened Model Systems

While many of the above systems have been modelled using *ab-initio* and complex semi-empirical potentials, these representations remain too complex for detailed thermodynamic calculations to be performed. There is much interest in the study of simpler models that attempt to approximate complex anisotropic interactions with a simple isotropic pair potential. One such class of models are core-softened pair potentials. In addition to the hard repulsive core of e.g. the Lennard-Jones fluid or the hard-sphere system, these models posses a second, softer repulsive region at larger radius. In some cases attractive regions are also included. In this fashion, these models attempt in some sense to encapsulate the energetics of complex systems in which bonding can occur at two characteristic distances.

Inversion of approximate structure factors obtained from scattering experiments leads to core-softened effective pair potentials for a variety of liquid metals (Yokoyama and Ono, 1985; Hoshine *et al.*, 1987) including some of those discussed in the previous section. Some of these resemble specific core softened models that will be discussed below. In addition, models which posses a soft outer repulsive region surrounding an inner hard core have obvious application in studies of colloidal systems.

6.2.1 Relevance to Water

Substantial new interest in core-softened models has been generated over the last decade due to their possible relevance to liquid water. Water exhibits a variety of liquid state anomalies. Examples include a compressibility maximum at $46\,^{o}$C, and the well known

density maximum at $4\,^{o}$C, associated with the anomalous contraction upon heating of water.

Poole *et al.* (1992) conducted molecular dynamics simulations of metastable supercooled water using the ST2 (Stillinger and Rahman, 1974) model. These contradicted the thermodynamics of the popular "stability-conjecture" in which the density maximum is explained in terms of a re-entrant liquid spinodal line. Isobars in the supercooled liquid exhibited points of inflexion that would be expected when approaching a critical point from above in temperature. The suggestion followed that this second critical point may mark the termination of a line of metastable liquid-liquid phase transitions. At lower temperatures, either side of the supposed liquid-liquid transition, structure similar to the high and low density amorphous phases of ice was observed. These results were later refined by Harrington *et al.* (1997b). In addition, simulations by Brovchenko *et al.* (2003) suggest the presence of *two* liquid-liquid transitions in supercooled water, one being at negative pressure.

Subsequent experiments reported by Mishima and Stanley (1998a) studied the melting line of ice IV. This is metastable with respect to the familiar ice Ih melting curve, and crosses the suggested line of metastable liquid-liquid transitions. A discontinuity in the slope of the ice IV melting curve was observed at the intersection. Clearly, one possible mechanism for this discontinuity could be an abrupt change in the liquid density due to a first-order phase transition. The suggested phase diagram is indicated in figure 6.4. The LLPT line is argued to be an extension of the experimentally verified transition between the low and high density forms of amorphous ice, into the metastable liquid region. Further simulations using the SPC/E (Berendsen *et al.*, 1987) model for water, also by Harrington *et al.* (1997a) exhibit less compelling evidence of the transition. However, the metastable liquid-liquid transition is indirectly supported by the TIP4P (Jorgensen, 1981) model simulations of Poole *et al.* (1993). This model has been shown to reproduce the experimental phase diagram with superior accuracy to SPC/E and other models (Sanz *et al.*, 2004a,b). The liquid-liquid transition is also supported in simulations of the TIP5P (Mahoney and Jorgensen, 2000) model by Yamada *et al.* (2002). Further support for the second critical point hypothesis has been presented by Tanaka (1998).

In further work, Mishima and Stanley (1998b) argued that the new critical point may arise due to a second minimum in the effective pair-potential between water molecules. The two minima represent different preferred orientations of two molecules as shown in figure 6.4. The possibility of modelling the general LLPT phenomenon using cheap, simple pair-potentials arises. This would allow extensive thermodynamic calculations to be performed. This conjecture has spawned several studies of core-softened pair potentials which will be reviewed below.

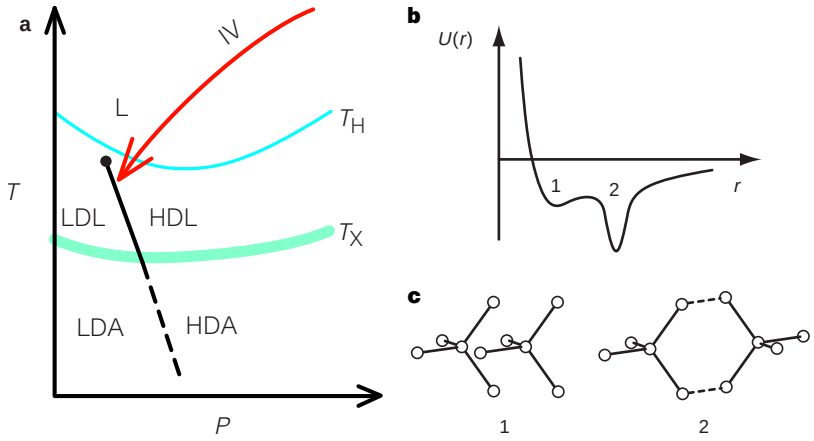

Figure 6.4: *2nd critical point hypothesis of Mishima and Stanley. The speculated phase diagram is shown in (a). T_H marks the thermodynamic melting temperature, and T_X the glass transition. The metastable ice IV transition crosses the proposed LLPT line. The proposed effective pair potential is shown in (b), the two minima corresponding to arrangements of water molecules shown in (c).*

With regards to water itself, the evidence for the metastable second critical point is far from conclusive. Alternative explanations of the anomalies in water do not require a liquid-liquid phase transition. This work leaves this controversy for other studies[2]. It should also be noted that water is not unique in possesing these anomalies.

6.2.2 Aims for Studies of Model Systems

In addition to any possible relevance to liquid metals, colloids or water, the study of core-softened pair potentials has become a problem of intrinsic interest. The properties of a model which result in the appearance of phase transitions has long been a fundamental issue. Core-softened potentials introduce the means to study the possible appearance of additional phase transitions and liquid state anomalies.

Long before the recent interest in liquid-liquid phase transitions, Hemmer and Stell (1970) proposed the interaction potential shown in figure 6.5. A simple expression for the Helmholtz free energy of this model in one dimension was calculated. This led to a set of parameters $V_0 d/a$ for each λ for which two phase transitions occur. A triple point at which all three fluid phases coexist was located for a subset of these parameters. These authors speculate that a smoothly varying form of the potential could be constructed that would have the same properties, and that the phenomenon may also occur in two and three dimensional systems. This is clearly relevent to the suggested pair-potential of Mishima and Stanley.

Detailed simulations of such models were not tractable at this time. With the recent revival

[2]See Glover (2004) for a review of work in this field

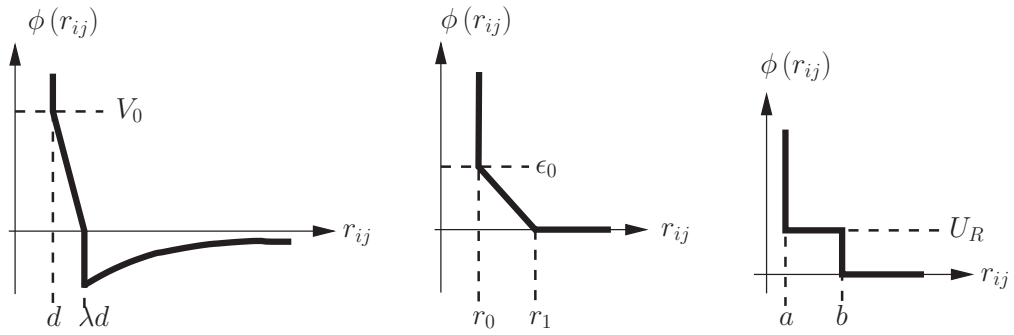

Figure 6.5: *Piecewise core-softened pair potentials. The Stell-Hemmer Pair potential is shown on the right. The tail is of the form $-a\gamma e^{-\gamma r_{ij}}$. The Jagla ramp potential is shown in the centre, with the collapsing hard spheres model of Stishov shown on the right.*

of interest in these models, the application of computer simulation has allowed studies to be conducted in more detail. It is useful to state the questions which recent studies of core-softened pair potentials aim to answer.

- Can these potentials generate a second liquid phase with an associated critical point?
- What are the characteristics of the two liquid phases and the critical point?
- Does the line of liquid-liquid phase transitions lie in the thermodynamically stable regime?
- What is the solid phase behaviour of these systems? How is it related to that of the liquid?
- How does the shape of the potential change the answers to these questions?
- What is the simplest model that will lead to a liquid-liquid transition?
- How does the behaviour change if the model is varied?

These are by no means easy questions to answer. Here work on several recent studies which attempt to provide some answers is reviewed. Due to the range of models adopted, several questions remain.

6.2.3 The Lennard-Jones Plus Spin Model

This model was presented by Lee and Swendsen (2001) as a possible means of mimicking short range order effects in real systems. A system of Lennard-Jones particles is modified

by giving each particle an extra spin-one-half degree of freedom. Pair interactions between particles with like spins take the usual Lennard-Jones form with length parameter σ_p. For opposite spins the repulsive part of the pair-potential only is used with different length parameter σ_{ap}.

The orientation of each spin is allowed to flip during the simulation with a probability determined by the change in total energy this would produce, according to the usual Monte-Carlo methodology. The authors conducted Monte-Carlo simulations with this potential in various ensembles, apparently tracing coexistence curves with a combination of Gibbs-Ensemble and multi-canonical methods. All simulations were conducted in two dimensions.

This model reproduces a stable liquid-liquid phase transition for the case where σ_{ap} is less than σ_p. The liquid-liquid coexistence line ends in a critical point which lies in the stable liquid region. As might be expected, the liquid-liquid transition lies along the transition from ferromagnetic to antiferromagetic ordering of this spins in the liquid. Similarly, a second line of phase transitions exist along this line within the solid.

6.2.4 The Collapsing Hard Spheres Model

The 'collapsing hard spheres model' has been studied by Stishov (2002). A sketch is shown in figure 6.5. The outer 'soft' core can be treated as a perturbation on a hard sphere system. Application of second order thermodynamic perturbation theory produces isotherms which exhibit the classic Van-der-Waals loop associated with a first order phase transition for $a = 1.5b$ (Ryzhov and Stishov, 2002, 2003). This model had previously been studied by Bolhuis and Frenkel (1997) and others in the context of isotructural solid-solid phase transitions (and a possible solid-solid critical point) for smaller values of a.

This indicates that systems with two characteristic repulsive distances are capable of exhibiting a liquid-liquid transition, and that the attractive part of the potential is not important. The second critical point is metastable for the range of parameters investigated by the author. No simulation studies of this potential have been reported. Note that it is generally accepted that the liquid-gas transition cannot be modelled without an attractive region in the pair-potential. This implies that the LLPT in the collapsing hard-spheres model is the only fluid-fluid transition present.

6.2.5 The Ramp Potential

Jagla (1998) has proposed a 'bare-bones' version of the original Stell-Hemmer piecewise ramp potential containing the repulsive components only as shown in figure 6.5. Monte-

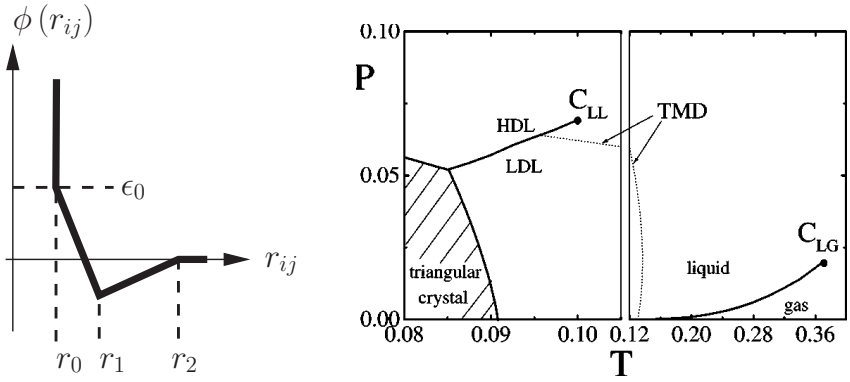

Figure 6.6: *Modified form of the Jagla ramp potential which includes an attractive component. The resulting phase diagram is shown on the right with a split temperature scale.*

Carlo studies of this potential in two dimensions were conducted, locating several solid structures and a maximum in the solid-fluid coexistence curve. The model shows no liquid-liquid transition (and in fact no liquid state), however the fluid phase does exhibit a temperature of maximum density (TMD).

A modification of this basic form which includes an attractive component was later presented (Jagla, 2001). This is shown in figure 6.6 and closely resembles the original Stell-Hemmer form. Using this potential, Monte-Carlo simulations were conducted in a variety of ensembles in two and three dimensions. Van der Waals loops were produced in both the two and three dimensional cases. These transitions occur in the stable liquid regime with a liquid-liquid critical point at lower temperature and higher pressure than the liquid-gas critical point. Wilding and Magee (2002) have accurately traced the three-dimensional liquid-liquid transition using the histogram reweighting and multi-canonical sampling technique described in section 5.6.1, and confirmed the presence of the density maximum. This places the presence of a liquid-liquid transition in this system beyond reasonable doubt.

6.2.6 The Shoulder Potential

The 'shoulder' potential has been studied in two forms. The first is discrete, and resembles the collapsing hard-sphere model above, with the addition of an attractive square well. The second is smooth and is generally constructed as a superposition of an outer Gaussian minimum onto the Lennard-Jones potential.

$$U\left(\mathbf{r}^N\right) = \sum_{j>i}^{N} 4\epsilon \left[\left(\frac{\sigma}{r_{ij}}\right)^{12} - \left(\frac{\sigma}{r_{ij}}\right)^{6} \right] - A \exp\left[-w\left(r_{ij} - r_0\right)^2\right] \tag{6.1}$$

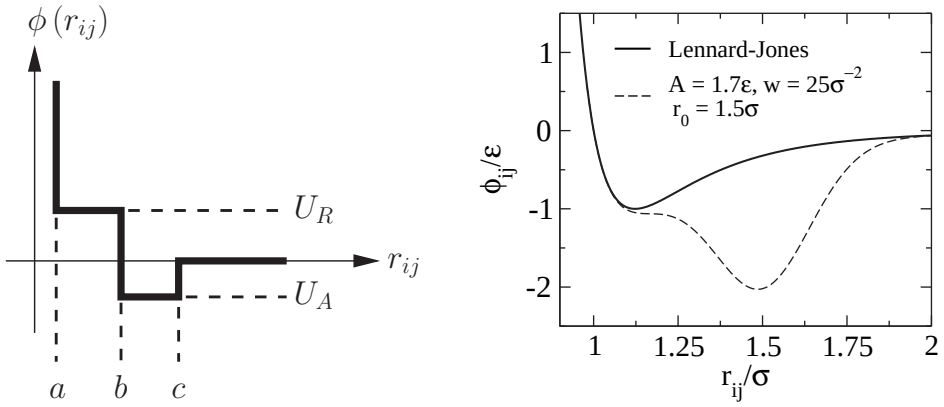

Figure 6.7: *Discrete (left) and smooth (right) forms of the shoulder potential. A second critical point is present in the three-dimensional discrete potential for various values of b/a and c/a only when $|U_A/U_R| > 2$.*

Both forms are shown in figure 6.7.

After confirming that these potentials give similar results in one dimension to the Stell-Hemmer potential, Sadr-Lahijany *et al.* (1998) conducted molecular dynamics simulations of both the smooth and discrete potentials in two dimensions. For the smooth version parameters of $A = 1.7\epsilon$, $r_0 = 1.5\sigma$ and $w = 25\sigma^{-2}$. were used. For both models, density and compressibility anomalies were observed, along with an unexpected increase in diffusion coefficient with increasing pressure. The authors suggest that these anomalies are related to two different local structures in the liquid. In a follow up paper, Scala *et al.* (2001) located two solid structures for the smooth potentials. An approximate phase diagram was obtained using single phase techniques. The transition between the high density square and the low density triangular solids causes the slope of the melting curve to change discontinuously with temperature. This occurs in the region close to the liquid anomalies. The justification of these anomalies relies on simulations in both the NVT and NPT ensemble. The authors use volume rescaling and the Berensden thermostat for sampling and hence the conclusions cannot be taken as entirely reliable.

Scala *et al.* (2000) present a thermodynamic argument that the smooth shoulder potential must posses an extra line of phase transitions. Specifically, it is shown that a second minimum in the enthalpy occurs as the pressure is increased. This argument relies on the enthalpy being independent of structure, i.e. the extra phase transition is either an isostructural solid-solid or liquid-liquid phase transition. Referring to the MD simulations above, it is argued (without simulation or calculation) that the anomalies observed can be explained if this line of phase transitions ends in a second metastable critical point within the supercooled liquid. This is a further suggestion that the shoulder potential is useful for understanding the anomalies of liquid water. Note that Smith and Bruce (1995) have performed multi-canonical Monte-Carlo simulations on a model colloid which resembles

the discrete potential without the shoulder. Only the attractive well is present, however this is sufficient for two fcc phases of different density to be observed.

As with the Jagla ramp potential, the smooth shoulder model in two dimensions has been tackled using state of the art Monte-Carlo methods by Wilding and Magee (2002). Using the same model parameters as Sadr-Lahijany *et al.* the presence of the two solid phases is confirmed, as are the liquid anomalies. No evidence is found to support the presence of a metastable second critical point. The density anomaly is shown to be a consequence of approaching the triangular solid freezing temperature. During this process clusters of lower density than the surrounding liquid are formed, lowering the average density and generating the expansion on cooling.

The first molecular dynamics simulations of a shoulder potential in three dimensions were conducted by Franzese *et al.* (2001). These were restricted to the discrete form. In contrast to the two dimensional case a metastable second critical point *was* identified for certain parameterisations, again using single phase methods. In a follow up paper Buldyrev *et al.* (2002) showed the absence of a density anomaly in these three dimensional simulations. Franzese *et al.* (2002) suggested that this may be due to the lack of a second solid phase. The single solid phase present was identified by crystal growth from a seed surrounded in a gaseous simulation. Skibinsky *et al.* (2004) have mapped in detail the location of the second critical point as a function of the parameters in this discrete potential. Note that in contrast to the hypothetical two dimensional (supposed waterlike) liquid-liquid transition, this metastable second critical point lies at *higher* temperature than the liquid-gas critical point in all cases mapped.

The smooth shoulder potential in three dimensions has been the subject of only two limited studies. The first (Mausbach and May, 2003) explores only the high temperature liquid, well above the melting line. Unsurprisingly, no liquid anomalies were found. No second critical point is found. The second study (Netz *et al.*, 2003) has measured a diffusion anomaly at somewhat lower temperatures in the microcanonical ensemble.[3] Both studies used a single parameterisation of equation 6.1.

In the following chapter, a detailed study of the three dimensional smooth shoulder potential is presented with a view to answering some of the questions posed in section 6.2.2 for this model. Of particular interest is the difference between the behaviour of the smooth and discrete forms of the shoulder potential in three-dimensions.

[3] Attempts to reproduce this result with the GOLDILOCS code indicate the diffusion anomaly is a consequence of cavitation in fixed-volume simulations.

Chapter 7

Phase Diagrams of Core-Softened Potentials

Previous studies of the smooth shoulder potential in two and three dimensions have concentrated on the location of liquid anomalies for a single parameterisation of equation 6.1. In this work a somewhat different approach is adopted. Explanations for unusual liquid properties of core-softened potentials universally incorporate the phase behaviour of the solid close to melting. It therefore seems logical to concentrate on quantifying the solid and melting phase behaviour as a function of the parameters A, r_0 and w. This may be interesting in itself, and will indicate where liquid anomalies are likely to occur based on existing knowledge of two dimensional systems. In this chapter the phase behaviour is mapped for a family of parameters in which r_0 and w are held fixed and A is varied.

As with the Lennard-Jones simulations reported in previous chapters, reduced units are employed here. Energies are quoted as multiples of the Lennard-Jones well depth ϵ, lengths as multiples of σ. Reduced temperature T^* is calculated as $k_B T/\epsilon$, with pressure $P^* = P\sigma^3/\epsilon$. Time is measured in units $t^* = (m/\epsilon)^{1/2}\sigma$ where m is the atomic mass.

7.1 Candidate Structures

Much insight into the solid phase behaviour of a model substance can be extracted from zero temperature enthalpy and volume characteristics as a function of pressure. For structures which can be expected to respond isotropically to hydrostatic pressure, energy is a one-dimensional function of volume that can be traced with a series of static calculations. The energetically relevant structures must first be identified.

The approach adopted here is to examine energy-volume curves for several simple isotropic

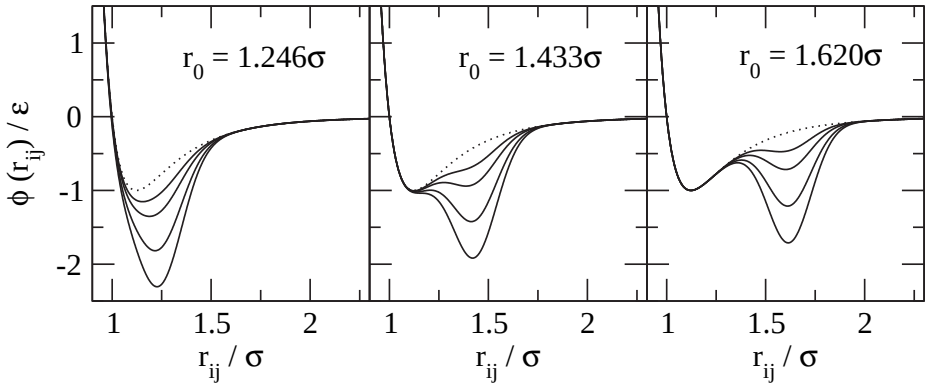

Figure 7.1: *Plots of the pair-potential described by equation 6.1 for three values of r_0. For each value of r_0 plots for A/ϵ =0.25, 0.5, 1.0 and 1.5 are shown. The parameter $w = 41.22\sigma^{-2}$ in all cases.*

structures. Specifically face-centred cubic (fcc), body-centred cubic (bcc), simple cubic (sc) and diamond. Meta-dynamics simulations can be initialised from any minima identified. These may locate further relevant structures. The hexagonal close-packed (hcp) structure does not respond isotropically to pressure, but will be considered later.

Curves of this kind were traced for various values of A, r_0 and w. Examples are shown in figure 7.2. Parameters for which the outer well represents a small perturbation do not alter the dominance of the fcc structure. The simple cubic structure dominates at intermediate r_0 values. Curves for r_0 in the region of 1.5 to 2σ show the diamond structure as substantially more stable than close packed structures. Pair potentials with r_0 in this region do not at all resemble the shoulder form. These are not relevent here but may be interesting for later studies in their own right.

Both the fcc and sc structure exhibit two energy minima in some cases. For all parameters explored the lower density sc minima is not energetically relevant, having only six nearest neighbours at r_0 compared to twelve in the lower density fcc case. The presence of two minima for a given structure is precisely the prediction of Scala *et al.*, although it is not yet clear if this also applies to the liquid.

Meta-dynamics simulations have concentrated on potentials for which $w = 41.22\sigma^{-2}$ and $r_0 = 1.433\sigma$. These values of w and r_0 have been selected by eye to provide a suitable shoulder to the pair-potential. Simulations for various values of A between 0.25 and 1.5σ have been conducted, using both fcc minima as well as the sc structure as initial conditions. In all cases zero external pressure is applied. Temperatures used ranged from $T^* = 0.16$ to 0.5.

The lowest energy structure with $A = \epsilon$ was generated from a run of 100 meta-steps as shown in fig. 7.3. A step δh of $1.16\,\sigma$ is used, with free energy augmentations $2.63\,\epsilon$ in height. The final configuration was optimised using conjugate gradient energy minimisa-

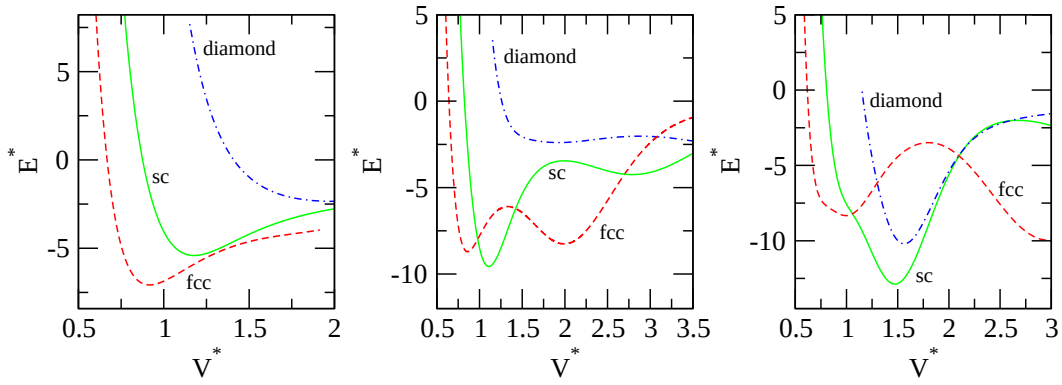

Figure 7.2: *Example energy-volume curves for the lowest energy isotropic structures. Parameters used are $A = \epsilon/4$, $r_0 = 1.433\sigma$ (left), $A = \epsilon$, $r_0 = 1.433\sigma$ (centre) and $A = 3\epsilon/2$, $r_0 = 1.587\sigma$ (right). Other isotropic phases considered lie well above this energy scale. $w = 41.22\sigma^{-2}$ in all cases.*

tion with respect to the atomic positions and cell vectors. The result is easily identified as a 5x5x5 repetition of a simple hexagonal (sh) primitive cell ($\alpha = \beta = 90°$,$\gamma = 120°$) with $a = b = 1.059\sigma$ and $c = 1.016\sigma$. The system size was 216 particles. It is easily confirmed via constant pressure simulation that this sh structure responds anisotropically to hydrostatic pressure. The density of this structure lies between that of the sc and fcc structures, however its energy is substantially lower than either with this A value. The stability of this structure can be understood in terms of neighbour distances. The nearest and second nearest neighbours lie at a distance c and a respectively, close to the position of the Lennard-Jones minimum, while the third nearest lie at $\sqrt{(a^2 + c^2)}$ which is very close to r_0. Both energy minima in the pair potential are therefore utilised.

A number of hybrid structures in which stacking alternates between sc and sh have also been located when employing smaller δh. These all lie midway in both energy and density between the pure structures. No other structures of energetic relevance have been obtained when employing alternative A values. It must however be stressed that the meta-dynamics search of configuration space may not be exhaustive. Other structures of importance may exist that have not been considered. The remainder of this chapter assumes this is not the case.

7.2 Choice of r_0 and w

The choice of parameters used for the meta-dynamics above is essentially arbitrary. For a given value of r_0, the effect of small changes in w is not likely to be significant at zero temperature. It is however prudent to examine the effect of altering r_0 on static energies for the structures of interest. Plots of the pair-potential for three values of r_0 are shown in

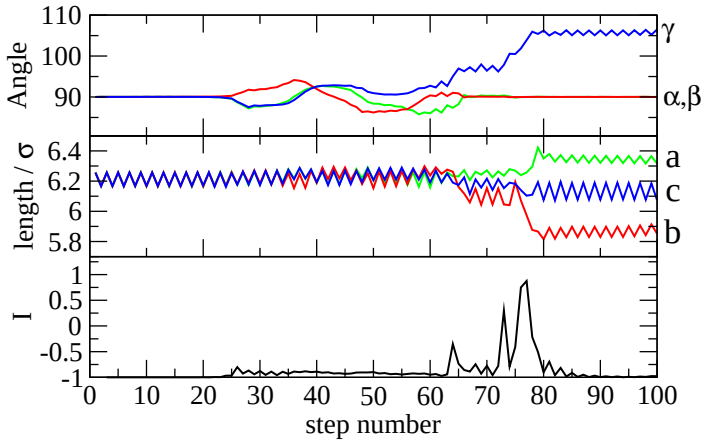

Figure 7.3: *Evolution of the cell angles and cell lengths during a meta-dynamics run initialised from the simple cubic minimum. The dimensionless quantity* $I = \mathbf{F}_{sd} \cdot \mathbf{F}_{aug} / |\mathbf{F}_{sd}| \, |\mathbf{F}_{aug}|$ *is expected to remain at* ≈ -1 *while exploring the initial basin of attraction, and peak sharply at* $+1$ *at the cusp between two minima.*

figure 7.1. The zero temperature behaviour of these three choices is studied below. The effect of w on the location of finite-temperature phase boundaries is explored in the next chapter. Static energy/enthalpy is by performing a conjugate-gradient (CG) minimisation of the enthalpy $U + PV$ with respect to both the cell vectors and the fractional atomic coordinates. For optimisation of a given structure, the cell angles are held fixed to avoid location of a lower energy structure.

Energies under zero pressure calculated in this way are shown in figure 7.4, as a function of the outer-well depth A. Positions $r_0 = 1.246\sigma$ and $r_0 = 1.620\sigma$ are used with the well width parameter $w = 41.22\sigma^{-2}$ in both cases.

7.2.1 $r_0 = 1.246\sigma$

With the outer Gaussian well close to the Lennard-Jones minimum, no interesting phase behaviour is apparent from the zero temperature data. The hcp structure has the lowest energy for all A values in the range studied. This is near-degenerate in energy to the fcc structure as in the pure Lennard-Jones case. The simple hexagonal structure is only mechanically stable above $A = \epsilon$. Structural optimisation of this structure at lower A values resulted in transformation to close packing. The sc structure is stable for all A, but with high energy.

As both the sc and sh structures are of lower density than the close packed structures, they cannot become lower in enthalpy under positive pressure at zero temperature. In addition the entropic contribution at finite temperature is unlikely to overcome the energy difference. The close-packed structures can therefore be expected to remain thermody-

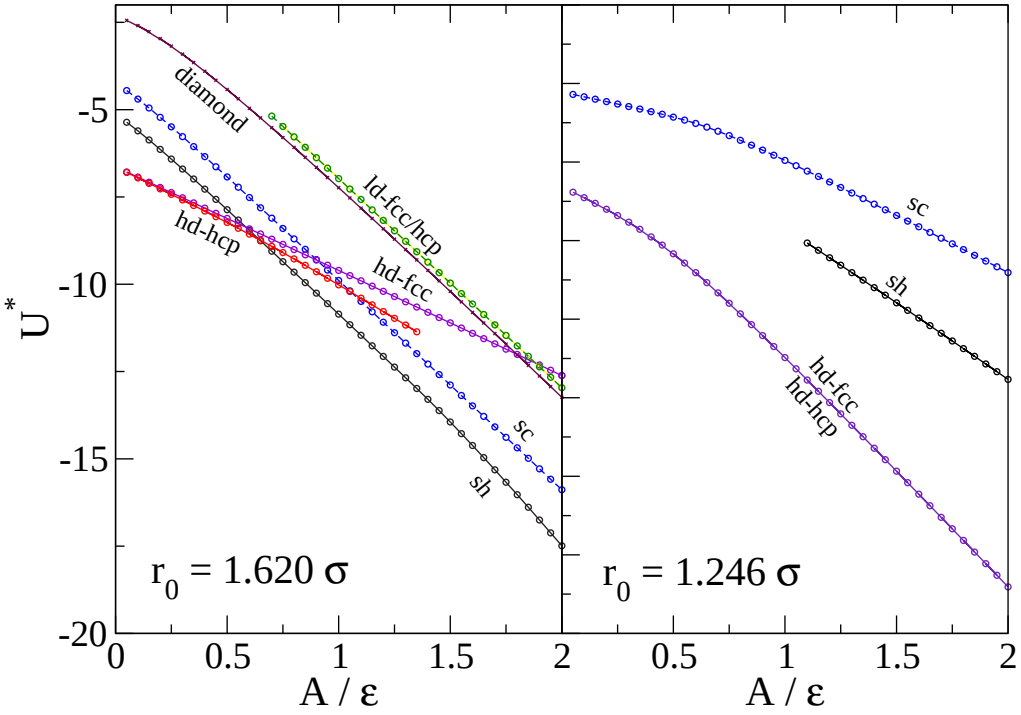

Figure 7.4: *Ground state structural energies for outer-well positions* $r_0 = 1.246\sigma$ *and* $r_0 = 1.620\sigma$ *as a function of the outer-well* A.

namically stable over the entire solid range for all A.

7.2.2 $r_0 = 1.620\sigma$

The data for $r_0 = 1.620\sigma$ are somewhat more interesting. Several trends are apparent from figure 7.4 and from the volume data (not plotted).

- For values of A greater than approximately 0.6ϵ the sh structure is lower in energy than the close-packed structures. As the sh structure is of lowest density, a transition to close packing can be expected under positive pressure.
- In the region of $A = \epsilon$ the sc structure also overtakes the close-packed structures. The sc density is lower than that of sh, and hence it can be concluded that the sc to close-packing transition will only ever be meta-stable.
- As A increases, the energy difference between the hcp and fcc structures increases. Beyond $A = 1.4\epsilon$ the hcp structure is mechanically unstable and only the fcc persists to higher A values.
- At around $A = 0.7\epsilon$, a second set of close packed structures becomes mechanically stable in which the nearest neighbour distance is r_0, rather than that associated with the Lennard-Jones minimum.

- At approximately $A = 1.8\epsilon$ the lines for the high and low density close-packed structures intersect. Beyond this, a metastable isostructural phase transition is expected under positive pressure.
- The energy of the diamond structure runs parallel to the low density close-packed phases with density between that of the two close-packed phases. Several metastable phase transitions will exist involving the diamond structure.

The nearest neighbours in the sc structure are close to the Lennard-Jones minimum at approximately 1.12ϵ. The favourability of sc over the high density close packed structures stems from second nearest neighbours which lie at $\sqrt{2}$ times this distance, which is close to r_0. Each atom has six neighbours close to the Lennard-Jones minimum plus six close to r_0. This compares to eight and twelve in the sh case which is therefore lower in energy.

From here on the two densities of close-packed structures will be denoted by the prefixes ld (low density) and hd (high density). Both densities decrease in energy on increasing A. The lower density structures contain more neighbours close to r_0 and hence the decrease is faster in these cases.

7.2.3 $r_0 = 1.433\sigma$

Data for the original choice of $r_0 = 1.433\sigma$ are plotted in figure 7.5. In this case the simple hexagonal structure overtakes the fcc at almost exactly $A = \epsilon/2$, with the parallel simple cubic line crossing at $A = 3\epsilon/4$. Meta-stable isostructural phase transitions under pressure may be realisable in potentials in the region $A > 1.2\epsilon$. The hd-hcp structure remains stable over the range of A studied. The energies of the two close packed structures do not diverge as in the $r_0 = 1.620\sigma$ case.

The initial choice of $r_0 = 1.433\sigma$ seems suitable for further study at finite temperature. A compromise between an abundance of interesting phase behaviour and simplicity is achieved. In addition, figure 7.1 indicates that smaller values reduce to a single well, and larger values generate a distinct second well. These cases may be of interest to further study, but cannot be considered to posses the shoulder of interest here. A similar argument applies to substantially altered values of w.

As is common, the hcp phase is neglected in the work that follows. The fcc-hcp transition is notoriously difficult to resolve, and is not of interest here provided the free energies of the two structures do not differ by much more than the pure Lennard-Jones case.[1] This

[1] It should be noted that the lattice-switch Monte-Carlo method has been used to study the Lennard-Jones fcc-hcp transition by Jackson *et al.* (2002). The application of this method to the hcp-fcc transition in core-softened potentials may be an interesting avenue for further study.

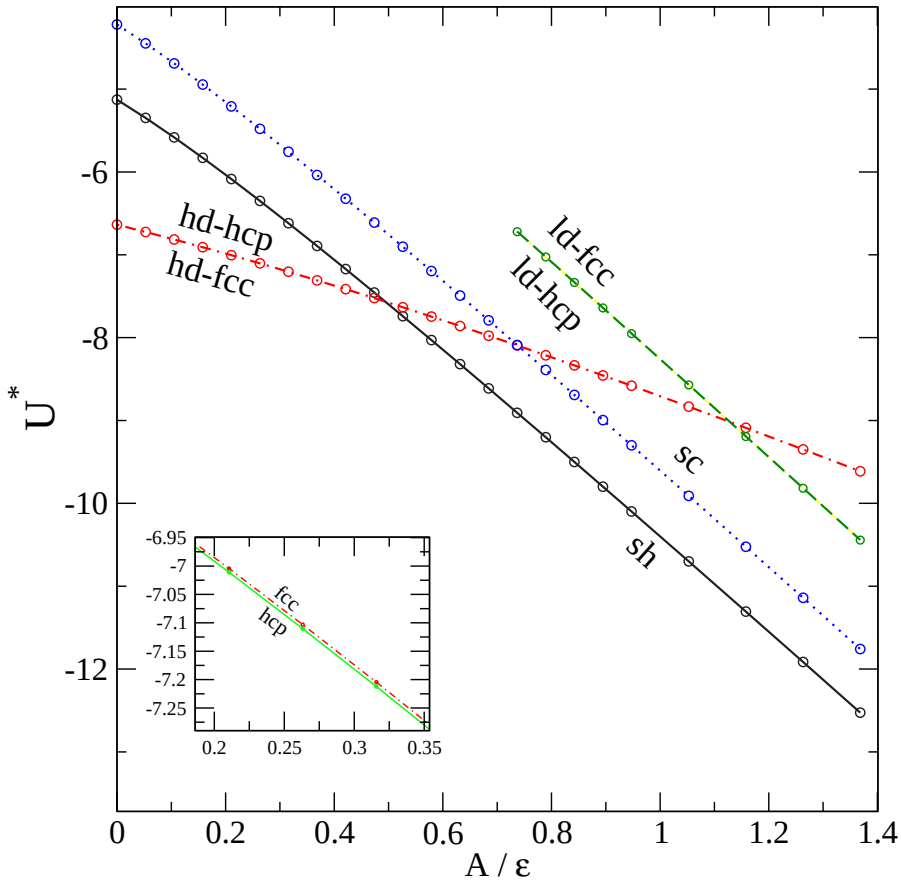

Figure 7.5: *Optimised energy under zero pressure for various structures as a function of the outer well depth parameter $r_0 = 1.433\sigma$ in all cases. The hcp and fcc structures are near-degenerate as indicated in the inset.*

will be checked during the work that follows.

Four values of A have been selected for detailed investigation.

- $A = \epsilon/4$ - In this regime little deviation from Lennard-Jones behaviour is expected, with the possibility that the sh/sc structures may come into play at high temperature if they preempt the melting transition.
- $A = \epsilon/2$ - This represents the region in which a sh to close-packing transition is expected under small positive pressure. It is indended to determine if this transition intersects the fcc melting line, resulting in stable melting of the sh structure.
- $A = \epsilon$ - Here the sh structure is expected to dominate, with transitions to close-packing at high pressure.
- $A = 3\epsilon/2$ - Which should manifest a metastable isostructural transition. This may approach the melting curve and influence the liquid in accordance with the theories of Scala *et al.* (2000).

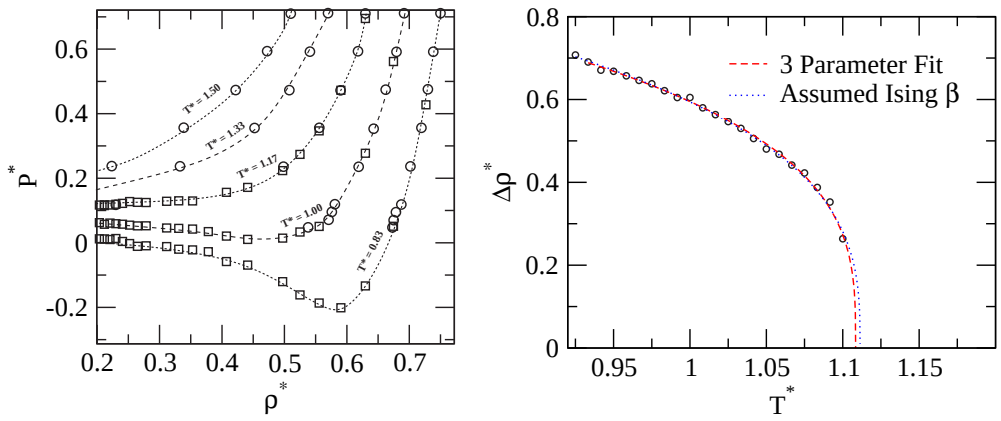

Figure 7.6: *Left, liquid isotherms for the $A = \epsilon/4$ potential. Simulations conducted at NPT are shown as circles, NVT simulations as squares. The isotherms place the critical temperature between $T^* = 1.0$ and $T^* = 1.17$. Right, density difference vs temperature along the liquid-vapour coexistence curve calculated using the histogram reweighting and muticanonical sampling process. Two fits to the appropriate power law are presented.*

The remainder of this chapter deals with detailed mapping of the above four phase diagrams using the computational methods described and tested in chapter 5.

7.3 Phase Behaviour for $A = \epsilon/4$

For this value of A the interest is in determining if any additional phases beyond those observed in the Lennard-Jones phase diagram are present. If not, the alteration of the phase diagram due to the perturbation may yield insight.

7.3.1 Liquid-Gas transition

Fluid Isotherms

To gain an initial approximation of the critical temperature, a series of isotherms were traced over the liquid and liquid-vapour regions. NPT Langevin dynamics simulations were employed in regions where the pressure varies rapidly with density. NVT simulations were used at lower densities and through the liquid-vapour equilibrium region. Each simulation length was $t^* = 400$ in both equilibration and production phases. The system size was 500 particles. The resulting isotherms are shown in figure 7.6.

These indicate that the critical isotherm lies between $T^* = 1.0$ and $T^* = 1.17$, providing a starting estimate from which to begin the histogram reweighting and multi-canonical sampling procedure.

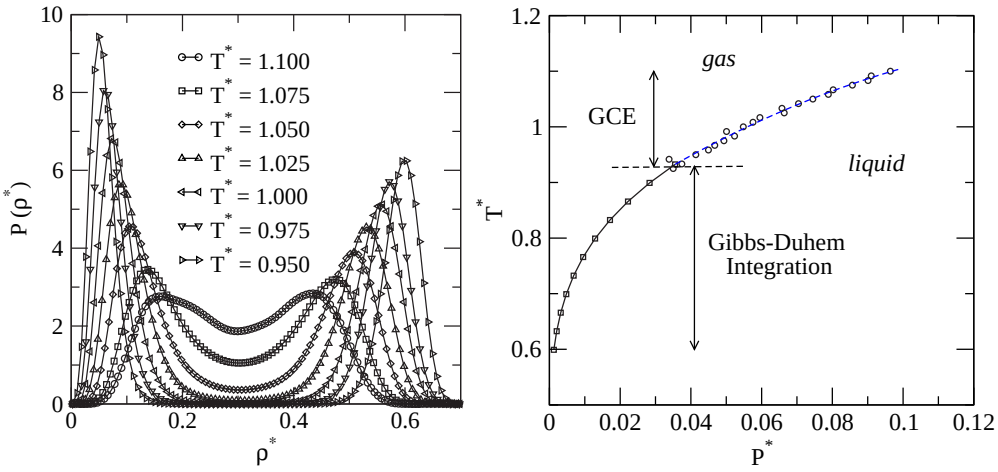

Figure 7.7: *Liquid-gas transition in the $A = \epsilon/4$ potential. The first few number density histograms employed in the multi-canonical sampling procedure are shown on the left. The Gibbs-Duhem continuation of the melting curve from these GCE simulations is shown in the right.*

Multi-canonical Monte-Carlo

Following the procedure in section 5.6.1, an initial bimodal histogram was obtained at $T^* = 1.100$ with a chemical potential of $\mu^* = -9.267$ in a cubic cell of side 7.13σ. From this starting point the liquid-vapour coexistence curve was traced to a temperature of $T^* = 0.925$ in 21 steps. Each multi-canonical GCE simulation employed $600,000$ cycles. Example histograms are shown in figure 7.7. These yield information on the density of the two phases, allowing a three parameter fit of equation 5.1a to be obtained. The extrapolation of this fit to zero density difference is shown in figure 7.6, yielding a critical temperature of $T_c^* = 1.108$. If the three-dimensional Ising $\beta = 0.3258$ is imposed, the critical temperature becomes $T_c^* = 1.111$. An estimate of the critical temperature is hence taken as $T_c^* = 1.108 \pm 0.003$. This is larger than that identified for the Lennard-Jones potential in the truncated and force-shifted case (0.961 ± 0.004 - see appendix A). A fit to the law of rectilinear diameters gives a critical density of $\rho_c^* = 0.302 \pm 0.003$.

Gibbs-Duhem Integration

Below $T^* = 0.925$ the continuation of the liquid-vapour coexistence curve has been traced with Gibbs-Duhem integration. A starting point for this series is taken from a quadratic fit to the pressure-temperature data unfolded from the multi-canonical Monte-Carlo simulations. The enthalpy and volume of both phases are sampled at each step using constant pressure Langevin dynamics simulations of $75,000$ Δt for the gas and $50,000$ Δt for the liquid. A time-step of $\Delta t^* = 0.0012$ was used for both phases with suitably identified thermostat and barostat parameters. Both phases used simulations of

500 atoms.

The join between the Monte-Carlo and Gibbs-Duhem data is shown in figure 7.7.

7.3.2 Solid

The solid structure for this potential is expected to remain close packed at low temperature and high pressure. To determine the full phase behaviour of the solid, free energy calculations have been performed at higher temperature as follows.

For temperatures in the range $T^* = 0.0833$ to 0.500 in steps of 0.042, the zero pressure cell dimensions were first calculated for the fcc, sc and sh structures using system sizes of 256, 343 and 392 atoms respectively. These calculations sampled using the fully flexible constant pressure Langevin dynamics algorithm over $100,000$ time-steps after equilibrating for $20,000\,\Delta t$. The time-step $\Delta t^* = 0.0013$ was chosen conservatively to be suitable for all structures, as were the cell mass and particle friction coefficient. At no temperature in this range were the sc and sh structures mechanically stable. As the fcc structure is of the highest density, it can be concluded that as with the Lennard-Jones system, the solid remains in this structure over the entire positive pressure range.

The free energies of the resulting fcc cells were computed using the methodology described in section 5.4.2, and compared to those for the hcp structure at zero pressure identified in the same fashion. Each calculation employed 50 short Langevin dynamics simulations of $3,000\,\Delta t$ (after $2,000\,\Delta t$ equilibration) along the path to the harmonic crystal. The time-step was unchanged from the constant pressure simulations above. The optimal spring constant for the reference crystal was determined from 10 parallel simulations of $10,000\,\Delta t$. For the system sizes employed (216 atoms for hcp, 256 for fcc) the difference in free energy between the two structures was less than 0.008ϵ for all temperatures. This is smaller than the finite-size error in the calculation. The small outer well has therefore done little to lift the hcp-fcc degeneracy at finite temperature.

7.3.3 Melting Curve

Two-Phase Simulations

A first attempt at locating the melting line for this potential was performed using two-phase NPT Langevin dynamics simulations in a fully flexible cell (see section 5.3.1). A system size of 1000 atoms was used, with each phase containing 500 atoms in a double-cubic configuration. Conservative values of the time-step and particle friction coefficient were used so as to be appropriate for the solid and liquid portions. A total simulation time

of $t^* = 280$ was used for each point sampled in the P-T plane. Pressures in the range $P^* = 0.047$ to 0.710 were sampled.

The results close to the melting line are shown in figure 7.8. 80 simulations were conducted in total. Each sampled point is identified as either solid or liquid. Simulations which did not transform to a pure phase within the simulation time (i.e. those close to the melting line) are not plotted. This method is clearly somewhat expensive, requiring many NPT simulations, however the melting line has been accurately bracketed. This method is therefore useful for determining the range of temperatures over which free energy calculations should be performed to accurately locate the melting line. This strategy will be adopted for the remainder of this chapter. Less simulations than used here are hence required.

Free Energy Calculations

The melting temperature at a pressure of $P^* = 0.047$ has been calculated from explicit free energy calculations. For the solid phase, densities at temperatures up to $T^* = 0.500$ in steps of 0.042 were identified for this pressure, again using the fully flexible NPT Langevin dynamics scheme. Simulation parameters used were identical to those in section 7.3.2 above. 256 atom cells were employed.

At the identified densities, Helmholtz free energies were computed with the Einstein-crystal method for system sizes of 256, 500 and 864, again using identical parameters in section 7.3.2, and extrapolated to the thermodynamic limit. This accounts only for the dominant finite-size effect in computing the Helmholtz free energy at a *given* density. There is a possibility of further error due to finite-size effects in the identification of density, i.e. in the initial NPT Langevin dynamics simulations. This will affect both the density used for the thermodynamic integration, and the PV term added to the Helmholtz free energy to give the chemical potential. This effect has been quantified by repeating a selection of the free energy calculations using densities identified from NPT calculations of 864 atoms. The change in free energy is less than $10^{-6}\epsilon$ in all cases. This effect has hence been neglected in subsequent calculations.

A reference point for liquid-free energy calculations was taken at $T^* = 1.000$ and total chemical potential $\mu^* = -10.526$. This is known to lie in the liquid region from the multi-canonical data. In a cubic cell of side 7.79σ, a GCE Monte-Carlo simulation of $500,000$ cycles (after equilibration for $50,000$) identifies $\langle N \rangle = 304.4 \pm 0.2$ and $\langle P^* \rangle = 0.357 \pm 0.006$, leading to a Helmholtz free energy per atom of $f^* = -11.080 \pm 0.003$.

Six free energies along the $P^* = 0.047$ isobar have been computed by thermodynamic integration from this reference point, at temperatures of $T^* = 0.375$ to 0.583. The density

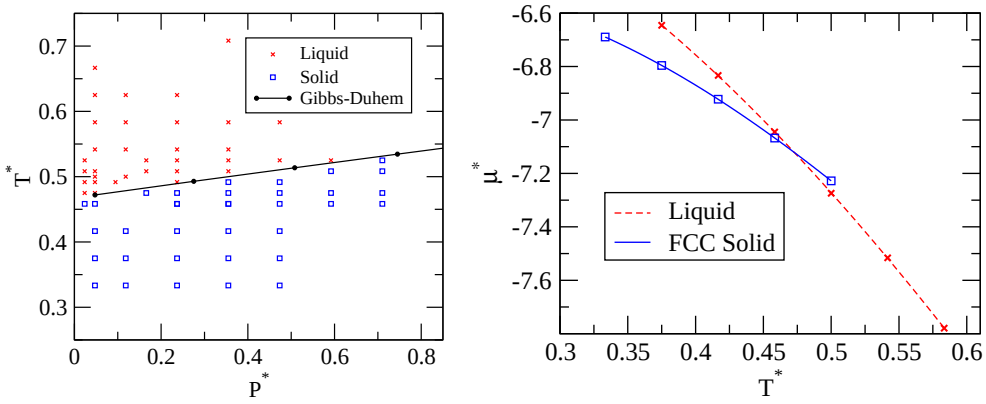

Figure 7.8: *Melting curve for the potential with $A = \epsilon/4$ (left) calculated using the two-phase NPT coexistence method described in section 5.3.1. The solid line is the melting curve computed from free energy calculations and traced with Gibbs-Duhem integration. The chemical potential of the solid and liquid phases along the $P^* = 0.047$ isobar is shown on the right.*

of the liquid at each temperature was first computed from an NPT Langevin dynamics simulation of $100,000$ time-steps with $\Delta t = 0.0026$. The system size was 350 atoms, with an equilibration period of $20,000\Delta t$. The integration itself employed 10 sampled points along both the isotherm and isochore needed to reach the temperature and density of interest. Each sample employed $10,000$ equilibration steps before sampling for $50,000$ steps, also using 350 atoms. To estimate the effect of finite-size, the entire process was repeated with 500 atoms. The resulting changes in free energy are much smaller than the statistical error on the reference point and have hence been neglected.

Plots of the resulting solid and liquid chemical potential along the $P^* = 0.047$ isobar are shown in figure 7.8. Interpolation to the intersection reveals a melting temperature of $T^* = 0.471$. The total error on this melting temperature is estimated as less than ± 0.008. This is dominated by the statistical error in the liquid reference free energy, which has been controlled to an acceptable level with the use of a long GCE Monte-Carlo simulation.

Gibbs-Duhem Integration

This melting point has been used as the starting point for a Gibbs-Duhem series in the direction of increasing temperature. An integration step size of $\Delta T^* = 0.021$ was employed. At each step the two phases were sampled using NPT Langevin dynamics simulations. Parameters were identical to those used for the full Lennard-Jones potential in section 5.5.2, with the exception of the time-step which was reduced to $\Delta t^* = 0.0028$. The first few steps of the resulting series are shown in figure 7.8 in comparison to the two-phase simulation results. To check for integration errors in the Gibbs-Duhem series,

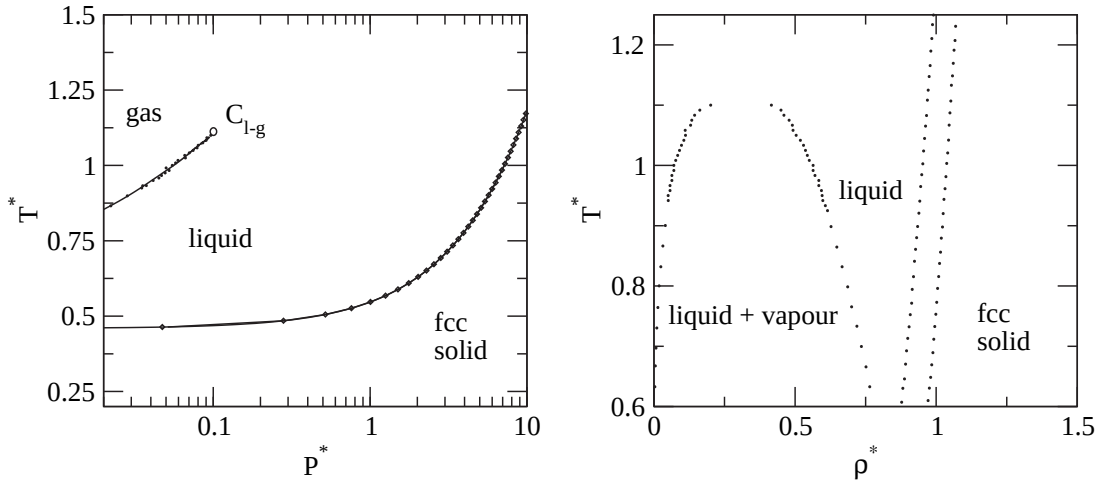

Figure 7.9: *Phase diagram of the $A = \epsilon/4$ potential. The temperature-pressure projection is shown on the left, with the density-temperature projection on the right. Both forward and reverse Gibbs-Duhem series are plotted. The two are indistinguishable on this scale. The low pressure region and triple point have not been studied in detail. Other than shifts in the melting and critical temperatures, no interesting phase behaviour over the Lennard-Jones case is observed.*

a portion of the melting curve was retraced in the direction of decreasing temperature between $T^* = 1.005$ and $T^* = 0.464$.

The phase diagram for this potential is shown in figure 7.9. Both forward and reverse Gibbs-Duhem series are plotted and are indistinguishable by eye.

7.4 Phase Behaviour for $A = \epsilon/2$

For this value of A the sh structure may remain thermodynamically stable at appreciable temperature, leading to a possible sh-fcc transition.

Much of the methodology has been exemplified in the previous section. For this potential some details of the simulations will be dispensed with, concentrating on the key parameters and findings. Substantial differences from the methodology used in the previous section will be noted where appropriate. In many cases new thermostat and barostat parameters are required for the Langevin dynamics sampling. The choice of these follows the procedures outlined in chapter 4 and will not be explicitly discussed here unless unusual.

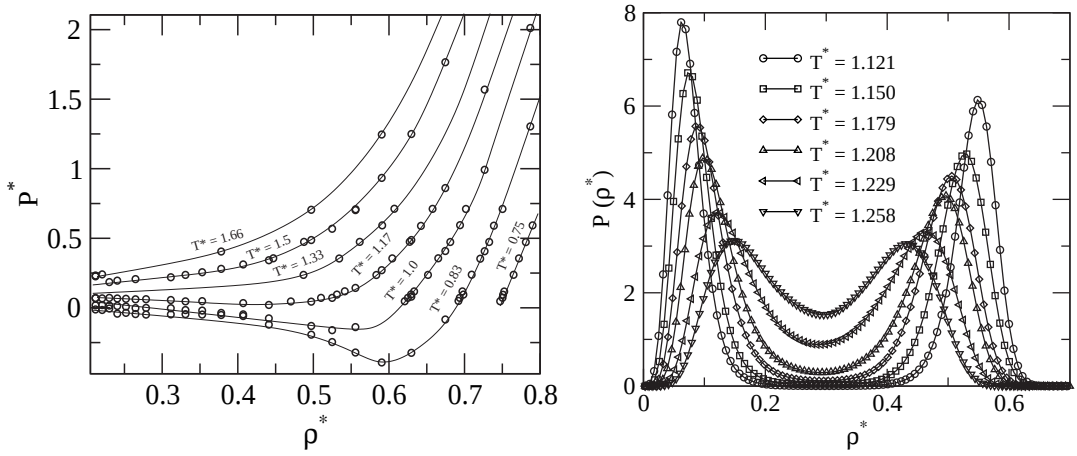

Figure 7.10: *Critical behaviour of the $A = \epsilon/2$ potential. The fluid isotherms used to find an approximate critical temperature are shown on the left. The first few number density histograms arising from the multi-canonical sampling procedure are shown on the right.*

7.4.1 Liquid-Gas Transition

Fluid Isotherms

As with the previous potential, an initial estimate of the liquid-gas critical temperature was obtained by seeking the first fluid isotherm on increasing temperature without indications of hysteresis. The isotherms are shown in figure 7.10. These indicate that the critical isotherm lies between $T^* = 1.17$ and $T^* = 1.33$.

Multi-canonical Monte-Carlo

At a temperature of $T^* = 1.279$ a bimodal histogram suitable as a starting point was obtained at a chemical potential of $\mu = -10.782$. A selection of the number density histograms obtained while stepping along the coexistence curve are shown in figure 7.10.

The critical parameters are identified as $T_c^* = 1.293 \pm 0.006$ and $\rho_c^* = 0.284 \pm 0.006$ indicating a further increase in critical temperature on increasing A.

Gibbs-Duhem Integration

Below temperatures of $T^* = 1.142$ the liquid-vapour curve was traced with Gibbs-Duhem integration. A fit to the pressure data unfolded from the multi-canonical simulations gives $P^* = 0.0592$ as the initial pressure for the series. A time-step of $\Delta T^* = 0.021$ was employed for both phases. Other parameters are unchanged from section 7.3.1. The resulting series is plotted in figure 7.12.

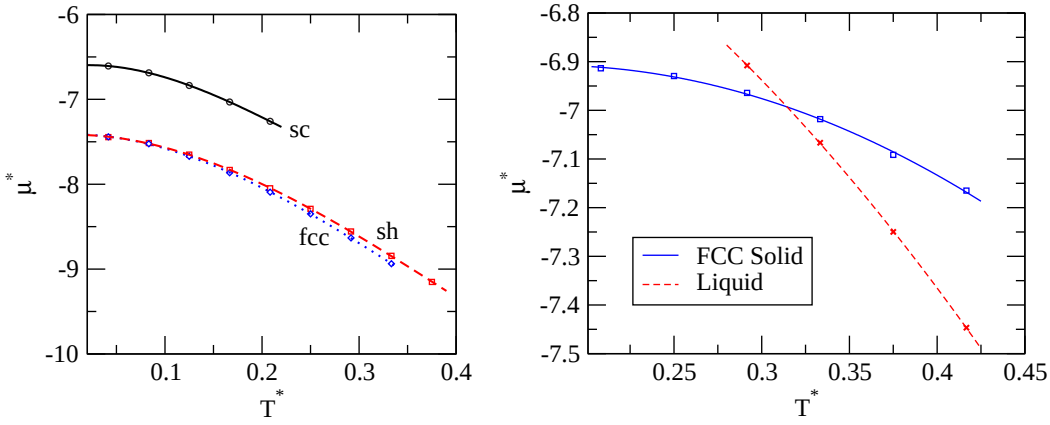

Figure 7.11: *Chemical potential as a function of temperature along the zero pressure isobar for the $A = \epsilon/2$ potential (left). Three structures are shown. The sc structure is mechanically unstable beyond $T^* = 0.25$. The chemical potential of the solid and liquid along the $P^* = 0.047$ isobar is shown on the right.*

7.4.2 Solid

Free energy calculations were performed along the zero pressure isobar for all relevant structures, again using densities identified from constant pressure Langevin dynamics simulation. Parameters for these and the resulting Einstein crystal calculations were unchanged from section 7.3.2. Results are shown in figure 7.11. These are uncorrected for finite-size effects.

The sc structure is now mechanically stable at finite temperature, but not beyond temperatures of $T^* = 0.25$. The sh structure is also stable, with comparable free energy to fcc. Although at zero temperature the energy of the sh structure is slightly less than that of the fcc, at no finite temperature realisable in a simulation is this the case. As temperature increases the separation between the fcc and sh structures increases. There must therefore be a transition between these two structures, but at temperatures below those readily accessible to the simulations methods used here.

Free energies for the hcp structure were also computed and found to be indistinguishable from the fcc values.

7.4.3 Melting Curve

Two-Phase Simulations

No attempt to achieve high accuracy with two phase simulations has been made in this case, the aim being to provide a starting point for accurate free energy calculations. A total of 63 NPT simulations were conducted, prepared and evolved as in section 7.3.3.

These bracket the melting temperature as lying between $T^* = 0.3$ and $T^* = 0.4$ for pressures $P^* < 0.7$.

Free Energy Calculations

A point on the melting curve was sought along the $P^* = 0.047$ isobar. For the solid phase, free energy calculations were performed for temperatures in the range 0.208 to 0.5 in steps of 0.042. The number of sampled points along the path to an Einstein crystal was decreased to 24 with no appreciable decrease in accuracy. Otherwise simulations proceded as in section 7.3.3.

Liquid free energy calculations also proceded as in section 7.3.3. A reference point at $T^* = 1.167$ with $\mu = -9.474$ was taken. Grand canonical Monte-Carlo simulation reveals $\langle N \rangle = 368.6 \pm 0.2$, and $\langle P^* \rangle = 2.56 \pm 0.01$. The Helmholtz free energy per atoms at the reference point is therefore $f^* = -12.75 \pm 0.01$. Thermodynamic integration to temperatures between 0.292 to 0.500 in steps of 0.042 was performed. Plots of chemical potential for both the solid and liquid along the $P^* = 0.047$ isobar are shown in figure 7.11. The melting temperature is identified as $T^* = 0.315 \pm 0.01$. Again the uncertainty is dominated by statistical error in the liquid reference free energy.

Gibbs-Duhem Integration

Gibbs-Duhem integration initiated from this point proceeded in the direction of positive temperature using simulation parameters and sizes unchanged from section 7.3.3. To check for integration errors the series was reversed from a temperature of $T^* = 1.002$ to $T^* = 0.606$. This reversed series is again indistinguishable from the original.

The phase diagram for the $A = \epsilon/2$ potential is shown in figure 7.12.

7.5 Phase Behaviour for $A = 0.55\epsilon$

It is clear that the choice of $A = \epsilon/2$ has not captured the interesting phase behaviour expected in this region. Increasing A to 0.55ϵ widens the energy difference between these two structures and should therefore manifest the transition at higher temperature and pressure. A study of the condensed phase behaviour of this model therefore seems appropriate.

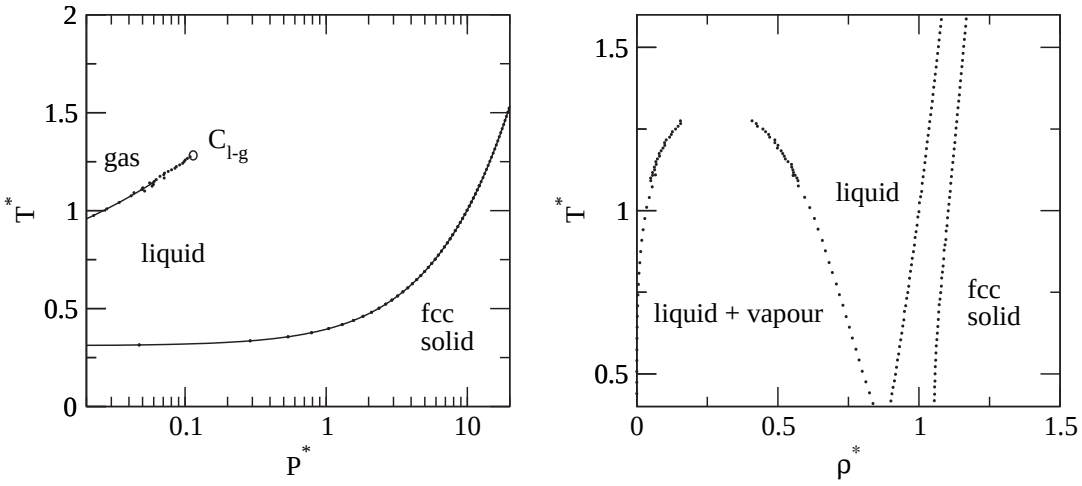

Figure 7.12: *Phase diagram of the $A = \epsilon/2$ potential. The temperature-pressure projection is shown on the left, with the density-temperature projection on the right. The forward and reverse Gibbs-Duhem series are again indistinguishable on this scale. This phase diagram represents a further decrease in melting temperature, and increase in critical temperature over the Lennard-Jones case.*

7.5.1 SH-FCC Transition

Zero Temperature

To locate the pressure of the sh-fcc transition at zero temperature, the optimised enthalpy as a function of pressure was plotted for both structures. Optimisation was performed with respect to atomic positions and cell vectors using conjugate gradient minimisation. A system size of 392 atoms was used for the sh structure, with 256 in the fcc simulations.

The two enthalpy curves intersect at approximately $P^* = 8.9$. At this pressure the sh structure is of lower density. By simple consideration of the Clausius-Clapeyron equation these results require that the transition at higher temperature occurs at lower pressure. This provides a range over which the finite temperature transition can be sought with free energy calculations.

Finite Temperature

A finite temperature point on the phase boundary was sought along the $T^* = 0.167$ isotherm. Using a system size of 392 atoms for the sh case, and 256 for the fcc case, densities for the pressure of interest were computed using NPT Langevin dynamics simulation in the usual fashion. Volume samples were taken over $100,000\Delta t$ ($\Delta t^* = 0.0012$) after a $20,000\Delta t$ equilibration process. It should be stressed that density responses to pressure and temperature in the sh structure occur anisotropically. Expansion along each crystal direction must be considered separately when constructing a cell for thermody-

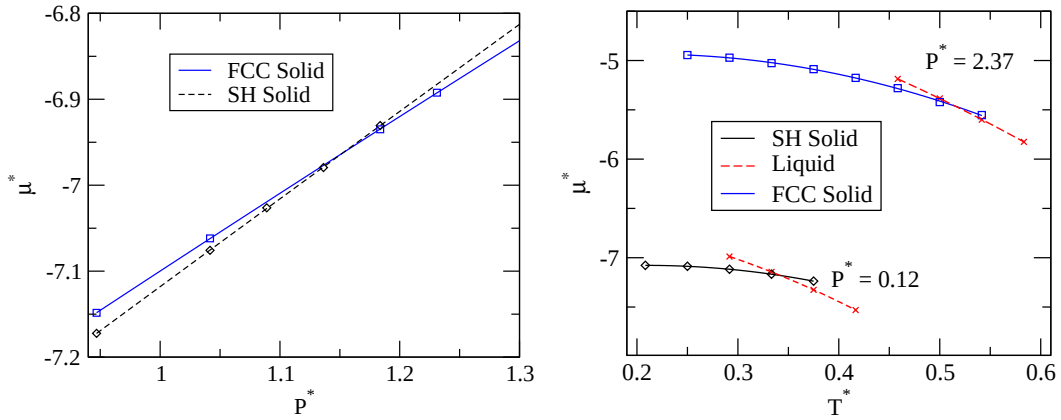

Figure 7.13: *Free-energy calculations for the $A = 0.55\epsilon$ potential. The location of the sh-fcc transition along the $T^* = 0.167$ isotherm is shown on the left. The right hand figure shows the location of the sh-liquid and fcc-liquid melting temperatures from free energies computed along the $P^* = 0.118$ and $P^* = 2.374$ isobars respectively. All solid free energies shown are those extrapolated to the thermodynamic limit.*

namic integration. Free energies were computed using the Frenkel-Ladd Einstein crystal method, with parameters matching those in section 7.4.2.

The process was repeated at increasing pressure until useful trends in the free energy could be identified. An extrapolation of the free energies at pressures in the range $P^* = 0.02$ to 0.35 indicated an intersection at pressures between 0.9 and 1.3. Further calculations in this region employed finite-size corrections. Additional systems sizes of 640 and 972 atoms were employed for the sh phase. 500 and 864 atom systems were used in the fcc case. The resulting intersection is shown in figure 7.13. Extrapolation between sampled points yields a transition at $P^* = 1.15$. The uncertainty on the pressure is estimated at approximately 0.01. This arises from the extent to which finite size errors may not be accounted for, as described in section are comparable to those in figure 5.6.

7.5.2 Melting Curves

The sh to liquid transition has been located at a pressure of $P^* = 0.118$. Parameters for the solid-free energies match those in section 7.4.2 with finite size corrections computed using system sizes of 392, 640 and 972 atoms. A reference point for computing liquid free energies was taken at $T^* = 1.171$ with chemical potential $\mu^* = -9.474$. A GCE Monte-Carlo simulation in a cubic cell of side 7.79σ results in $\langle N \rangle = 370.7 \pm 0.3$ and $\langle P^* \rangle = 2.730 \pm 0.009$. The Helmholtz free energy per atom at this density and chemical potential is therefore $f^* = -12.95 \pm 0.01$. As with the solid free energy calculations, parameters for the thermodynamic integration are identical to the $A = \epsilon/2$ case.

The intersection of the sh-solid and liquid chemical potentials along this isobar is shown

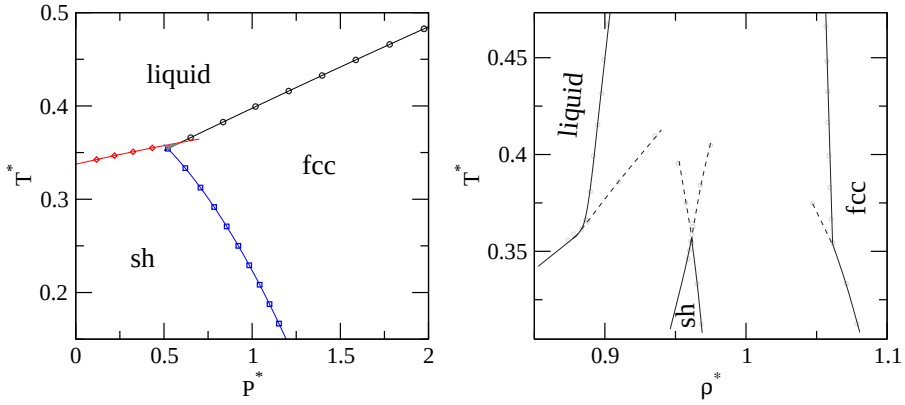

Figure 7.14: *Phase diagram for the potential with $A = 0.55\epsilon$ in the region of the sh-fcc-liquid triple point. The pressure temperature projection is shown on the left. Points shown are the three Gibbs-Duhem series described in the text. The triple point lies within the shaded triangle formed by the three intersecting series. The temperature density projection is shown on the right. Dashed lines indicate meta-stable continuations of the phase boundaries.*

in figure 7.13. The value for the melting temperature obtained is $T^* = 0.343 \pm 0.008$, again dominated by the statistical error in the reference free energy.

By a similar process, the fcc melting temperature at $P^* = 2.373$ was determined. Solid free energies were calculated with parameters identical to those used in computing the fcc melting temperature for the $A = \epsilon/2$ potential in (section 7.4.3). The same liquid reference state employed for the sh melting temperature was used for thermodynamic integration. The intersection of the fcc and liquid free energies is shown in figure 7.13, locating the melting temperature at $T^* = 0.516 \pm 0.008$.

7.5.3 SH-FCC-Liquid Triple Point

The three pairs of free energy calculations have each provided a point on a coexistence curve which can be used as the starting point for a Gibbs-Duhem series.

The sh-liquid curve was traced in the direction of increasing temperature, initially in steps of $\Delta T^* = 0.02$. 640 atoms are used in the NPT Langevin dynamics simulations for each phase. These employed a time-step of $\Delta t^* = 0.0012$ with suitably identified friction coefficients and cell masses. The total length of each simulation was $50,000\Delta t$ after equilibrating for $5,000$. The use of the fully-flexible variant is required for sampling the sh phase in which the volume fluctuations are anisotropic. The fcc-liquid curve was traced in both directions using systems sizes of 500 atoms in each phase using equivalent parameters, but with shorter relaxation times enabled by the fcc structure.

The fcc melting curve intersects that of the sh structure close to its initial point. Repetition of the sh-liquid series with a smaller step of $\Delta T^* = 0.004$ was required to accurately

locate the intersection. At this point, the sh and fcc structures posses equal free energy, and hence this point should lie along the sh-fcc line of phase transitions. To confirm this, a third Gibbs-Duhem series initialised from the the previously identified point on this curve was conducted in the direction of increasing temperature. A step size of $\Delta T^* = 0.021$ was employed with 500 atoms in the fcc phase and 640 in the sh. Simulation lengths and parameters were identical to those used for the respective phases when tracing their melting curves.

The three Gibbs-Duhem series are shown in figure 7.14 along with the corresponding temperature-density information. The sh-fcc series does indeed meet the intersection of the two melting lines, forming a triple point to within the error of the initial transition temperatures. The same triple point is located by the intersection of any two series, and is independently confirmed by the third. No further consideration of the error in the Gibbs-Duhem series is therefore required. The location of the triple point is hence $T^*_{tp} = 0.358 \pm 0.002$, $P^*_{tp} = 0.54 \pm 0.02$.

The Gibbs-Duhem information also confirms that both melting points measured are thermodynamically stable, information which was not available from the above free energy calculations alone.

7.6 Phase Behaviour for $A = \epsilon$

Here the sh structure is expected to dominate at low pressure. The transition to fcc is expected to occur at significantly higher pressures than the $A = 0.55\epsilon$ case. The temperature-density projection shown in figure 7.14 indicates a decreasing density difference between the sh and liquid phases with increasing temperature. In the limit that this difference becomes zero, a maximum in the melting temperature with respect to pressure will be observed. Although preempted in the $A = 0.55\epsilon$ case, this may be realised here.

7.6.1 Liquid-Gas Transition

Fluid Isotherms

Fluid isotherms for the $A = \epsilon$ potential are shown in figure 7.15. The critical temperature is suggested as lying marginally above $T^* = 1.5$ from these plots.

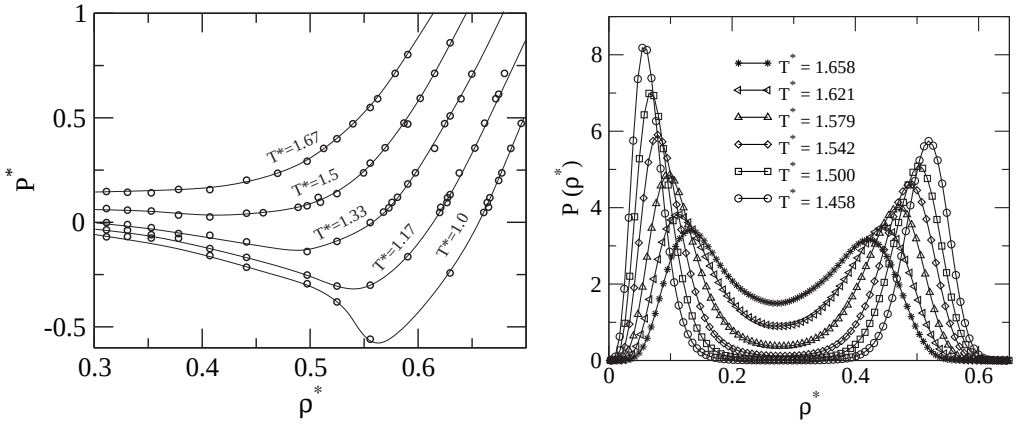

Figure 7.15: *Critical behaviour for the $A = \epsilon$ potential. Isotherms plotted to locate an approximate critical temperature are shown on the left. Number density histograms along the liquid-gas transition for temperature close to the critical point are shown on the right.*

Multi-canonical Monte-Carlo

In fact, a suitable bimodal number density histogram from which to begin the histogram reweighting/multi-canonical sampling procedure was identified at $T^* = 1.671$ when using a chemical potential of μ^*=-14.137. This suggests that the hysteresis effect between $T^* = 2.5$ and the 1.671 is negligible for the system size used in plotting the above isotherms.

From this initial point, stepping along the liquid-vapour coexistence proceeded in steps of $\Delta T^* = -0.008$, other parameters are unchanged from section 7.3.1. The critical parameters are idendified as $T_c^* = 1.680 \pm 0.004$, $\rho_c^* = 0.2716 \pm 0.0005$. The reduced step size has led to a substantial accuracy improvement in the critical density.

Gibbs-Duhem Integration

Below temperatures of $T^* = 1.450$ the probability of traversing the mixed phase region is negligible, and hence the remainder of the curve can be traced using Gibbs-Duhem integration. The vapour pressure is identified at $P^* = 0.067$ at this temperature from a fit to the multi-canonical data. Note that the temperature step used is increased from previous cases to $\Delta T^* = -0.03$ with no loss of accuracy.

7.6.2 Solid

Zero Pressure Isotherm

Again the free energy for all relevant structures has been computed along the zero pressure isotherm up to temperatures of $T^* = 0.600$ in steps of 0.042. With the exception of

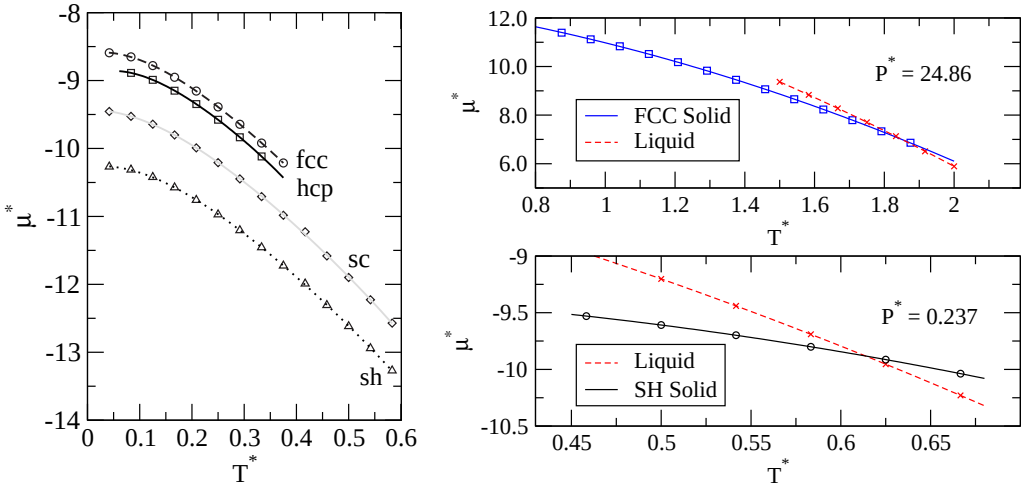

Figure 7.16: *Free energy calculations for the $A = \epsilon$ potential. The zero pressure free energy per atom against temperature is shown on the left for all energetically relevant structures. Location of melting temperatures by free energy calculation are shown on the right for the fcc structure (top) and the sh structure (bottom).*

relaxation times for the thermostat and barostat, all parameters used were identical to previous cases. The resulting chemical potentials are shown in figure 7.16.

With this value of A, the sc structure is now mechanically stable over a wider temperature range. The free energy difference between this and the sh structure is substantially constant with increasing temperature. As the sc structure is of lower density it can be concluded that the effect of positive pressure will increase this difference. The sc structure can therefore never be more than metastable.

The meta-dynamics procedure has identified a number of hybrid structures in which the stacking alternates between sc and sh. A number of sample free energies were computed for these structures. In all cases the values lie part way between the sh and sc energies, indicating that such hybrids are not energetically favourable.

In contrast to smaller A values, the close-packed fcc and hcp structures become mechanically unstable beyond temperatures of approximately $T^* = 0.4$. In addition the two structures are resolved in figure 7.16 with the hcp structure lower in energy. The difference is still however small and may be reversed on applying finite-size corrections. The hcp phase is therefore still neglected in what follows.

As with the $A = 0.55\epsilon$ potential a stable sh-fcc transition is expected, at somewhat larger pressures. A metastable sc-fcc transition under positive pressure is also implied. This would be expected to occur at pressures below the sh-fcc transition due to the smaller free energy difference.

No finite-size corrections have been computed along the zero pressure isobar.

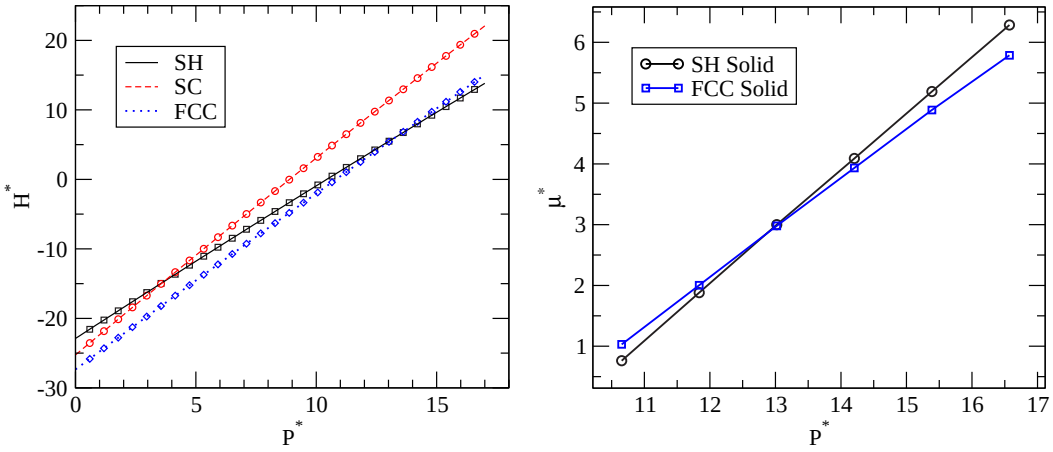

Figure 7.17: *Solid-solid transitions in the $A = \epsilon$ potential. Zero temperature enthalpies for the sc, sh and fcc structures are plotted as a function of pressure on the left. The chemical potential of the sh and fcc structures along the $T^* = 0.292$ isotherm are plotted on the right.*

Solid-Solid Transitions

As with the $A = 0.55\epsilon$ potential, the static sh-fcc transition has been located to indicate a suitable range in which to search at finite temperature. Plots of enthalpy against pressure for the sc, sh and fcc structures are shown in figure 7.17. Enthalpy was optimised at each pressure using CG minimisation. The metastable sc-fcc transition occurs at a pressure of $P^* = 3.63$, with the sh-fcc transition at $P^* = 13.31$.

The sh-fcc transition at finite temperature was located by performing six Einstein crystal calculations for each phase in the pressure range $P^* = 10$ to 17 at a temperature of $T^* = 0.292$. Parameters used for the calculation and finite-size corrections were identical to section 7.5.1. Results are shown in figure 7.17. The transition at this temperature is located at $P^* = 12.86 \pm 0.01$.

The metastable sc-fcc transition has not been explored at finite temperature. It can be expected that each of the hybrid sh-sc states will also undergo a transition to close-packing under pressure. The sh-fcc transition therefore marks the stable boundary of a continuum of meta-stable transitions which terminates at the sc structure.

7.6.3 Melting Curves

Two Phase Simulations

These were conducted for the sh-liquid transition only. Initial conditions were constructed with 332 atoms in the solid phase and 332 in the liquid. The interface was constructed along the $(10\bar{1}0)$ direction. Using NPT simulations of equal length to those previously

used in fcc melting simulations, the melting temperature was identified as lying between $T^* = 0.58$ and 0.63 for pressures up to approximately $P^* = 1$.

In addition, the NPH two-phase method described in section 5.3.1 was found to be useful in this case. With a conserved quantity of $8.2\,\epsilon$/atom, and a volume relaxation time of $t^*_{cell} = 70.0$, the r.m.s. fluctuation in enthalpy is less than $0.05\,\epsilon$/atom at a pressure of $P^* = 0.237$. This compares to a subsequently identified (during Gibbs-Duhem integration) latent heat of 2.16ϵ/atom. The corresponding average temperature in this simulation (at equilibrium) was measured to be $T^* = 0.609 \pm 0.002$. The total simulation length was $100,000$ time-steps of $\Delta t^* = 0.0023$.

This NPH approach has not been successful when applied to the fcc-liquid transition in this or any other parameterisation of the shoulder potential. No combination of simulation parameters which lead to fluctuations in the cell kinetic energy of less than the latent heat per atom can be found in these cases. For the $A = 0.0$, $\epsilon/4$ and $\epsilon/2$ fcc melting at $P^* = 0.047$, the latent heats are $\Delta H^* = -0.965$, 0.646 and 0.604 respectively. These significantly lower values suggest why the approach was not useful.

Free Energy Calculations

As with the $A = 0.55\epsilon$ case the same liquid reference point was used to compute free energies for melting of both structures. A point at $T^* = 1.500$ with $\mu = -12.368$ was taken. Grand canonical Monte-Carlo simulation reveals $\langle N \rangle = 366.1 \pm 0.5$, and $\langle P^* \rangle = 3.59 \pm 0.01$ under these conditions. The simulation length and size is identical to that used for previous liquid reference points. The Helmholtz free energy per atom of the reference point is hence computed as $f^* = -16.99 \pm 0.01$.

Based on the information provided by the two-phase simulations, the sh melting temperature was sought along the $P^* = 0.237$ isobar. Free energies for both phases were computed at points between $T^* = 0.471$ and 0.671 in steps of 0.041. Both solid and liquid free energies were computed as in section 7.5.2. Results are shown in figure 7.16. Interpolation to the intersection provides a melting temperature of $T^* = 0.614 \pm 0.009$ which is in agreement with the result of the two-phase simulations.

The fcc melting temperature has been located at a pressure of $P^* = 24.86$. For the solid phase, free energy calculations employed a longer simulation time of $15,000$ sampled steps after equilibrating for $5,000\,\Delta t$. 30 points along the path to the harmonic crystal were sampled. Other parameters and system sizes were unchanged from section 7.5.2. At pressures in this regime, small differences in density result in large free energy changes. The longer simulation times allowed confirmation that the density identified

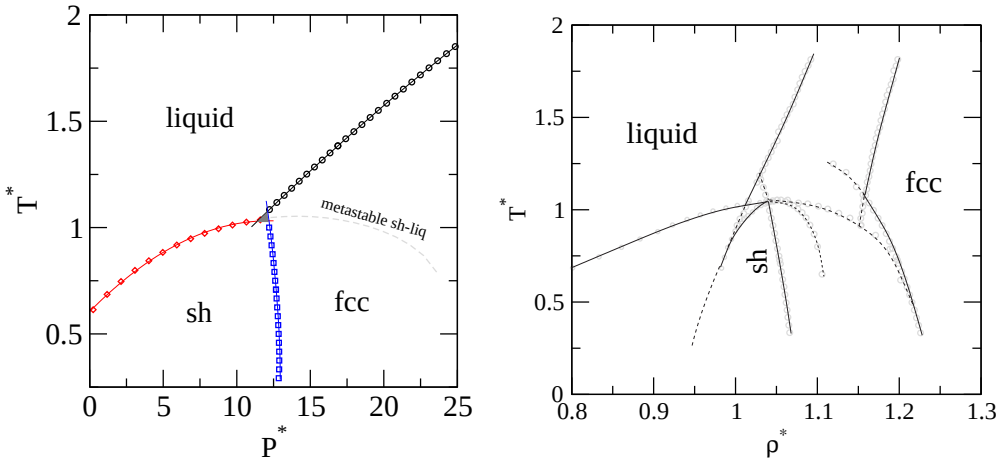

Figure 7.18: *Phase diagram for the potential with $A = \epsilon$ in the region of the sh-fcc-liquid triple point. The pressure temperature projection is shown on the left. The triple point lies within the shaded triangle. Points shown are the three Gibbs-Duhem series described in the text. The temperature density projection is shown on the right. Dashed lines indicate meta-stable continuations of the phase boundaries.*

from Langevin NPT simulations did indeed result in the pressure desired to suitable accuracy. The liquid thermodynamic integration procedure is unchanged from section 7.5.2. The resulting chemical potentials are plotted in figure 7.16 locating the melting temperature at $T^* = 1.851 \pm 0.009$.

As in previous cases, the error on both of these melting temperatures is dominated by the statistical uncertainty in the liquid reference point.

7.6.4 SH-FCC-Liquid Triple Point

As with the $A = 0.55\epsilon$ potential, the three pairs of free energy calculations have been used as starting points for Gibbs-Duhem integration. To ensure long term numerical accuracy in the sh-liquid series (which must now cover more distance to reach the triple point), the time-step for both phases was further optimised to $\Delta t^* = 0.0017$ while keeping the number of sampled time-steps unchanged. Averages are therefore computed over a longer time. The number of equilibration steps for each phase was increased to $10,000$. A temperature step of $\Delta T^* = 0.029$ is used. Similar increases in time-step and equilibration time were made for the fcc-liquid series.

Tracing the melting curve maximum with a positive temperature step is clearly not possible. In this region the inverse of equation 5.25 was integrated to compute melting temperature as a function of pressure. A pressure step of $\Delta P^* = 0.237$ is employed.

For the sh-fcc series, substantial changes were required in the barostat parameter. As dis-

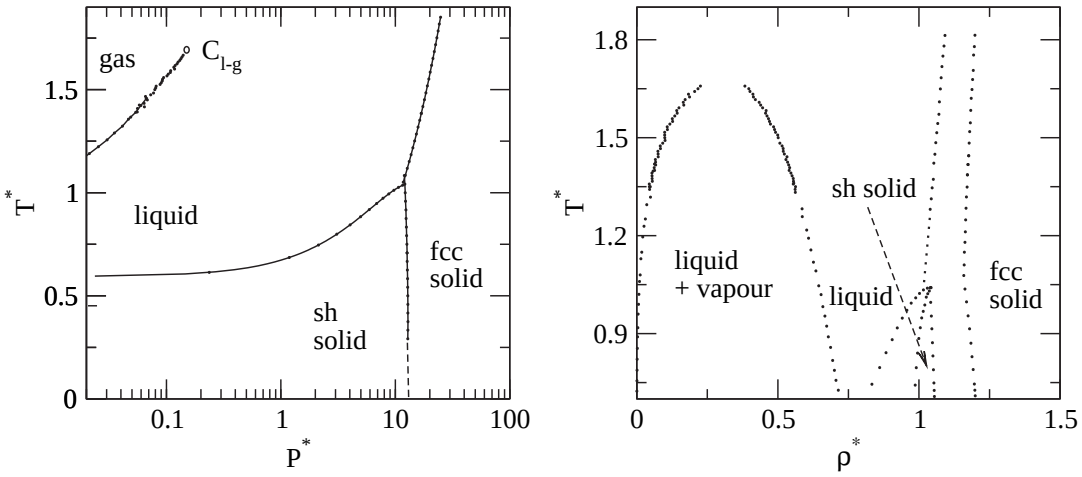

Figure 7.19: *Phase diagram of the $A = \epsilon$ potential in both the pressure-temperature and temperature-density planes. The sh phase now dominates at low pressure. A maximum in the sh melting curve is marginally preempted by the fcc phase. A further increase in critical temperature with A is observed.*

cussed in section 4.6.2 the wide frequency influence of the constant pressure Langevin dynamics scheme can require long volume relaxation times if operated at both low temperature and high pressure. In this case a relaxation time six times longer than used in the $A = 0.55\epsilon$ case is required. The cell does not however decouple from the dynamics and correct sampling is achieved.

System sizes employed are unchanged from the $A = 0.55\epsilon$ case. The resulting three series can be seen explicitly in figure 7.18. Again, any two of the three series can be used to locate the same triple point to within the error of the initial free energy calculations. The triple point is located at $T^*_{tp} = 1.04 \pm 0.01$, $P^*_{tp} = 11.7 \pm 0.2$. The sh melting curve can be traced deep into the fcc region with a large range of metastability. Within this range, a maximum in the melting curve appears at slightly higher pressures than the sh-fcc triple point.

The phase diagram for this value of A is plotted in figure 7.19.

7.7 Phase Behaviour for $A = 3\epsilon/2$

In this potential the sh melting curve may exhibit a maximum in the stable regime. In addition, an isostructural fcc-fcc transition is expected at positive pressure.

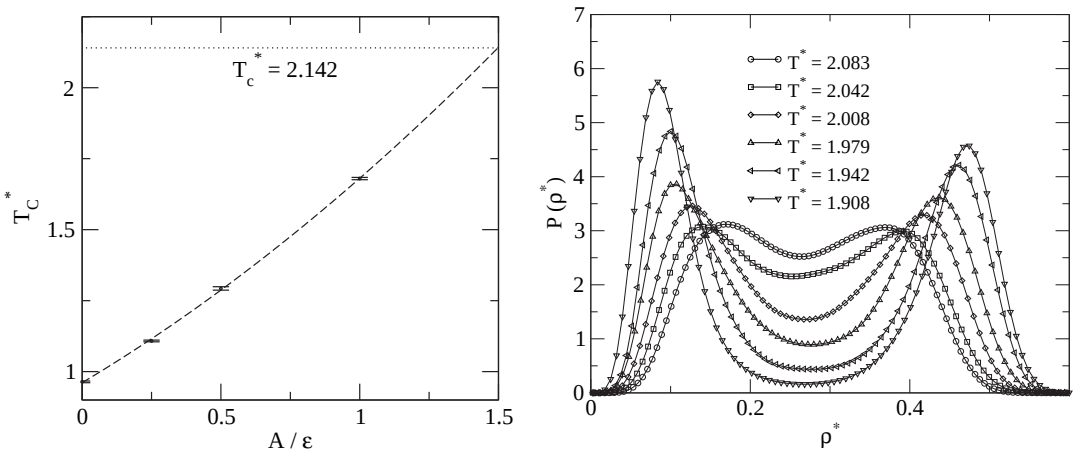

Figure 7.20: *Critical behaviour for the $A = 3\epsilon/2$ potential. The critical temperatures identified for smaller values of A are shown on the left. A quadratic extrapolation to the current A is shown. Histograms resulting from the subsequent reweighting and multi-canonical sampling procedure are shown on the right.*

7.7.1 Liquid-Gas Transition

Extrapolation of Starting Point

Rather than repeat the expensive process of tracing fluid isotherms, a starting point for the multi-canonical sampling procedure was obtained by extrapolation from previous A values. Figure 7.20 shows a plot of critical temperature against A. A quadratic fit to the previously identified critical temperatures yields $T_c^* = 2.142$ when extrapolated to $A = 1.5$.

Multi-canonical Monte-Carlo

Based on this estimate, a suitable bimodal histogram from which to begin tracing the liquid vapour coexistence curve was identified at $T^* = 2.083$ with a chemical potential of $\mu^* = -17.705$. Again a step of $\Delta T^* = -0.008$ was employed to trace the coexistence curve to temperatures of 1.867. Extrapolation of the resulting data to zero density difference yields a critical temperature of $T_c^* = 2.12 \pm 0.04$. The large uncertaintly reflects a significant deviation from the 3D Ising exponent in the three-parameter fit. The critical density is identified as $\rho_c^* = 0.265 \pm 0.002$.

7.7.2 Metastable FCC-FCC Transition

Zero Temperature

The isostructural transition was first located at zero temperature using conjugate-gradient enthalpy minimisation. A system size of 256 atoms was used for both fcc phases, optimising at pressures between $P^* = 0.237$ and $P^* = 2.37$ in steps of 0.12. The resulting enthalpy per atom for both phases is shown in figure 7.21. The intersection reveals a transition pressure of $P^* = 1.09$. Note that above $P^* = 1.4$ the lower density phase collapses to the higher density structure during optimisation, indicating mechanical instability.

Finite-Temperature

To locate the transition at finite temperature, free energy calculations were performed for both phases along the $T^* = 0.208$ isotherm. Pressures employed matched the zero temperature case. Suitable densities for the Einstein crystal procedure were identified from $100,000\,\Delta t$ constant pressure Langevin dynamics simulations following $10,000\,\Delta t$ equilibration periods. The timestep used was $\Delta t^* = 0.0012$, and the system size was 256 atoms for both phases.

Subsequent free energy calculations at the identified densities employed 24 points along the path to an Einstein crystal. The free energy derivative at each point was averaged over $3,000\,\Delta t$ after equilibrating for $2,000$. As in all other cases the optimal spring constant was identified from parallel simulations of $10,000\,\Delta t$. The time-step is unchanged from the NPT calculations. Finite-size corrections were computed by employing system sizes of 256, 500 and 864 atoms. The chemical potentials derived from these free energies are plotted in figure 7.21, locating the transition pressure for this temperature as $P^* = 1.27$. As with sh-fcc transitions the error on this value is small, being approximately 0.01.

Gibbs-Duhem Integration

The isostructural transition predicted by Scala *et al.* has now been identified as fcc-fcc at low temperature. If this is to generate a density anomaly via the second critical point hypothesis of Mishima and Stanley, then it must extend directly into the supercooled liquid. To locate the extent of the fcc-fcc transition, Gibbs-Duhem integration has been employed with a temperature step of $\Delta T^* = 0.03$ in the direction of increasing temperature. Simulation lengths matched those used to good effect in the sh-fcc transitions traced above. 500 atoms were used in each phase.

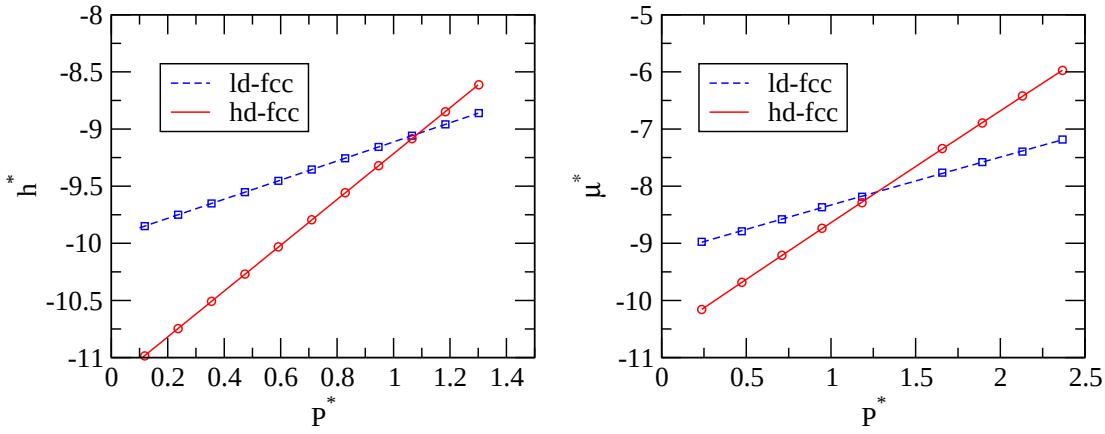

Figure 7.21: *Metastable isostructural transition in the $A = 3\epsilon/2$ potential. The enthalpy per atom at zero temperature is plotted on the left for low and high density fcc phases. The results of free energy calculations along the $T^* = 0.21$ isotherm are shown on the right.*

The resulting series indicates an increase in transition pressure with increasing temperature. However, after just six steps the lower density fcc phase becomes mechanically unstable. At this point a large density difference between the two phases still exists. The isostructural transition does *not* end in a critical point, but terminates at the low density fcc spinodal line.

The location of this line in relation to the limit of supercooled liquid metastability will be examined in the next chapter.

7.7.3 SH-FCC Transition

This was identified by the same procedure as the $A = \epsilon$ case. The zero temperature transition is located by CG enthalpy minimisation at $P^* = 25.27$. The transition along the $T^* = 0.208$ isotherm was then determined by computing the free energy of both phases at ten pressures between $P^* = 23.67$ and $P^* = 26.04$.

In computing densities at each of these pressures, the low-temperature high-pressure limitations of the constant pressure Langevin dynamics methods was reached. No suitable relaxation time for the barostat could be identified which did not disrupt the particle motions, or result in cell decoupling. Instead, the Nosé-Hoover method was used with separate five-thermostat chains on each degree of freedom. Other parameters and system sizes used for the Einstein crystal calculations are unchanged from section 7.6.2. As plotted in figure 7.22, the transition is located at $P^* = 25.17$. The estimated error in this pressure is approximately 0.01.

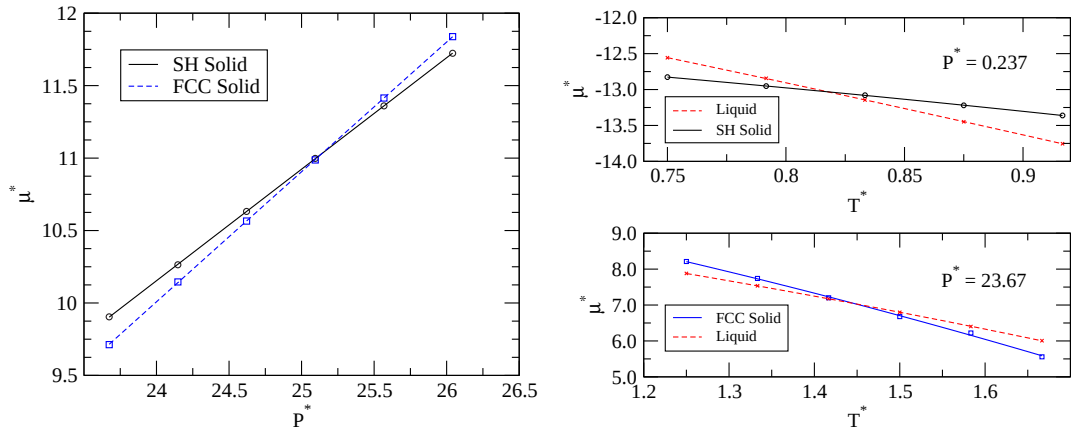

Figure 7.22: *Free-energy calculations for the $A = 3\epsilon/2$ potential. The chemical potential of the sh and fcc phases along the $T^* = 0.208$ isotherm are shown on the left. Results of free energy calculations used to locate melting temperatures are shown on the right for the sh and fcc structures at $P^* = 0.237$ and 23.67 respectively.*

7.7.4 Melting Curves

The sh and fcc melting temperature were sought along the $P^* = 0.237$ and 23.67 isobars respectively. No two-phase simulations were performed in this case. A suitable range over which to perform free energy calculations was estimated from trends in earlier data. A reference point at $T^* = 1.500$ with $\mu = -12.368$ was used in computing the liquid free energies along both isobars. Grand canonical Monte-Carlo simulation provides $\langle N \rangle = 415.6 \pm 0.5$, and $\langle P^* \rangle = 4.52 \pm 0.01$, leading to a Helmholtz free energy per atom of $f^* = -20.79 \pm 0.04$. Thermodynamic integration from this reference point to the isobars of interest employed parameters unchanged from section 7.6.3 as did the solid free energy calculations.

The resulting chemical potential along each isobar is shown in figure 7.22. The sh melting temperature is located at $T^* = 0.80$, with the fcc melting at $T^* = 1.45$. In both cases the uncertainty is approximately 0.01. As with all other melting points, this is dominated by statistical error in the liquid reference free energy.

7.7.5 SH-FCC-Liquid Triple Point

Gibbs-Duhem series for the sh-fcc, sh-liquid and fcc-liquid transitions have been computed to trace the remainder of the phase diagram. Simulation lengths, parameters and systems sizes were unchanged from the three-series traced in section 7.6.4, with the exception that Nosé-Hoover chains were used for the low temperature portion of the sh-fcc transition. As in the previous case, any two of the three curves indicate a triple point, the

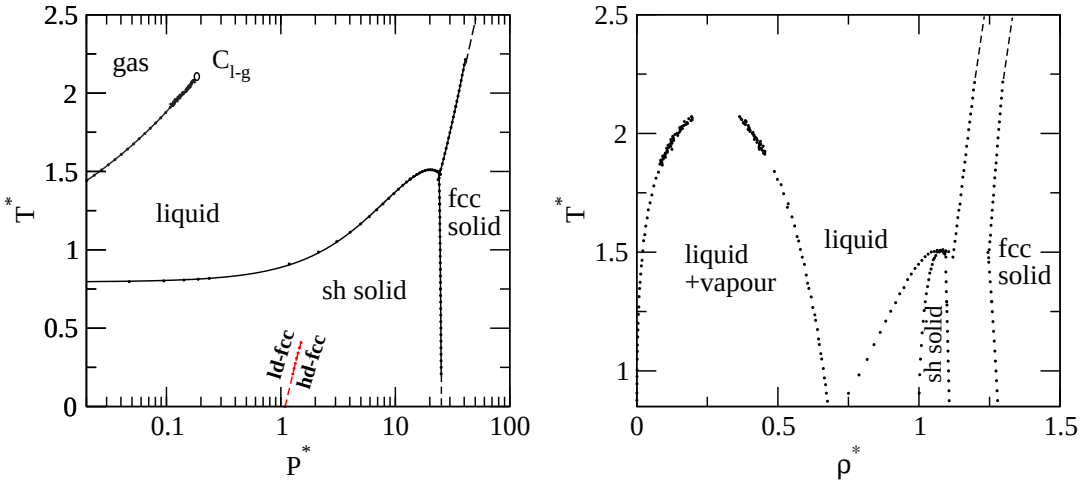

Figure 7.23: *Phase diagram of the $A = 3\epsilon/2$ potential. The pressure-temperature projection in shown on the left, with the temperature density projection on the right. The maximum in the sh melting curve is clearly visible.*

location of which is confirmed by the third to within the error of the initial free energy calculations. The triple points lies at $T^* = 1.48 \pm 0.01$, $P^* = 24.3 \pm 0.1$.

As can be seen in figure 7.23, the sh melting curve maximum now lies within the stable regime. The fcc melting curve intersects at slightly higher temperature. There is hence a small range visible in both the temperature-pressure and temperature-density projections for which melting is reentrant. The metastable fcc-fcc transition is also plotted in figure 7.23. The termination of this lies well below the thermodynamic melting temperature.

7.8 Summary

Here, the observed trends in phase behaviour on increasing A with w and r_0 fixed at the values employed above are summarised. For comparison purposes, the phase diagrams of all four potentials are plotted together in figure 7.24

The liquid-gas critical temperature has been seen to increase quadratically with increasing A. The pressure of the critical point also increases. No evidence of a thermodynamically stable liquid-liquid phase transition has emerged. In particular data from Gibbs-Duhem integration reveals that density is continuous along the liquid side of all melting and vaporisation curves. In addition no third fluid peak has emerged during multi-canonical sampling. A stable LLPT must meet either the melting or vaporisation curves at a triple point and can hence be ruled out.

As A is initially increased, the fcc melting temperature is found to reduce, perhaps contrary to the expected behaviour. This decrease in melting temperature can be understood

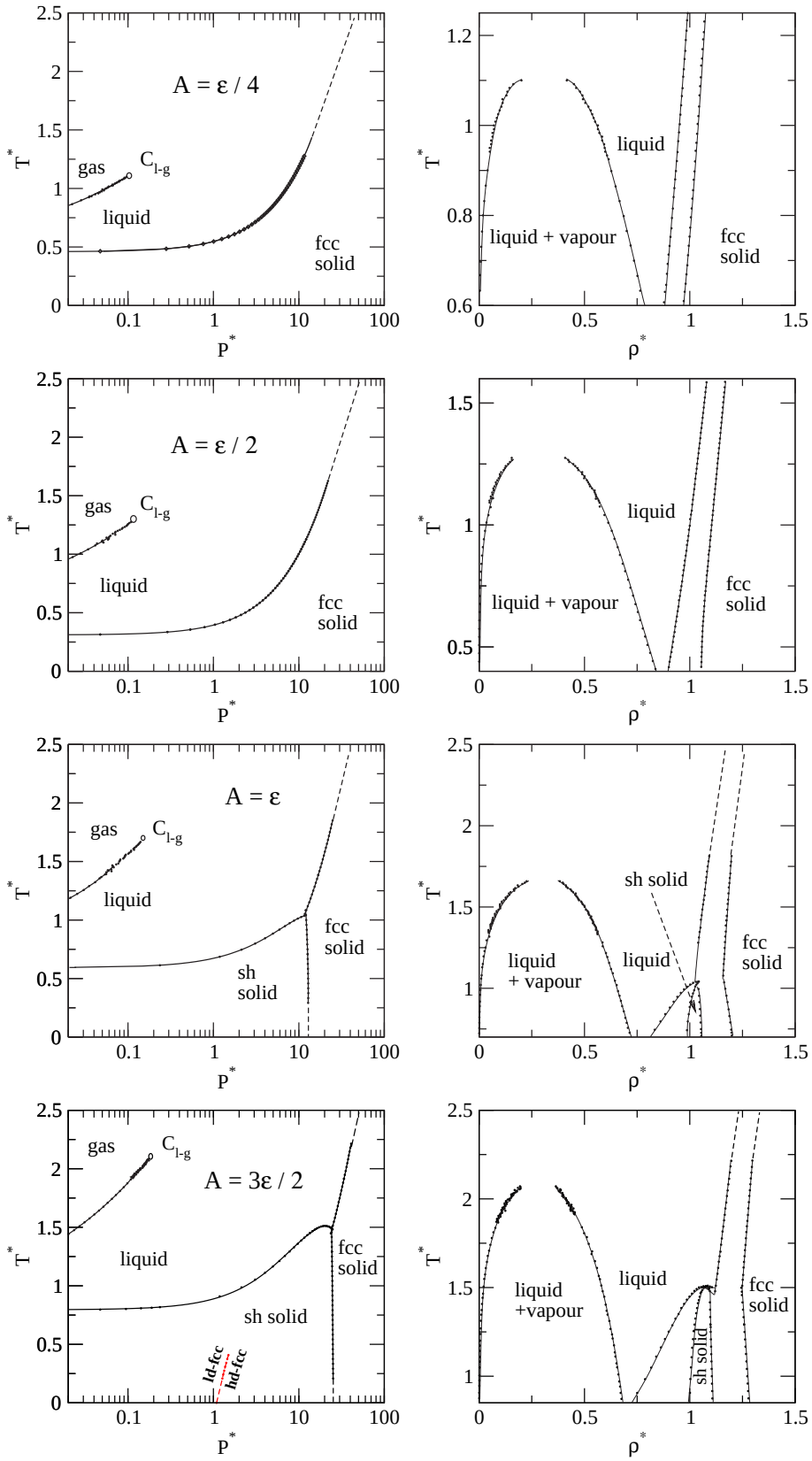

Figure 7.24: *Complete sequence of phase diagrams in the $P - T$ (left) and $\rho - T$ planes (right). The depth of the outer well A increases from top to bottom.*

by examining figure 7.1. For A values in this region, the effect of the Gaussian is to widen the existing Lennard-Jones minimum. This allows larger fluctuations about equilibrium lattice positions for a given temperature. The well known empirical rule of Lindemann (Lindemann, 1910) states that melting will occur when the root-mean-square fluctuation is $\sim 15\%$ of the nearest neighbour distance. This will occur at lower temperatures for wider potential wells.

As the Gaussian outer minimum becomes distinct from the Lennard-Jones minima, the simple hexagonal structure becomes lower in energy. The expected transition to fcc under pressure has been observed and is seen to intersect the melting line. The resulting simple hexagonal melting temperature increases with increasing A. The pressure of the sh-fcc transition increases with increasing A, as expected from the larger enthalpy difference.

It has also been seen that the sh structure exhibits a maximum melting temperature, which for larger A values is manifested in the thermodynamically stable regime. In the following chapter the liquid will be studied in the region of this maximum.

The predicted isostructural transition has been observed for the fcc structure only. Although two energy minima are also observed for sc symmetry (figure 7.2), the higher energy structure is not mechanically stable when the atoms are permitted to move away from lattice sites. The fcc-fcc transition does not approach the melting line. The possibility of this occurring with alternative parameterisations is investigated in the following chapter.

The two dominant sources of error in this study are the finite-size error in the solid and the statistical error associated with computing a liquid reference point for thermodynamic integration. The former has been largely corrected for by repeating calculations with larger system sizes. The latter dominates over the liquid finite-size error, but has been controlled to an acceptably low level. All phase boundaries shown in figure 7.24 can be considered accurate to within temperatures of $\Delta T^* = \pm 0.05$ and pressures of $\Delta P^* = \pm 0.1$.

Chapter 8

Exploration of Unusual Phase Behaviour

The four phase diagrams computed in the previous chapter, combined with that of the Lennard-Jones potential in appendix A provide valuable insight. The progression of phase behaviour on increasing the outer well depth A is now known at *fixed* position and width parameters r_0 and w. No evidence of a thermodynamically *stable* liquid-liquid phase transition has emerged. The possibility of liquid anomalies, in particular a density anomaly, has not yet been investigated. In section 6.2 two suggested mechanisms for generation of liquid anomalies (based on 2D simulations) were reported. These are

1. A *metastable* liquid-liquid phase transition in the supercooled regime.
2. Formation of solid clusters close to the melting line in regions where the solid is of lower density than the liquid.

An isostructural fcc-fcc transition has been identified at large A. If both of the phases involved are metastable at temperatures within the supercooled liquid, (i.e. above the glass temperature), then heating beyond their respective spinodal lines may generate liquids of differing density and hence a metastable liquid-liquid phase transition. Such behaviour would be consistent with the predictions of Scala *et al.* and relevant to supercooled water.

Our aims for this chapter are therefore as follows. First in section 8.1, the isostructural transition mapped in section 7.7 will be studied in more detail. In particular it will be determined if this reaches the supercooled liquid and if so, if supercooled liquids of two different densities are generated. This process will involve identification of the glass temperature. With this known, the possibility of generating high and low density amorphous phases arises, which may also be relevant to a supercooled liquid-liquid transition.

The choice of r_0 and w employed in chapter 7 was essentially arbitrary. The extent of the isostructural phase transition may be increased by altering these parameters, or by further tuning of the depth parameter A. This will be investigated in section 8.2.

A pressure region in which the solid is of lower density than the solid exists for the three-dimensional potential when $A = 3\epsilon/2$. The liquid in this region will be probed for anomalies in section 8.3.

8.1 Isostructural Phase Transition

In this section the properties of the fcc-fcc transition mapped in section 7.7 ($A = 3\epsilon/2$) are considered in greater detail. In particular the low density spinodal line and the relative location of the glass transition, i.e. the limit of metastability for the supercooled liquid.

8.1.1 LD-FCC Spinodal Line

This has been mapped in the pressure-temperature plane. The mechanical stability at each temperature and pressure is determined using a constant pressure Langevin dynamics simulation of 256 atoms over $50,000$ time-steps of $\Delta t^* = 0.0012$. Each simulation was initialised in the ld-fcc state. Those which remained in this structure over the simulation length were marked as mechanically stable. Temperatures and pressures sampled in this fashion are shown in figure 8.1. The spinodal line is drawn between the regions of metastability and instability. The limiting factor to progression of the isostructural transition into the supercooled liquid is therefore the stability of the low density phase.

8.1.2 Glass Transition

The glass transition marks the lower temperature limit of metastability for the supercooled liquid. Below this temperature atoms freeze into an amorphous glassy solid. Experimentally, the transition can be located by plotting the specific volume as a function of decreasing temperature in the supercooled liquid. This exhibits a discontinuity in slope at the glass transition. The temperature at which this occurs is however dependent on cooling rate, hence glass formation is not a true thermodynamic phase transition.

Application of this criteria to computer simulation requires non-equilibrium molecular dynamics methods to ensure an equal cooling rate is used to reach all temperatures. An alternative method has been proposed by Wendt and Abraham (1978). This is based on

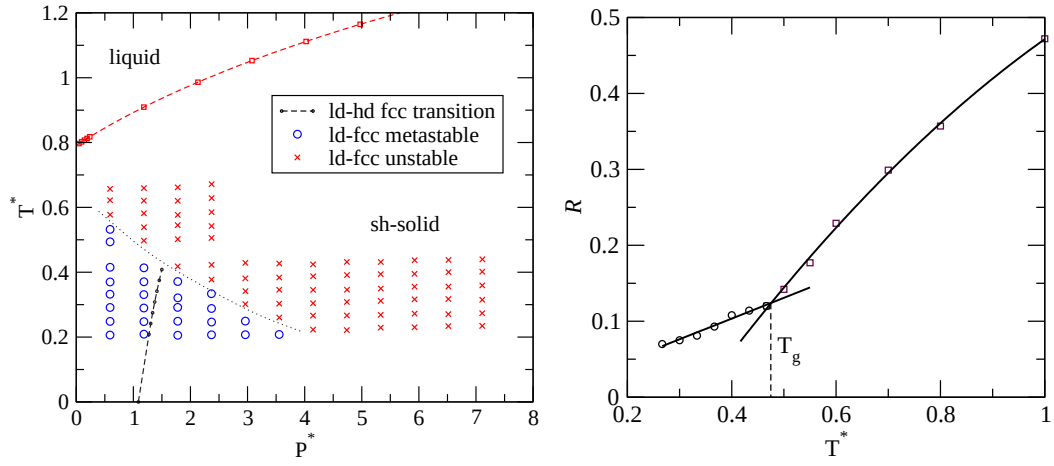

Figure 8.1: *Limits of metastability relevant to the fcc-fcc transition. The left hand plot shows the identification of the ld-fcc spinodal line. The glass temperature along the $P^* = 1.50$ isobar is identified via the method of Wendt and Abraham in the right hand plot.*

characteristics of the pair-correlation function $g(r)$ at a series of equilibrium simulations in the metastable liquid and glassy states. The pair correlation function is defined as

$$g\left(r\right) = \frac{1}{4\pi r^2 \rho N} \left\langle \sum_{i=1}^{N} \sum_{j \neq i} \delta(r - r_{ij}) \right\rangle , \tag{8.1}$$

which was met briefly in chapter 5. It gives the ensemble averaged distribution of pair distances r_{ij}. It is easily calculated from either a molecular dynamics or Monte-Carlo simulation in the ensemble of interest. Wendt and Abraham define the quantity R as the ratio of the first minimum in $g(r)$ to the first maximum. This is a convenient function of local structure which varies more rapidly with temperature in the liquid than the glass. The transition is located at a discontinuity in the slope of R with respect to temperature.

Using this methodology, the location of the glass transition for the current potential was determined along the $P^* = 1.50$ isotherm. Data for the calculation of $g(r)$ were obtained using constant pressure Langevin dynamics simulation. Each simulation was initialised with a random configuration of 500 atoms subject to the condition that no two atoms are separated by less than 0.85σ. This was equilibrated for $10,000\,\Delta t$ before accumulating statistics over a further $40,000\,\Delta t$. Temperatures in the range $T^* = 0.267$ to 1.00 were studied. The values of R obtained from the resulting pair-correlation functions are shown in figure 8.1. The glass temperature is identified as approximately $T_g^* = 0.47$.

Plots of $g(r)$ in the glass region show significant peaks at both the Lennard-Jones minimum, and at r_0. Attempts have been made to create a low density glass by randomly placing atoms in a simulation cell subject to the condition that no two atoms are less than $0.99r_0$ apart. Simulation of these configurations at temperatures below the glass temper-

ature have been conducted over pressures in the range $P^* = 0$ to 0.5. In all cases the system collapses to the same high density glass observed in figure 8.1. If the density is constrained at that of the ld-fcc phase or larger, the system cavitates and exhibits negative pressure. This indicates that no stable low density amorphous phase exists in which the nearest neighbour distance is r_0. A large degree of crystalline order is required to stabilise low density phases.

These results show that the fcc-fcc transition does not extend into the supercooled liquid region. The distance between the ld-fcc spinodal line and the glass temperature is however small. Small changes in the pair-potential may therefore allow the isostructural transition to reach the supercooled liquid. The conjecture that this will generate a liquid-liquid phase transition can then be investigated.

8.2 Adjustment of A, r_0 and w

8.2.1 Free Energy Derivatives

In this section the effect of changing the parameters A, r_0 and w on the Gibbs free energy of the phases involved is investigated. By comparing the magnitudes of free energy derivatives with respect to these parameters, their relative importance in determining stability can be assessed.

Evaluation

First, consider the parameter A. The specific Gibbs free energy is written

$$g = -\frac{k_B T}{N} \ln \Delta \tag{8.2}$$

with

$$\begin{aligned} \Delta &= \frac{1}{V_0 N! h^{3N}} \int_0^\infty \int_{-\infty}^\infty \int_{D(V)} \mathrm{d}\mathbf{r}^N \mathrm{d}\mathbf{p}^N \mathrm{d}V \exp\left[-\beta\mathcal{H} - \beta P\mathcal{V}\right] \\ \Delta &= \frac{1}{V_0 N! \Lambda^{3N}} \int_0^\infty \int_{D(V)} \mathrm{d}\mathbf{r}^N \mathrm{d}V \exp\left[-\beta U - \beta P\mathcal{V}\right]. \end{aligned} \tag{8.3}$$

as defined in sections 2.2.3 and 2.4.3. The derivative of interest is

$$\left.\frac{\partial g}{\partial A}\right|_{NPT} = -\left(\frac{k_B T}{N}\right) \frac{1}{\Delta} \left.\frac{\partial \Delta}{\partial A}\right|_{NPT}. \tag{8.4}$$

The parameter A appears in the NPT partition function Δ only through the potential energy U, and hence

$$\begin{aligned}\frac{1}{\Delta}\left.\frac{\partial\Delta}{\partial A}\right|_{NPT} &= \frac{1}{\Delta}\left(\frac{1}{V_0 N!\Lambda^{3N}}\right)\int_0^\infty\int_{D(V)} \mathrm{d}\mathbf{r}^N \mathrm{d}V \frac{\partial}{\partial A}\exp\left[-\beta U - \beta P\mathcal{V}\right] \\ &= -\frac{1}{\Delta}\left(\frac{1}{V_0 N!\Lambda^{3N}}\right)\int_0^\infty\int_{D(V)} \mathrm{d}\mathbf{r}^N \mathrm{d}V \beta\left(\frac{\partial U}{\partial A}\right)\exp\left[-\beta U - \beta P\mathcal{V}\right]\end{aligned} \tag{8.5}$$

which can be identified from equation 2.18 as an ensemble average,

$$\frac{1}{\Delta}\left.\frac{\partial\Delta}{\partial A}\right|_{NPT} = -\beta\left\langle\frac{\partial U}{\partial A}\right\rangle_{NPT}. \tag{8.6}$$

Equation 8.4 then becomes

$$\left.\frac{\partial g}{\partial A}\right|_{NPT} = \frac{1}{N}\left\langle\frac{\partial U}{\partial A}\right\rangle_{NPT}. \tag{8.7}$$

The potential energy U is written as a pair potential,

$$U = \sum_{i=1}^{N}\sum_{j>i}^{N}\phi_{LJ} - A\exp\left[-w\left(r_{ij}-r_0\right)^2\right] \tag{8.8}$$

where ϕ_{LJ} is the Lennard-Jones potential. Hence the free energy derivative becomes

$$\left.\frac{\partial g}{\partial A}\right|_{NPT} = -\frac{1}{N}\left\langle\sum_{i=1}^{N}\sum_{j>i}^{N}\exp\left[-w\left(r_{ij}-r_0\right)^2\right]\right\rangle_{NPT}. \tag{8.9}$$

The ensemble average can be written in terms of the pair correlation function,

$$\left.\frac{\partial g}{\partial A}\right|_{NPT} = -\rho\int_0^\infty 4\pi r^2 g(r)\exp\left[-w\left(r_{ij}-r_0\right)^2\right]dr \tag{8.10}$$

where $g(r)$ is evaluated in the NPT ensemble. Similarly, for the parameters w and r_0,

$$\left.\frac{\partial g}{\partial w}\right|_{NPT} = A\rho\int_0^\infty 4\pi r^2 g(r)\left(r_{ij}-r_0\right)^2\exp\left[-w\left(r_{ij}-r_0\right)^2\right]dr, \tag{8.11}$$

and

$$\left.\frac{\partial g}{\partial r_0}\right|_{NPT} = -2Aw\rho\int_0^\infty 4\pi r^2 g(r)\left(r_{ij}-r_0\right)\exp\left[-w\left(r_{ij}-r_0\right)^2\right]dr. \tag{8.12}$$

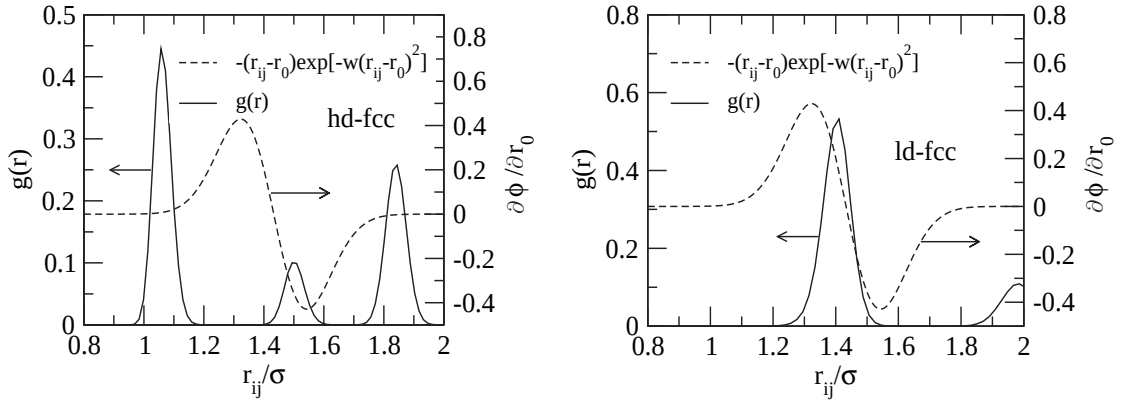

Figure 8.2: *Free energy derivatives with respect to r_0. The pair correlation function $g(r)$ and $\partial\phi/\partial r_0$ are shown for both the high density (left) and low density (right) fcc structures. The integral over the product of the two functions is clearly of opposite sign in each case.*

Behaviour

Several observations can be made from the above derivatives without numerical calculation. The value of equation 8.10 is always negative. Increasing the A parameter will always lower the Gibbs free energy regardless of structure. The rate of decrease is largest for structures with larger peaks in $g(r)$ close to r_0. This is consistent with the increasing favourability of open structures as observed in chapter 7 which was explained in terms of zero temperature energies and nearest neighbour distances. Note that the free energy derivative is independent of A itself. Increasing A is unlikely to significantly change $g(r)$ for a given structure, suggesting that the free energy as a function of A is approximately linear.

Equation 8.11 will always be positive for $A > 0$. Increasing w narrows the width of the outer well in the pair-potential, limiting the area of phase-space accessible at a given energy and therefore lowering entropy. The decrease in free energy on widening the outer well also favours open structures. As w decreases, the spread of r_0 values that contribute to equation 8.11 increases. The rate of free energy decrease is therefore expected to increase with increasing w.

The value of equation 8.12 combines both positive and negative contributions. Pair separations r_{ij} close to but less than r_0 act to increase the free energy. Separations larger than r_0 lead to free energy decreases. Any peaks in $g(r)$ at r_0 are expected to move as r_0 is varied. The free energy gradient arising from such peaks is therefore approximately constant as r_0 changes. However, structures such as the higher density fcc contain dominant contributions from peaks close to σ. The effect on the free energy derivative of these neighbour distances will increase as r_0 is moved towards σ.

Plots of $g(r)$ for both the low and high density fcc structures are shown in figure 8.2

with $\partial\phi/\partial r_0$ superimposed. These were calculated at a temperature of $T^* = 0.308$ and pressure $P^* = 1.374$ which lies on the isostuctural transition. Simulations employed $10,000$ equilibration steps, with $g(r)$ computed over a further $40,000$ steps. A time-step of $\Delta t^* = 0.0017$ was employed. It can be seen that the total contribution to the free energy derivative will be negative for the high-density structure, and positive in the low density case. The effect of *decreasing* r_0 will therefore increase the free energy of ld-fcc, while simultaneously decreasing that of hd-fcc. As changes in either w or A can only change both free energies in the same direction, the parameter r_0 seems the most promising for inducing significant changes in the location of the fcc-fcc transition. Despite this, differences between the free energy gradients of the two phases with respect to A and r_0 cannot be discounted.

8.2.2 Tracing Phase Boundaries

Given the derivatives 8.10, 8.11 and 8.12, it is possible to compute (for any phase) free energy differences due to changes in A, r_0 and w using thermodynamic integration. The free energies computed in chapter 7 (or the free energy of the Lennard-Jones system) can be used as reference points. For example

$$G^{A_2}(N,P,T) = G^{A_1}(N,P,T) + \int_{A_1}^{A_2} \left.\frac{\partial G}{\partial A}\right|_{NPT} dA. \tag{8.13}$$

This requires computing the free energy derivatives as ensemble averages over a series of points between two parameterisations for each temperature and pressure. The intersection of free energies is then used to locate new phase boundaries. This requires considerable computational effort, not substantially less than needed to compute the phase diagram of a new parameterisation from scratch.

The above method can only be used if a reference point exists for the phase in question. This limits the exploration of parameter space to small changes in A, r_0 and w where it can be safely assumed that no new phases emerge. The application of thermodynamic perturbation theory may therefore be of use. Here the first-order correction to the free energy due to a perturbation in the Hamiltonian of $\Delta\mathcal{H}$ is computed as the ensemble average $\langle\Delta\mathcal{H}\rangle$ over the unperturbed system. In the case of a pair-potential, this can be evaluated from $g(r)$ with minimal computation. The data for $g(r)$ in the unperturbed system has already been accumulated in chapter 7. Despite being essentially 'free' this correction is not exact, and will require evaluating at many state points to locate intersections in the free energy of two phases.

A more desirable approach is to directly trace the phase transition along a path in parame-

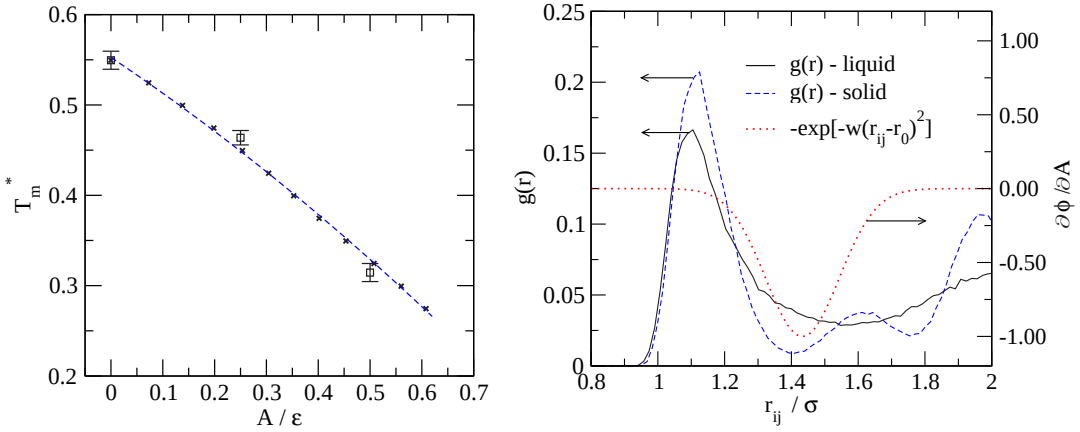

Figure 8.3: *Variation in fcc melting temperature with A. The Gibbs-Duhem series initialised from the $A = 0$ (Lennard-Jones) melting temperature at $P^* = 0.047$ is shown in comparison with results from explicit free energy calculations in the left. The right hand plot shows $g(r)$ for the liquid and solid along with the functional form of $\partial G/\partial A$ at the initial point.*

ter space. A generalised Gibbs-Duhem methodology, such as that employed by Vega *et al.* (2005) is ideally suited to this task. The total change in Gibbs free energy upon changing pressure, temperature and some parameter λ (representing A, w or r_0) by infinitesimal amounts is

$$dG = -SdT + Vdp + Xd\lambda, \tag{8.14}$$

where $X = \partial G/\partial\lambda$. At constant pressure, a step along the phase-boundary in the $\lambda - T$ plane requires that

$$-S_\alpha dT + X_\alpha d\lambda = -S_\beta dT + X_\beta d\lambda \tag{8.15}$$

where α and β denote the two phases involed. This leads to a generalised Clausius-Clapeyron equation

$$\left.\frac{\partial\lambda}{\partial\beta}\right|_{N,P} = -\frac{\Delta H}{\beta\Delta X} \tag{8.16}$$

where $\Delta X = X_\alpha - X_\beta$. Similarly, at constant pressure

$$\left.\frac{\partial\lambda}{\partial P}\right|_{N,T} = -\frac{\Delta V}{\beta\Delta X}. \tag{8.17}$$

To trace phase boundaries as a function of A, w and r_0, the relevant derivative X is given by equations 8.10 to 8.12. The resulting Clausius-Clapeyron equations can be numerically integrated with minor modifications to the tools employed in tracing P-T phase boundaries (see section 5.5.2). This methodology can be used to confirm trends observed in the previous chapter, such as the decrease in fcc melting temperature on increasing A. Beginning from the force-shifted Lennard-Jones melting temperature identified in appendix A, the melting temperature at $P^* = 0.047$ can be traced as a function of A. Results of

this procedure are shown in figure 8.3. A fixed step in temperature of $\Delta T^* = -0.025$ is used in the Runge-Kutta integration. Equation 8.16 is computed at each step using 500 atom constant pressure Langevin dynamics simulations. Enthalpy and $\partial G/\partial A$ are averaged over $20,000$ time-steps of $\Delta t^* = 0.0017$ following a $10,000\,\Delta t$ equilibration period. Integration error was checked by tracing the reverse series and found to be negligible.

When initialised in the centre of the Lennard-Jones error-bar, agreement with the explicit free energy calculations is obtained. It can be expected that using the top or bottom of the Lennard-Jones error bar will result in a series which passes though one of the other points. The functional form of $\partial G/\partial A$ is also shown in figure 8.3 along with g(r) for the solid and liquid phases on the Lennard-Jones melting line. This indicates via equation 8.10 that the free energy of the liquid will decrease faster than the solid on increasing A, explaining the observed decrease in melting temperature.

8.2.3 Melting Curves

The effect of A, w and r_0 on the sh melting temperature must be considered if the isostructural transition is to be extended into the supercooled liquid. The influence of the A parameter was effectively determined in the previous chapter, leaving the effect of w and r_0 to be traced.

The pressure dependence of the sh melting temperature is approximately linear in the region of the isostructural transition. Changes in this temperature will therefore be computed at a single pressure with the expectation that the same constant shift will apply to all pressures of interest.

Gibbs-Duhem series have been traced in the $T - w$ and $T - r_0$ planes. In each case the value of A is fixed at $3\epsilon/2$. Each series is initialised from the melting line traced in section 7.7 at the point $T^* = 0.80$, $P^* = 0.237$, with parameters $w = 41.22\sigma^{-2}$ and $r_0 = 1.433\sigma$. System sizes of 642 atoms are used for each phase.

w Parameter

Integration of equation 8.16 employed a step size of $\Delta T^* = 0.02$. Separate series were employed for integration in the direction of increasing and decreasing temperature. At each step the relevant free energy derivatives for each phase were computed from simulations of $50,000\,\Delta t$ following equilibration for $10,000\,\Delta t$. A time-step $\Delta t^* = 0.0017$ was employed. The resulting melting curve in the $T - w$ plane is shown in figure 8.4. The entire range of stability for the sh phase is shown. Above and below the range plotted the

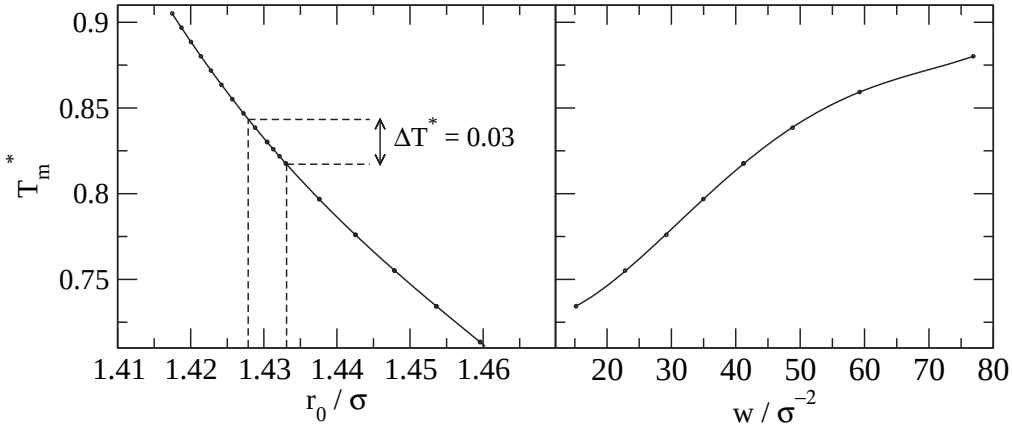

Figure 8.4: *Variation of sh melting temperature with r_0 (left) and w (right) at $P^* = 0.237$. The range of r_0 shown is that relevant to the isostructural transition. For w the entire range over which the sh structure is stable at the melting line is shown.*

sh structure is mechanically unstable at the predicted melting temperature. Both series were reversed to check for integration errors, which were found to be negligible.

r_0 Parameter

The equivalent curve for the r_0 parameter was traced in the same fashion, employing a step size of $\Delta T^* = 0.008$ in the positive direction and $\Delta T^* = -0.02$ in the negative. Larger step sizes in the positive direction produced an irreversible series, implying excessive integration error. The two series are also shown in figure 8.4. The sh structure remains stable at the melting line beyond the range of r_0 shown.

8.2.4 Influence of A on Isostructural Phase Transition

Decreasing A is known to lower the sh melting temperature and may therefore allow the fcc-fcc transition to reach into the supercooled liquid. An initial point at $T^* = 0.308$, $P^* = 1.274$ was used for the Gibbs-Duhem integration. This lies on the isostructural transition plotted in figure 8.1. Initially the transition temperature was mapped as a function of A using a step size of $\Delta T^* = 0.025$. Free-energy derivatives at each step were computed using $60,000\,\Delta t$ constant pressure Langevin dynamics simulations, following a $10,000\,\Delta t$ equilibration period. A time-step of $\Delta t^* = 0.0017$ was employed, with 500 atoms in each phase. The limit of ld-fcc metastability was encountered after three-steps, corresponding to a decrease in A of 0.034ϵ. The transition pressure was then mapped (from the same initial point) as a function of A using a step $\Delta P^* = -0.12$. Simulation lengths and sizes used were unchanged from the temperature series. The limit of ld-fcc stability was reached in 10 steps, corresponding to a change in A of -0.426ϵ.

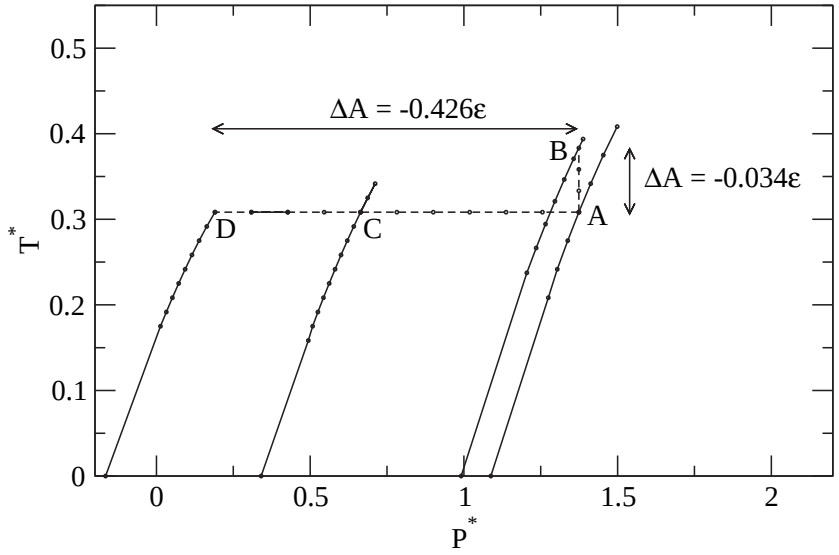

Figure 8.5: *Location of isostructural transition on decreasing the outer well depth. Two Gibbs-Duhem series are initialised from point A. The first traces the transition as a function of temperature up to the point B. The second traces the transition as a function of pressure, through the point C to D. Beyond B and D the ld-fcc phase is mechanically unstable. Gibbs-Duhem series in the $P-T$ plane are initialised from B, C and D and are shown along with zero temperature transition pressure computed via enthalpy minimisation.*

From the end points of the two series, and a third point lying half-way along the pressure series, the fcc-fcc transition was traced at the resulting A values in the $P-T$ plane. Parameters used were identical to the original $A = 3\epsilon/2$ case. In all cases the zero temperature transition pressure was computed from explicit enthalpy optimisation of the two phases over a series of pressures. Series were traced up to the maximum temperature of ld-fcc metastability. The resulting series are shown in figure 8.5. The effect of decreasing the A parameter can be seen as translation of the isostructural transition, combined with a lowering of the ld-fcc spinodal line. Both effects are easily understood in terms of the decreasing outer well-depth on which the ld-fcc structure is based.

From the above data, the rate at which the maximum temperature of ld-fcc stability *increases* with A is approximately $0.23\epsilon^{-1}$. Melting temperature for the sh phase increases at approximately $0.4\epsilon^{-1}$ based on data in the previous chapter. Increasing the A parameter is therefore not useful in extending the isostructural transition toward the liquid. The 'best case' scenario lies at low A where the gap between the melting temperature and the ld-fcc spinodal line is the smallest. The smallest A for which the isostructural transition occurs at positive pressure does not however lead to a useful extension toward the melting curve.

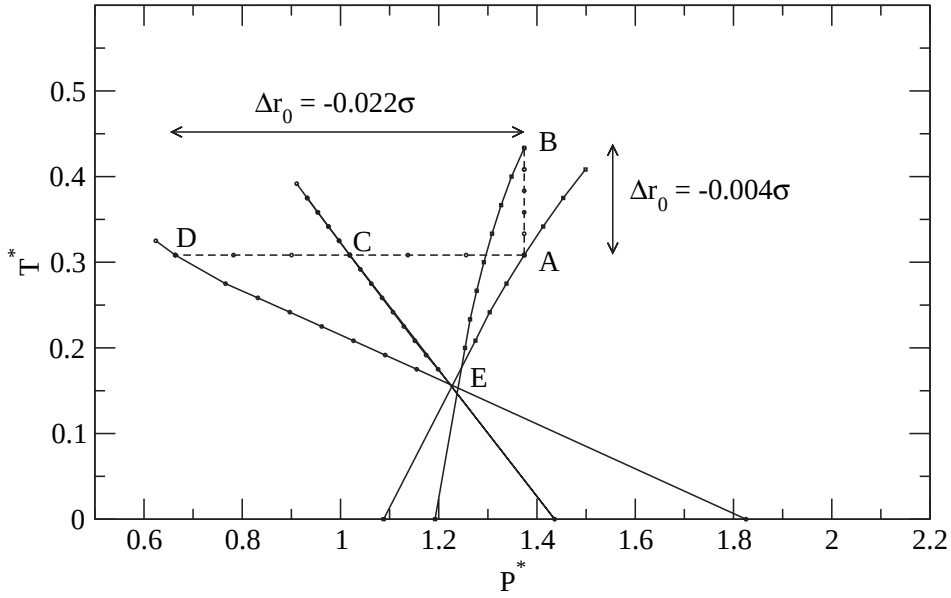

Figure 8.6: *Location of isostructural transition with r_0. Two Gibbs-Duhem series are initialised from the point A on the original phase boundary. The first traces temperature as a function of r_0 up to the ld-fcc spinodal line in the $T - r_0$ plane, where it reaches the point B in the $P - T$ plane. Similarly, the transition pressure is traced from A as a function of r_0 passing though C and reaching the hd-fcc limit of metastability at D. Gibbs-Duhem series in the $P - T$ plane are initialised from B, C and D. Zero temperature points are calculated explicitly using enthalpy minimisation. The effect of altering r_0 is seen to be a near pure rotation about the point E.*

8.2.5 Influence of r_0 on Isostructural Phase Transition

As with the A parameter, the effect of the r_0 parameter has been investigated with two Gibbs-Duhem series beginning from the point $T^* = 0.308$, $P^* = 1.274$. The series traced in the direction of increasing temperature encounters the limit of ld-fcc metastability after five steps of $\Delta T^* = 0.025$. At this point a total change of $\Delta r_0 = -0.004$ has occurred. In the direction of decreasing pressure the series terminates after six steps of $\Delta P^* = -0.12$, corresponding to a change $\Delta r_0 = -0.022$. In this case it is the spinodal line of the *high* density fcc structure which prevents progression to lower pressures. All series used identical simulations sizes/lengths to those employed in section 8.2.4 above.

Gibbs-Duhem series in the $P - T$ plane were initialised from both end points, and from a point half-way along the decreasing pressure series. These are shown in figure 8.6 along with zero temperature transition pressures computed explicitly for each value of r_0. The effect of changing the r_0 parameter is an almost pure rotation of the isostructural transition in the $P - T$ plane. Note that for all cases with negative slope the transition terminates at the hd-fcc spinodal.

The density difference between the two phases does not change sign. The rotation can only be reconciled with the Clausius-Clapeyron equation if decreasing r_0 changes the sign

of the entropy difference between the two phases. Figure 8.6 suggests that the maximum reach of the isostructural transition occurs when the coexistence line is vertical. In this case the entropy of the two phases is equal along the phase boundary. This situation will occur for approximately $r_0 \approx 1.427\sigma$. To confirm that the isostructural transition cannot reach higher temperatures when r_0 is increased, a second Gibbs-Duhem series in the $P - r_0$ plane was traced in the direction of increasing pressure. Beginning from the point $T^* = 0.308$, $P^* = 1.274$, this encountered the ld-fcc spinodal after 13 steps, corresponding to a change $\Delta r_0 = +0.335\sigma$. For temperatures greater than $T^* = 0.308$ the ld-fcc phase is mechanically unstable at this r_0, indicating that the maximum temperature of ld-fcc metastability continues to decrease on increasing r_0. Note that the Gibbs-Duhem series in the $P - T$ plane calculated at this r_0 (1.768) does *not* pass close to the point E in figure 8.6. The stationary nature of this point is therefore manifested for small changes in r_0 only.

It can be concluded that the maximum reach of the fcc-fcc transition achievable by varying r_0 is approximately $T^* \approx 0.45$ at $r_0 \approx 1.427\sigma$. It is clear from figure 8.4 that this increase over the $r_0 = 1.433\sigma$ case is matched by an increase in the sh melting temperature of $\Delta T^* = 0.03$, and hence adjustment of the r_0 parameter is not useful in significantly extending the isostructural transition toward the liquid.

8.2.6 w Parameter

Widening the outer Gaussian well is shown to decrease the sh melting temperature in figure 8.4. This corresponds to a decrease of the parameter w. The effect of this decrease on the isostructural transition has been investigated from the same starting point used above, i.e. $T^* = 0.308$, $P^* = 1.274$ in the case $w = 41.22\sigma^{-2}$. Again the transition was first traced in the direction of increasing temperature using a step size of $\Delta T^* = 0.025$. The limit of ld-fcc metastability was reached in just two steps corresponding to a change in w of $-5.11\sigma^{-2}$. A second series traced the transition as a function of pressure in steps of $\Delta P^* = -0.12$. Here the limit of ld-fcc metastability was reached in three-steps corresponding to $\Delta w = -11.45\sigma^{-2}$. Both series used identical simulation sizes/lengths to those used in section 8.2.4 above.

Beginning from the two endpoints of these series, the isostructural transition in the $P-T$ plane was traced with further Gibbs-Duhem integration. This proceeded as in section 7.7.2. As in the above cases, the zero temperature transition pressure was calculated explicitly using conjugate-gradient enthalpy minimisation of both phases at a series of pressures. The resulting set of isostructural transitions is shown in figure 8.7. The result of decreasing w is similar to that of decreasing A, i.e. a translation of the isostructural

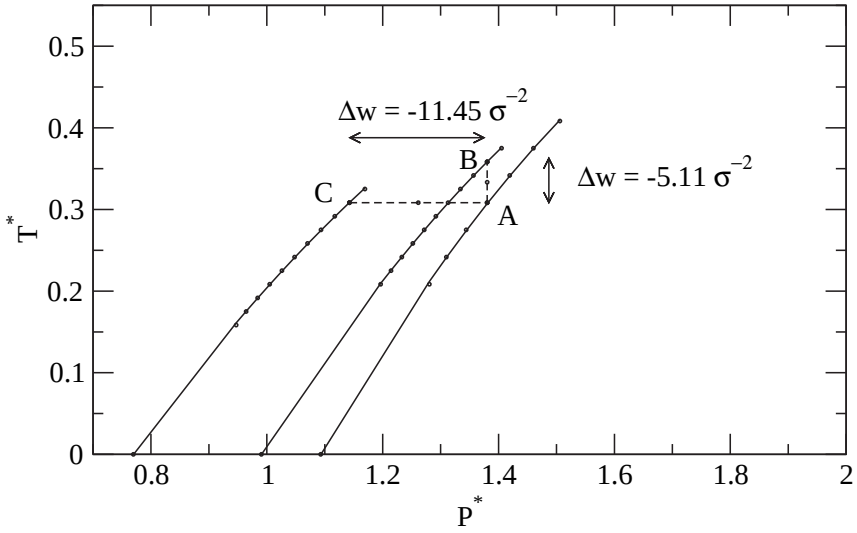

Figure 8.7: *Location of isostructural transition on decreasing w. Two series are initialised from the point A on the original fcc-fcc transition. The first traces the transition in the direction of increasing temperature toward the point B where the spinodal of the low density fcc structure is encountered. The second traces the transition in the direction of decreasing pressure, encountering the low density spinodal at C. Gibbs-Duhem series in the $P-T$ plane are initialised from points B and C. Zero temperature points are calculated explicitly using enthalpy minimisation.*

transition in the direction of decreasing pressure, accompanied by a lowering of the maximum temperature of ld-fcc metastability. As the outer well widens, the entropy of the ld-fcc phase can be expected to increase, requiring less mechanical work to overcome the difference in Helmholtz potential between the two phases, hence explaining the lower pressure required. The rate of increase in the maximum temperature of ld-fcc metastability is approximately $7.3 \times 10^{-3}\sigma^2$ as w is increased. This is approximately twice as fast as the increase in melting temperature. Increasing w therefore represents a useful mechanism for increasing the reach of the isostructural transition toward the sh melting line.

8.2.7 Optimal Parameters

As has been shown, adjustment of the A and r_0 parameters does little to extend the reach of the isostructural transition into the supercooled liquid. Increasing the w parameter is however useful. This can be increased up to a maximum of approximately $79\sigma^{-2}$. Above this value the sh structure is no longer mechanically stable at the melting line. The phase behaviour is therefore qualitatively different from that studied in chapter 7, and cannot be determined using the available reference systems. With r_0 and A at their original values, the pressure of the isostructural transition was traced as a function of increasing w using the methodology above. The point $T^* = 0.308$, $P^* = 1.274$ with $w = 41.22\sigma^{-2}$ was

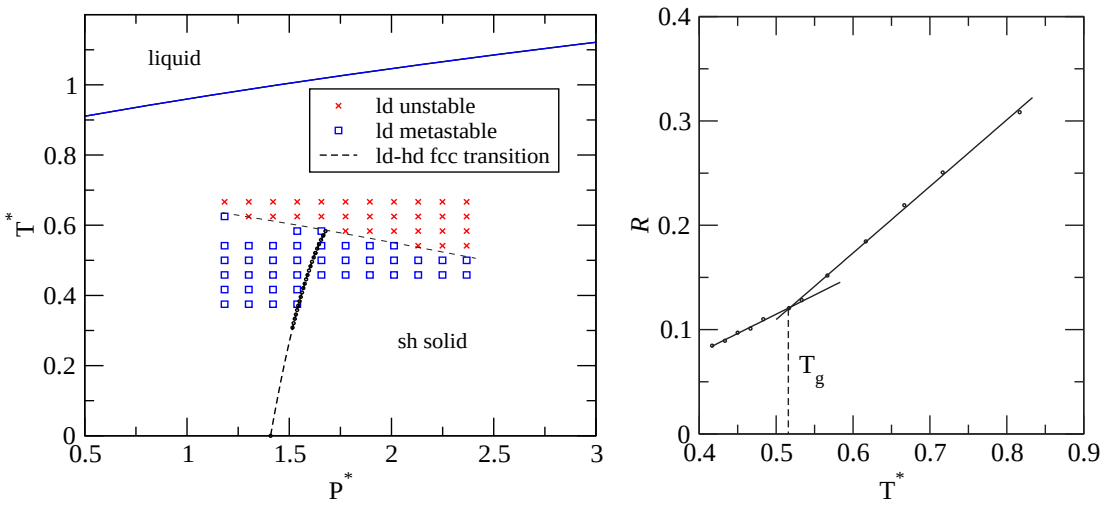

Figure 8.8: *Isostructural transition at optimised w. The location of the fcc-fcc transition with w increased to $w = 78.48\sigma^{-2}$ is shown on the left in relation to the sh melting curve and the ld-fcc spinodal line. The location of the glass temperature is shown in the right.*

used as the reference point. At $w = 78.48\sigma^{-2}$ the transition pressure at this temperature has increased to $P^* = 1.516$. This provides a reference point for tracing the isostructural transition at this w. A smaller step in temperature of $\Delta T^* = 0.013$ was employed in this case for enhanced location of the ld-fcc spinodal line. In addition, data in figure 8.4 provides a starting point for tracing the melting curve. Tracing of this melting curve proceeded as for the $w = 41.22\sigma^{-2}$ case in section 7.7.

The resulting phase boundaries are plotted in figure 8.8. As with the original parameterisation, the ld-fcc spinodal line has been mapped with a series of constant pressure Langevin dynamics simulations. The glass temperature has been located along the $P^* = 1.61$ isobar using the method of Wendt and Abraham. Simulation parameters and sizes match those employed in sections 8.1.1 and 8.1.2.

In this case, the spinodal line of the ld-fcc structure lies significantly above the glass temperature. Increasing the w parameter has therefore achieved the desired effect of increasing the reach of the isostructural transition into the supercooled liquid.

As with the original parameterisation, glassy configurations in which the nearest neighbour distance is r_0 are mechanically unstable. Only a single density glass can be generated. The only low density solid which can possibly destabilise to a second liquid is ld-fcc. Heating of this solid at a constant pressure of $P^* = 1.5$ to beyond the spinodal line does not however generate a low density liquid. Instead the ld-fcc structure collapses to a the same high density liquid previously observed. If the density is constrained to that of the ld-fcc a cavitated high density liquid is formed with negative pressure. The fact that low density liquid and amorphous solid structures with nearest neighbours at r_0 are

not energetically favourable is perhaps not surprising. However these finding suggest that such structures are entirely *unstable*.

A final attempt to locate a supercooled liquid-liquid transition was made by seeking hysteresis along the $T^* = 0.6$, 0.7 and 0.8 isotherms at pressure in the range $P^* = 0$ to 3 at intervals of $\Delta P^* = 0.25$. At each point two simulations were conducted, the first initialised from the ld-fcc density, and the second from the density of the liquid at the sh melting line. The system of 500 atoms was allowed to equilibrate over $20,000$ time-steps of $\Delta t^* = 0.0017$. In all cases no statistically significant difference in the resulting volume was observed. No liquid-liquid transition exists in the supercooled regime of this potential.

8.3 Melting Curve Maximum

Liquid anomalies in three dimensions due to a second critical point have been ruled out by the above. For completeness, this investigation should address the possibility of a density anomaly in the liquid close to the melting line in regions where the solid is less dense than the liquid. Such anomalies in the two-dimensional shoulder model have been discussed in chapter 6. In two dimensions the freezing transition is quasi-continuous. There is no significant energy barrier to nucleation of the solid phase. As the liquid is cooled toward the freezing temperature clusters can therefore form of lower density than the liquid, generating a density anomaly.

In three dimensions the situation is somewhat different. For the potential studied in section 7.7 a melting curve maximum is observed at high pressure, followed by a region in which the liquid freezes to a lower density solid. This transition is however not continuous. The latent heat of formation per particle (obtained from the Gibbs-Duhem series computed in section 7.7.4) is $30 - 40\epsilon$ in the region at and beyond the melting curve maximum. The transition is therefore strongly first order implying a significant energy barrier to solid nucleation which will dominate purely Boltzmann sampling of a finite-size simulation. It is expected therefore that no density anomaly will be observable in simulations near the melting curve maximum.

To confirm this expectation, a series of simulations have been conducted in the region of this melting curve maximum. The mesh of sampled points is shown in figure 8.9. Note that points which are supercooled with respect to both the sh and fcc phases have been included. A system size of 500 atoms is used with a time-step of $\Delta t^* = 0.0017$. At each point the system is sampled for $40,000$ time-steps after equilibrating for $10,000\,\Delta t$. The isotropic constant pressure Langevin dynamics algorithm is used. Plots of density along

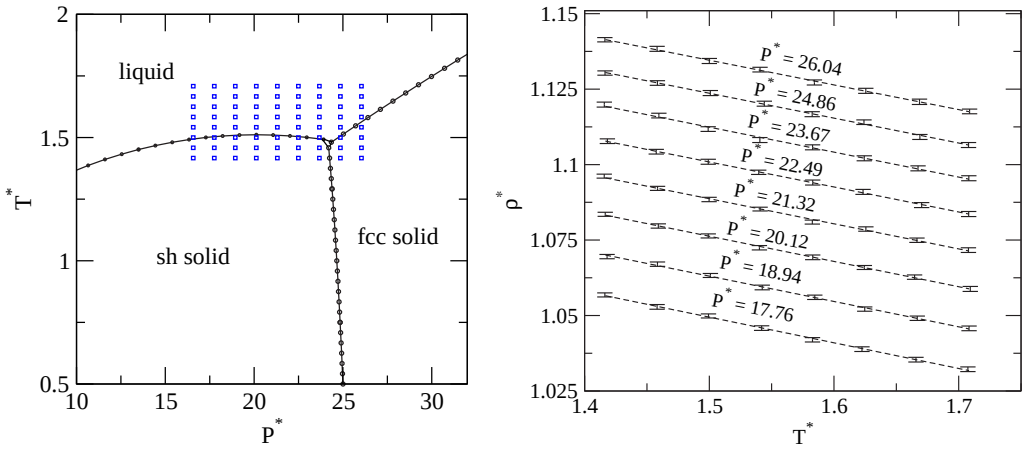

Figure 8.9: *Liquid density close to the sh melting line. Points sampled are shown in the left. These sample the liquid in the region where the sh solid is less dense than the liquid. Density against temperature along the four isobars is shown on the right.*

each isobar are shown in figure 8.9 along with the calculated statistical error. No anomaly in the density is observed as the melting line is approached. In addition bulk modulus and heat capacity have been computed from these results using equations 2.23 and 2.24. Diffusion coefficients have been calculated at each sampled point from the gradient of the mean squared displacement curve (see e.g. Allen and Tildesley (1987)). No anomalies in any of these quantities have been measured.

Advanced simulation and sampling methods may go some way to overcoming finite-size suppression of nucleation and exhibit a density anomaly due to low density cluster formation. This has not been pursued here. It should be noted that if present, anomalies of this kind would not be unique to core-softened models, but would be expected close to *any* melting where the solid is of lower density than the liquid.

Chapter 9

Conclusions

The utility of Langevin dynamics simulation for statistical sampling of the canonical ensemble has been discussed in chapter 4. Sampling of this kind has been shown to be useful in Einstein crystal free energy calculations (where the most popular thermostats fail) in chapter 5 and has been employed in chapter 7 in all thermodynamic integration.

Justification that Langevin dynamics can be extended to sampling the isothermal-isobaric ensemble has also been presented in chapter 4. This has involved consideration of a point previously unaddressed in the literature. Specifically the validity of the Einstein diffusion relation in non-Hamiltonian systems. Exploration of this issue has led to the conclusion that Langevin dynamics in non-Hamiltonian systems is indeed a valid method of sampling the NPT ensemble, provided no stochastic or friction forces are applied along phase-space directions in which the system exhibits intrinsic probability gradients.

Implementation of this strategy has been shown to correctly sample both the Lennard-Jones system and a model for bulk silicon with similar accuracy to a massive Nosé-Hoover chain scheme in both fully flexible and fixed-shape simulations cells. In addition, the sampling scheme has been shown to produce identical results to NPT Monte-Carlo when employed in Gibbs-Duhem integration and has largely performed well in a study of phase behaviour in core-softened pair-potentials. Some difficulties have however been encountered under combined extremes of low temperature and high pressure.

The stochastic component of the Langevin dynamics is essentially white noise and hence influences the dynamics over a large frequency range. Choosing a barostat frequency which does not disrupt this influence is key to correct sampling. At extremes of high pressures and low temperature, the barostat forces can easily dominate over the stochastic forces if this is not chosen carefully, leading to incorrect temperature control and sampling. For one core-softened potential investigated in chapter 7 no suitable values could be determined under these extremes. It is not clear if problems of this kind will appear in

real systems, the choice of appropriate frequencies being heavily dependent on the model in question.

Despite this potential concern, the method of Langevin dynamics within non-Hamiltonian pressure regulating systems is clearly a viable alternative to purely deterministic schemes for sampling the isothermal-isobaric ensemble. As has been stated, both approaches have merits. Deterministic schemes require that no unexpected conservations laws are generated in order to sample correctly but can be shown to exactly sample the appropriate ensemble. In contrast the Langevin dynamics method can only be justified at the level of linear response, but guarantees that no extra conservation laws are generated. The constant pressure Langevin dynamics method may therefore be most useful for checking results obtained from purely deterministic molecular dynamics schemes.

In addition to the work reported here using GOLDILOCS, both variants of the constant pressure Langevin dynamics methodology have been implemented by the author within the CASTEP (Segall *et al.*, 2002). This is a density functional based *ab-initio* simulation package.

The analysis presented in chapter 4 has been extended to the case of dissipative particle dynamics simulations by Jakobsen (2005). This work also shows that a finite particle friction coefficient *can* be used in the Parrinello-Rahman style system in the special case of a constrained orthorhombic cell.

In chapter 7 the phase behaviour of a family of core-softened pair potentials with possible relevance to liquid water has been mapped in detail using a combination of meta-dynamics, free energy calculation, multi-canonical Monte-Carlo and Gibbs-Duhem integration. The potentials are constructed from a Lennard-Jones potential plus an outer Gaussian minimum. As the outer Gaussian is introduced, a lowering of the fcc melting temperature is observed, a result explained in terms of free energy derivatives in section 8.2.2, and in terms of Lindemann ratios in section 7.8.

At large values of A the low pressure phase diagram is dominated by the emergence of a simple hexagonal phase. This structure benefits energetically from *both* minima in the pair potential. No other structures which have this property have been identified by the meta-dynamics, but cannot be ruled out. The phase diagrams presented assume that no such energetically relevant structures have been omitted from the analysis. Transitions under pressure to a high density fcc structure have been mapped.

At larger still values of A, a maximum in the melting temperature has been observed at high pressure, a property in common with many elemental melts which exhibit liquid-liquid transitions. In addition a meta-stable isostructural phase transition between two fcc structures of different density has been located with possible relevance to modelling

anomalies of liquid water.

Sublimation at low pressures has not been studied for any A value. No qualitatively new physics is expected in this regime beyond that of the Lennard-Jones potential.

An important limitation of this work has been the inability to accurately locate fcc-hcp phase boundaries. Free energy differences between these phases are small, and hence transitions are difficult to locate by the methods employed here. Hexagonal close-packed phases have hence been broadly omitted from the analysis, and assumed to occupy similar regions of the face diagram to the face-centred cubic structure. As has been mentioned, application of lattice-switching Monte-Carlo (see section 5.6.2) may clarify this situation.

On a methodological note, it has been shown in chapter 7 that both NPT and pseudo-NPH two-phase melting simulations produce results consistent with free energy calculations. This is contrary to the recent findings of Wang *et al.* (2005) who find substantial disagreement with the free energy calculations of Vega *et al.* (2005) when applying the NPH method to the melting temperature of TIP4P and TIP5P ice. Wang *et al.* employed an Andersen barostat *without* consideration of enthalpy fluctuations. Investigating the effect of this omission may be a useful topic for further study.

In chapter 8 the thermodynamic limitations of the isostructural phase transition have been explored, and to some extent overcome by integrating along paths to alternate parameterisations of the pair-potential. The Gibbs-Duhem methodology employed is valid over the parameter range for which phase behaviour is *qualitatively* the same as that mapped in chapter 7. It is clear that increasing the outer-well distance r_0 much beyond 1.5σ stabilises extra solid phases, and that increasing w beyond approximately $80\sigma^{-2}$ destabilises the sh phase. Further calculations in these regions may significantly alter the conclusions drawn but will require mapping of a new reference system.

Within the explorable parameter range, it has been shown that although the isostructural transition can reach into the supercooled liquid, this does not result in a metastable liquid-liquid phase transition. Furthermore, no randomly ordered phases are stable which do not access the inner minimum of the core-softened potential.

The lack of a second liquid phase may be due a fundamental limitation of the functional form used to construct the pair potential. The aim has been to generate a low density liquid by heating the ld-fcc phase (or an amorphous phase which explores only the outer minimum) beyond its spinodal line. Destabilisation to a low density liquid requires that the Lindemann criterion is satisfied in the ld-fcc structure at energies much lower than the depth of the outer minimum, such that exploration of the inner minima is highly improbable. It would seem that this is not possible with the parameters studied in this thesis. Creating this situation requires decreasing either r_0 and hence the nearest neighbour dis-

tance, or decreasing w to increase the magnitude of position fluctuations at low energies. Both changes act to merge the Gaussian minimum into that of the Lennard-Jones potential as seen in figure 7.1, removing any possibility of isostructural or liquid-liquid transitions. Identification of parameters, for which the Lindemann criterion can be satisfied in a structure with nearest neighbour distance r_0, may therefore be impossible.

An alternative argument can be made based on neighbour distances. Any particle in a disordered phase will possess more particles in its second neighbour shell than the first if interacting via an isotropic pair potential. In order for the inner Lennard-Jones minimum to constitute a 'shoulder', the outer Gaussian well must lie at approximately the distance of this second neighbour shell. Higher density disordered phases therefore benefit preferentially from the outer minimum in a similar fashion to the simple hexagonal structure in which twelve third nearest neighbours lie at r_0 (see section 7.2.2). Discrete interpretations of the shoulder potential reported by Skibinsky *et al.* (2004), which do exhibit two liquid phases, contain a much higher energy shoulder. High density disordered phases therefore suffer an energy penalty from particles in the first neighbour shell, which counteracts the benefit from large numbers of second shell neighbours at the outer minimum. Such high energy shoulders are not achievable with the Lennard-Jones plus Gaussian form. These issue were not considered in the argument of Scala *et al.* (2000) when predicting that such potentials will generate a second critical point, but have emerged as important in light of the findings in this thesis. Investigation of alternate forms for continuous shoulder potentials may be in order.

With regard to liquid water, support for the second critical point hypothesis has continued to grow during the writing of this thesis. In particular Brovchenko *et al.* (2005) have mapped a liquid-liquid transition in supercooled water for a variety of models using Gibbs ensemble techniques and Paschek (2005) has studied the influence of the transition on solubility of hydrophobic particles. The work presented in chapter 8 suggests that a metastable second critical point is not reproducible with a core-softened Lennard-Jones plus Gaussian shoulder potential, but does not exclude the possibility of the phenomenon in other simple models. In light of the growing evidence favouring the presence of the LLPT, this may be a valuable source of further investigation.

A further step to understanding liquid-liquid transitions may be possible by determining if effective pair-potentials derived from experimental or *ab-initio* data can reproduce the phenomenon in elemental melts, such as those surveyed in chapter 6. The extent to which these potentials resemble the various forms of core-softened model is certainly promising.

Appendix A

Phase Diagram of the Force-Shifted Lennard-Jones Potential

As previously stated, computational results presented in chapters 7 and 8 employ pair potentials with the interaction truncated at 2.5σ. The force-shifting method is employed as described in section 3.5.2. The resulting short-ranged model is self consistent, but differs substantially from the 'full' potential in which long range effects are included. Many results in chapter 5 were calculated using various approximations to the 'full' Lennard-Jones potential for validating methods against results in the literature. The complete phase diagram of the truncated and force-shifted Lennard-Jones potential has not been presented. This is rectified here, allowing direct comparison to the core-softened phase diagrams in chapter 7.

A.1 Liquid-Gas Transition

This was traced using the multi-canonical Monte-Carlo method described in section 5.6.1, where the first few histograms for the force-shifted Lennard-Jones case have already been plotted. From the initial point at $T^* = 0.958$ the liquid-vapour curve was traced to 0.858 in steps of $\Delta T^* = -0.008$. As with simulations of core-softened potentials, grand canonical Monte-Carlo simulations at each step employed $600,000$ cycles after equilibrating for $40,000$ cycles. The density difference along the coexistence curve as a function on temperature is plotted in figure A.1. Fits to the power law $\Delta\rho^* \propto (T^* - T_c^*)^\beta$, and to the law of rectilinear diameters yields an *estimate* of the critical parameters as $T_c^* = 0.961 \pm 0.004$, $\rho_c^* = 0.316 \pm 0.005$. As with the core-softened potentials no account has been made of finite-size effects in the region of the critical point. The critical properties of Lennard-Jones fluids are known to be heavily dependent on the truncation method. For studies of

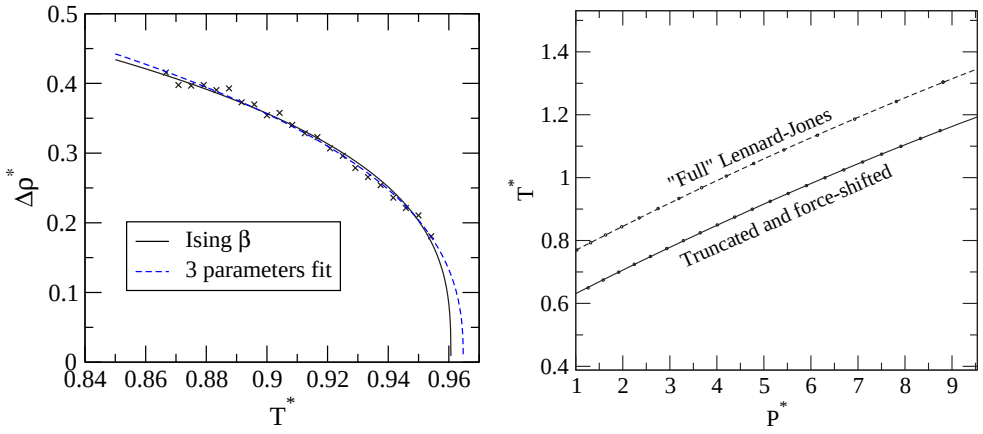

Figure A.1: *Lennard-Jones liquid-vapour and melting transitions. The difference in liquid and gaseous densities along the coexistence curve is shown on the left as extracted from multi-canonical Monte-Carlo simulations. The two fits used to estimate the critical temperature are shown. The melting curve for both the full and force-shifted potentials is shown on the right.*

liquid-vapour coexistence and criticality, the most commonly studied form is that truncated at 2.5σ but *not* shifted. Wilding (1995) has accurately computed the critical parameters as $T^* = 1.1876 \pm 0.0003$, $\rho_c^* = 0.3197 \pm 0.0004$ in this case. The critical temperature for the full potential (truncated at 4σ plus long range corrections) has been estimated from the Johnson *et al.* (1993) equation for state as $T^* = 1.246$. Adaption to truncation (at 2.5σ) and shifting (with no long range correction) yields $T^* = 1.00 \pm 0.04$. No measurement of critical temperature for the *force*-shifted case has been found in the literature. The estimate obtained above does not seem unreasonable.

Below $T^* = 0.858$ the liquid-vapour curve was traced with Gibbs-Duhem integration. A temperature step of $\Delta T^* = -0.03$ was employed. Simulation lengths and sizes matched those used for the equivalent series in the $A = \epsilon/4$ core-softened case.

A.2 Melting Transition

This has been calculated by computing the solid and liquid free energies along the $P^* = 0.047$ isobar. For the solid, Einstein crystal calculations were performed for temperatures in the interval $T^* = 0.458$ to 0.583 in steps of 0.042. Appropriate densities for the calculations were obtained from $100,000\,\Delta t$ constant pressure Langevin dynamics simulations employing a time-step of $\Delta t^* = 0.0023$ and an equilibration period of $5,000\,\Delta t$ in a 256 atom system. The integration procedure itself utilised 50 sampled points along the path to the harmonic crystal. Each point consisted of a $2,000\,\Delta t$ equilibration before averaging the free energy derivative over a further $3,000\,\Delta t$. The free energy was extrapolated to the thermodynamic limit by repeating the calculation with system sizes of 256, 500 and

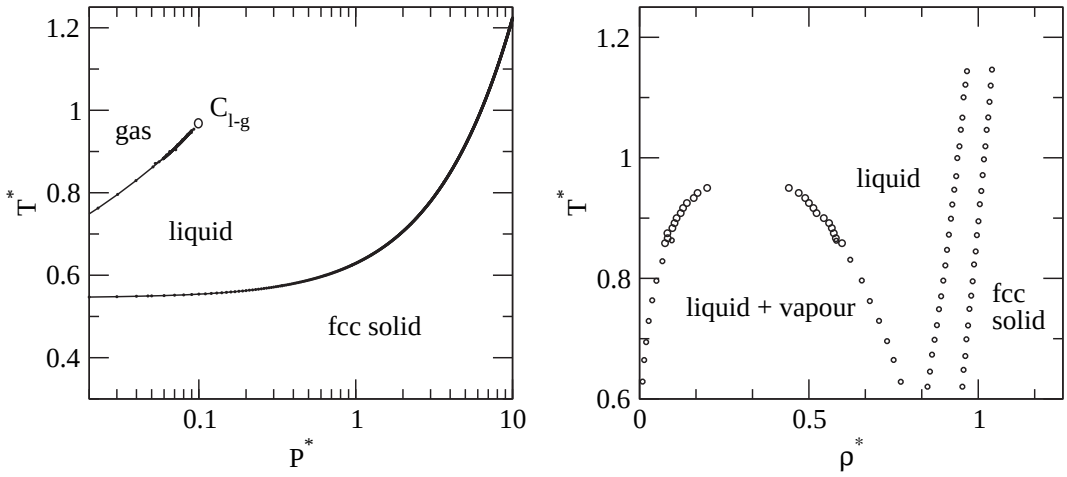

Figure A.2: *Phase diagram of the force-shifted Lennard-Jones potential. The pressure-temperature projection is shown on the left. Projection into the density-temperature plane is shown on the right. The low pressure region and sublimation have not been studied.*

864 atoms. Finite-size corrections are of similar magnitude to those shown in figure 5.6.

For the liquid free energies, a reference point at $T^* = 0.917$ and $\mu^* = -7.368$ was taken. Grand canonical Monte-Carlo simulations at this point yield $\langle N \rangle = 376.2 \pm 0.4$ and $\langle P^* \rangle = 1.77 \pm 0.03$ in a cube of side 7.79σ. This leads to a Helmholtz free energy per atom of $f^* = -9.58 \pm 0.04$. From this reference point, thermodynamic integration was used to compute the free energy at temperatures in the range 0.500 to 0.667. Required densities along the $P^* = 0.047$ isobar were computed from constant pressure Langevin dynamics simulations as in the solid case. Each isochore/isotherm used in the thermodynamic integration consisted of 10 simulations of $50,000$ time-steps each. An equilibration period of $20,000$ steps was used with $\Delta t^* = 0.0012$.

Interpolation between the resulting Gibbs free energies reveals the melting temperature as $T^* = 0.55 \pm 0.01$. The error estimate is dominated by statistical uncertainty when simulating at the liquid reference point.

Using this melting temperature as the first point, Gibbs-Duhem integration was then used to trace the melting curve in the direction of increasing temperature. A step in temperature of $\Delta T^* = 0.025$ was employed. At each step the Clapeyron equation is evaluated from $50,000\,\Delta t$ constant pressure Langevin dynamics simulations of each phase following a $20,000\,\Delta t$ equilibration period. A time-step of $\Delta t^* = 0.0028$ was used. The resulting series is shown in figure A.1 in comparison with the melting curve for the 'full' Lennard-Jones potential computed in section 5.5.2. The effect of the truncation and force-shifting is a lowering of the melting temperature by approximately $\Delta T^* = 0.12$ over the entire pressure range. The phase diagram of this potential is shown in figure A.2.

Bibliography

Abell, G. C. (1985). Empirical chemical pseudopotential theory of molecular and metallic bonding. *Phys. Rev. B*, **31**, 6184–6196.

Agrawal, R. and Kofke, D. A. (1995). Thermodynamic and structural properties of model systems at solid-fluid coexistence. ii. Melting and sublimation of Lennard-Jonesium. *Mol. Phys.*, **85**, 43–59.

Alder, B. and Wainwright, T. E. (1957). Phase transition for a hard sphere system. *J. Chem. Phys.*, **27**, 1208–1209.

Alfè, D. (2003). First-principles simulations of direct coexistence of solid and liquid aluminium. *Phys. Rev. B.*, **68**, 064423.

Allen, M. P. and Tildesley, D. J. (1987). *Computer Simulation of Liquids*. Oxford University Press, New York.

Andersen, H. C. (1980). Molecular dynamics simulations at constant pressure and/or temperature. *J. Chem. Phys.*, **71**, 2384.

Angilella, G. G. N., Leys, F. E., March, N. H., and Pucci, R. (2003). Phase transitions wholly within the liquid state. *Phys. Chem. Liq.*, **41**, 211–226.

Ballone, P. and Jones, R. O. (2004). A reactive force field simulation of liquid-liquid phase transitions in phosphorus. *J. Chem. Phys.*, **121**(16), 8147–8157.

Berendsen, H. J. C., Postma, J. P. M., Vangunsteren, W. F., Dinola, A., and Haak, J. R. (1984). Molecular-dynamics with coupling to an external bath. *J. Chem. Phys.*, **81**, 3684–3690.

Berendsen, H. J. C., Grigera, J. R., and Straatsma, T. P. (1987). The missing term in effective pair potentials. *J. Phys. Chem.*, **91**, 6269–6271.

Berg, B. and Neuhaus, T. (1991). Multicanonical algorithms for first order phase transitions. *Phys. Lett. B.*, **267**(2), 249–253.

Boinepalli, S. and Attard, P. (2003). Grand canonical molecular dynamics. *J. Chem. Phys.*, **119**(24), 12769–12775.

Bolhuis, P. and Frenkel, D. (1997). Isostructural solid-solid transitions in systems with a repulsive 'shoulder' potential. *J. Phys.- Condens. Matter*, **9**, 381–387.

Bond, S. D., Leimkuhler, B. J., and Laird, B. B. (1999). The Nose-Poincare method for constant temperature molecular dynamics. *J. Comput. Phys.*, **151**, 114–134.

Bonev, S. A., Schwegler, E., Ogitsu, T., and Galli, G. (2004). A quantum fluid of metallic hydrogen suggested by first-principles calculations. *nature*, **431**, 669–672.

Branca, A. C. (2000). Nosé-Hoover chain method for nonequilibrium molecular dynamics simulation. *Phys. Rev. E*, **61**, 4767–4773.

Branka, A. C., Kowalik, M., and Wojciechowski, K. W. (2003). Generalization of the Nose-Hoover approach. *J. Chem. Phys*, **119**(4), 1929–1937.

Brazhkin, V. V., Voloshin, R. N., Popova, S. V., and Umnov, A. G. (1992). Pressure temperature phase-diagram of solid and liquid te under pressures up to 10 gpa. *J. Phys.-Condes. Matter*, **4**, 1419–1425.

Brazhkin, V. V., Popova, S. V., and Voloshin, R. N. (1999). Pressure-temperature phase diagram of molten elements: selenium, sulfur and iodine. *Physica B*, **265**, 64–71.

Brenner, D. W. (1990). Empirical potential for hydrocarbons for use in simulating the chemical vapor-deposition of diamond films. *Phys. Rev. B*, **42**, 9458–9471.

Brenner, D. W., Harrison, J. A., White, C. T., and Colton, R. J. (1991). Molecular-dynamics simulations of the nanometer-scale mechanical-properties of compressed buckminsterfullerene. *Thin Solid Films*, **206**, 220–223.

Brenner, D. W., Shenderova, O. A., Harrison, J. A., Stuart, S. J., Ni, B., and Sinnott, S. B. (2002). A second-generation reactive empirical bond order (REBO) potential energy expression for hydrocarbons. *J. Phys.-Condes. Matter*, **14**, 783–802.

Brovchenko, I., Geiger, A., and Oleinikova, A. (2003). Multiple liquid-liquid transitions in supercooled water. *J. Chem. Phys.*, **118**(21), 9473–9476.

Brovchenko, I., Geiger, A., and Oleinikova, A. (2005). Liquid-liquid phase transitions in supercooled water studied by computer simulations of various water models. *J. Chem. Phys.*, **123**, 044515.

Bruce, A. D. and Wilding, N. B. (1992). Scaling fields and universality of the liquid-gas critical point. *Phys. Rev. Lett.*, **68**(2), 193–196.

Bruce, A. D. and Wilding, N. B. (2003). Computational strategies for mapping equilibrium phase diagrams. *Adv. Chem. Phys*, **127**, 1–64.

Bruce, A. D., Wilding, N., and Ackland, G. J. (1997). Free energy of crystalline solids: A lattice-switch Monte-Carlo method. *Phys. Rev. Lett.*, **79**(16), 3002–3005.

Bruce, A. D., Jackson, A. N., Ackland, G. J., and Wilding, N. B. (2000). Lattice-switch Monte-Carlo method. *Phys. Rev. E.*, **61**(1), 906–919.

Buldyrev, S., Franzese, G., Giovambattista, N., Malescio, G., Sadr-Lahijany, M. R., Scala, A., Skibinsky, A., and Stanley, H. E. (2002). Models for a liquid-liquid phase transition. *Physica A*, **304**, 23–42.

Bulgac, A. and Kusnezov, D. (1990). Canonical ensemble averages from pseudomicrocanonical dynamics. *Phys. Rev. A*, **42**, 5045–5048.

Bundy, F. P. (1989). Pressure-temperature phase-diagram of elemental carbon. *Physica A*, **156**, 169–178.

Bundy, F. P., Bassett, W. A., Weathers, M. S., Hemley, R. J., Mao, H. K., and Goncharov, A. F. (1996). The pressure-temperature phase and transformation diagram for carbon; updated through 1994. *Carbon*, **34**, 141–153.

Chandrasekhar, S. (1943). Stochastic problems in physics and astronomy. *Rev. Mod. Phys.*, **15**(1), 1–89.

Cleveland, C. L. (1988). New equations of motion for molecular dynamics systems that change shape. *J. Chem. Phys.*, **89**, 4987.

Crain, J., Clark, S. J., Ackland, G. J., Payne, M. C., Milman, V., Hatton, P. D., and Reid, B. J. (1994). Theoretical study of high-density phases of covalent semiconductors. i. ab-initio treatment. *Phys. Rev. B.*, **49**(8), 5329–5340.

Datchi, F., Loubeyre, P., and LeToullec, R. (2000). Extended and accurate determination of the melting curves of argon, helium, ice (h2o), and hydrogen (h2). *Phys. Rev. B.*, **61**(1), 6535–6546.

Delaney, K. (2005). Private Communication.

Dettmann, C. P. and Morriss, G. P. (1997). Hamiltonian reformulation and pairing of Lyapunov exponents for Nosé-Hoover dynamics. *Phys. Rev. E*, **55**, 3693–3696.

Ensing, B., Laio, A., Gervasio, F. L., Parrinello, M., and Klein, M. L. (2004). A minimum free energy reaction path for the E2 reaction between fluoro ethane and a fluoride ion. *J. Am. Chem. Soc.*, **126**, 9492–9493.

Errington, J. R. (2003). Solid-liquid phase coexistence of the Lennard-Jones system though phase-switch Monte Carlo simulation. *J. Chem. Phys.*, **120**(7), 3130–3141.

Evans, D. J., Hoover, W. G., Fallor, B. H., Moran, B., and Ladd, A. J. C. (1983). Nonequilibrium molecular dynamics via Gauss's principle of least constraint. *Phys. Rev. A*, **28**, 1016–1021.

Feller, S. E., Zhang, Y., and W., P. R. (1995). Constant pressure molecular dynamics simulation: The Langevin piston method. *J. Chem. Phys*, **103**, 4613.

Ferrenberg, A. M. and Swendsen, R. H. (1988). New Monte-Carlo technique for studying phase transitions. *Phys. Rev. Lett.*, **61**(23), 2635–2638.

Franzese, G., Malescio, G., Skibinsky, A., Buldyrev, S. V., and Stanley, H. E. (2001). Generic mechanism for generating a liquid-liquid phase transition. *Nature*, **409**, 692–695.

Franzese, G., Malescio, G., Skibinsky, A., Buldyrev, S. V., and Stanley, H. E. (2002). Metastable liquid-liquid phase transition in a single- component system with only one crystal phase and no density anomaly. *Phys. Rev. E*, **66**, 051206.

Frenkel, D. and Ladd, A. J. C. (1984). New Monte-Carlo method to compute the free energy of arbitrary solids. application to the fcc and hcp phases of hard spheres. *J. Chem. Phys*, **81**(7), 3188–3193.

Frenkel, D. and Smit, B. (1996). *Understanding Molecular Simulation: From Algorithms to Applications*. Academic Press, San Diego.

Funamori, N. and Tsuji, K. (2002). Structural transformation of liquid tellurium at high pressures and temperatures. *Phys. Rev. B*, **65**, 014105.

Galli, G., Martin, R. M., Car, R., and Parrinello, M. (1989). Carbon - the nature of the liquid-state. *Phys. Rev. Lett.*, **63**, 988–991.

Gervasio, F. L., Laio, A., Iannuzzi, M., and Parrinello, M. (2004). Influence of dna structure on the reactivity of the guanine radical cation. *Chem.-Eur. J.*, **10**, 4846–4852.

Ghiringhelli, L. M. and Meijer, E. (2005). Phosphorus: First principle simulation of a liquid-liquid phase transition. *J. Chem. Phys.*, **122**, 184510.

Gibson, J. B., Goland, A. N., Milgram, M., and Vineyard, G. H. (1960). Dynamics of radiation damage. *Phys. Rev.*, **120**, 1229–1253.

Glosli, J. N. and Ree, F. H. (1999). Liquid-liquid phase transformation in carbon. *Phys. Rev. Lett.*, **82**, 4659–4662.

Glover, M. J. (2004). *Path Integral Computer Simulations of Liquid Water*. Ph.D. thesis, Department of Physics, University of York.

Grumbach, M. P. and Martin, R. M. (1996). Phase diagram of carbon at high pressures and temperatures. *Phys. Rev. B*, **54**, 15730–15741.

Harrington, S., Poole, P. H., Sciortino, F., and Stanley, H. E. (1997a). Equation of state of supercooled water simulated using the extended simple point charge intermolecular potential. *J. Chem. Phys.*, **107**, 7443–7450.

Harrington, S., Zhang, R., Poole, P. H., Sciortino, F., and Stanley, H. E. (1997b). Liquid-liquid phase transition: Evidence from simulations. *Phys. Rev. Lett.*, **78**, 2409–2412.

Hemmer, P. and Stell, G. (1970). Fluids with several phase transitions. *Phys. Rev. Lett.*, **24**(23), 1284–1287.

Hernandez, E. (2001). Metric-tensor flexible-cell algorithm for isothermal- isobaric molecular dynamics simulations. *J. Chem. Phys.*, **115**, 10282–10290.

Hohl, D. and Jones, R. O. (1994). Polymerization in liquid phosphorus - simulation of a phase- transition. *Phys. Rev. B*, **50**, 17047–17053.

Hoover, W. G. (1985). Canonical dynamics - equilibrium phase-space distributions. *Phys. Rev. A*, **31**, 1695–1697.

Hoover, W. G. and Holian, B. L. (1996). Kinetic moments method for the canonical ensemble distribution. *Phys. Lett. A*, **211**, 253.

Hoover, W. G., Evans, D. J., Hickman, R. B. Ladd, A. J. C., Ashurst, W. T., and Moran, B. (1980). Lennard-Jones triple-point bulk and shear viscosities. green-kubo theory, Hamiltonian mechanics, and nonequilibrium molecular dynamics. *Phys. Rev. A*, page 1690.

Hoover, W. G., Ladd, A. J. C., and Moran, B. (1982). High-strain-rate plastic flow studied via nonequilibrium molecular dynamics. *Phys. Rev. Lett.*, **48**, 1818–1820.

Hoover, W. G., Aoki, K., Hoover, C. G., and v. de Groot, S. (2004). Time-reversible deterministic thermostats. *Physica D*, **187**, 253–267.

Hoshine, K., Leung, C. H., McLaughlin, I. L., Rahman, S. M. M., and Young, W. H. (1987). Pair potential trends from the evidence of observed liquid-metal structure factors. *J. Phys. F: Met Phys.*, **17**, 787.

Iannuzzi, M., Laio, A., and Parrinello, M. (2003). Efficient exploration of reactive potential energy surfaces using car-parrinello molecular dynamics. *Phys. Rev. Lett.*, **90**, 238302.

Jackson, A., Bruce, A. D., and Ackland, G. J. (2002). Lattice-switch Monte Carlo method: Application to soft potentials. *Phys. Rev. E.*, **65**(3), 036710.

Jagla, E. A. (1998). Phase behavior of a system of particles with core collapse. *Phys. Rev. E*, **58**, 1478–1486.

Jagla, E. A. (2001). Liquid-liquid equilibrium for monodisperse spherical particles. *Phys. Rev. E*, **63**, 061501.

Jakobsen, A. (2005). Constant-pressure and constant-surface tension simulations in dissipative particle dynamics. *J. Chem. Phys.*, **144**, 124901.

Jedlovszky, P. and Mezei, M. (1999). The anisotropic virial-biased sampling for monte carlo simulations in the isothermal-isobaric ensemble. *Mol. Phys.*, **96**(2), 293–296.

Johnson, J. K., Zollweg, J. A., and Gubbins, K. E. (1993). The Lennard-Jones equation of state revisited. *Mol. Phys.*, **78**, 591–618.

Jorgensen, W. L. (1981). Quantum and statistical mechanical studies of liquids .10. transferable intermolecular potential functions for water, alcohols, and ethers - application to liquid water. *J. Am. Chem. Soc.*, **103**, 335–340.

Katayama, Y. (2001). XAFS study on liquid selenium under high pressure. *J. Synchrot. Radiat.*, **8**, 182–185.

Katayama, Y. (2002). In situ observation of a first-order liquid-liquid transition in phosphorus. *J. Non-Cryst. Solids*, **312**, 8–14.

Katayama, Y., Mizutani, T., Utsumi, W., Shimomura, O., Yamakata, M., and Funakoshi, K. (2000). A first-order liquid-liquid phase transition in phosphorus. *Nature*, **403**, 170–173.

Katayama, Y., Mizutani, T., Utsumi, W., Shimomura, O., and Tsuji, K. (2001). X-ray diffraction study on structural change in liquid selenium under high pressure. *Phys. Status Solidi B-Basic Res.*, **223**, 401–404.

Katayama, Y., Yamakata, M., Utsumi, W., and Shimomura, O. (2004). Macroscopic separation of dense fluid phase and liquid phase of phosphorus. *Science*, **306**, 848–851.

Kneller, G. R. and Hinsen, K. (2001). Computing memory functions from molecular dynamics simulations. *J. Chem. Phys.*, **115**, 11097–11105.

Kofke, D. (1993). Direct evaluation of phase coexistence. *J. Chem. Phys*, **98**(5), 4149.

Kolb, A. and Dunweg, B. (1999). Optimized constant pressure stochastic dynamics. *J. Chem. Phys.*, **111**, 4453–4459.

Koslowski, T. and Stepanov, I. A. (2003). A tight-binding potential for the simulation of solid and liquid iodine. *J. Phys.-Condes. Matter*, **15**, 2951–2960.

Kubo, R. (1966). The fluctuation-dissipation theorem. *Rep. Prog. Phys.*, **29**, 255–284.

Kum, O., Ree, F. H., Stuart, S. J., and Wu, C. J. (2003). Molecular dynamics investigation in liquid-liquid phase change in carbon with empirical bond-order potentials. *J. Chem. Phys.*, **119**(12), 6053–6057.

Laio, A. and Parrinello, M. (2002). Escaping free energy minima. *Proc. Natl. Acad. Sci. U.S.A.*, **99**(12), 562.

Laird, B. B. and Leimkuhler, B. J. (2003). Generalized dynamical thermostating technique. *Phys. Rev. E.*, **68**, 016704.

Landau, A. I. (2002). A new method of molecular dynamic computer simulation at constant pressure. *J. Chem. Phys.*, **117**, 8607–8612.

Lee, H. K. and Swendsen, R. H. (2001). Simple model of liquid-liquid phase transitions. *Phys. Rev. B*, **6421**, 214102.

Leimkuhler, B. J. and Sweet, C. R. (2004). The canonical ensemble via symplectic integrators using Nosé and Nosé-Poincare chains. *J. Chem. Phys*, **121**(1), 108–116.

Lennard-Jones, J. E. (1924). *Proc. R. Soc. London, Ser. A.*, **106**, 463.

Likalter, A. A. (2002). Metallization of liquid iodine. *Physica A*, **308**, 355–367.

Lindemann, F. A. (1910). *Phys. Z.*, **11**, 609.

Liu, Y. and Tuckerman, M. E. (2000). Generalized Gaussian moment thermostatting: A new continuous dynamical approach to the canonical ensemble. *J. Chem. Phys.*, **112**, 1685–1700.

Mahoney, M. W. and Jorgensen, W. L. (2000). A five-site model for liquid water and the reproduction of the density anomaly by rigid, nonpolarizable potential functions. *J. Chem. Phys.*, **112**, 8910–8922.

Martonak, R., Laio, A., and Parrinello, M. (2003). Predicting crystal structures: The Parrinello-Rahman method revisited. *Phys. Rev. Lett.*, **90**(7), 075503.

Martyna, G. J., Klein, M. L., and Tuckerman, M. (1992). Nosé-Hoover chains - the canonical ensemble via continuous dynamics. *J. Chem. Phys.*, **97**, 2635–2643.

Martyna, G. J., Tobias, J. T., and Klein, M. L. (1994). Constant pressure molecular dynamics algorithms. *J. Chem. Phys.*, **101**(5), 4177–4189.

Martyna, G. J., Tuckerman, M. E., Tobias, D. J., and Klein, M. L. (1996). Explicit reversible integrators for extended systems dynamics. *Mol. Phys.*, **87**, 1117–1157.

Mausbach, P. and May, H. O. (2003). A MBWR equation of state of a core-softened fluid in 3d. *Fluid Phase Equil.*, **214**, 1–9.

McBride, C., Vega, C., Sanz, E., Macdowell, L. G., and Abascal, J. L. F. (2005). The range of meta stability of ice-water melting for two simple models of water. *Mol. Phys.*, **103**, 1–5.

Melchionna, S., Ciccotti, G., and Holian, B. L. (1993). Hoover NPT dynamics for systems varying in shape and size. *Mol. Phys.*, **78**, 533–544.

Metropolis, N., Rosenbluth, A. W., Rosenbluth, M. N., Teller, A., and Teller, E. (1953). Equation of state calculations by fast computing machines. *J. Chem. Phys.*, **21**(6), 1087–1092.

Mezei, M. (1980). Viral bias Monte-Carlo methods: efficient sampling in the (T,P,N) ensemble. *Mol. Phys.*, **40**, 901–906.

Militzer, B., Magro, W., and Ceperley, D. (1999). *Contrib. Plasma. Physics.*, **39**, 151–154.

Minary, P., Martyna, G. J., and Tuckerman, M. E. (2003a). Algorithms and novel applications based on the isokinetic ensemble. i. Biophysical and path integral molecular dynamics. *J. Chem. Phys.*, **118**, 2510–2526.

Minary, P., Martyna, G. J., and Tuckerman, M. E. (2003b). Algorithms and novel applications based on the isokinetic ensemble. ii. *Ab-initio* molecular dynamics. *J. Chem. Phys.*, **118**, 2527–2538.

Mishima, O. and Stanley, H. E. (1998a). Decompression-induced melting of ice-IV and the liquid-liquid transition in water. *Nature*, **392**, 364–168.

Mishima, O. and Stanley, H. E. (1998b). The relationship between liquid, supercooled and glassy water. *Nature*, **396**, 329–335.

Monaco, G., Falconi, S., Crichton, W. A., and Mezouar, M. (2003). Nature of the first-order phase transition in fluid phosphorus at high temperature and pressure. *Phys. Rev. Lett.*, **90**, 255701.

Morishita, T. (2001a). Liquid-liquid phase transitions of phosphorus via constant- pressure first-principles molecular dynamics simulations. *Phys. Rev. Lett.*, **8710**, 105701.

Morishita, T. (2001b). Structure of liquid phosphorus: A liquid-liquid phase transition via constant-pressure first-principles molecular dynamics. *Comput. Phys. Commun.*, **142**, 356–360.

Morishita, T. (2002). Phase transitions of liquid phosphorus: constant-pressure first-principles molecular dynamics simulations. *J. Non-Cryst. Solids*, **312**, 22–25.

Morris, J. R. and Song, X. (2002). The melting lines of model systems calculated from coexistence simulations. *J. Chem. Phys.*, **116**(21), 9352–9358.

Morris, J. R., Wang, C. Z., and Ho, K. M. (1995). Relationship between structure and conductivity in liquid carbon. *Phys. Rev. B*, **52**, 4138–4145.

Netz, P., Raymundi, J., Camera, A., and Barbosa, M. (2003). Dynamic anomalies of fluids with isotropic double-ranged potential. *Physica A*, **342**, 48–53.

Nosé, S. (1984a). A molecular-dynamics method for simulations in the canonical ensemble. *Mol. Phys.*, **52**, 255–268.

Nosé, S. (1984b). A unified formulation of the constant temperature molecular- dynamics methods. *J. Chem. Phys.*, **81**, 511–519.

Ogata, S. and Shibutani, Y. (2003). Ideal tensile strength and band gap of single-walled carbon nanotubes. *Phys. Rev. B.*, **68**, 165409.

Panagiotopoulos, A. Z. (1987). Direct determination of phase coexistence properties of fluids by Monte Carlo simulation in a new ensemble. *Mol. Phys.*, **61**, 813–826.

Pangali, C. and Rao, M. Berne, B. J. (1978). On a novel monte carlo scheme for simulating water and aqueous solutions. *Chem. Phys. Lett.*, **55**(3), 413–417.

Parrinello, M. and Rahman, A. (1980). Crystal structure and pair potentials: A molecular-dynamics study. *Phys. Rev. Lett.*, page 1196.

Parrinello, M. and Rahman, A. (1981). Polymorphic transitions in single-crystals - a new molecular- dynamics method. *J. Appl. Phys.*, **52**, 7182–7190.

Paschek, D. (2005). How the liquid-liquid transition affects hydrophobic hydration in deeply supercooled water. *Phys. Rev. Lett.*, **94**(21), 21780.

Pfaffenzeller, O. and Hohl, D. (1997). Structure and electrical conductivity in fluid high-density hydrogen. *J. Phys.: Cond. Matt.*, **9**(50), 11023–11034.

Polson, J. M., Trizac, E., Pronk, S., and Frenkel, D. (2000). Finite-size corrections to the free energies of crystalline solids. *J. Chem. Phys*, **112**(12), 5339–5342.

Poole, P. H., Sciortino, F., Essman, U., and Stanley, H. E. (1992). Phase behaviour of metastable water. *nature*, **360**, 324–328.

Poole, P. H., Sciortino, F., Essman, U., and Stanley, H. E. (1993). Spinodal of liquid water. *Phys. Rev. E.*, **48**(5), 3799–3817.

Press, W. H., Teukolsky, S. A., Vetterling, W. T., and Flannery, B. P. (1986). *Numerical Recipes*. Cambridge University Press.

Quigley, D. and Probert, M. I. J. (2004). Langevin dynamics in constant pressure extended systems. *J.Chem.Phys*, **120**(24), 11432–11442.

Quigley, D. and Probert, M. I. J. (2005). Constant pressure Langevin dynamics: Theory and application. *Comp. Phys. Comm.*, **169**, 322–325.

Rahman, A. (1964). Correlation in the motion of atoms in liquid argon. *Phys. Rev.*, pages A204–A411.

Ray, J. R. and Rahman, A. (1984). Statistical ensembles and molecular dynamics studies of anisotropic solids. *J. Chem. Phys.*, **80**(4423).

Rog, T., Murzyn, K., Hinsen, K., and Kneller, G. R. (2003). nmoldyn: A program package for a neutron scattering oriented analysis of molecular dynamics simulations. *J. Comput. Chem.*, **24**, 657–667.

Rosso, L., Minary, P., and Zhu, Z. (2001). On the use of the adiabatic molecular dynamics technique in the calculation of free energy profiles. *J. Chem. Phys*, **116**, 4389–4402.

Ryzhov, V. N. and Stishov, S. M. (2002). A liquid-liquid phase transition in the "collapsing" hard sphere system. *J. Exp. Theor. Phys.*, **95**, 710–713.

Ryzhov, V. N. and Stishov, S. M. (2003). Repulsive step potential: A model for a liquid-liquid phase transition. *Phys. Rev. E*, **67**, 010201.

Sadr-Lahijany, M. R., Scala, A., Buldyrev, S. V., and Stanley, H. E. (1998). Liquid-state anomalies and the Stell-Hemmer core-softened potential. *Phys. Rev. Lett.*, **81**, 4895–4898.

Sanz, E., Vega, C., Abascal, J. L. F., and Macdowell, L. G. (2004a). Phase diagram of water from computer simulation. *Phys. Rev. Lett.*, **92**, 255701.

Sanz, E., Vega, C., Abascal, J. L. F., and Macdowell, L. G. (2004b). Tracing the phase diagram of the four-site water potential (tip4p). *J. Chem. Phys.*, **121**, 1165–1166.

Sastry, S. and Angell, A. (2003). Liquid-liquid phase transition in supercooled silicon. *Nature. Mat.*, **2**, 739–743.

Scala, A., Sadr-Lahijany, M. R., Giovambattista, N., Buldyrev, S. V., and Stanley, H. E. (2000). Applications of the Stell-Hemmer potential to understanding second critical points in real systems. *J. Stat. Phys.*, **100**, 97–106.

Scala, A., Sadr-Lahijany, M. R., Giovambattista, N., Buldyrev, S. V., and Stanley, H. E. (2001). Waterlike anomalies for core-softened models of fluids: Two- dimensional systems. *Phys. Rev. E*, **6304**, 041202.

Scandolo, S. (2002). Liquid-liquid phase transition in compressed hydrogen from first-principles simulations. *Proc. Natl. Acad. Sci. U.S.A.*, **100**(6), 3051–3053.

Segall, M. D., Lindan, P. L. D., Probert, M. J., Pickard, C. J., Hasnip, P. J., Clark, S. J., and Payne, M. C. (2002). First-principles simulation: Ideas, illustrations and the CASTEP code. *J. Phys.: Cond. Matt.*, **14**(11), 2717–2743.

Senda, Y., Shimojo, F., and Hoshino, K. (2002a). The liquid-liquid phase transition of liquid phosphorus studied by *ab initio* molecular-dynamics simulations. *J. Non-Cryst. Solids*, **312**, 80–84.

Senda, Y., Shimojo, F., and Hoshino, K. (2002b). The metal-nonmetal transition of liquid phosphorus by *ab initio* molecular-dynamics simulations. *J. Phys.-Condes. Matter*, **14**, 3715–3723.

Sergi, A. (2003). Non-Hamiltonian equilibrium statistical mechanics. *Phys. Rev. E*, **67**, 021101.

Sergi, A., Ferrario, M., and Costa, D. (1999). Reversible integrators for basic extended system molecular dynamics. *Mol. Phys.*, **97**, 825–832.

Siepmann, J. I., McDonald, I. R., and Frenkel, D. (1992). Finite-size corrections to the chemical potential. *J. Phys.: Cond. Matt.*, **4**, 679–691.

Skibinsky, A., Buldyrev, S. V., Franzese, G., Malescio, G., and Stanley, H. E. (2004). Liquid-liquid phase transitions for soft-core attractive potentials. *Phys. Rev. E.*, **69**, 061206.

Smargiassi, E. and Madden, P. A. (1995). Free-energy calculations in solids from first-principles molecular dynamics: Vacancy formation in sodium. *Phys. Rev. B*, pages 117–128.

Smith, G. R. and Bruce, A. D. (1995). Multicanonical Monte Carlo study of solid-solid phase coexistence in a model colloid. *Phys. Rev. E.*, **53**(6), 6530–6543.

Souza, I. and Martins, J. L. (1997). Metric tensor as the dynamical variable for variable-cell- shape molecular dynamics. *Phys. Rev. B*, **55**, 8733–8742.

Stanley, H. E. (1971). *Introduction to phase transitions and critical phenomena*. Oxford University Press, New York.

Stillinger, F. and Rahman, A. (1974). Improved simulation of liquid water by molecular dynamics. *J. Chem. Phys.*, **40**(4), 1545–1557.

Stillinger, F. H. and Weber, T. A. (1985). Computer simulation of local order in condensed phases of silicon. *Phys. Rev. B.*, **31**, 5262–5271.

Stishov, S. M. (2002). On phase diagram of the system of "collapsing" hard spheres. *J. Exp. Theor. Phys.*, **95**, 64–66.

Sturgeon, J. B. and Laird, B. B. (2000). Symplectic algorithm for constant-pressure molecular dynamics using a Nosé-Poincare thermostat. *J. Chem. Phys.*, **112**, 3474–3482.

Sugino, O. (1999). Semi-empirical molecular dynamics study of the phase diagram of carbon at low pressure. *New Diam. Front. Carbon Technol.*, **9**, 93–105.

Sun, D. Y. and Gong, X. G. (2002). A new constant-pressure molcular dynamics algorithm for finite systems. *J. Phys.- Condens. Matter*, **14**, 487–493.

Tanaka, H. (1998). Fluctuation of local order and connectivity of water molecules in two phases of supercooled water. *Phys. Rev. Lett.*, **80**, 113–116.

Tersoff, J. (1986). New empirical-model for the structural-properties of silicon. *Phys. Rev. Lett.*, **56**, 632–635.

Tersoff, J. (1988). Empirical interatomic potential for silicon with improved elastic properties. *Phys. Rev. B*, **38**, 9902–9905.

Tersoff, J. (1989). Modeling solid-state chemistry - interatomic potentials for multicomponent systems. *Phys. Rev. B*, **39**, 5566–5568.

Togaya, M. (1997). Pressure dependences of the melting temperature of graphite and the electrical resistivity of liquid carbon. *Phys. Rev. Lett.*, **79**, 2474–2477.

Torrie, G. and Valleau, J. (1974). Monte Carlo free energy estimates using non-boltzmann sampling: Application to the sub-critical Lennard-Jones fluid. *Chem. Phys. Lett.*, **28**(4), 578–581.

Trebst, S., Huse, D., and Troyer, M. (2004). Optimizing the ensemble for equilibration in broad-histogram Monte Carlo simulations. *Phys. Rev. E.*, **70**, 046701.

Tse, J. S. and Klug, D. D. (1999). Structure and dynamics of liquid sulphur. *Phys. Rev. B*, **59**, 34–37.

Tuckerman, M., Berne, B. J., and Martyna, G. J. (1992). Reversible multiple time scale molecular-dynamics. *J. Chem. Phys.*, **97**, 1990–2001.

Tuckerman, M. E., Mundy, C. J., and Martyna, G. J. (1999). On the classical statistical mechanics of non-Hamiltonian systems. *Europhys. Lett.*, **45**, 149–155.

Tuckerman, M. E., Liu, Y., Ciccotti, G., and Martyna, G. J. (2001). Non-Hamiltonian molecular dynamics: Generalizing Hamiltonian phase space principles to non-Hamiltonian systems. *J. Chem. Phys.*, **115**, 1678–1702.

Umnov, A. G., Brazhkin, V. V., Popova, S. V., and Voloshin, R. N. (1992). Pressure temperature diagram of liquid bismuth. *J. Phys.-Condes. Matter*, **4**, 1427–1431.

van der Hoef, M. A. (2000). Free energy of the Lennard-Jones solid. *J. Chem. Phys*, **113**(18), 8142–8148.

Vanthiel, M. and Ree, F. H. (1989). Theoretical description of the graphite, diamond, and liquid- phases of carbon. *Int. J. Thermophys.*, **10**, 227–236.

Vega, C. (2005). "If you have an NPT, you have a Gibbs-Duhem" - Private communication.

Vega, C., Sanz, E., and Abascal, J. L. F. (2005). The melting temperature of the most common models of water. *J. Chem. Phys.*, **122**, 114507.

Verlet, L. (1967). Computer experiments on classical fluids. i. thermodynamical properties of Lennard-Jones molecules. *Phys. Rev.*, **159**, 98–103.

Wang, J. S, Y., Bai, J., Morris, J., and Zeng, X. C. (2005). Melting temperature of ice ih calculated from coexisting solid-liquid phases. *J. Chem. Phys.*, **123**, 036101.

Weir, S. T. and Mitchell, A. C. Nellis, W. J. (1995). Metallization of fluid molecular hydrogen at 140 GPa (1.4 mbar). *Phys. Rev. Lett.*, **76**(11), 1860–1863.

Wendt, H. R. and Abraham, F. (1978). Empirical criterion for the glass transition region based on Monte-Carlo simulation. *Phys. Rev. Lett.*, **41**(18), 1244–1246.

Wentzcovitch, R. M. (1991). Invariant molecular-dynamics approach to structural phase transitions. *Phys. Rev. B.*, **44**, 2358.

Widom, B. (1963). Some topics in the theory of fluids. *J. Chem. Phys*, **39**(11), 2808–2812.

Wilding, N. B. (1995). Critical-point and coexistence-curve properties of the Lennard-Jones fluid: A finite-size scaling study. *Phys. Rev. E.*, **52**(1), 602–611.

Wilding, N. B. (2001). Computer simulation of fluid phase transitions. *Am. J. Phys.*, **69**, 1147.

Wilding, N. B. and Bruce, A. D. (2000). Freezing by Monte-Carlo phase-switch. *Phys. Rev. Lett.*, **85**, 5138.

Wilding, N. B. and Magee, J. E. (2002). Phase behavior and thermodynamic anomalies of core-softened fluids. *Phys. Rev. E*, **66**, 031509.

Wu, C. J., Glosli, J. N., Galli, G., and Ree, F. H. (2002). Liquid-liquid phase transition in elemental carbon: A first- principles investigation. *Phys. Rev. Lett.*, **89**, 135701.

Yamada, M., Mossa, S., Stanley, H. E., and Sciortino, F. (2002). Interplay between time-temperature transformation and the liquid-liquid phase transition in water. *Phys. Rev. Lett.*, **88**, 195701.

Yokoyama, O. and Ono, S. (1985). Effective interatomic pair potentials in liquid polyvalent metals from observed structure data. *J. Phys. F: Met Phys.*, **15**, 1215.